WASM: Minerals, Energy and Chemical Engineering

Characterization of attenuation parameters at a variety of scales in volcanic rocks

María Del Pilar Di Martino Pérez

This thesis is presented for the collaborative Degree of
Doctor of Philosophy
of

University of Aberdeen
and

Curtin University

January 2022

Declaration

No portion of the work contained in this document has been submitted in support of an application for a degree or qualification of this or any other university or other institution of learning. All verbatim extracts have been distinguished by quotation marks, and all sources of information have been specifically acknowledged.

This work was done wholly while in candidature for a joint research degree between the University of Aberdeen (Home Institution) and Curtin University (Host Institution) as part of the Aberdeen-Curtin Alliance.

Signed: María Del Pilar Di Martino Pérez

Date: 31st January 2022 

Revision: 21st July 2022 

Abstract

Interpretation of seismic data is the most common geophysical method used for mapping and characterizing the interior of the Earth. Seismic imaging through heterogeneous structures is especially challenging in volcanic environments, in which an important portion of the seismic data is attenuated by seismic scattering and absorption, which manifest themselves as seismic coda waves. The relationship between the stochastic wave-packets comprised in the seismic coda, the total attenuation we can measure from them, and the intrinsic physical properties of the propagating medium are unclear. In this framework, this thesis explores the connection between advanced seismic imaging techniques, performed using attenuation and scattering parameters as attributes, with volcanic rock properties (petrophysical/mineralogical) and lays down the use of these parameters to develop new imaging techniques for heterogeneous sequences. This is tackled in three phases: First, I performed rock physics characterization of scattered wavefield to determine the main controls on coda attenuation. This was done by linking scattering attenuation measured from S-wave ultrasonic waveforms with the pore and grain systems of volcanic rocks defined by microscopy and imaging techniques. In this phase, the pore space was identified as the main driver of scattering in dry volcanic rocks. To sustain this conclusion, the second phase consisted of modelling elastic wavefields using spectral element methods. Here the individual impact of the number, size and location of the pores on the S-wave velocity, amplitudes and phases of the acquired waveforms was modelled and analysed. The results confirmed that for volcanic rocks of similar porosity the pore space topology controls ultrasonic S-wave propagation, as the transmitted waveform depends on the distribution and geometry of the pore structure. Finally, to upscale these observations to a real volcanic environment, seismic attenuation tomography was applied to field data. It was demonstrated that scattering and absorption mapping of a highly porous medium can provide structural constrains and map fluid pathways. The findings show the relevance of including stochastic attenuation parameters in the characterization of heterogeneous settings, like volcanoes, in which the analysis of phases provides insufficient details on the interactive processes taking place. This thesis is a multi-scale experimental, modelling and data-driven effort towards identifying and modelling the parameters that drive seismic attenuation, as a necessary step to interpret observations in the field.

Acknowledgements

First and foremost, I thank Prof Luca De Siena, for offering me the opportunity to develop this project and giving me the drive to keep going despite my constant pessimism. You are the best supervisor anyone could ask for. I would also like to express my gratitude to my co-supervisors, Dr Stephanie Vialle, Dr David Healy, and Prof Andrew Putnis for all your helpful feedback and advice that improved my work.

This work was funded by the Aberdeen-Curtin Alliance. I acknowledge the financial support and the help received from your administrative staff. Also, I thank the geophysics staff at both institutions. I am especially grateful to Maxim Lebedev and Andreas Beinlich for collaborating with me in the laboratory and helping me to further develop my experimental skills.

I acknowledge the funding received from the Mainz Institute of Multiscale Modeling for my research visit to the JGU of Mainz. I wish to extend my special thanks to the Cow's angels group, for making me feel welcome in your group and keeping me sane during the final writing period.

I would like to thank Joe and Mirella for your friendship. I owe a very special debt of gratitude to my friends Paola, Fabiola and Lourdes, for being there, believing in me and encouraging me in the hardest times. I also thank the friends for life I made in Aberdeen (Ying and Esti) and Perth (Ferial, Louis and Sophie) for always bringing joy to my life.

I want to express gratitude to my family for their unconditional love and support. And finally, Alberto, thanks for being my rock all these years.

Contents

List of Figures

List of Tables

Chapter 1

Introduction

1.1 Rationale and aims of this thesis

The primary source of information about the heterogeneous Earth comes from seismic data. As a result, a large and growing body of research has been published on seismic waves. Especially body- and surface waves have been extensively studied by many researchers to describe the dynamics of the Earth and to characterize reservoirs. However, seismic data from highly heterogeneous environments, such as volcanoes, are challenging to interpret because seismic waves are attenuated by multiple scattering and absorption (Sato et al., 2012). Consequently, imaging through basaltic sequences suffers from a loss in resolution caused by the high-frequency absorption of the volcanic rocks (Gallagher and Dromgoole, 2007; Eide et al., 2018). In recent years, a considerable amount of literature has focused on overcoming seismic attenuation effects to enhance the illumination of intra-basaltic sequences (e.g., Fliedner and White, 2001; Martini and Bean, 2002; Gallagher and Dromgoole, 2007; Woodburn et al., 2014).

Nevertheless, the attenuation information contained in all kinds of seismic data is routinely not used in industrial/seismological applications, mainly focusing on phases of coherent waves. New techniques like seismic wave interferometry have challenged the community, showing the need to consider and use multiple-scattering waves as

information sources (e.g., Grêt et al., 2006; Snieder, 2006; Planès and Larose 2013). However, such advanced techniques still disregard or simplify the effect of attenuation, anomalous scattering, and absorption in their forward modelling.

Attenuation information can be obtained from coda waves. Coda waves are late-time incoherent seismic intensities produced by scattering processes triggered by the presence of heterogeneities in the propagation medium (Aki, 1969; Sato et al., 2012). However, coda waves have not been researched similarly to coherent waves. Yet, they have proven to play a leading role in seismology, allowing to measure absorption and scattering properties of the medium from seismic observation (e.g., Calvet et al., 2013; De Siena et al., 2016; Del Pezzo et al., 2018). More recently, they have been used in tomographic approaches, especially in volcanic and fault media, as a tool with better sensitivity to magmatic intrusions and fluid flow than seismic velocity (e.g., Mayor et al., 2016; Prudencio et al., 2017; Napolitano et al., 2020).

This project proposes that better interpretation of heterogeneous sequences and monitoring of stored fluids/gases can be obtained by connecting seismic, petrophysical and mineralogical parameters. It aims to exploit novel advanced seismic imaging techniques, i.e. those using attenuation, scattering and absorption, and connects the retrieved parameters with measured petrophysical and mineralogical quantities. The results are a first step to calibrating and providing quantitative predictions of spatially varying properties of the medium using coda waves.

The final scope is to contribute to building computational forward models of seismic signals in heterogeneous volcanic media. To do that, we need to understand how this signal is scattered and attenuated based on rock physical controllers. As seismic coda attenuation has demonstrated potential in heterogeneous media (volcanoes, faults) but no proven quantitative link to rock properties, it is essential to perform rock-physics characterization of seismic attenuation from scattered wavefields. This can be achieved by studying the attenuation of coda waves at the sample scale. Accordingly, I conducted measurements of seismic and petrophysical properties of volcanic core samples and acquired optical and electron microscopy images, these methodologies are crucial to

characterize the heterogeneous medium. The qualitative analysis contributes to defining the main parameters controlling seismic attenuation at multiple scales. The outcome is used to simulate the propagation of elastic waves. A numerical modelling approach is applied to reconstruct the experimental observations in synthetic samples that mimic the volcanic rocks. Finally, the attenuation markers, like scattering and absorption, are used with field data to assess their contribution towards characterizing volcanic environments: scattering and absorption mapping provide complementary geophysical images that help to better constrain the structure and fluid location in volcanoes.

A definitive link between rock physics parameters, mineralogy and seismic attenuation parameters in volcanic rocks is not straightforward to deliver because of the number of variables contributing to the relation between the stochastic wave-packets comprised in the seismic coda, the total attenuation we can measure from them and the intrinsic physical properties of the propagation medium. After all the research done in this thesis, there is still room to reach a benchmark. Notwithstanding, the outcome of this study provides valuable insights such as the role of pore space topology on the propagation of elastic waves, and the relevance of including attenuation parameters in the characterization of the heterogenous medium. This study demonstrates through volcano imaging that attenuation information obtained from coda waves is useful to reduce uncertainties in the modelling of sub-basaltic reservoirs, including the mapping of fluid pathways in hydrothermal systems, setting up the basis for their wider application in industrial settings. Consequently, this thesis sets the basis for future use of attenuation parameters to contribute to imaging techniques in the field.

1.2 Seismic Attenuation

Traditionally, seismic imaging has been focussed on travel time tomography (e.g., by raytracing of body or surface waves). Recently, attenuation tomography has become a standard imaging technique (e.g., De Siena et al., 2016, 2017a; Del Pezzo et al., 2016;

Sketsiou et al., 2020; Nardoni et al., 2021). Seismic attenuation refers to the loss in energy that the seismic waves experience when propagating through a medium. Several mechanisms are involved in the dissipation of seismic energy: the energy of the wavefront decreases with the distance travelled away from the source (this is known as spherical divergence or geometrical spreading). On the other hand, during propagation, the seismic energy is attenuated by the interaction with the properties of the medium through absorption and scattering. Absorption (also called intrinsic or anelastic attenuation) is the energy loss due to anelastic processes or internal friction, while scattering (also called extrinsic or elastic attenuation) is the energy redistribution due to the presence of scatterers. These energy dissipations can occur at any scale, from grain/pores to field scale, consequently, seismic attenuation is becoming a key instrument to improve the characterization of heterogeneous Earth media from lithospheric ([100-1000 km] Mayor et al., 2016) to a fault ([10-50 km] Napolitano et al., 2020) and, especially, volcanic scale ([5-10 km] Prudencio et al., 2013; [0.5-5 km] De Siena et al., 2017b). In this thesis, I estimated coda attenuation parameters at the rock sample scale ([mm-cm] laboratory, Chapter 2) and the field scale ([m] near-surface, Chapter 4).

The attenuation of seismic waves due to the properties of the propagating medium is usually described by the quality factor Q. This term is used to describe attenuation as an anelastic damping system, Q is defined as a dimensionless quantity related to the fractional loss of energy per cycle (Aki and Richards, 1980; Mckenzie et al., 1982):

$$Q = -\frac{2\pi E}{\Delta E} \qquad \text{(Eq. 1.1)}$$

where E is the total elastic energy of the wave, and ΔE is the energy loss per cycle. That being the case, the energy dissipated in a cycle, as the waves propagate through a heterogeneous medium, is inversely proportional to the quality factor: a high-quality factor indicates low attenuation and vice-versa. Thus, the total attenuation Q^{-1} is quantified as the inverse of the quality factor. The total attenuation is expressed as:

$$Q_T^{-1} = Q_i^{-1} + Q_s^{-1} \quad \text{(Eq. 1.2)}$$

where Q_i^{-1} and Q_s^{-1} denote the intrinsic and scattering attenuation respectively. The intrinsic attenuation, also known as absorption, is related to the conversion of energy into heat while passing through a medium; while scattering attenuation is related to the energy changes caused by the presence of inhomogeneities in the medium. The scattering losses depend on the ratio between the wavelength (λ) and the dimension of the heterogeneities (d) (Mavko et al., 2009). The choice of the computational method to simulate elastic wave propagation depends strongly on this relation (Igel, 2016).

Following the pioneering work of Kuster and Toksöz (1974), theoretical and experimental formulations of the attenuation of seismic waves have been investigated by using rock samples in the laboratory. Sandstones and carbonates rocks have been the main focus of these analyses, given the industry interest to interpret seismic measurements at reservoir scale in terms of petrophysical parameters (Nur et al., 1998). In recent years, there has been an increasing interest in researching volcanic rocks (e.g., Durán et al., 2019; Heap et al., 2020; Butler, 2020; Heap and Violay, 2021) to provide a better interpretation of volcanic processes. Broadly speaking, wave propagation in volcanic heterogeneous media is affected by numerous factors including porosity, mineralogical composition, alteration, and microstructure (pores and grains sizes and shapes), among others. The understanding of their contribution represents a significant challenge because the complex composition of volcanic rocks makes it difficult to determine the influence of a single variable (Liu et al., 2017). Over the past decade, major advances in the apparata used to measure seismic attenuation at the laboratory (e.g., Tisato and Madonna, 2012; Subramaniyan et al., 2014) have allowed calibrating sample-to-field scale observations (e.g., Pistone et al., 2021).

Coda Wave Attenuation

The quantification of Q^{-1} can vary based on the segment of the seismogram used to measure the attenuation of the seismic waves (Calvet and Margerin, 2013). Research usually focuses on three types of total attenuation Q_p^{-1}, Q_s^{-1}, and Q_c^{-1}. The Q_p^{-1} and Q_s^{-1} describe the energy losses of the coherent *P*- and *S*- waves packets, respectively, while Q_c^{-1} refers to the attenuation of the coda waves. Coda waves are incoherent wave packets arriving at late times in the seismogram. These wave trains are stochastic in nature and highly sensitive to small-scale heterogeneities (Aki, 1969). Coda waves in the seismograms are mostly comprised of S-waves (Shapiro et al., 2000). Hereafter, the mention of coda waves in this thesis refers to the waves arriving after the direct S-wave packet. In coda waves, the scattering attenuation produces a re-distribution of the energy for which the propagation characteristics, along the path between source and receiver, can be described by the single-scattering regime (Aki and Chouet, 1975). As the lapse time (or travel distance) increases, multiple scattering occurs, and then the multiple scattering regime dominates (Margerin et al., 2000). In the presence of strong scattering interactions, the phase information of the coherent waves is completely lost, and the diffusion regime takes place (Wegler, 2003). These scattering regimes depend on frequency and lapse time (De Siena et al., 2013). Generally, multiple scattering is considered the most appropriate to describe coda waves, as the single-scattering regime is only suitable for the early coda while the relevance of multiple scattering increases at late coda times (Del Pezzo et al., 2018).

The amplitude of coda waves tends to decrease with increasing lapse time; this decay is evident in the envelope of the seismograms (Aki and Richards, 1980; Sato et al., 2012). Thus Q_c^{-1} is usually quantified from the envelope of the coda waves. Following equation 1.2, coda wave attenuation Q_c^{-1} is expressed as: $Q_c^{-1} = Q_{ci}^{-1} + Q_{cs}^{-1}$ (Calvet et al., 2013; Shapiro et al., 2000). To quantify the independent contribution that intrinsic attenuation and scattering attenuation have on the total coda attenuation is challenging. Qualitatively, intrinsic attenuation of coda waves is usually attributed to fluid flow and thermal relaxation while scattering attenuation is mainly credited to structural changes along the path (Sato et al., 2012). It is important to clarify that for the means of this study,

I interpreted the coda attenuation measured at the laboratory scale as a direct measurement of scattering, given the absence of fluids in the medium (see Chapter 2 for a deeper insight); while at the field scale the coda attenuation is considered a direct measurement of intrinsic absorption, given the multiple scattering taking place (see Chapter 4 for a deeper insight).

In this thesis, I applied two methodologies for measuring seismic attenuation parameters: (1) the coda decay method (Aki and Chouet, 1975; Calvet and Margerin, 2013), in section 2.3.1 (Fig. 2.2) I describe the expressions to quantify coda attenuation using the coda decay method in waveforms measured at the laboratory scale [mm-cm], while in section 4.3.2 this method is used to map seismic absorption at the field scale; and (2) the peak delay method (Saito et al., 2002; Takahashi et al., 2007), in section 4.3.1 I describe the expressions for the use of this method to map scattering attenuation. Mapping attenuation parameters as absorption and scattering is called attenuation tomography. In practice, as with travel-time tomography, attenuation tomography requires solving an inverse problem to match the model parameters with the observed data. In attenuation tomography, the spatio-temporal variations of coda attenuation can be estimated using sensitivity kernels (e.g., Prudencio et al., 2013; Obermann et al., 2013; Sketsiou et al., 2020). These sensitivity kernels are space-weighting functions created assuming or imposing a spatially homogeneous medium. (Del Pezzo et al., 2016, 2018). The energy envelopes of the seismograms used to compute these kernels are described using the approximation of the energy transport equation developed by Paasschens (1997). Synthetic tests, like the checkerboard test, are often used to assess the reliability of the solutions. In the last decade, attenuation tomography has been successfully applied to map: the volcanic system of Tenerife Island (Prudencio et al., 2013); the crustal structure of the Alps (Mayor et al., 2016); the seismogenic transition zone in the Southern Apennines (Napolitano et al., 2020); the Mt Etna volcanic region (Ibáñez et al., 2020); and to reconstruct local, regional, and global structural features across Italy and the Tyrrhenian Sea (Nardoni et al., 2021), among other applications. In Chapter 4, I applied attenuation tomography for mapping the hydrothermal system of the Solfatara Volcano.

1.2.1 Modelling of seismic wave propagation.

Computational modelling for the propagation of seismic waves in heterogeneous media can be tackled by several methods (Carcione, 2015). Within this project, I applied two different approaches: (1) radiative transfer theory (RTT) to forward-model coda envelopes (e.g., Appendix D), because RTT is an appropriate method to connect the stochastic nature of the coda waves propagating in random media with their energy changes recorded in the seismograms (Przybilla and Korn, 2008); and (2) spectral element methods (SEM) to model elastic wave propagation (in Chapter 3), given that SEM allows to accurately model ultrasonic propagation in a heterogeneous medium (Rosenkrantz et al., 2019).

Radiative Transfer Theory (RTT)

Radiative Transfer Theory was originally developed to describe electromagnetic radiation and has been adapted to many disciplines including seismic wave propagation. RTT can be numerically solved by Monte Carlos simulations to describe statistically the propagation of seismic waves in heterogeneous media following a Born approximation (Przybilla and Korn, 2008). It is the predominant approach used for modelling seismic coda envelopes in multiple scattering and diffusive regimes because allows describing a background medium based on statistics approximations that fit autocorrelation functions (Margerin et al., 2000; Przybilla et al., 2006). This condition gives the advantage of modelling challenging structures without the need to define dense meshes. Two main parameters are key to modelling the random perturbation field: the correlation length a, an indicator of the characteristic scale length of the heterogeneities; and the root mean square of velocity fluctuations ε, an indicator of the strength of the scattering (Sato et al., 2012). Radiative transfer solutions are comparable with solutions obtained using full-waveform modelling with a finite difference method (e.g., Przybilla et al., 2006; Obermann et al., 2013). Wei and Fu (2014) and Hu et al. (2018) used this approach at the laboratory scale to understand stress-associated mechanisms on the ultrasonic coda. In this thesis, I directly implemented RTT by transforming a standard code of the 2D field-scale approach for the modelling of stochastic seismic envelopes (De Siena et al., 2013)

to its 3D form, downscaling it to the rock sample scale, and including boundary conditions.

Spectral Element Method (SEM)

SEM is a tool developed for fluid dynamics whose application has recently extended to seismic wave propagation. The SEM merges the accuracy of the global pseudo-spectral method with the flexibility of the finite-element method (Komatitsch and Tromp, 1999). It is a continuous Galerkin technique well suited to work with non-structured meshes, that works to solve the elastodynamics equation in the time domain (Rosenkrantz et al., 2019). In seismology, the SEM is built upon an integral (mathematically known to be a weak implementation) of the equation of motion over the study domain. First, the volume (or area) is meshed, i.e. subdivided into non-overlapping elements for mapping. The wavefield on these elements is discretized using Lagrange polynomials that are integrated over the domain using the Gauss-Lobatto-Legendre integrations rule (Tromp et al., 2008). In this thesis, I implemented SEM to simulate ultrasonic wave propagation using the software package SPECFEM2D (Komatitsch and Vilotte, 1998).

1.3 Data and Methods

This section presents an overview of the data used and the experimental, modelling, and imaging methodologies applied within this thesis. These are presented in an order broadly following their application from Chapter 2 to Chapter 4.

1.3.1 Experimental methods

Volcanic rock samples

Seismic imaging through heterogenous structures is especially challenging in volcanic environments. Volcanic media are then the ideal setting to calibrate coda attenuation parameters. Hence volcanic rock samples are appropriate to test the hypotheses posed in this thesis. Given that sub-basaltic and intra-basaltic sequences are responsible for high-frequency absorption which corrupts and biases imaging (Woodburn et al., 2014), basalts rocks were chosen to perform the experimental phase of this thesis. Initially, the study dataset consisted of 180 volcanic rocks from three regions: field-based (outcrops) collected samples from Iceland and Skype Island, and borehole collected samples from Hawaii. These core samples cover a diverse range of volcanic facies from dense crystalline basalt to highly porous vesicular basalt and hyaloclastites. Given the required time and costs necessary to evaluate each sample the dataset was eventually reduced to 25 cored samples. A unique source location (Hawaii) was preferred in order to have consistency in the geology of the samples (e.g., age, lithology, etc.). The selection of the samples was based on the tangible quality of the core and the availability of a range of porosity within the dataset.

Figure 1. 1. Photograph of some volcanic rock samples used in this project. From left to right: sample 2H, 4H, 6H, 7H, 14H and 20H.

The 25 selected rock samples presented in this thesis were provided by the Volcanic Basin Petroleum Research (VBPR). These rocks are volcanic facies from the Big Island of Hawai'i (Figure 1.1), cored on the PTA2 and KMA1 boreholes located within the Mauna Kea and Mauna Loa volcanoes (Figure 1.2). The core plugs used in this study were drilled over a depth interval of 300 m to 1800 m, they correspond to sequences of 'A'ā Lava and Pāhoehoe lava with various degrees of alteration and secondary mineralization. These volcanic rocks contain a wide distribution of minerals and pores. In volcanic rocks, vesicles from lava flow sequences are an indication of the degassing processes that drive most volcanic eruptions (Shea et al., 2010).

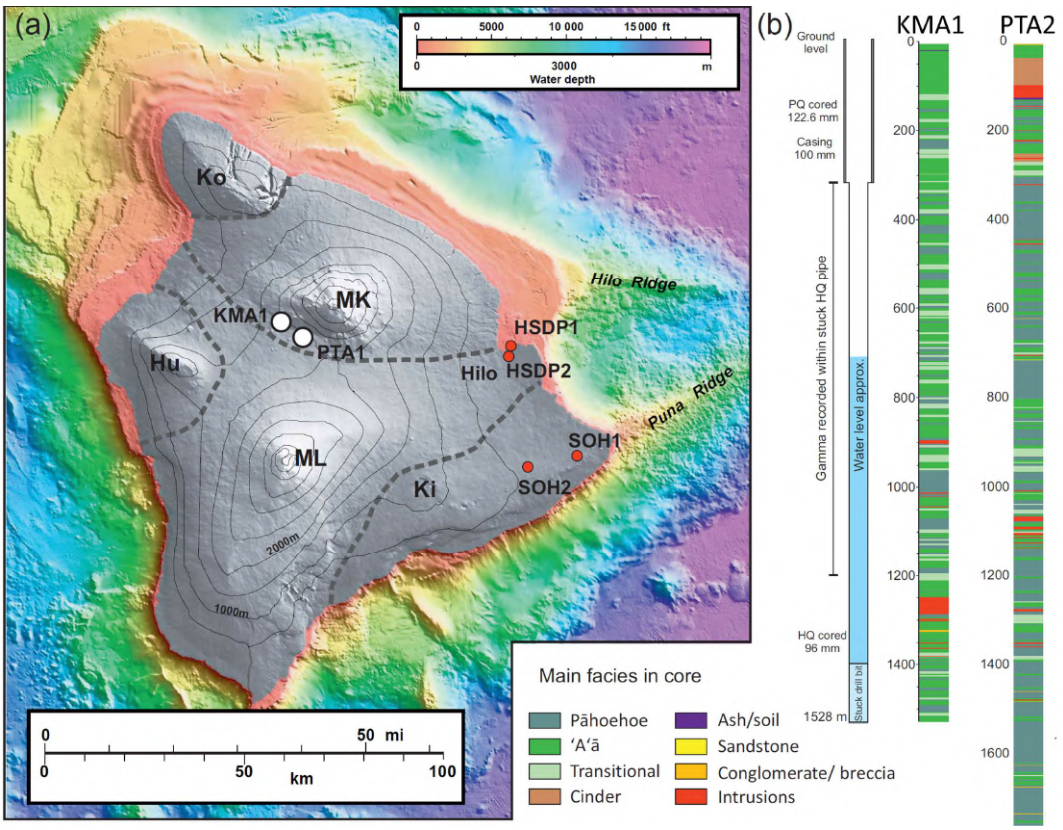

Figure 1. 2. Location map and cored sections of the PTA2 and KMA1 boreholes. MK: Mauna Kea, ML: Mauna Loa. Modified from Fig 1 in Jerram et al. (2019).

The description of the samples and the methods utilized to estimate their petrophysical properties are outlined in section 2.2 and Appendices A1 and A2. The volcanic rock samples were used to link petrological and mineralogical properties to coda attenuation parameters for the analysis presented in chapter 2. The variety of pores geometry and vesicles between and within the samples was appropriate to evaluate the effect of pores and grain system in ultrasonic propagation, given the impact that the dimension of the scatters have on driving seismic attenuation in heterogenous environments. However, the preservation of frequency when doing the acquisition of ultrasonic waveforms was a major drawback of using these samples, because the loss of high-frequency information limited the number of wavelengths recorded on the samples.

Ultrasonic measurements

Laboratory experiments are a common approach to characterize the relations between the elastic properties of rock samples and their physical properties. Typically, the seismic attenuation measured at the laboratory is related to shear wave attenuation Q_s^{-1} and/or compressional wave attenuation Q_p^{-1}. At seismic frequencies, the forced oscillation method is an appropriate methodology to measure attenuation from the phase shift between applied stress and the resultant strain (Subramaniyan et al., 2014; e.g., Tisato and Madonna, 2012; Tisato and Quintal, 2013). While at ultrasonic frequencies, $Q_p^{-1}$and Q_s^{-1} are usually measured by the spectral ratio method where the spectrum of the wave package acquired in the rock is compared to the one acquired in a reference material of low attenuation (e.g., aluminium) (Toksöz et al., 1979; e.g., Guo and Fu, 2007). In the laboratory, measuring of amplitude dependant parameters, like coda wave attenuation Q_c^{-1}, is challenging. The repeatability of the experiments is hindered by a range of experimental conditions: reflections and conversions of coherent waves at the physical boundaries of the samples, the sample size that restricts the number of wavelengths that could propagate, the roughness of the samples and their coupling with the electronics, the limitations of the laboratory apparatuses (McKenzie et al., 1982; Fujisawa and Takei, 2009; Zhang et al., 2014; Subramaniyan et al., 2014; Yoshimitsu et al., 2016). In this thesis, I tried out different methods and strategies to acquire ultrasonic waveforms with enough signal-to-noise ratio at late times in order to record coda waves (see Appendix

A3). The results presented in the thesis correspond with the ultrasonic S-wave transmission method (implementation details in section 2.3.1), where two transducers are employed at both end-sides of the rock sample, to act as source and receiver respectively. In this method, the attenuation is measured from the amplitude decay of the energy of the transmitted pulse with time. The S-wave transmission method was appropriate for the analysis presented in chapter 2 because: (1) it allowed me to acquire waveforms long enough to have a coda window suitable to apply the coda decay method; and (2) it gave higher accuracy with regards to the repeatability of the measurements between the tested methods. However, despite the efforts done in this study to overcome the experimental challenges of acquiring coda waves in rock samples, the uncertainty of the coda attenuation estimation is relatively high. Better calibrations are still needed for scattering attenuation measurements at ultrasonic frequencies.

Image analysis

The analysis of optical microscope images provides a powerful tool for quantifying microstructural properties within rock samples. Hence, this method was chosen to do a petrological characterization of the volcanic samples. The acquired digital images were appropriate to develop a 2D textural analysis that allow me to quantify the heterogeneity level of the samples. The images were acquired from polished thin sections of 21 rock samples (Appendix A5). To create the thin sections, I cut a slice of the rock from one end of all the core plugs. After polishing them, the discs were sent to the Adelaide Petrographic Laboratories to produce thin sections of 32 μm thick. Then, I acquired the images using an optical microscope (Figure 1.3).

The optical microscope is a visualization instrument used to enlarge the sizes of specimens that otherwise could not be observed by the human eye. It works by focusing a beam of light through a thin sectioned object and then using a system of glass lenses to magnify the images. I acquired the digital images of the thin sections using the microscope Zeiss Axio Imager.M2m under plane-polarized and cross-polarized light conditions (Figures 1.3 and A5). The cross-polarized images help to observe the cleavage and colour characteristics of the minerals for their identification. To perform this analysis,

I received training on the use of the microscope from the Geology Department at Curtin University. I used the digital images as a first instance to describe the samples qualitatively in terms of their matrix type and mineral content, then to estimate porosity using binary segmentation in the software ImageJ (Figure A1.1).

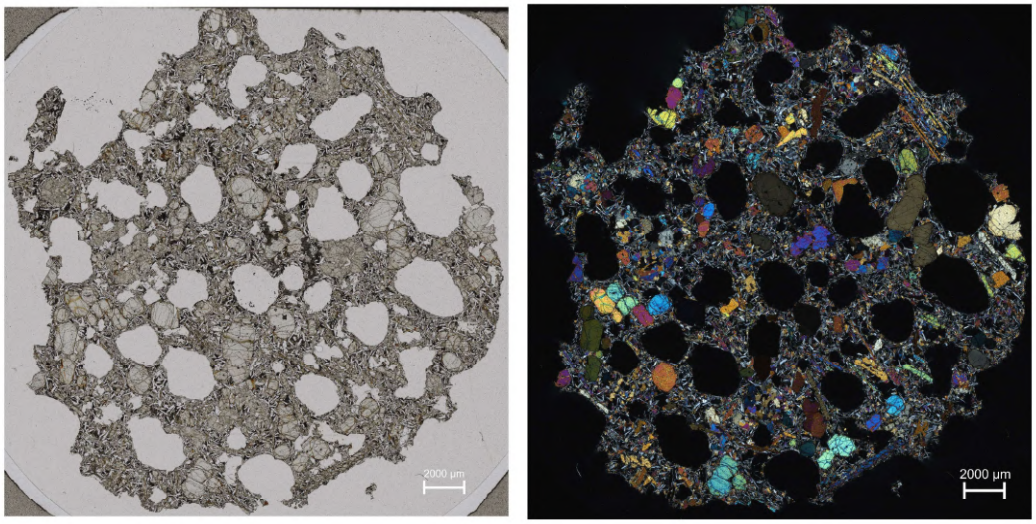

Figure 1. 3. Optical images for rock sample 6H under plane-polarized (left) and cross-polarized (right) light conditions.

Mineral mapping

The mineral mapping method was chosen to characterize the mineral distribution in the samples in terms of grain size and composition. I produced a mineral mapping of the samples using the automatic mineral segmentation of the Tescan Integrated Mineral Analyzer (TIMA) acquisition system (Figure 1.4). To perform this analysis, I received training in Microanalysis and Scanning Electron Microscope (SEM) at the Jhon de Laeter Centre, certified by the Australian Microscopy & Microanalysis Research Facility. The TIMA is an analytical field emission scanning electron microscope (FESEM) that allows the classification of the composition and morphology of the samples. It is equipped with backscattered electron (BSE) imaging and energy-dispersive X-ray spectroscopy (EDS)

detectors. The BSE image and EDS data are collected simultaneously to detect boundaries between mineral phases. The polished thin sections are examined in an electron microscope.

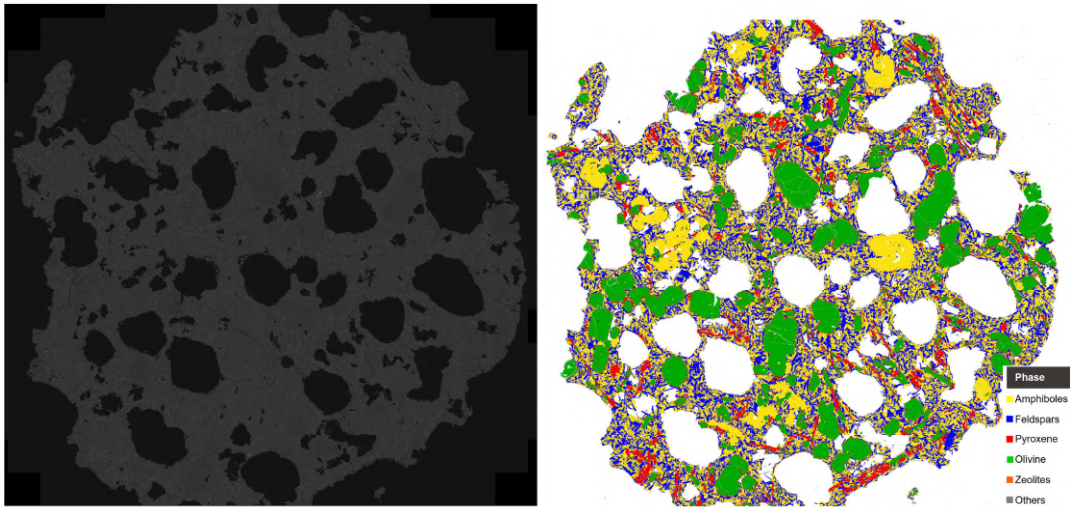

Figure 1. 4. Backscattered Electron image (BSE-left) and mineral mapping (right) for the rock sample 6H.

The underlying principle is that an electron beam is focused on the sample, as this sample is made up of atoms, the primary electron beam spread and penetrates the sample interacting with the atoms of the sample. This interaction typically produces three types of signals: secondary electrons SE, backscattered electrons BSE, and X-rays. The spatial resolution of these signals gives information about the shape, atomic number Z, and elements, respectively. The BSE will form different patterns based on the composition and orientation of the grains that are recorded and imaged by The TIMA acquisition system. On the other hand, the X-rays, detected by the energy dispersive detector, are displayed as a spectrum of the intensity of the signal versus energy. This spectrum allows me to identify the mineral composition of the sample, given that the elements in the samples can be identified by their characteristics X-ray energies, and their concentration by the intensity of their Characteristics X-ray peaks. After identifying and delimiting the minerals in the sample, it is possible to quantify phase abundance and grain size (Figures

2.7 and 2.8). The resultant mineral mapping of the thin sections is in Appendix A5. This method was appropriate to evaluate if and how the mineralogical arrangement in the volcanic rock samples drives the coda attenuation in Chapter 2.

X-ray computed tomography

Digital rock physics (DRP) has proved to be successful in providing information on the microstructural properties of rocks (Andrä et al., 2013; Ikeda et al., 2020). The technique is based on scanning the rock samples employing X-ray microcomputed tomography μxCT, a non-invasive acquisition method for visualizing the interior of solid objects. In this thesis, this technique was applied to characterize the pore space. Only five samples were analysed due to limited resources, the chosen five samples cover the full range of porosities. This method was appropriate to describe the samples in terms of their pore size distribution, as it allows to do a 3D map of the internal structure of the cores and quantify the sphericity level and size of the pores, and the relative measurement of heterogeneities level (correlation length) at the pore scale. The 3D digital images of the internal microstructure were generated using the micro-CT scanner Versa XRM 500 from Zeiss-XRadia at the Rock Physics Laboratory of Curtin University. The acquisition consists of a source that emits X-rays at an object with a rotational geometry, as the electrons interact with the object along multiple-beam paths the X-ray intensity is attenuated, and then the decrease in intensity is measured by a series of detectors that quantify the proportion of X-rays attenuated (either scattered or absorbed) as they pass through the object (Cnudde and Boone, 2013). The digital information is processed as CT images, each image corresponds to a slice of the object along the rotational axis. The 3D images are made up of elements called voxels. The stack of these images turns into a volume (Withers et al., 2021). After digital imaging, the next step is processing the raw images to separate pores and matrix phases through segmentation (Andrä et al., 2013). Segmentation consists in assigning a material (e.g., pore, mineral) to each voxel of the image. A common segmentation technique is the watershed algorithm (Beucher and Meyer, 1993). This algorithm simulates the flooding of a topological profile: the high- and low-intensity values of an image represent hills and valleys, respectively; the local minimal (isolated valleys) are filled up with different labels (water type) until the water

level reaches the highest peak; this will create a profile partitioned into regions (or basins separated by dams) called watersheds (Markussen et al., 2019). I performed this processing using the software Avizo (AVIZO, 2019), see details in section 2.3.2. A major drawback when analysing the microstructure of rock samples using X-ray microcomputed tomography is the resolution of the tomogram concerning the pore space size. In this study, the resolution of the images acquired (22 μm) is enough for the analyses performed in chapter 2 because pores with sizes below 0.022 mm are not comparable with the wavelength acquired in the ultrasonic experiments, hence it is suitable to use this method to measure the heterogeneity level.

1.3.2 Modelling methods

In this study, I apply a 2D numerical simulation of elastic wave propagation inside rock samples to obtain insights into the waveform behaviour as a function of the pore distribution. To achieve this, I use the software SPECFEM2D (Komatitsch and Vilotte, 1998), an open-source code for two-dimensional seismic wave propagation based upon the spectral-element method (SEM) (Tromp et al., 2008). The SEM solves the integral (or weak form) of the wave equation in the time domain over a non-structured mesh of elements (i.e., spectral elements). This method was chosen because it is computational stable to model ultrasonic waves at a laboratory scale (mm-cm). As the intrinsical equations of the SEM naturally smooth boundary conditions inside the medium, this is an appropriate method for the simulations done in Chapter 3, in which I wanted to avoid internal interactions at the boundaries of the pores. SPECFEM2D was selected to apply SEM because it is an open-source software of relatively easy implementation. However, in this software perfectly matched layer (PML) boundary conditions are not implemented for S-wave propagation, hence I used Stacey boundaries conditions.

Here, I present a brief overview of the implementation of the code for the simulations computed for this thesis. The following equations are taken from Komatitsch and Tromp

(1999), Tape et al. (2007), Tromp et al. (2008), Rosenkrantz et al. (2019) and the user manual of SPECFEM2D.

Equation of motion

The elastic wave equation (in its strong form) can be expressed as:

$$\rho \partial_t^2 s - \nabla T = f \qquad \text{(Eq 1.3)}$$

Where ρ is the density; ∂_t^2 is the second partial derivative in time t; s is the displacement; T is the stress tensor in terms of strains, which in the isotropic case is related to the stiffness tensor in terms of bulk and shear moduli; and f is the force that represents the seismic source.

The force f can be written in terms of the moment tensor M as:

$$f = -M \cdot \nabla \delta(x - x_s) S(t) \qquad \text{(Eq 1.4)}$$

Where $S(t)$ is the source-time function, x_s is the source location, and δ is the Dirac delta.

For computational purposes, SEM works with a weak form (integral) of the wave equation. This is done by dotting (1.3) with an arbitrary test vector w and integrating by parts over the study domain Ω, as follows:

$$\int_\Omega \rho w \partial_t^2 s \, d^2x = -\int_\Omega \nabla w : T \, d^2x + M : \nabla w(x_s) S(t) \qquad \text{(Eq 1.5)}$$

In Eq 1.5, the left term represents the mass matrix, the middle term the stiffness matrix and the right term the source factor. Note that the ':' symbol represents a double tensorial contraction operation. The boundary conditions ($\partial\Omega$) vanish at the free boundaries Γ in which the traction vector $T \cdot \hat{n} = 0$, where $\hat{n}$ is a vector normal to the surface. At the internal

boundaries, both the displacement and the traction need to be continuous, while the waves that travel out of the domain need to be absorbed. For transversely isotropic media this is:

$$T \cdot \hat{n} = \rho[v_n(\hat{n} \cdot \partial_t s)\hat{n} + v_1(\hat{t_1} \cdot \partial_t s)\hat{t_1} + v_2(\hat{t_2} \cdot \partial_t s)\hat{t_2}] \qquad \text{(Eq 1.6)}$$

where $\hat{t_1}$ and $\hat{t_2}$ are orthogonal unit vector tangential to the absorbing boundary Γ with unit outward normal $\hat{n}$, v_n refers to the P-wave velocity in the $\hat{n}$ direction; v_1 the S-wave velocity in the $\hat{t_1}$ direction and v_2 the S-wave velocity in the $\hat{t_2}$ direction. This equation is added as a fourth term to Eq. 1.5 integrated over Γ when boundary conditions are imposed.

Meshing

The model domain Ω is subdivided into a number of non-overlapping elements Ω_e, e=1,…,n_e. The SEM in 3D is generally restricted to hexahedral elements (i.e., deformed cubes). In 2D quadrangles (i.e., deformed squares) may be used. I created the meshing using a frontal-Delaunay algorithm with GMSH (GNU finite element mesh generator - Geuzaine and Remacle, 2009). For mapping, an element of area $d^2x=dxdz$ within a given Ω_e is related to an element of area $d^2\zeta=d\zeta dn$ in the reference square by $d^2x=Jd^2\zeta$ where J is the Jacobian. The mesh generation should ensure a positive Jacobian to guarantee that the mapping from the reference cube is unique and invertible. The geometry of an element Ω_e is defined in a local coordinate system (ε,η), with a set of control points $x_a=x(\varepsilon_a,\eta_a)$ and shape functions $N_a(\varepsilon,\eta)$, typically products of Lagrange polynomials of degree n_l, which correspond to n_l +1 Gauss-Lobatto-Legendre (GLL) points to simplify the algorithm. For the meshes of the synthetic samples, I used 4-node convection (i.e., 5 GLL).

Solution

Any function g that can be resolved by the SEM can be expressed in discrete form as:

$$g(x(\varepsilon,\mathfrak{y})) \approx \sum_{\alpha,\beta=0}^{\mathfrak{y}_l} g^{\alpha\beta} l_\alpha(\varepsilon) l_\beta(\mathfrak{y}) \qquad \text{(Eq 1.7)}$$

Where $g^{\alpha\beta} = g(x(\varepsilon_\alpha, \mathfrak{y}_\beta)$, and l_α and l_β are Lagrange polynomials of degrees α and β, respectively. Using this polynomial representation, the gradient of a function ∇g evaluated at any of the Gauss-Lobatto-Legendre points $x(\varepsilon_{\alpha'}, \mathfrak{y}_{\beta'})$, where a prime denotes differentiation, may be written in the form:

$$\nabla g(x(\varepsilon,\mathfrak{y})) \approx \sum_{i=0}^{2} \hat{x}_i \left[\sum_{\alpha=0}^{\mathfrak{y}_l} g^{\alpha\beta'} l'_\alpha(\varepsilon_{\alpha'}) \partial_i \varepsilon + \sum_{\beta=0}^{\mathfrak{y}_l} g^{\alpha'\beta} l'_\beta(\mathfrak{y}_{\beta'}) \partial_i \mathfrak{y} \right] \qquad \text{(Eq 1.8)}$$

Integration over the surface elements Γ_b using the GLL rule leads to:

$$\int_{\Gamma_b} g(x) d^2x = \int_{-1}^{1} \int_{-1}^{1} g(x(\varepsilon,\mathfrak{y})) J_b(\varepsilon,\mathfrak{y})\, d\varepsilon d\mathfrak{y} \approx \sum_{\alpha,\beta=0}^{\mathfrak{y}_l} \omega_\alpha \omega_\beta g^{\alpha\beta} J_b{}^{\alpha\beta} \qquad \text{(Eq 1.9)}$$

Where $J_b^{\alpha\beta} = J_b(\varepsilon_\alpha, \mathfrak{y}_\beta)$ and $\omega_\alpha, \omega_\beta$ denote the weights associated with the Gauss-Lobatto-Legendre points of integration.

Thus, to solve the momentum equation (Eq 1.5), we evaluate each of the three terms, in terms of the Lagrange polynomials using the GLL integration rule. The elemental SEM source matrix is determined by: (Eq 1.10)

$$\int_{\Omega_e} \rho w \partial_t^2 s \, d^2x$$

$$= \int_{-1}^{1} \int_{-1}^{1} \rho\big(x(\varepsilon)\big) w\big(x(\varepsilon)\big) \cdot \partial_t^2 s(x(\varepsilon), t) J(\varepsilon) d^2\varepsilon \qquad \text{(Eq 1.10)}$$

$$= \sum_{\alpha=0}^{\eta} \sum_{\beta=0}^{\eta} \omega_\alpha \omega_\beta J^{\alpha\beta} \rho^{\alpha\beta} \sum_{i=1}^{2} \omega_i^{\alpha\beta} s_i^{\alpha\beta}$$

The final ordinary differential equation can be written as:

$$M\ddot{U} = -KU + F \qquad \text{(Eq 1.11)}$$

where *U* is the global displacement, *M* is the global mass matrix, *K* is the global stiffness matrix, and *F* is the global source vector. This discrete system is solved by a second-order Newmark finite-difference time scheme (Berland et al., 2006).

Propagation of ultrasonic shear waves.

In chapter 4, I used SH waves travelling in the x-z plane with a vertical (y) component of motion. The elastic wave equation for the vertical component of displacement *s(x,z,t)* is given by:

$$\rho \partial_t^2 s = \partial_x(\mu \partial_x s) + \partial_z(\mu \partial_z s) + f \qquad \text{(Eq 1.12)}$$

Where ρ denotes the density and $\mu(x,z)$ the shear modulus. The source f is given by

$$f(x, z, t) = h(t)\delta(x - x_s)\delta(z - z_s) \qquad \text{(Eq 1.13)}$$

Where $h(t)$ denotes the source-time function and (x_s, z_s) the source location. I used a Ricker wavelet as the source-time function of the form:

$$h(t) = (1 - 2at^2)e^{-at^2} \quad \text{(Eq 1.14)}$$

with $a = \pi^2 f_o^2$ with a dominant frequency f_o of 100 kHz.

In the case of immersed objects in a matrix, as in the synthetic scenarios simulated here, the SPECFEM code uses scalar instead of vectors to reduce the computational time. In the pore space occupied by air, the equation of motion is:

$$\rho \partial_t v = -\nabla P \quad \text{(Eq 1.15)}$$

Where *v* denotes the velocity in the pore, and the pressure *P* is determined by

$$\partial_t P = -k \nabla \cdot v \quad \text{(Eq 1.16)}$$

Where *k* is the bulk modulus of the fluid. To solve the system of equations (1.15) and (1.16) a scalar potential *X* is introduced such that:

$$P = -\partial_t^2 X \quad \text{(Eq 1.17)}$$

From (1.15) and the initial conditions (*s=0* at *t=0*),

$$s = \rho^{-1} \nabla X \quad \text{(Eq 1.18)}$$

Upon substituting (1.17) and (1.18) into (1.16) we obtain the scalar equation for *X*

$$\partial_t^2 k \nabla \cdot (\rho^{-1} \nabla X) \quad \text{(Eq 1.19)}$$

Finally, the weak form of the equation, to be solved using the SEM method, is obtained by multiplying it by a scalar test function *w* and integrating by the parts over the domain Ω:

$$\int_{\Omega} k^{-1} w \partial_t^2 X \, d\Omega = -\int_{\Omega} \rho^{-1} \nabla w \cdot \nabla X \, d\Omega \qquad \text{(Eq 1.20)}$$

Note that on solid-solid and solid-fluid boundaries the SPECFEM code imposes continuity in both the traction -P$\hat{n}$ and the normal component of velocity $\hat{n}$·v. This is enforced explicitly by the SEM integrals. At the physical boundaries of the Ω domain, the seismic energy is absorbed using Stacey absorbing boundary conditions (Stacey, 1988).

1.3.3 Imaging methods

The Solfatara Array

In the present thesis, I provide the first scattering and absorption maps of the very-shallow (<30 m depth) hydrothermal system of the Solfatara Crater (Southern Italy). The Solfatara crater, located in the Campi Flegrei volcanic complex, has been for decades the focus of interest in countless geophysical surveys (e.g., Chiodini et al., 2005, 2017, 2021; Bruno et al., 2007, 2017; Letort et al., 2012; Petrosino et al., 2012; Byrdina et al., 2014; Isaia et al., 2015; Gresse et al., 2017; De Landro et al., 2019), given the escalating ongoing unrest of the caldera from its hydrothermal magmatic system and the raising hazard over an eruption. I used part of the 3D active seismic data collected during the Repeated Induced Earthquake and Noise (RICEN) campaign held in September 2013, in the framework of the European Mediterranean Supersite Volcanoes (MED-SUV) (Serra et al., 2016). The experiment covers a dense regular grid of 90 m x 115 m at the Solfatara crater (see Figures 4.1 and C1.1). The seismic source is Vibroseis with the dominant frequency linearly increasing with time from 5 to 125 Hz with a 15 s long sweep, and the network comprises 240 sensors (vertical-component geophones) evenly distributed. This study is limited to the analysis of 2144 seismograms. De Landro et al. (2017) performed a preliminary analysis of the dataset and provide me with the processed seismograms (including the

picking of the P-wave arrival time), the velocity model of the study volume, and the seismic rays in the velocity model. In general, the processing of signals consisted of cross-correlation of the Green's function of the medium with the vibroseis sweep to remove the source time function from the velocity records, and application of a minimum phase filter after cross-correlation to preserve causality (Serra et al., 2016; De Landro et al., 2017; Scala et al., 2019). The Solfatara seismic dataset was appropriate to do attenuation tomography in this thesis because: (1) of its good ray coverage; (2) the data was already pre-processed and ready to use; and (3) the availability of several geophysical surveys in the same area, which allows endorsing the interpretation of the results obtained in Chapter 4.

Coda attenuation tomography

Coda Attenuation tomography method was chosen because of its potential to map lateral variations as those present in volcanic environments. The analysis was performed using the Matlab package MuRAT (Multi-Resolution seismic Attenuation Tomography - https://github.com/LucaDeSiena/MuRAT.git). The code is designed to work with passive seismic data in which the source is far from the receivers. Thus, to be able to use this code on the active seismic data of the Solfatara array, in which both the sources and the receivers are located at the surface, I downscaled it to the meter scale and created a subroutine in the code for reading the rays in the velocity model. Afterwards, I successfully applied MuRAT to measure and model scattering attenuation and absorption in space using the seismograms acquired at the Solfatara crater.

Scattering attenuation is modelled by the regionalization of the peak delay measurements. This method is appropriate to examine volcanic medium because allows for mapping structural changes in the study area. Peak delay (*Pd*) also known as envelope broadening, refers to the delay of the maximum energy in the signal, measured as the range of time between the onset of the direct S-wave and the maximum amplitude of the seismic energy. The underlying principle is that the envelope of direct wave packets broadens due to multiple forward scattering by inhomogeneities (Saito et al., 2002). Takahashi et al., (2007) developed a tomographic method to map heterogeneities in Japan

using the peak delay time. Calvet et al. (2013) followed this method to map the scattering anomalies of the Pyrenees. For this study, in section 4.3.1, I adopted the same approach: (1) measure *Pd* for all the waveforms filtered at the study frequency bands. Note that the arrival times of the S-wave are not available for the Solfatara dataset, this phase is usually challenging to pick in volcanic environments, then the peak delay was measured with respect to the P-wave, an approach previously applied by De Siena et al. (2016) to map 2D scattering at Mount St Helens volcano; (2) cross-plot the *Pd* values against travel time (Figure 4.3); (3) perform a linear regression of the dependence of peak delay increasing with travel time; (4) allocate positive and negative variations of *Pd* with respect to the linear trend to identify strong and weak scattering, respectively; (5) map *Pd* in space using regionalization. Regionalization consists in dividing the mapped volume into blocks, each block is crossed by several rays, each ray has an allocated *Pd* value measured from its seismogram, and the average *Pd* of all these rays is given to the block. Then the variations between blocks are smoothed by taking the average of the mean *Pd* values between neighbour blocks.

Absorption is modelled by an inversion procedure of the coda attenuation measurements. The decay of the envelope of coda waves with time is a method to measure coda attenuation Q_c^{-1}. When the coda waves enter the diffusive regime, the measured Q_c^{-1} is a marker of seismic absorption (Calvet and Margerin, 2013; Prudencio et al., 2013; Sketsiou et al., 2020). Then the spatial distribution of Q_c^{-1} in a certain zone can be used to produce maps of its absorption structure. De Siena et al. (2017a) used space-weighted sensitivity functions to invert for the spatial distribution of coda wave attenuation at Campi Flegrei. In the same study area, Akande et al. (2019) followed this method to produce the first 3D kernel-based coda attenuation model using an inversion approach that involved 3D sensitivity kernels. For this study, I adopted the same approach in section 4.3.2: (1) compute the seismic envelopes at each study frequency; (2) compute Q_c^{-1} from the least square fitting of the logarithm of the envelope versus time. This regression approach is easy to implement, however, the uncertainty is high when the data distribution does not have a linear fitting ; (3) compute the sensitivity kernels for the event-station couples. This is done by solving the energy transport equations (Paasschens, 1997; see Appendix C3); (4) creating the inversion matrix *G* using the computed kernels; (5)

performing the tomographic inversion. The linear inversion problem consists of solving the general expression $d=G(m)$; where the data vector d contains the Qc values measured for each seismogram; the operator matrix G, which represents the mathematical relation between the observed and the modelled Qc^{-1}, corresponds to the normalized sensitivity kernels. The model vector m contains the attenuation values Qc^{-1} for each block of the volume. The modelled Qc^{-1} are adjusted to satisfy the observed data by using an iterative regularization that leads to choosing adequate damping parameters using conjugate gradients that minimize the problem from L2-norm misfit and cost functions; (6) Produce a checkboard test to assess the accuracy of the inversion. These tests consist of alternating patterns of positive and negative anomalies that must be reconstructed, the areas with good recovery are assumed to be well constrained. This synthetic test is one of the advantages of using inversion procedures, as the resolution and stability of the results can be evaluated.

1.4 Chapters Overview

This thesis is organized into three main chapters that encompass the work developed for this project. First, the experimental work developed at the rock sample scale (laboratory) is presented. Next, the findings of that work are modelled using numerical methods. Finally, the observations are applied at the meter scale (field) in a real volcano. The chapters are formatted as research papers, as they have been (or are being) submitted to journals for peer review. The appendixes contain a large number of complementary information that shows the work behind the main manuscripts. The contents of Chapters 2 to 5 are outlined below:

Chapter 2: In this chapter, I characterized parameters used by the field-scale community (seismic attenuation) at the rock-sample scale (laboratory). For this study, I establish a relation between physical rock properties and scattering attenuation measured from coda waves using volcanic rocks at the laboratory scale. Determining the primary petrophysical

and/or mineralogical drivers of seismic attenuation is an important contribution to the Earth Sciences community because: (1) these controlling parameters can be used to link the measured seismic wavefield with properties of geological relevance; (2) I targeted the decay of coda wave with time which is increasingly used as a seismic tomography attribute; and (3) this is a seminal step to build rock-physics/coda forward models to improve imaging techniques of heterogeneous sequences.

Chapter 3: in this chapter, I modelled ultrasonic wave propagation in volcanic rocks as a function of pore space. The study builds on years of experimental work on dry volcanic rock samples, which have allowed me to characterize their petrophysical and mineralogical characteristics while measuring ultrasonic waves. Using this knowledge, I developed forward wave simulations with the state-of-the-art code SPECFEM2D, demonstrating the effect of pore space topology on ultrasonic waveforms. These results have consequences on the way we measure and associate rock properties to seismic observations. Researchers use analytical solutions to connect seismic observations with materials, developing solutions for fluid inclusions in homogeneous rock matrices. However, this study proves that this matrix produces relevant changes in phases and amplitudes in volcaniclastics without the need for fluids. Medium inhomogeneity becomes a trigger of anomalous changes in phases and amplitudes even if wavelengths are much larger than inclusions, and of the order of the sample dimension. This, in turn, proves that analytic solutions will always fall short in the heterogeneous Earth, and, more importantly, that we need to tackle full computational modelling of seismic waveforms in these environments.

Chapter 4: this chapter is a direct application of attenuation imaging to field data. Hydrothermal systems in volcanoes comprise a complex mixture of magmatic and hydrothermal fluids, which sometimes migrate just a few meters below the surface, opening vents and feeding phreatic eruptions. Solfatara Volcano is one of the best-known, and best-monitored volcanic craters globally, and the location of one of the densest active seismic experiments (meter-scale) ever attempted at a volcano. I used data from this experiment to map seismic scattering and absorption and obtain a 3D model of very-shallow hydrothermal structures and processes. The maps reveal the sensitivity of these

parameters to known faults separating liquid- from vapour-rich fluids in the first 30 meters under the surface. Comparing the maps with the rich knowledge of the crater activity and structure supports the existence of a very-shallow migration system that connects the centre of the crater to its eastern fumaroles. Applying the technique to similar high-resolution arrays promises to bridge the gap between rock physics and km-scale monitoring and imaging data.

Chapter 5: this chapter encloses the findings presented in the previous chapters, states the general conclusions obtained from this thesis and set recommendations for future research.

Chapter 2

Petro-mineralogical controls on coda attenuation in volcanic rock samples

In this chapter, I worked on identifying the main petrological and mineralogical factors controlling coda attenuation in volcanic rocks at the laboratory scale, as a necessary step before modelling seismic waves in real volcanic media. To quantify the heterogeneity of the rocks and link them with coda parameters, I fully characterized the pore and grain systems of the samples, by using microscopy and imaging techniques, and I acquired waveforms of ultrasonic S-wave looking to register coda waves to measure attenuation parameters. Then I performed several statistical analyses to deduce the relationship between the intrinsic properties of the host rock and the coda attenuation measurements. The results pointed out that the pore space is the main trigger for seismic attenuation in the analysed samples.

The chapter was written as a research paper submitted to Geophysical Journal International. It was published in May 2021 and the full citation is as follows: Di Martino M.D.P., De Siena L., Healy D., and Vialle S. (2021). Petro-mineralogical controls on coda attenuation in volcanic rock samples, *Geophysical Journal International*, https://doi.org/10.1093/gji/ggab198. I wrote the manuscript, carried out the experiments, data processing and analysis and created all the figures. The co-authors supervised my work, guide me to improve the discussion section and proofread the manuscript. The labels of figures, tables and supporting information have been renamed to be in line with

this thesis. The mentions of "supporting information" in the paper corresponds to Appendix A in this thesis. In the same order, the references are included in the bibliography section.

Summary

Seismic attenuation measurements, especially those obtained from coda decay analysis, are becoming a key data source for the characterization of the heterogeneous Earth due to their sensitivity to small-scale heterogeneities. However, the relation between the scattering attenuation measured from coda waves and physical rock properties is still unclear. The goal of this study is to identify the main petrophysical and mineralogical factors controlling coda attenuation in volcanic rocks at the laboratory scale, as a necessary step before modelling seismic waves in real volcanic media. Coda wave attenuation was estimated from ultrasonic S-wave waveforms. To quantify the heterogeneity of the rocks and link them with this attenuation parameter, we performed several categorizations of the pore and grain systems of volcanic samples. Considering that seismic attenuation in rock samples can be modelled using the framework of wave propagation in random media, a statistical analysis of shear-wave velocity fluctuations was performed: this analysis gives correlation lengths ranging from 0.09 mm to 1.20 mm, which represents the length scale of heterogeneity in the samples. The individual evaluation of the pore space and mineral content revealed that the pores of the samples (characterized by large vesicles) have a bigger effect than the grains on the heterogeneity level. We have developed a framework where intrinsic properties of the host rocks drive seismic attenuation by correlating the petro-mineralogical characteristics obtained from image data processing and analysis, with the coda attenuation measured at ultrasonic frequencies. There is conclusive evidence that porosity alone is not the primary controller of coda attenuation: it is also changed by the alteration level (i.e., oxidation, coating of the vesicles, secondary minerals) and the size of grains and pores. Among all the parameters analysed, it appears that the pore space topology is the main contributor to scattering attenuation in the volcanic samples.

2.1 Introduction

Seismic waves provide some of the most detailed information about the heterogeneous crust of the Earth. However, an important portion of the energy used to interpret this information from coherent waves is dispersed by seismic scattering and absorption (Sato et al., 2012). Scattering on small-scale heterogeneities inside the Earth manifests itself as seismic coda waves, the tail portion of direct- and surface- wave seismograms (Aki, 1969). Coda waves can be used to estimate earthquake magnitudes (e.g., Del Pezzo et al., 1991) and constrain site amplification factors to assess seismic hazards (e.g., Parolai, 2014). The attenuation of coda waves (Q_c^{-1}), measured from the decay of seismic energy with time, has been extensively used to infer the tectonic state of an area (Aki and Chouet, 1975) at the regional (e.g., Yoshimoto et al., 1993), volcanic (e.g., Rahimi et al., 2010), and fault scales (e.g., Sertçelik, 2012).

Laboratory experiments are widely used to estimate the characteristics of elastic waves transmitted through a rock sample and to calibrate field-scale observations. At the laboratory scale, techniques that focus on the phase of coda waves, like coda wave interferometry, are becoming a standard technique to characterize Earth samples and upscale information to the field (Azzola et al., 2020; Grêt et al., 2006; Planès and Larose, 2013; Snieder, 2006). At the same time, seismic attenuation is becoming a state-of-the-art attribute for the description of physical phenomena at different scales (Tisato and Quintal, 2013), with an increasing number of apparata devoted exclusively to its accurate measurements (e.g., Tisato and Madonna, 2012). These developments spark the need for appropriate experimental settings to measure a quantity like Q_c^{-1} in heterogeneous samples, where both sample size (Yoshimitsu et al., 2016) and scattering (Mavko et al., 2009) dominate coda waves. This quantity is increasingly used as a marker of seismic absorption in field-scale imaging (Sketsiou et al., 2020).

Whereas seismic experiments at the ultrasonic scale routinely focus on the information contained in the wave-arrival package, in this study we focus on the information contained in the coda waves. In the field, the attenuation of coda waves Q_c^{-1} is given by $Q_c^{-1}=Q_i^{-1}+Q_{cs}^{-1}$ (Shapiro et al., 2000; Calvet et al., 2013; following the single-

scattering approximation of Aki and Chouet, 1975), where Q_i^{-1} and Q_{cs}^{-1} refer to the coda attenuation produced by intrinsic absorption and scattering, respectively. An intrinsic energy loss can be triggered by various mechanisms like fluid/squirt flow, internal friction, viscosity, and thermal relaxation (Barton, 2006); these mechanisms are mainly controlled by the presence of fluids. In the absence of intrinsic attenuation, the amplitude decay is caused by the perturbation of the seismic wavefield (change in wave-direction and/or phase) due to changes in the medium properties (i.e., inhomogeneities). Measuring the decay of seismic energy with time in small samples is challenging: reflections and conversions of coherent waves on the boundaries of the sample are likely to contribute to this decay (Yoshimitsu et al., 2016; Zhang et al., 2014); the number of wavelengths that will propagate into the sample is constrained by the sample size (Guo and Fu, 2007); and phase and amplitudes of the coda waveform depend on the experimental settings (Fujisawa and Takei, 2009), especially on the coupling between the source/receiver and the rock sample. It is established that changes in coupling generate uncertainties in experiments, thereby hindering the repeatability of the analyses (McKenzie et al., 1982; Subramaniyan et al., 2014).

Coherent-wave scattering in heterogeneous media depends on the ratio of the seismic wavelength λ (related to frequency and velocity) to the size of the scattering heterogeneity d. Based on this relation, scattering can be described as Rayleigh scattering ($\lambda > d$), Mie scattering ($\lambda \approx d$), and diffusion scattering ($\lambda < d$) (Mavko et al., 2009). At the laboratory scale, the diameter of the scattering heterogeneity depends either on the pore space size or on the grain size (Liu et al., 2017; Matsunami, 1991; Nishizawa and Fukushima, 2008; Wei and Fu, 2014). The diameter of scattering heterogeneities could represent clusters of grains (or pores) that are comparable with the wavelength (Blair, 1990; Lucet and Zinszner, 1992). Therefore, we could expect that at sample scale scattering can be best described by the Rayleigh and Mie regimes. How large, if any, is the effect of the grain texture on seismic attenuation? Calvet and Margerin (2016) described how attenuation varies with the grain shape/size in polycrystalline materials. Their findings demonstrate that, in the Rayleigh regime, attenuation depends on the effective volume of the grain, while in the Mie regime it depends on the grain dimension in the direction of propagation.

There is a growing interest of the rock physics community for targeting volcanic rocks to provide more reliable quantifications of: elastic properties to be used in modelling volcanic processes (Heap et al., 2020; Pistone et al., 2021); attenuation mechanisms to enhance the interpretation of volcano-seismicity (Clarke et al., 2020; Vedanti et al., 2018); and microstructural changes at ultrasonic frequencies (Durán et al., 2019; Vanorio et al., 2002). Because recent advances in microscopy techniques and digital rock physics (Andrä et al., 2013; Cnudde and Boone, 2013; Markussen et al., 2019) allow quantification of the spatial heterogeneity of the samples, we can use this measured heterogeneity to forward model both direct and scattered seismic wavefield. Using this spatial heterogeneity as a marker of velocity fluctuations can provide a realistic representation of the coda wavefield (Fukushima et al., 2003; Holliger and Levander, 1992; Spetzler et al., 2002).

There are three important challenges to overcome when characterizing Q_c^{-1} at the laboratory scale: (1) the lack of a link between petro-mineralogical and scattering parameters affecting coda decay with time, analogous to those existing for phase-dependent imaging at subduction zones and mantle scales (Holtzman et al., 2003; Karato and Weidner, 2008; Wagner et al., 2008); (2) the absence of laboratory calibrations (Subramaniyan et al., 2014; Tisato and Madonna, 2012; Yoshimitsu et al., 2016) specifically targeting coda-decay measurements; (3) the need for a joint description of coda waves in terms of radiative transfer theory and the wave equation, similar to those performed at field scale (Obermann et al., 2013; Przybilla and Korn, 2008). Overcoming these obstacles will eventually enable the quantification of the petro-mineralogical state of volcanic and geothermal environments by using their dispersive effects on seismic waves, efficiently calibrating the interpretation of imaging studies that use scattering and absorption as seismic attributes (Calvet et al., 2013; De Siena et al., 2016; Mayor et al., 2016; Sketsiou et al., 2020; Takahashi et al., 2007; Prudencio et al., 2017).

In this article, we tackle the first two challenges. To do so, we characterized heterogeneous rocks by an extensive petrological and mineralogical description of volcanic samples in terms of their pore and grain system, using optical and electron microscopy techniques along with image processing and analyses. An experimental link

between the rock properties and seismic parameters at laboratory scale was established by: (1) determining the length scale of the heterogeneities and its relationship to porosity; (2) identifying the main contributor to scattering attenuation using coda wave analysis of ultrasonic S-wave waveforms; (3) analysing how the mineralogical composition of the samples impact coda attenuation parameters; (4) evaluating the effect of the grain size and alteration level of the sample; and (5) assessing the use of 3D image analysis versus conventional 2D microscopy images to predict spatial heterogeneity. The results were discussed considering the trade-offs reverberations and surface waves generated by the limited size of the samples produce on coda envelopes. They provide valuable insights to interpret coda attenuation parameters as a marker of petro-mineralogical properties in volcanic rocks.

2.2 Data

This study focuses on volcanic samples. The dataset comes from two cored boreholes (PTA2 and KMA1) on the Big Island of Hawai'i (Jerram et al., 2019). These boreholes penetrate lava flow sequences covering a diverse range of volcaniclastic facies. We chose 25 core samples at variable depth intervals, 18 cores from the PTA2 borehole, and 7 cores from the KMA1 borehole. The specimens are cylindrical cores of around 2.54 cm in diameter and 5.08 to 6.35 cm in length.

We provide a summary of the petrophysical properties of the samples in Table 2.1 (see Appendix A, A1-A3 for a detailed description and measurement procedures). All the experiments in this study were done in dry conditions, at ambient room temperature (~18-20 °C) and atmospheric pressure (1 bar, ~0.1 MPa). The samples have porosities ranging from 0.1 to 50% (values highly influenced by the presence of vesicles), and ultrasonic P-wave velocity from 2.5 to 5 km/s for the entire dataset. Cross plots between the rock physics properties (velocity, porosity, permeability, and density) do not follow trends

close to theoretical models (Figure A2), an indication of the high heterogeneity of the samples.

Table 2. 1. Petrophysical properties of the core samples.

BH	*ID*	*Depth m*	*Length cm*	*Vp km/s*	*Vs km/s*	*Vp/ Vs*	*Grain density g/cc*	*Bulk density g/cc*	*Porosity %*	*Permeability m^2*
PTA2	**1H**	641.4	4.99	2.86	1.50	1.91	2.94	2.25	24.1	1.60E-15
	2H	889.0	4.91	3.14	1.91	1.65	3.08	2.88	6.4	9.38E-18
	3H	889.0	5.06	3.25	1.96	1.66	3.07	2.87	6.3	3.45E-18
	4H	954.6	5.12	4.95	2.41	2.04	3.03	1.85	38.8	4.68E-12
	5H	1020.7	5.11	3.39	1.95	1.70	3.01	2.31	23.1	2.02E-16
	6H	1038.1	5.06	2.25	1.52	1.48	3.15	1.95	38.1	8.05E-14
	7H	1179.1	5.14	3.43	1.93	1.77	2.80	2.45	12.7	1.33E-16
	8H	1230.9	5.06	3.56	1.74	2.05	2.85	2.33	18.2	1.92E-16
	9H	1686.2	5.10	3.35	1.95	1.72	2.97	2.05	30.9	1.32E-15
	10H	1686.2	5.05	3.23	1.87	1.73	2.96	2.05	30.7	1.6E-15
	11H	1689.7	4.98	3.88	2.00	1.94	2.99	1.83	38.6	4.84E-11
	12H	1716.4	5.07	4.19	2.10	1.99	2.95	2.12	28.2	2.94E-16
	13H	1716.4	4.99	3.90	2.05	1.90	2.94	2.11	28.5	1.75E-16
	14H	1727.9	4.99	3.06	1.49	2.05	2.90	2.39	17.7	1.01E-16
	15H	1729.6	4.88	3.42	1.88	1.82	2.91	2.32	20.4	1.41E-16
	16H	1729.6	4.97	3.32	1.91	1.73	2.91	2.27	22.2	8.55E-17
	17H	1738.0	5.07	5.03	2.58	1.95	2.93	2.92	0.2	1.78E-18
	18H	1747.8	4.44	2.77	1.52	1.82	2.65	2.47	6.9	5.1E-16
KMA1	**19H**	337.5	6.30	3.28	1.32	2.48	3.13	2.74	12.4	1.01E-15
	20H	692.8	5.12	4.00	2.19	1.83	3.00	1.95	34.9	3.68E-15
	21H	818.1	6.47	3.80	2.14	1.78	3.03	1.58	47.7	1.92E-15

22H	969.0	5.04	3.41	2.09	1.63	3.02	2.59	14.1	8.03E-17
23H	1122.8	6.39	4.44	2.42	1.83	2.99	2.09	30.2	1.05E-16
24H	1283.0	5.09	3.07	1.63	1.88	2.95	2.47	16.4	3.14E-16
25H	1456.7	6.54	5.07	2.64	1.93	2.95	2.08	29.5	3.04E-16

Note. The porosity, permeability, and density values were provided by Volcanic Basin Petroleum Research VBPR, while the ultrasonic *P*- and *S*- wave velocities were measured as part of this study (section 2.3.1).

2.3 Methodology

To relate seismic attenuation parameters with the heterogeneity level of the volcanic rocks, the samples were analysed in terms of: (1) the coda attenuation measured at ultrasonic frequencies; (2) their petro-mineralogical characteristics, via measurements of pore space geometry, 2D textural heterogeneity, and mineral phase distribution; and (3) a statistical characterization of the random media.

2.3.1 Seismic measurements

Ultrasonic velocity experiments

In ultrasonic experiments, the seismic survey consists of generating elastic waves using an ultrasonic sensor (transducer) as the pulsing source. This pulse vibration travels inside the rock sample until it is acquired by a second transducer working as a receiver. The acquired waveform is a record of the change in time of the voltage pulse (source signal) due to its propagation through the specimen.

The first step was to acquire waveforms at ultrasonic frequencies. We used a shear-wave source as coda-waves in the seismograms are primarily comprised of shear waves (Fukushima et al., 2003; Shapiro et al., 2000). The transducers belong to the Olympus Videoscan series. The shear-type piezoelectric crystal has a disk shape, 13 mm

in diameter and a characteristic frequency of 1 MHz. The source and receiver were positioned at the ends of the central axis of the core sample. The transducers were placed in a box-holder coupled to an internal spring to guarantee constant pressure conditions, as it allows the coupling force to be independent of the assembly system (Figure 2.1). To ensure repeatability, these holders were attached to a bracket system to give stability and to hold the sample in the middle of both transducers while keeping them aligned. The pulse repetition frequency was set at 100 Hz and the pulser voltage at 400 V using an ultrasonic square wave pulser/receiver unit (Olympus 5077PR). The waves are received perpendicular to the transducer/sample interface (i.e., the longitudinal vibration travels along the vertical axis) and the output signal is displayed on a digital oscilloscope (Tektronix TDS 3012C). Each survey was conducted with identical sensors and parameters to keep consistency in the acquisition settings.

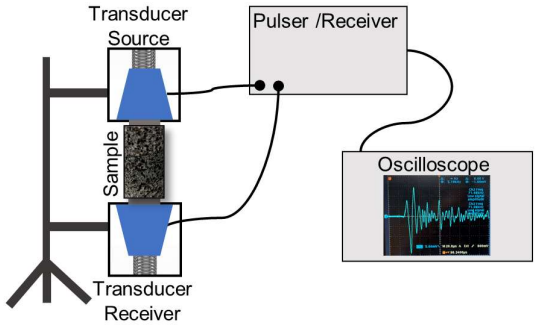

Figure 2. 1. Schematic illustration of the experimental set-up for the ultrasonic measurements.

Coda wave attenuation measurements

Aki and Chouet (1975) described coda waves and modelled their energy loss as a function of frequency (f) and time (t) as:

$$E(f,t) = S(f)t^{-\propto}exp^{\frac{-2\pi ft}{Qc}} \quad \text{(Eq. 2.1)}$$

where E is the power spectra of coda waves, $S(f)$ is the frequency-dependent source factor, $\propto$ is a constant factor related to the geometrical spreading and Q_c is the coda quality factor (inverse of coda attenuation), which may or may not be dependent on frequency. In our experiment, the frequency-dependent source factor ($S(f)$) and geometrical spreading are assumed to be constant for all the acquired waveforms. Therefore, the relative variations in the total attenuation measured is attributed to scattering attenuation. To obtain Q_c^{-1} values we rearrange equation 1 by taking the natural logarithm:

$$\frac{\ln[E(f,t)t^{\alpha}]}{2\pi f} = \frac{\ln[S(f)]}{2\pi f} - \frac{t}{Qc} \quad \text{(Eq. 2.2)}$$

To compute the coda attenuation, we used the coda-wave decay method: the envelope of the coda window is calculated through a smoothed Hilbert transform. Then, by cross-plotting the natural logarithm of the envelope for a central frequency of 150 kHz (left parameter in Eq. 2.2; Q_c computed at other frequencies in Appendix A8) versus time, we determine Q_c^{-1} from the slope of a straight line fitting the data in a least-squares sense (Figure 2.2d).

All the waveforms acquired in this study have a length of 4e-04 seconds from the origin time. To compute coda envelopes, we use a window starting 1.75e-04 seconds after the origin time with a length of 1.75e-04 seconds (Figures 2.2a and 2.2b). We discuss the implications of considering a different coda window as done by other studies (e.g., Guo and Fu, 2007; Guo et al., 2009; Hu et al., 2018) in the Appendix A4, where we observed that the amplitude and frequency of secondary reflections can be disregarded, as their impact is weakened by the loss of high-frequency content in the coda (Fu et al., 2016; Figures A4.1 and A4.2).

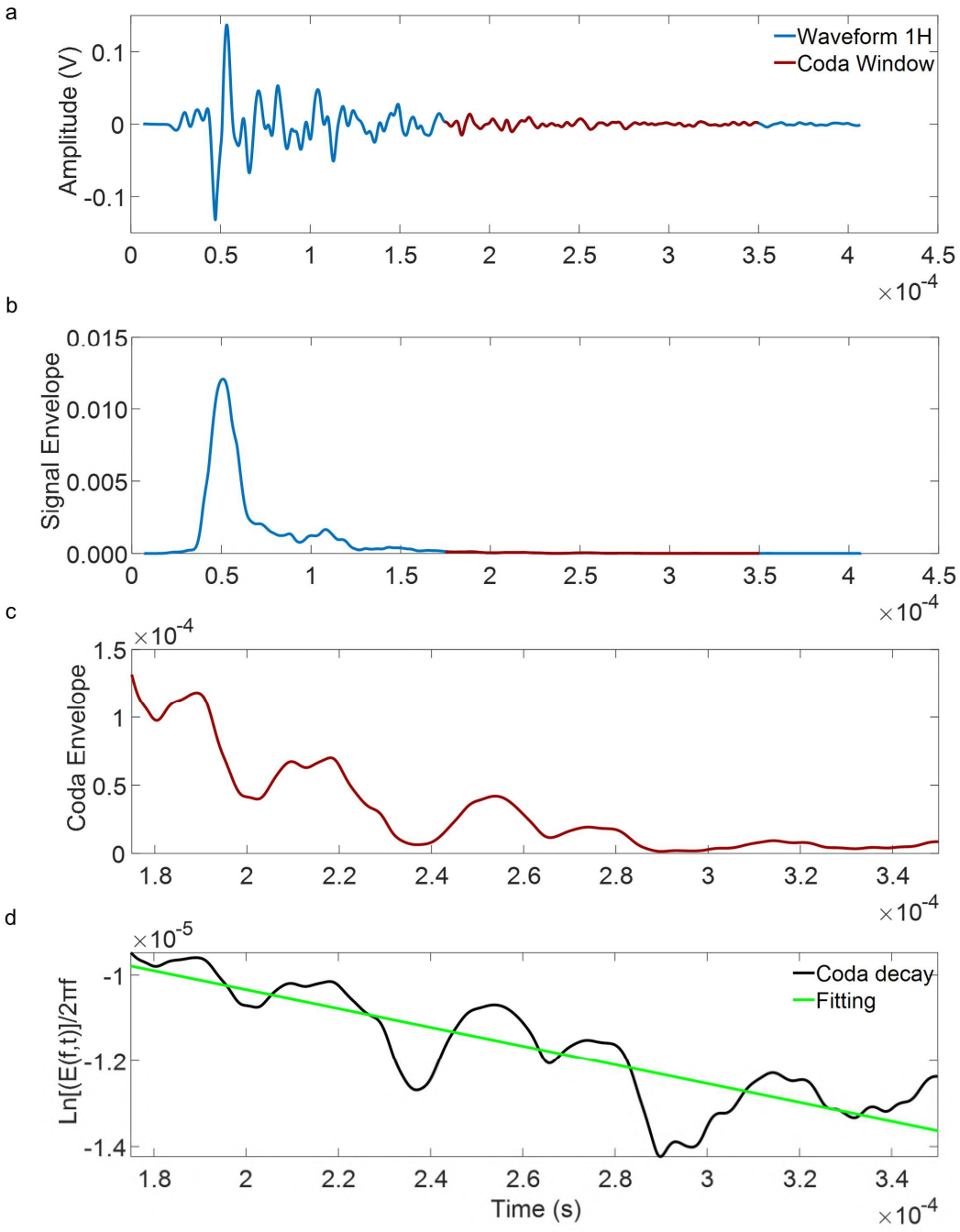

Figure 2. 2. Illustration of coda wave analysis on sample 1H. Recorded waveform after applying a Butterworth bandpass filter between frequencies 20-800 kHz (a) and its envelope (b); coda wave envelope (c); logarithm of the coda envelope and the linear fitting to obtain Q_c^{-1} (d).

2.3.2 Petro-mineralogical description

Pore space analysis

3D digital images of the internal microstructure (e.g., Figure 2.3a), a proxy of the heterogeneities in rock samples (Andrä et al., 2013), were acquired for samples 1H, 9H, 11H, 14H, and 18H, with a resolution of ~22 μm using X-ray microcomputed tomography 'μxCT', a non-destructive acquisition technique (Cnudde and Boone, 2013). Only five samples were analysed due to limited resources, the chosen five samples cover the full range of porosities (Table 2.1). Here, we describe the samples in terms of pore size distribution, aspect ratio, and relative measurement of heterogeneity level at the pore scale (correlation length). We consider the resolution of the tomogram sufficient for these quantifications of the pore space, as the structures (pores) smaller than 0.022 mm are too small to be comparable to the size of the ultrasonic wavelength of our seismic experiments. The processing was done using the software Avizo (AVIZO, 2019). The workflow can be summarized as:

1. Import the 2D slice images generated from the micro-CT scanner (Versa XRM 500 from Zeiss-XRadia);
2. produce a 3D volume using the internal software XM Reconstructor (XRadia);
3. processing on the raw data: first crop the side-ends of the scanning to take out images with a shadow, which can compromise the intensity distribution, then apply a median filter for noise reduction;
4. perform manual segmentation of the data, separating voxels with CT values that refer to pores from those associated with the grains, then refine the segmentation by removing disconnected regions and smoothing to reduce the roughness in the grain-pore boundaries;
5. complete an object separation using the watershed method (Beucher and Meyer, 1993);

6. measure of pore space parameters such as equivalent diameter, sphericity, volume, and area. The sphericity is expressed as $\theta = \frac{\pi^{1/3}(6V)^{2/3}}{A}$ (Eq. 2.3), where V is the volume of a particle and A is its surface area. The equivalent diameter computes the diameter of the spherical particle of the same volume; it is given by $EqD = \sqrt[3]{\frac{6\,x\,V}{\pi}}$ (Eq 2.4).

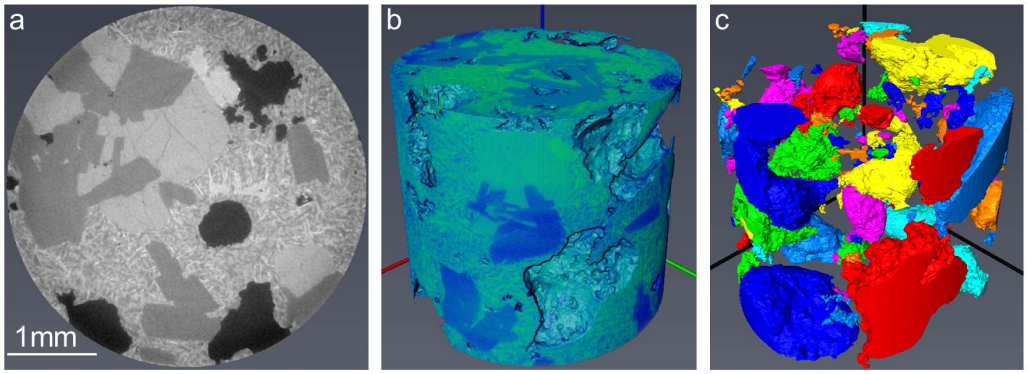

Figure 2. 3. Illustration of the digital image acquisition and processing (sample 1H is shown here). (a) Ortho slice of the intensity image, map view. The black areas are the pores, and the rest are the minerals. (b) 3D image, color intensity is related to the mineral composition (atomic number). (c) Pore space network, the colours do not represent a scale but help to better visualize the pores.

Textural heterogeneity

The analysis of the grain system was conducted on images derived from polished thin sections, based on the hypothesis that textural heterogeneity controls seismic scattering. These polished thin sections were made from a slice of the rock samples cut from one end of all the core plugs. To describe their mineralogy, the samples were imaged using a Zeiss Axio Imager M2m optical imaging system under plane-polarized light conditions (Figure A5).

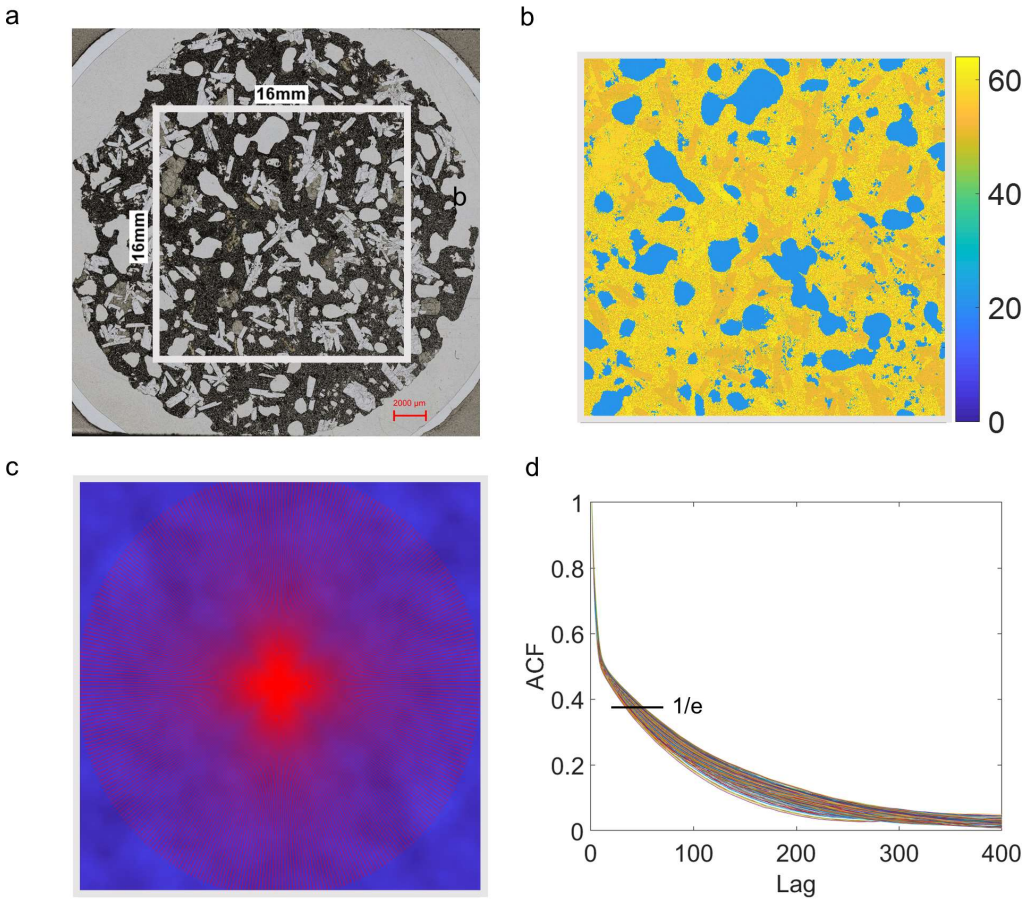

Figure 2. 4. Illustration of 2D Textural Heterogeneity analysis for sample 1H: CV=49.25%, CL=0.14 mm; AR=1.54. (a) Light microscope image (plane-polarized); (b) intensity image for the area (256mm^2) contoured by the square drawn in panel (a). The variations in the yellow color represent mineral compositions, the intensity scale is based on the x-ray emission in the scanning electron microscope, while the pore space is shown in blue; (c) 2D spatial auto-correlation (background) of the image in pane (b) and 180 radials profiles (red lines); (d) ACF computed for each profile, the black line indicates the drop of amplitude to 1/e (~0.37).

The 2D heterogeneity was quantified using the textural arrangement, following the procedure describe by Mukerji and Prasad (2007). The spatial texture heterogeneity is quantified by three parameters estimated from the intensity images (relative to X-ray absorption): coefficient of variation (CV), correlation length (CL), and anisotropy ratio (AR). The procedure is described as follow and illustrated in Figure 2.4 for sample 1H:

1. The CV (analogue to the 2D textural heterogeneity) was assessed as the ratio between the standard deviation and the mean of the intensity images (Figures 2.4a and 2.4b);

2. to obtain the CL we first computed the autocorrelation (ACF) of the entire image, next we extracted 180 radial profiles of the ACF (Figure 2.4c). The correlation length was estimated for each profile as the lag value where the auto-correlation drops to 1/e of its maximum (Figure 2.4d). Their average gave the CL;

3. the AR was measured as the ratio of the maximum to the minimum correlation length over all the profiles.

Phase distribution

The composition and morphology of the samples were measured on the polished thin sections using an automated mineralogy mapping (TIMA: Tescan Integrated Mineral Analyzer acquisition system) to test if changes in chemical compositions affect seismic attenuation parameters. The backscattered electron (BSE) images contain information on the atomic number and X-ray emission of the element present, which allocates their chemical composition. The initial mineral segmentation output was reprocessed for quality control and to assign minerals to unidentified phases in the measured data. The processing consisted of analysing the unknown spectra in terms of the elements that must be present in the mineral and their characteristic atomic concentrations (e.g., Figure A6.1). This allowed us to compute phase abundance and analyse various mineral texture properties and grain size distributions from the mineral mapping image (Figure A5, Table A6.1, Table A6.3). The grain size is defined as the diameter of an equivalent circle with the same area as the detected grain. To report the grain size (*Gs*) in μm the TIMA software (TIMA 2019) use $Gs = 2\sqrt{\frac{A}{\pi}}P$ (Eq. 2.5), where A is the number of pixels inside the particle and P the pixel spacing.

2.3.3 Statistical characterization of a random medium

Our assumption is that scattering attenuation in the datasets depends on the contrast between the elastic properties of the mineral grains and pores. At the sample scale, these contrasts are randomly distributed and can be described as a random medium. In such a medium the level of heterogeneity can be characterized by statistical functions (e.g., Gaussian, Exponential, and von Karman), computing the spatial autocorrelation function ACF of their statistical velocity functions (Sato et al., 2012; Holliger and Lavander, 1992, 1994). We thus use differences in grain size and mineralogical composition as a proxy for velocity fluctuations in the samples. We analysed the shear-wave velocity fluctuations in the rock samples following a modified version of the methodology applied by Sivaji et al. (2002) for compressional-waves, and Fukushima et al. (2003) for shear-waves to characterize the rock heterogeneities. Our workflow can be summarized as follow:

1. we use as the initial image the one corresponding to the mineral mapping (Figure 2.5a). A square section of 256 mm^2 of the input image was transformed into a greyscale intensity image using ImageJ software (Figure 2.5b);

2. we compute the average shear-wave velocity using the percentage of minerals in the samples and their velocities (Tables A6.1 and A6.2). The velocity values were selected from literature assuming isotropic minerals. The zeolites (observed on the thin sections during the microscopy analysis) show different levels of alteration in different samples, and the velocity for this phase group is then chosen within a range, where the chosen value depends on the level of mineral alteration;

3. we substitute the intensity data of each mineral with its shear-wave velocities (Table A6.2) to create a velocity image (Figure 2.5c). For the vesicles we used air elastic properties (i.e., Vs=0 Km/s);

4. we compute velocity fluctuations by subtracting the average velocity;

5. we apply a median filter to smooth the mapping from abrupt changes between small grains and pores, which are going to be averaged as part of the sample

matrix. Then the main contribution in the fluctuations comes from particles (grains or pores) with size bigger than the median grain size in the sample;

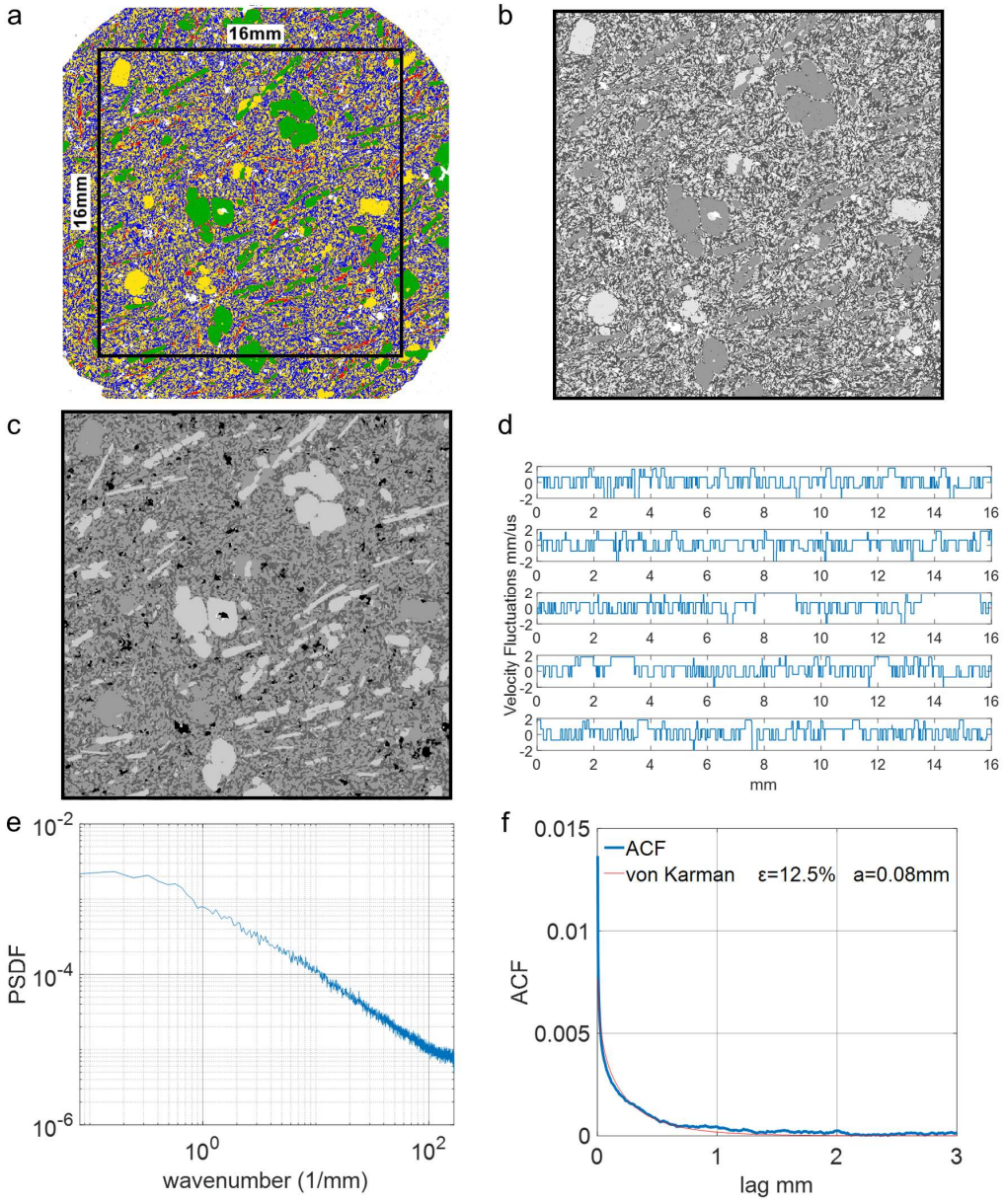

Figure 2. 5. Statistical description of the medium for sample 2H. (a) mineral map; (b) greyscale intensity image of the 256 mm^2 section indicated by the black square in panel a; (c) map of the velocity fluctuations (after filtering), pores in black; (d) example of 5

vertical profiles along with panel c; (e) averaged PSDF; (f) ACF fitted by a von-Karman function, a and ε values are indicated.

1. we generate 30 1-D profiles evenly distributed within the image (Figure 2.5d);
2. we calculate the Probability Spectral Density Function (PSDF) by Fourier transforming the profiles and estimated the averaged PSDF (Figure 2.5e);
3. the ACF is obtained by the inverse Fourier transform of the averaged PSDF. The resultant ACFs are best modelled by the 1D von Karman ACF:

   $R(x) = \frac{\varepsilon^2 2^{1-h}}{\Gamma(h)}\left(\frac{x}{a}\right)^h B_h\left(\frac{x}{a}\right)$ (Eq. 2.6); where x is the spatial lag, a is the correlation length (scale-length of the heterogeneity), ε is the root-mean-square of the fractional velocity fluctuations, $\Gamma(h)$ and Bh are the gamma function and modified Bessel function of the second kind of order h, h is the Hurst number rounding between 0-1. Our data fit for h=0.10. The value of a and ε are estimated by fitting this function (Eq. 2.6) to the computed ACF (Figure 2.5f).

2.4 Results

Coda attenuation at sample scale

The coda attenuation values in the samples range from 0.016 to 0.031, corresponding to coda quality factors (Q_c) between 32 and 61 (+/- 1). Given the uncertainties associated with each measurement, coda attenuation (Figure 2.6a) shows no simple dependency on porosity values. While coda attenuation seems to decrease with porosity, the lack of a simple polynomial attenuation-porosity trend suggests that, apart from porosity, other rock physical properties control attenuation in the volcanic dataset being analysed. In addition to the porosity level, the pore space was characterized by its pore size distribution

and sphericity level (Figures 2.6c and 2.6d). Pore size refers to the equivalent diameter of the pores of a given volume, and sphericity is a measure of how spherical the pores are.

Characterizing the pore space is important as, for instance, samples 1H and 5H have similar porosity levels but different coda attenuation values and textural features (Figure 2.6b). The discrepancies in their coda attenuation could be related to: (1) the differences in pore shape – the pore sphericity level is higher in sample 1H than in 5H, where pores follow a preferential direction; and (2) the fact that sample 1H has minerals of a size comparable to the pores, while sample 5H has a more homogeneous matrix of minerals characterized by smaller grain sizes. On the other hand, the sizes and shapes of pores and minerals in samples 9H and 23H are similar. Their different coda attenuation values could thus be explained by (1) the presence of secondary minerals, coating the boundaries of the vesicles in sample 9H, and (2) the moderate alteration (notice the darker colour produced by the oxidation) of sample 23H. The dependence of coda attenuation on intra-pore minerals could be related to changes in shear compliance (Barton, 2006) produced by the intrinsic properties of these secondary minerals layering the pores. A robust link is expected for the cases in which the alteration level is controlled by secondary minerals with high clay content, as the relationship between clay content and (total)attenuation confirmed by Klimentos and McCann (1990) for compressional waves in sandstones. As the attenuation of clay minerals is highly influenced by water saturation and temperature (Biryukov et al., 2016), further experiments with fluid interaction could help to establish causality between secondary minerals (alteration) and coda attenuation.

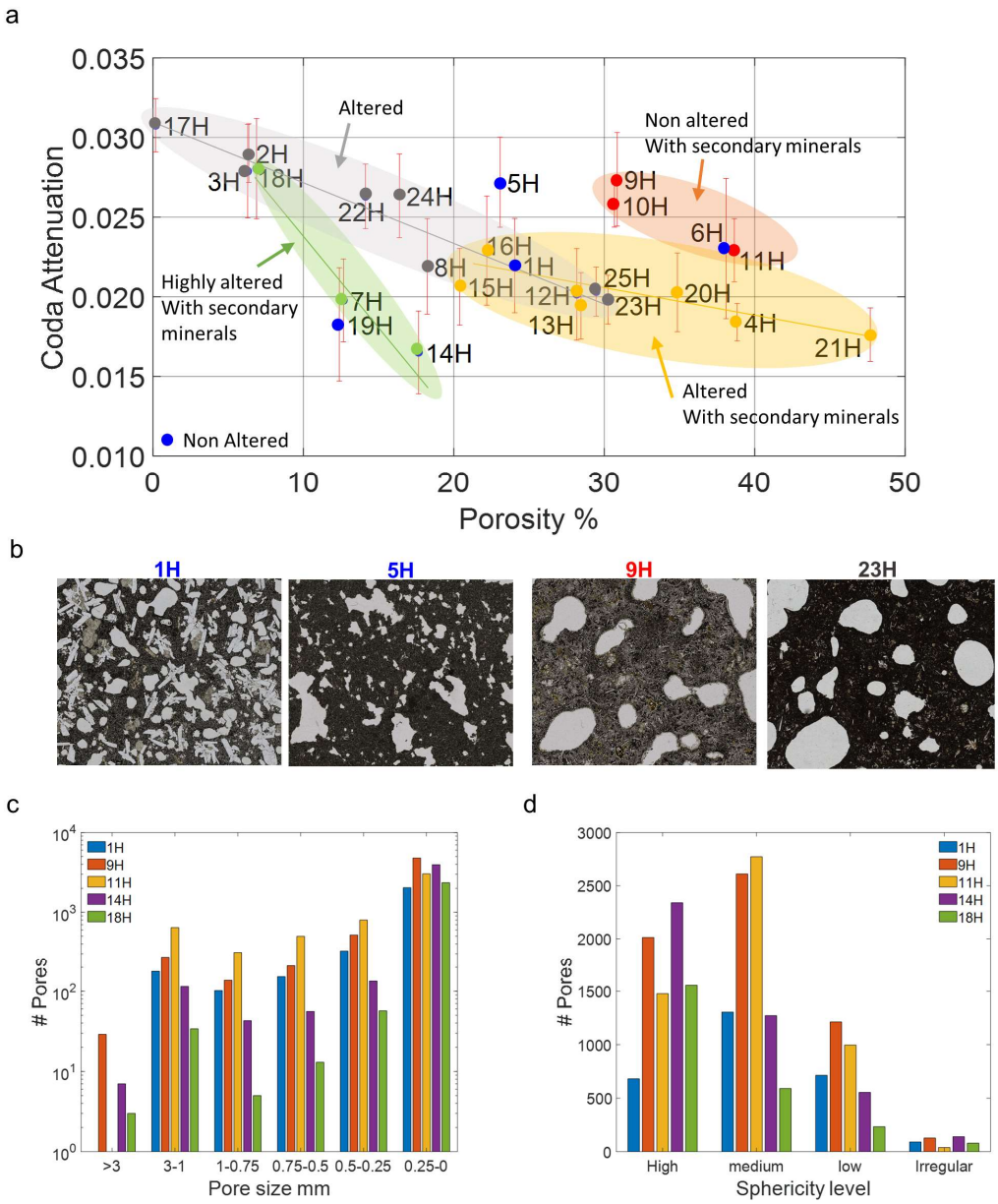

Figure 2. 6. (a) Dependency of coda attenuation on porosity in the samples. Error bars correspond to the fitting in Figure 2.2d. Samples have been grouped in color-zones based on the alteration level and the presence of secondary minerals. (b) Light microscope images for samples 1H, 5H, 9H, and 23H. The distribution of pore sizes (c) and pore sphericity (d) are shown for the five samples analysed using the 3D digital images. A sphere has sphericity equal to 1, thus here 'irregular' corresponds to values lower than 0.25, 'low' to values between 0.25-0.5, 'medium' to values between 0.5-0.75 and 'high' to values higher than 0.75.

Mineralogical composition of the samples

Five main groups of mineral phases were classified in the samples: feldspars, amphiboles, pyroxenes, olivine, and zeolites. The remaining minerals represented less than 5% of the sample composition (others, Figure 2.7a). All the samples are matrix-supported, with a matrix mainly composed of minerals of the amphibole and feldspar groups, with some samples having a high concentration of either olivine or pyroxenes (or both). Zeolites with different alteration levels are encountered in some samples, mainly filling (or coating) the vesicles, but also as a detached mineral. The mineral concentration and grain size vary sample by sample (Figures. 2.7b and 2.8). There is no clear correlation between the distribution of the phases and the coda attenuation levels; we argue though that the samples with median grain size larger than pore size (coincidental with the lowest porosity in the dataset) and strong variations in mineral concentration (e.g., 18H, 2H, and 17H, Figure 2.7b) show the highest attenuation values (Q_c^{-1}>0.028).

Once computed the mineral mapping of the sample, it was possible to calculate the equivalent diameter of the grains, described as grain size. The biggest grain size in the dataset is less than 1.65 mm. The P80 (percentile 80) of the grain sizes is lower than 0.50 mm in most of the samples, this means that 80% of the grains in the samples are smaller than 0.50 mm (Figure 2.8a; Table A6.3). This represents around 2.5%-5% the size of the wavelength at a central frequency of 150 kHz at which the attenuation values were computed (9-20 mm). Large grains correspond to the second peak of the bimodal distribution shown in Figure 2.8b and about 20% of the total grains, not included in the P80 statistic. What effect could these large grains have on the elastic parameters? We compare the ratio between the size of the large grains in the sample and their P80 (grain size ratio, Figure 2.8c) to assess the influence of grain size differences in the samples on coda attenuation. Only a third of the samples have a ratio higher than 4. The samples with the highest ratio (1H and 19H) show low-to-average coda attenuation. When comparing the size of the large grains with the wavelength (dots in Figure 2.8a), we consider that these grains influence the wave propagation only in samples in which the grain size is at least 5% of the wavelength (dash line); for the rest, they will act as a matrix with average elastic properties.

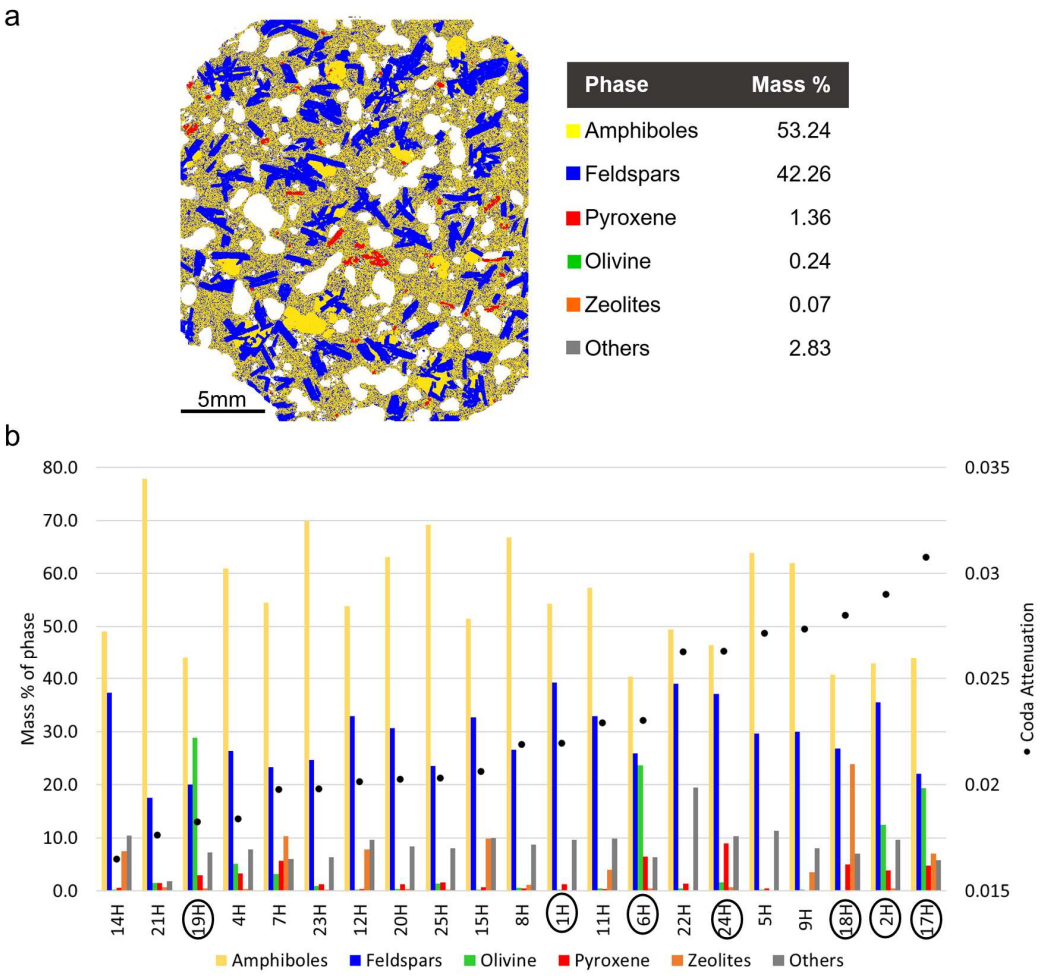

Figure 2. 7. Mineral Mapping. (a) Phase identification map for sample 1H. The color code represents the phases (mineral group), the white areas are the pore space. On the right is displayed the distribution in mass % per phase. (b) Phases distribution per sample. Samples are arranged from lower to higher coda attenuation (left to right). The ID into ovals corresponds to samples with large grains comparable to the pores size and their wavelength.

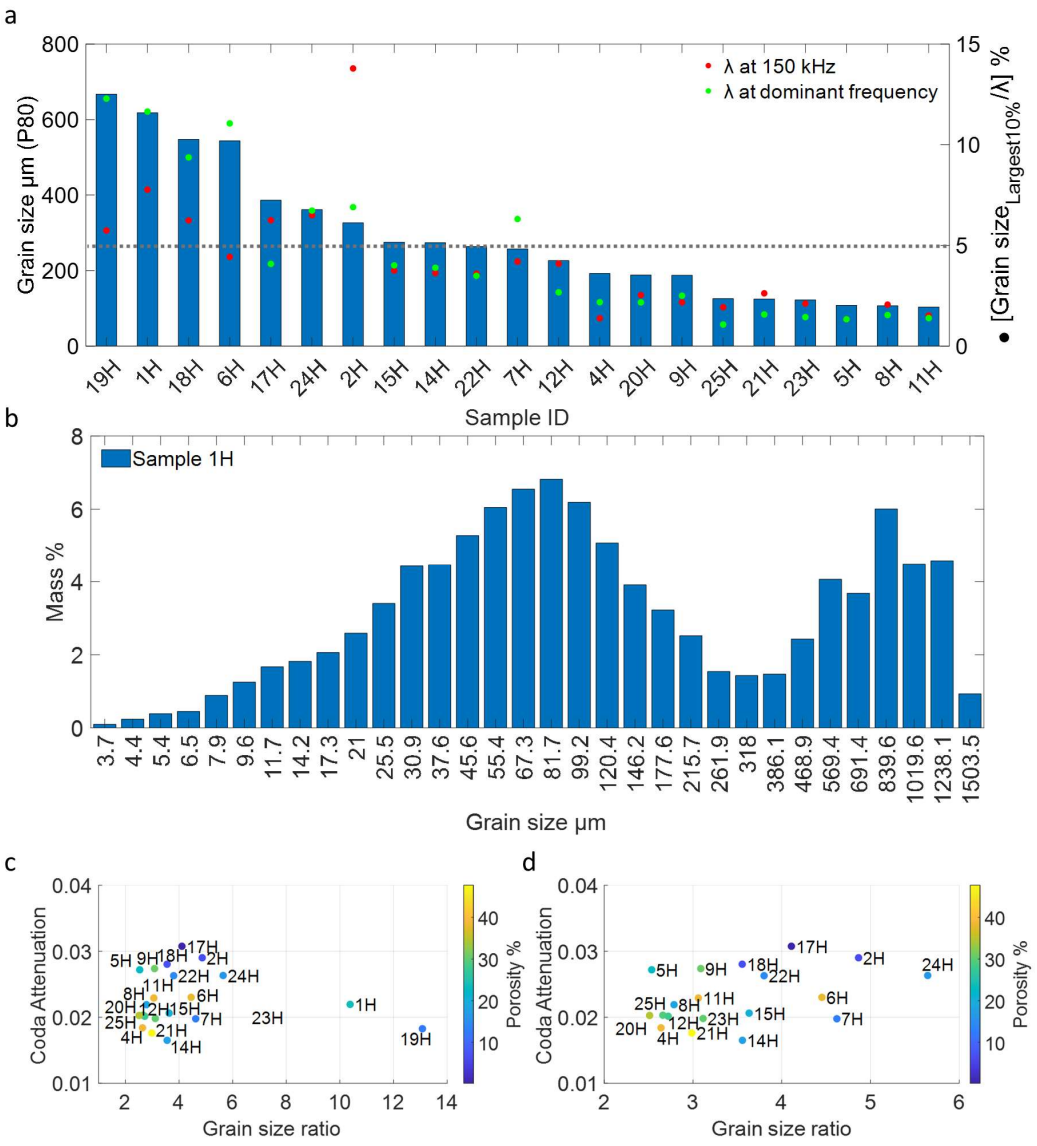

Figure 2. 8. Grain size. (a) distribution below which 80% of the particles reside in each sample. In the secondary y-axis, we observe the ratio between the grain size (for the largest 10%) and the samples wavelength λ (computed at 150 kHz in red and at the dominant frequency recorded in the ultrasonic seismograms in green) reported in percentages. (b) grain size distribution for sample 1H, the horizontal axis shows midpoint ranges; bars indicate the mass % (area multiplied by density) of minerals. (c) Dependency of coda attenuation on grain size ratio, coloured by porosity level in the sample. (d) display a zoom of (c) for grain ratios between 2 and 6 to appreciate the distribution.

Characterization of the heterogeneous medium

We quantified the heterogeneity level in the samples by three different approaches: the measure of 2D textural heterogeneity, 3D pore space analysis, and statistical characterization of the random media. The 2D textural heterogeneity parameters (CV, CL, AR) cannot be directly correlated to attenuation values (Figure 2.9a). The samples have a coefficient of variation CV between 40-50% (which we consider as the heterogeneity level), except for sample 18H, in which CV is 29.8% (this data tip was excluded from the plot to highlight variations for the rest of the dataset). The anisotropy ratio varies from 1.38 to 1.85, except for sample 4H for which the anisotropy reaches 6.88 (again not included in the plot; this high value can be related to the presence of vesicles with a diameter as large as ~8 mm – Figure A5). The correlation length varies from 0.04 mm to 0.40 mm (errors range from 0.028 mm - sample 8H to 0.189 mm - sample 1H). These values are an average of the textural mineralogy present in a 256mm^2 segment of the thin sections. To understand how variable this quantification is at different scales, we divided the segment into 256 subsegments of 1mm^2 (Figure 2.9b). The range of values changes sample by sample, especially for CV, a marker of the heterogeneity of the dataset. AR and CL have lower uncertainty than CV except for samples 1H, 11H, 5H, and 7H.

The spatial autocorrelation of the pore space was best fitted by an exponential function $F(x) = \varepsilon^2 exp^{(-x/a)}$ (Eq. 2.7), where x is the spatial lag, a the correlation length, and ε the standard deviation of the spatial fluctuations of the pores. Then we estimated the correlation length from the exponential fitting to the observed autocorrelation function (ACF – Figure 2.10a). This correlation length is a relative measurement of the heterogeneity level associated with the presence of pores (Figure 2.10b). Only five samples were analysed, the results will have to be tested on a wider dataset to determine a dependency of coda attenuation on correlation lengths.

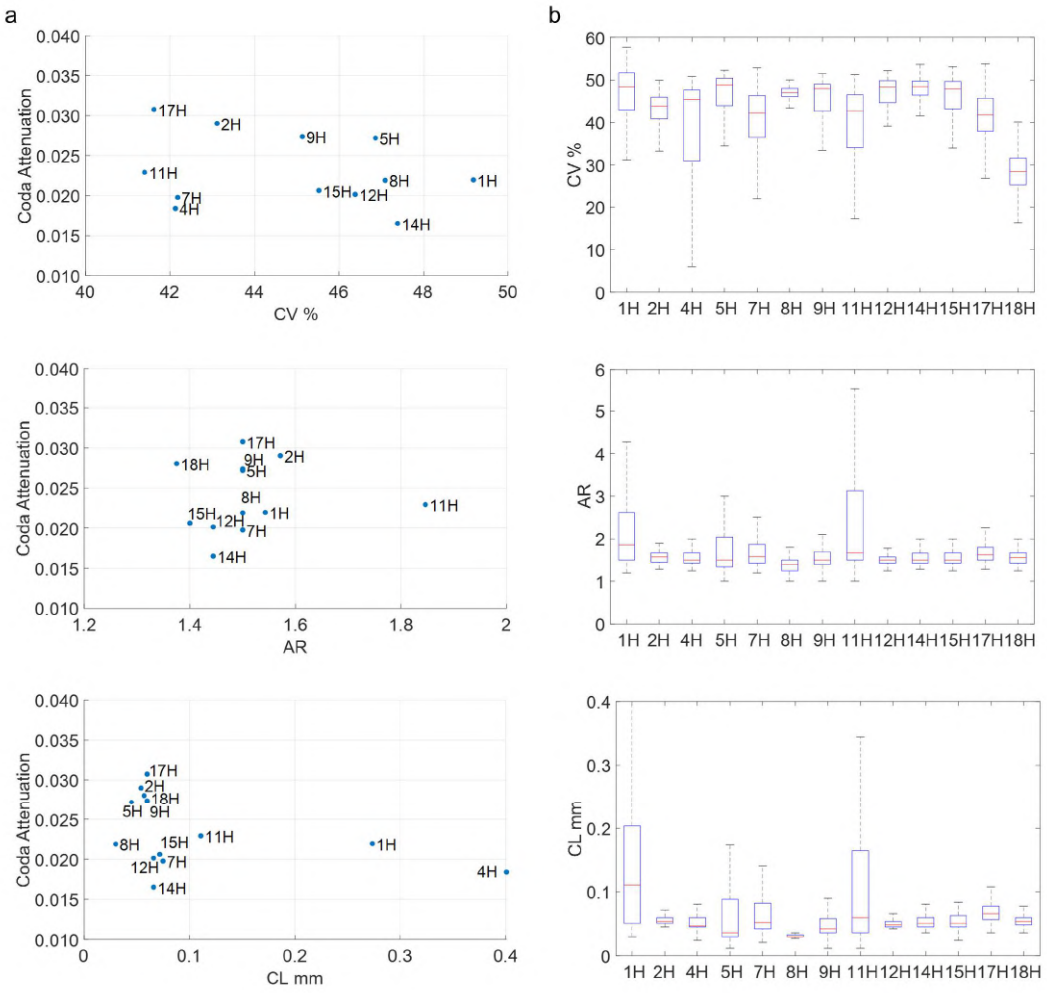

Figure 2. 9. 2D Textural heterogeneity. (a) Relation of CV, AR, and CL with coda attenuation in a 256 mm^2 section of the samples. (b) variation of each parameter measure on 256 subsections of 1mm^2.

The statistical analysis of the random media consisted of determining the correlation length a of the samples, this time considering both pores and minerals, and building up the estimations from the shear-wave velocity fluctuations. The values of ε range from 8% to 13% while a range from 0.09 mm to 1.20 mm (Table A7.1). This relatively small variation in ε indicates that the heterogeneities in the dataset have similar intensity (as was noted from the values of CV) but with distinctive characteristic scale

lengths. The statistical method gave us by far the best correlation with the rock's physical properties (porosity). Samples with porosity lower than 30% show that porosity increases linearly with increasing correlation length (R= 0.72), which translates as well into an increase of the scattering strength (Figure 2.11).

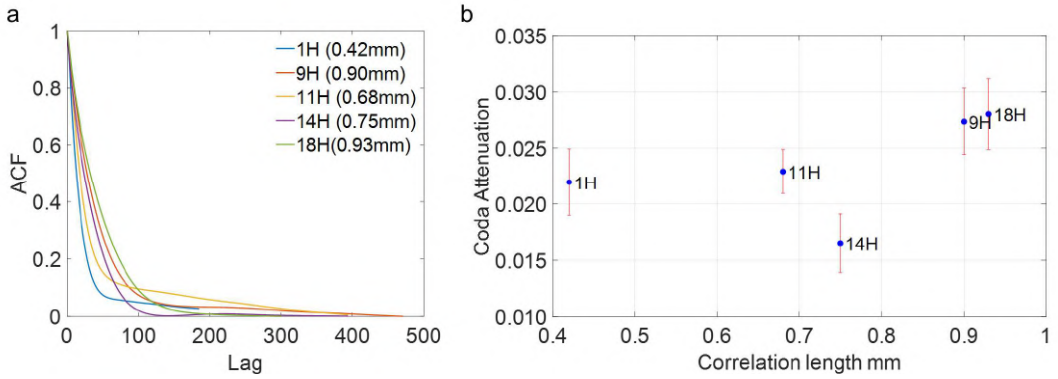

Figure 2. 10. 3D Pore Space heterogeneity. (a) ACF, values of correlation length '*a*' in parenthesis. (b) Dependency of the coda attenuation on the spatial correlation length.

For samples with porosity higher than 30%, parameters other than porosity have a greater effect and the linear relationship is lost. For instance, if we compare samples 4H, 6H, 11H (which have similar porosity levels): (1) the anomalously-high *a* value for sample 4H is due to the size of the vesicles; (2), the anomalously-low *a* value for sample 6H is related to the presence of grains with sizes comparable to the pore sizes; and (3) the lowest *a* value of sample 11H is associated to the irregular pore shapes and the presence of secondary minerals filling the vesicles. On the other hand, why does the sample with the highest porosity has such a small correlation length? The pores in sample 21H have high sphericity, the composition of the sample has one predominant phase mineral (80% amphibolite), and the median grain size is 0.064 mm. Therefore, despite its high porosity, sample 21H is one of the most homogenous samples in the dataset: porosity level on its own is not enough to estimate the level of heterogeneity in the sample.

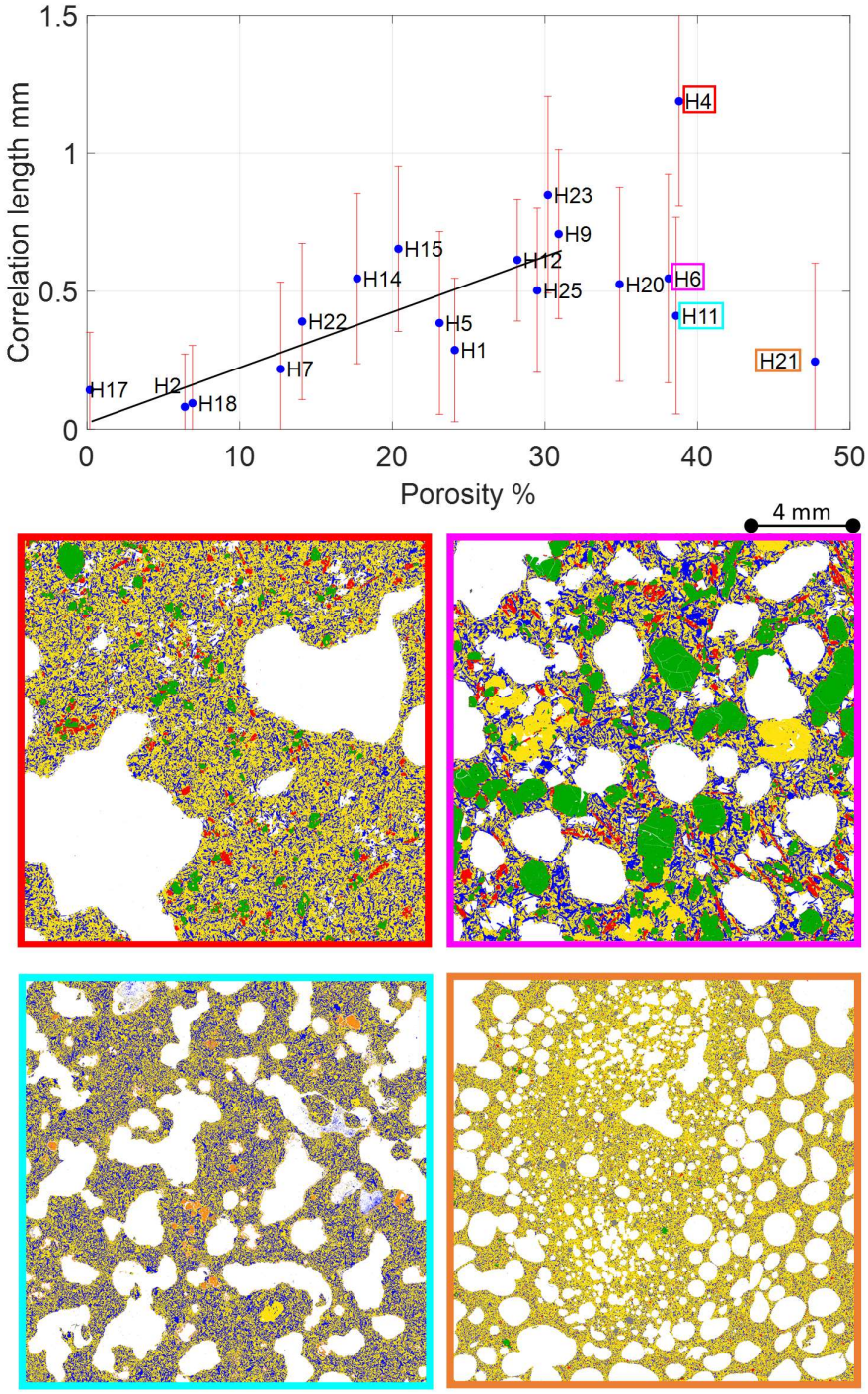

Figure 2. 11. Top: correlation length computed from the statistical analysis of the media versus porosity for the whole dataset, the black line is the linear polynomial fitting. Bottom: section of 2D TIMA images for samples 4H (red), 6H (fuchsia), 11H (cyan), and 21H (orange).

2.5 Discussions

Numerous studies have intended to differentiate between scattering and intrinsic (anelastic) attenuation. We consider that the estimated coda attenuation at ultrasonic frequencies in the studied samples is dominated by scattering attenuation based on the following assumptions: (1) the coda wave field is a product of the multiple scattering inside the samples (i.e. driven by the physical properties of the rock); (2) intrinsic attenuation is mainly related to the geometrical spreading which we consider relatively equal between the samples (given the laboratory setting used for the experimental acquisition and the similar geometry of the samples); (3) as the system was not disturbed by external forces, the changes observed in the waveforms are create by changes in the wave propagation; and (4) there is consistency of internal surfaces forces between grains from sample to sample, then other mechanisms that could contribute to anelastic attenuation (converting seismic energy into heat) at dry conditions (e.g. frictional sliding between grain boundaries, grain contact adhesion) are neglected: they have an insignificant weight over the coda attenuation calculated in this study.

Scaling law of scattering attenuation

Following the scattering classification by Aki and Richards (1980), we projected the relation between ka and kL at a central frequency of 150 kHz (Figure 2.12a), in which k is the wavenumber ($k=2\pi f/V$, where f is the frequency and V the S wave velocity), a is the correlation length, and L is the length of the sample. Note that L is relatively constant (around 5 cm) in the dataset, as we were looking to recreate similar conditions for the acquisition of the ultrasonic waves. Larger samples could allow a larger mapping of the scattering inside the sample. However, different interactions with the borders of the samples would be registered within coda waves, making our analysis more difficult.

In this study we have quantified three different length scales of heterogeneity: when a corresponds to the correlation length from the pore space analysis (blue in Figure 2.12a), the medium perturbation falls into the wide scattering regime: $0.1<ka<1$ and, at

such frequencies, it can be described by effective medium theory (Carcione 2015; Igel 2016). When a relates to the mineral grains then ka<0.1: thus, if textural heterogeneity controls scattering, the sample could be defined as a homogeneous body (orange in Figure 2.12a), with weak scattering for wavelengths corresponding to a frequency of 150 kHz. If the correlation length a is the one computed from the statistical fluctuations of the velocity in the media (yellow in Figure 2.12a), the scattering in the samples varies between weak and moderate and can thus be modelled by using either effective medium theory or an equivalent homogeneous medium. As this is the method showing the lowest uncertainties, this result shows that at the sample scale we cannot work with a single scattering regime.

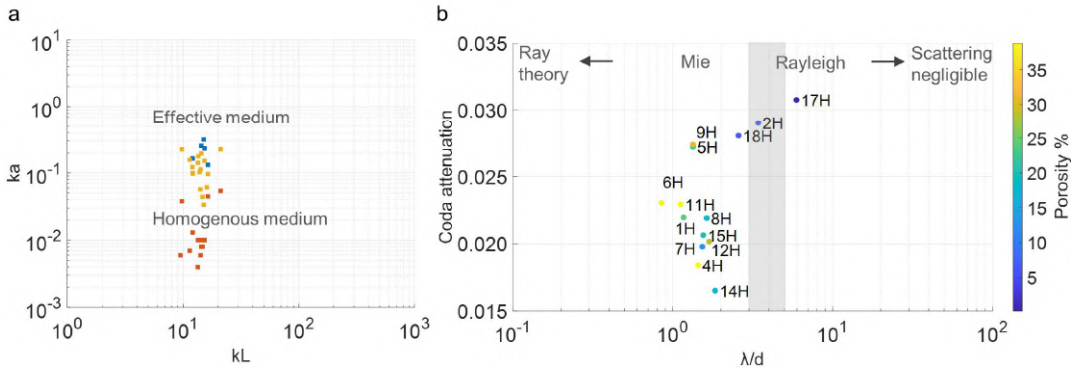

Figure 2. 12. (a) *ka-kL* diagram (*k*: wavenumber at a frequency of 150 kHz, *L*: propagation length *a*: correlation length from the 3D pore space analysis in blue, the 2D textural analysis in orange, and the statistical analysis in yellow); (b) coda attenuation versus λ/d (λ: seismic wavelength at 150 kHz, *d*: size of heterogeneities related to the equivalent diameter of the pores in the sample). The area with grey background represents the transition zone between Mie and Rayleigh regimes.

The need to work between scattering regimes is confirmed by using the ratio between the wavelength λ and the size of the heterogeneity *d* (Figure 2.12b), a common approach in the rock physics community (Blair, 1990; Mavko et al., 2009). Most of the coda attenuation measurements in the samples were taken in media that are described by the Mie scattering regime (less than $\lambda/d \approx 2\pi$). In sample 17H λ>10*d*, meaning that the

heterogeneous rock behaves as a homogenous medium, in which the waves propagate through the sample without scattering on pores and grains; in that case, the contribution of scattering on the coda attenuation is low. In Figure 2.12b, λ is fixed at a frequency of 150 kHz: increasing this frequency results in the scatterers moving towards Mie scattering (lower λ/d ratio).

Coda attenuation versus heterogeneity level

The primary hypothesis in this study was that "as porosity is a direct expression of heterogeneity level in rock samples, and scattering attenuation is a measure of the heterogeneity in the media, then scattering attenuation is controlled by the porosity in the samples". However, as we have demonstrated in this paper, many other factors influence the attenuation parameters at the laboratory scale, such as the shape and size of the pore space (Figures 2.6 and 2.10), the grain dimensions (Figure 2.8; also reported by Calvet and Margerin 2016), the mineral composition (Figures 2.7 and 2.11), and the presence of secondary minerals (Figures 2.6 and 2.11; consistent with Best et al., 1994). It is problematic to establish the exact level of contribution of each factor. A similar level of complexity exists when correlating the velocity of elastic waves with petrophysical properties (Garia et al., 2019; Vedanti et al., 2018). Nonetheless, we have evidence that pore space is the main contributor to scattering (Figures 2.6 and 2.11). The correlation length from the statistical analysis provided the most reliable connection between elastic parameters and rock physics (Figure 2.11). This result is consistent with previous studies that measured velocity fluctuations at the field scale (Holliger and Levander 1992).

The scattering in the dataset is best defined by the Mie scattering regime (Figure 2.12; Liu et al., 2017), a result already obtained when analysing shales (Hu et al., 2018). This outcome is contrary to the notion that the Rayleigh regime is sufficient to describe scattering in rock samples at the laboratory scale, allowing to describe seismic waveforms in samples by analogy to the small-scattering assumption used in the far-field (Sivaji et al., 2002). In seismic exploration, the typical wavelength for shear waves is around 150 m at a dominant frequency of 20 Hz, then the scattering regime for a given scale of inhomogeneities in the media fluctuates based on the resolvable frequency content. If

wavelength and scatterers have a similar dimension (*ka* and/or *kL* becomes larger), ray theory cannot be applied, and techniques specific to computational wave propagation and random media theory play a major role in modelling seismic energy (Figure 2.12a; discussed also in Igel 2016).

Laboratory calibrations for the acquisition of coda waves

Researchers have recognized and tackled the need for appropriate laboratory settings to measure seismic attenuation (e.g., Best et al., 2007; Fujisawa and Takei 2009; Fukushima et al., 2003; Guo and Fu 2007; Sivaji et al., 2002; Subramaniyan et al., 2014; Tisato and Quintal 2013; Tisato and Madonna 2012). Most of these works have targeted the attenuation of direct wave packages, but there is still a significant lack of laboratory guidance for measuring coda wave attenuation. One major drawback of ultrasonic experiments is the high uncertainty associated with the quantification of amplitude-dependent parameters measured from the tail portion of the seismogram (Wei and Fu 2014; Yoshimitsu et al., 2016). As there is a need for calibrating stochastic attenuation parameters on real rock samples, we have assessed the best experimental setting to acquire suitable waveforms for performing reliable analyses on coda decay (Appendix A3 and A4). Despite these efforts, the uncertainty of the coda attenuation estimation is relatively high (Figure 2.6a).

Up-scaling rock physics properties of volcanic rocks.

Upscaling results between nanometres and micrometres, millimetres or kilometres has its trade-off. In this study, we assume that quantifications performed at the micrometre scale (image analysis) hold at the core scale (mm). For example, correlation length values show low variations when measured in subsamples of 1 mm^2 in comparison to measures done over wider areas (256 mm^2) (Figure 2.9). Similar results were obtained when measuring porosity using different methods (Figure A1.1). We infer that measures performed on 2D planes are a reliable representation of the 3D core. There are more systematic methods to assess if the size of the sample over which the properties are computed is large enough (referred to as REV Representative Elementary Volume, e.g., Singh et al., 2020) but this

is beyond the scope of this paper; furthermore, no single method has been validated for all rock physics parameters.

Seismic measurements at the laboratory scale are taken at ultrasonic frequencies because the sensitivity of ultrasonic waves allows us to detect pores, grains, and cracks at a scale of less than half a millimetre. While the transducer used in the experiments emitted a signal with a characteristic frequency of 1 MHz, the output signal had a central frequency of around 150 kHz. This is half of the received dominant frequency for shear-waves in sandstones for the same type of source transducers (Fu et al., 2020). Given the velocity ranges of the samples and their average length, we could only record one to three wavelengths per sample: therefore, we could not map individual heterogeneities of the order of the grain size (max 1-2 mm, but on average ~0.1-1 mm). Grains and (micro)pores act as a group, turning into effective clusters with dimensions comparable to the wavelength (Lucet and Zinszner, 1992). We acquired waveforms using compressional-wave transducers of higher-frequency (5 MHz) targeting smaller wavelengths, but the dominant frequency observed in the volcanic dataset was again lower than 200 kHz.

A similar loss of high-frequency information is a central problem in volcanic imaging exploration of sub-basaltic reservoirs using direct wave phases and amplitudes (Eide et al., 2018; Gallagher and Dromgoole, 2007). Coda attenuation modelling at the field scale shows that the coda wavefield is sensitive to lateral changes in scattering regime (from Rayleigh to Mie) that depend on the ratio between wavelengths and scale of heterogeneity (e.g., at Campi Flegrei caldera: De Siena et al., 2013 and De Siena et al., 2017).

Pore space could thus be the main controller of coda wave techniques, widely used to image and monitor volcanoes. In order to upscale our results, it will be necessary to model coda waves at both field and sample scales. While this can be done analytically, e.g., in the Rayleigh regime and for more homogeneous samples (Calvet and Margerin, 2016), wave equation modelling and radiative transfer techniques including boundary conditions (Obermann et al., 2013; De Siena et al., 2013) are likely necessary in the volcanic case. Then, similar experiments and modelling will have to be performed in

fluid-saturated volcanic samples to properly characterize the effect of fluids on coda waves.

2.6 Conclusions

We characterized volcanic samples in terms of their rock physics properties, pore space topology, texture, and mineralogy to deduce their relationship with coda attenuation measurements. The parameters measured from the rocks (velocity, porosity, and density) as a function of those measured from the scattered wavefield (coda attenuation) do not follow simple polynomial trends. Our findings suggest that:

- The correlation length estimated from statistical functions gives a good approximation of the scale length of the heterogeneities. The intensity of the velocity fluctuations represented by the root-mean-square of the velocity fluctuations is quite similar within the dataset. The differences in these heterogeneous rocks are defined by their scale length. For samples with porosity lower than 30%, there is a linear trend of increasing correlation length with increasing porosity.

- There is no conclusive evidence to quantify the individual contribution of each of the analysed parameters in coda attenuation. However, the results point to pore space as the primary driver of seismic attenuation in volcanic samples, given that the heterogeneities triggering the perturbation of the ultrasonic seismic wavefield mainly correspond to the size and shape of the vesicles.

- The relationship between porosity and coda attenuation is likely influenced by mineral alteration in the samples (i.e., secondary minerals, coating of vesicles and oxidation), the pore size and shape (sphericity level), and the presence of grains with sizes similar to or larger than the pore size.

- The mineral phases and size of the grains determine if we can assume the sample as homogenous. When the grain size is not comparable with the vesicles size, or when

the largest grains are smaller than 5% of the wavelength size, the medium becomes an agglomeration of grains (independently of their mineralogy), which act as a bulk matrix with averaged elastic properties and where the wave travels without interference. Otherwise, the mineral grains and their mineralogy would render the matrix inhomogeneous.

- We consider that parameters computed from 3D X-ray images and those computed from 2D petrographic images are appropriate to characterize the heterogeneity level of the dataset. However, the textural analysis was ineffective in establishing a relationship with coda attenuation.

The analysis of volcanic samples undertaken here strengthens the idea that more laboratory-scale studies should focus on complex samples (e.g., volcanic rocks), which better represent field conditions when trying to model the full seismic wavefield. Further modelling work will help define the individual contribution of the rock physics properties analysed in this study to the attenuation parameters. This new understanding will guide the identification of controlling parameters that can be upscaled to model geophysical observations in the field.

Chapter 3

Pore space topology controls ultrasonic waveforms in dry volcanic rocks.

In this chapter, I modelled ultrasonic wave propagation in volcanic rocks as a function of pore space parameters to confirm that the pore space topology is a primary factor controlling elastic waves. The computational framework applied was spectral element methods. Here I show the individual impact that the amount, size and location of the pores have on ultrasonic wave propagation on dry volcanic rocks independently of porosity.

The chapter was written as a research paper with Dr Luca De Siena and Dr Nicola Tisato as co-authors. It has been submitted to Geophysical Research Letters. I wrote the manuscript, carried out the simulations and assessments and created all the figures. Luca De Siena guide me to improve the analysis and proofread the manuscript, while Nicola Tisato reviewed all the work and its recommendations helped towards the completion of the current version of the paper presented here. The labels of figures, tables and supplementary material have been renamed to be in line with this thesis; in the same order, the references are included in the bibliography section. The mentions of the "supplementary material" in the paper refer to Appendix B in this thesis. Note that some contents of the supplementary material have been merged into the chapter, and extra analysis is presented in the thesis in Appendix B5.

Abstract.

Pore space controls the mechanical and transport properties of rocks. At the laboratory scale, seismic modelling is usually performed in relatively homogeneous settings, and the influence of the pore space on the recorded wavefields is determined by rock-fluid interactions. Understanding this influence in dry rocks is instrumental for assessing the impact of pore topology on waves propagating in heterogeneous environments, such as volcanoes. Here, we simulated the propagation of shear waves as a function of pore space parameters in computational models built as proxies for volcanic rocks. The spectral-element simulations provide results comparable with the results of ultrasonic experiments, and the outcome shows that the size, shape, volume, and location of pores impact amplitudes and phases. These variations intensify in waveform coda after multiple scattering. Our results confirm that pore topology is one of the primary regulators of the propagation of elastic waves in dry rocks regardless of the porosity value.

Plain Language Summary

Pores control the non-elastic behaviour and, in general, the petrophysical and mechanical properties of rocks. Such properties are essential to assess potential resources such as aquifers and reservoirs or hazards posed by earthquakes, volcanoes and constructions. The factors controlling the elasticity of rocks are texture, pore space and the fluids filling the pores. While volcanoes represent a key target for rock characterization, measuring and modelling these factors in volcanic rocks remains challenging due to their intrinsic heterogeneities. In this study, we analyzed how pore space parameters influence the overall elastic properties of rocks by changing one parameter at a time. We created synthetic samples and performed computational simulations that show the individual contribution of the amount, size, location, and shape on waveform phases and amplitudes. The findings demonstrate that we can constrain the pore space in heterogeneous rocks in simple but realistic scenarios. Our results are the first step to providing computationally-driven forward models of seismic signals in heterogeneous volcanic media, necessary to predict the responses of volcanic rocks to stress.

3.1 Introduction

Linking elastic properties of rocks with pore-space parameters is a longstanding focus when characterizing hydrocarbon reservoirs, exploring geothermal resources, assessing volcanic and hydrothermal processes, and applying CO_2 sequestration techniques. This link requires evaluating the role of pore space for permeability models (e.g., Sarout, 2012) and characterizing carbonate rocks (e.g., Baechle et al., 2008) in which pore type and shape dominate the effective rock properties (Xu and Payne, 2009). The pore structure is also relevant in civil and geotechnical engineering, where pore size distribution influences how waves propagate in construction materials (e.g., Zhao et al., 2014). Recent studies provide numerical algorithms to evaluate changes in pore space topology as a function of flow parameters (reactive transport - Lisitsa et al., 2020; Prokhorov et al., 2021). However, many of these studies have focused on sedimentary rocks (as main reservoir targets) and overlooked volcanic rocks, even though large porosities characterize the latter. Recent studies have focused primarily on the fluid-rock interaction within such rocks (e.g., Adam and Otheim, 2013; Adelinet et al., 2010; Benson et al., 2008; Clarke et al., 2020; Fazio et al., 2017).

Rock physics models typically relate velocities of elastic waves with porosity (Nur et al., 1998). However, such relations are often disregarded due to variations in rock texture, comprising pore space topology and mineral composition. For natural rocks, elastic properties cannot be accurately predicted by a single pore-space property such as the porosity value, and the rock physics model should include additional parameters dependent on the topology of inclusions or pores (Dou and Sullivan, 2011; Durán et al., 2019; Ju et al., 2013; Zhang and Sharma, 2005; Zhao et al., 2014). Heap and Violay (2021) recently discussed how the pore size, shape and distribution can also influence the mechanical properties and failure modes of volcanic rocks. Several theoretical models that describe effective elastic moduli in media characterized by inclusions (pores) interacting with the host matrix (e.g., Kuster and Toksöz, 1974; Differential Effective Medium – DEM: Norris, 1985; Zimmerman, 1991) and have been used to explore the influence of pore on elastic wave velocities. Berryman (1995) summarized the expressions for the most used inclusion shapes in these models, in which the interactions

between pores and the background medium are limited within effective medium approximations (Adelinet and Le Ravalec, 2015; Cheng et al., 2020; Fortin and Guéguen, 2021). Dry volcanic rocks have a complex pore system characterized by large pores (or vesicles) (Shea et al., 2010) where the effective medium approach can provide reliable estimates in case of fluid saturation (Hurwitz et al., 2003). However, numerical modelling and analyses of the phase and amplitude of elastic waves can reduce gaps between data and models in these media. When coupled with field-scale seismic modelling (e.g., Rasht-Behesht et al., 2020), they become instrumental to understand the imaging and interpretational potential of seismic waves propagating on fluid reservoirs and melt.

Several studies have described volcanic rocks in terms of texture, porosity, permeability, elastic moduli, and ultrasonic velocities (Durán et al., 2019; Fortin et al., 2011; Heap et al., 2020; Rossetti et al., 2019; Vanorio et al., 2002). Body wave velocities have been estimated as a function of porosity and pore shape in basaltic rocks, even as a representation of Martian rocks (Heap, 2019). However, few studies have targeted the effect of pore space topology on seismic-wave propagation in volcanic rocks. Working with dry samples and separating mineral texture and fluid interactions is one approach to constrain the effect of pore space on the effective elastic properties of rocks. Pore fluids have a prevailing effect on wave velocities, hiding the effects of pore geometry on waveforms (David and Zimmerman, 2012). While fluids are often present in volcanic rocks, they are not omnipresent (e.g., Hurwitz et al., 2003; Delcamp et al., 2016; Rowley et al., 2021). Thus, such modelling might help calibrate field measurements and recognize the difference in elastic wave signatures of saturated versus dry rocks.

Volcanic rocks are usually characterized using laboratory measurements (core analysis) or microscopy (on thin sections). More recently, digital rock physics (DRP) has proven to be a good approach to estimate physical properties without compromising the samples (e.g., Andrä et al., 2013; Ikeda et al., 2020). DRP consist of analysing 3D digital high-resolution images of the internal microstructure of rock cores. However, DRP methods are computationally expensive and often unavailable to researchers as it requires access to X-ray microcomputed tomography equipment. Computational simulations of ultrasonic wave propagation are a non-invasive way of testing the elastic response of

rocks under different scenarios. Such simulations allow unravelling the effect of pore space topology parameters on the waveforms and, in turn, on the elastic properties of the rocks. Simulations of waves can be performed at different scales, e.g., from ultrasonic to sub-seismic frequencies. Apart from wave arrivals and direct amplitudes, ultrasonic waveforms present coda waves that are caused by dispersion of the coherent waves and are highly sensitive to small-scale heterogeneities (Aki, 1969). These waves are key to characterising media at all scales. For example, at the mantle scale, wave scattering marks compositional heterogeneities (e.g., Faccenda et al., 2019). In the laboratory, these heterogeneities are the pore space and mineral grains of sizes comparable with the wavelength size (e.g., Di Martino et al., 2021).

In this study, we performed computational simulations to illustrate the effect of pore space topology on the propagation of ultrasonic waves in synthetic analogues to dry volcanic rocks. We used the software SPECFEM2D (Komatitsch and Vilotte, 1998) based on the spectral element method (SEM - Tromp et al., 2008) to simulate 2D elastic wave propagation, which allows us to accurately model ultrasonic propagation in a heterogeneous medium (Rosenkranztz et al., 2019). This approach allowed us to evaluate the impact of different pore space parameters on the full ultrasonic wavefield. We simulated shear waves propagating in synthetic samples, creating a medium described by properties previously characterized in a rock sample in the laboratory. We identified the individual contributions of pores number, size, and location; the results show that the transmitted waveforms depend on the distribution and geometry of the pore structure.

3.2 Methods

We performed simulations of the ultrasonic wavefield in synthetic samples resembling the ultrasonic S-wave transmission method. Full wavefields were simulated using the 2D spectral-element method code SPECFEM2D (Komatitsch and Vilotte, 1998; Implementation details in Appendix B1). The source is a Ricker time wavelet with a

dominant frequency of 100 kHz, in order to simulate the source conditions and characteristic frequency observed in chapter 2 when acquiring ultrasonic waveforms from volcanic samples at the laboratory scale. Sources and receivers covered a line of 13 mm length (i.e., half of the width of the sample), centered along the vertical axis of the sample to simulate the recording at the laboratory scale and obtain a plane-wave. In such a way, we obtained a quasi-plane wave source, where the single wavelets received at the nodes representing the receiver were averaged into one waveform.

The 2D model is rectangular (25 mm wide and 50 mm long) and represents a 2D section of a rock sample. The model is meshed using GMSH (GNU finite element mesh generator – Geuzaine and Remacle, 2009), and it includes 8945 elements, with a maximum and minimum grid size of 0.96 mm and 0.11 mm, respectively. We compute waveforms of 4 ms discretized with 100,000-time steps (i.e., each step has a duration of 4 ns), satisfying the stability conditions in space for the fourth-order grid and in time for the Newmark second-order stepping scheme (Berland et al., 2006). Stacey absorbing boundary conditions (Stacey, 1988; Komatitsch and Tromp, 2003) were applied along the physical boundaries of the sample to limit reflections and conversions at the boundaries of the samples that perturbed the wave propagation. We neglect the effect of internal interactions on the sample mesh (pore-mineral interfaces) because the SPECFEM code imposes smoothness at such sharp boundaries (Rosenkrantz et al., 2019). The synthetic media mimics volcaniclastic rock resembling the rock sample 1H in Di Martino et al. (2021). Sample 1H is a basaltic rock plug of ‘A‘ā lava flow facies cored in Hawaii from well PTA2 (Figure 1.2); it is densely plagioclase phyric with small isolated vesicles. This sample was chosen because it was fully characterized in chapter 2, thus it is well known. On the other side, it is an appropriate choice for this analysis due to its pore space distribution. The media consists of two elastic velocity models: (1) a model representing the homogenous rock matrix with the elastic properties corresponding to the core rock (density ρ_r = 2940 kg/m3, P-wave velocity Vp_r= 2860 m/s and S-wave velocity Vs_r= 1490 m/s); and (2) a model representing the pore space with density ρ_a = 1.020 kg/m3, and the P- and S- wave velocities (Vp_a= 330 m/s, Vs_a= 0 m/s) corresponding to air properties.

3.2.1. Voigt and Reuss bounds

Before the analysis, we tested the stability of the simulation on layered materials representing the Voigt ($M_V = \sum_{i=1}^{n} f_i M_i$) and Reuss ($\frac{1}{M_R} = \sum_{i=1}^{n} \frac{f_i}{M_i}$) bounds, where f_i and M_i are the volume fraction and the modulus of the i-th component, respectively. To compute the effective dynamic modulus, both P- and S- waves were propagated into two synthetic samples, one for the Voigt (or upper bound), in which the layers are arranged in the vertical direction, and the second for the Reuss (or lower bound), in which the layers are arranged in the horizontal direction. Then we picked the V_p and V_s first arrivals and the bulk modulus (K) of the samples was computed as $K = \rho\left(V_p^2 - \frac{4}{3}V_s^2\right)$. The dynamic bulk moduli estimated for two different porosities show a good agreement (Figure 3.1) with the upper and lower bounds, giving us confidence in the waveforms generated for more complex scenarios.

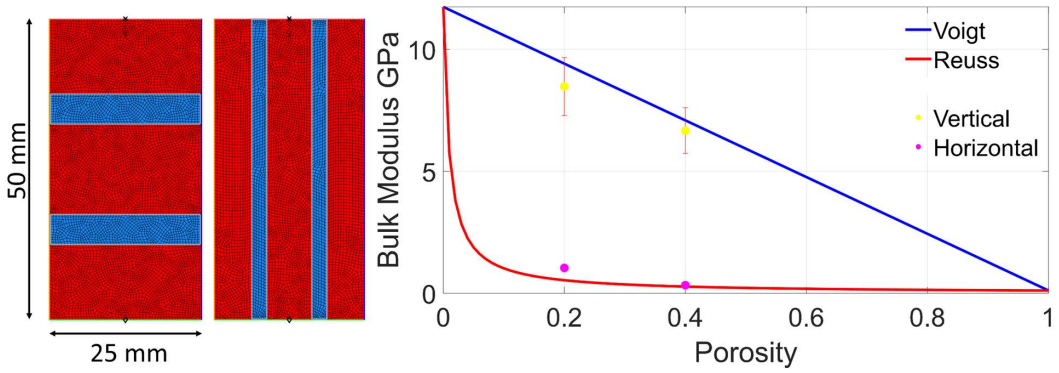

Figure 3. 1. Representation of the Voigt and Reuss bound on the elastic bulk modulus. Left: synthetic samples used in the simulation: the rock mineral matrix in red and the pore space in blue, here the pores occupied 20% of the area. Right: Upper and lower bounds of the bulk modulus for sample 1H and dynamic bulk modulus (dots) calculated from the simulated waveforms for samples with 20 and 40% porosity.

3.3 Results and discussion.

We present three case scenarios in which the geometry of the samples is constant but their pore distribution and characteristics vary to test the hypothesis that the pore space topology controls the ultrasonic waveforms. The S-wave velocity was measured from the relation between the first break (arrival time) in the waveform and the source-receiver distance. The sensitivity of the S-waveform to pore space was investigated by changing one characteristic of the pore topology at a time. The results (Figures 3.2, 3.3, 3.4) correspond to SH-wave propagation in 15 synthetic samples made for 2D grid meshes, where the pore space occupies 22% of the area (i.e., representative of a sample with 22% porosity). We kept porosity constant to diminish its influence on the effective properties and to focus on the topology of the pore space. In the same way, the aspect ratio of the pores has been kept constant (α=1): we represent spherical pores in all the scenarios. The amplitude (or energy) decay observed in the following results is highly associated with the ratio (λ/d) between the seismic wavelength (in this study, $\lambda=f/v$=15 mm) and the size of the scattering heterogeneities (d- here the diameter of the pores): when $\lambda>>d$ the medium behaves like an effective homogenous medium, for $\lambda>d$ the medium falls in the Rayleigh domain, while for $\lambda\approx d$ the medium response is described by Mie scattering (Mavko et al., 2009). The Pearson correlation coefficient (cc) between the different waveforms and the energy ratio of direct and coda waves for each case quantifies the statistical relation between the samples for the three cases.

3.3.1 Case-1: Pore location

With the first simulation, we test if the location of the pores in the sample plays a role in the transmitted waveform. This case consists of 5 wave propagation models in synthetic samples (L1, L2, L3, L4 and L5, Figure 3.2) having 22% porosity and 10 pores with size d= 6 mm; however, pores are located randomly in the grid to evaluate the effect of the pore location on the wave propagation. The correlation coefficient between samples shows that there is a strong to a very-strong correlation between the waveforms (Table 3.1). The S-wave velocities, measured from the arrival time of the first break in the waveform and the propagation distance, range from 1350.0 to 1359.6 m/s. Waveform

shapes are similar, especially in the arrival of the wave package; however, there is still a shift in phases and amplitude in the maximum of the envelope signal and the coda. The maximum peak amplitude ranges from 1.02 to 3.59.

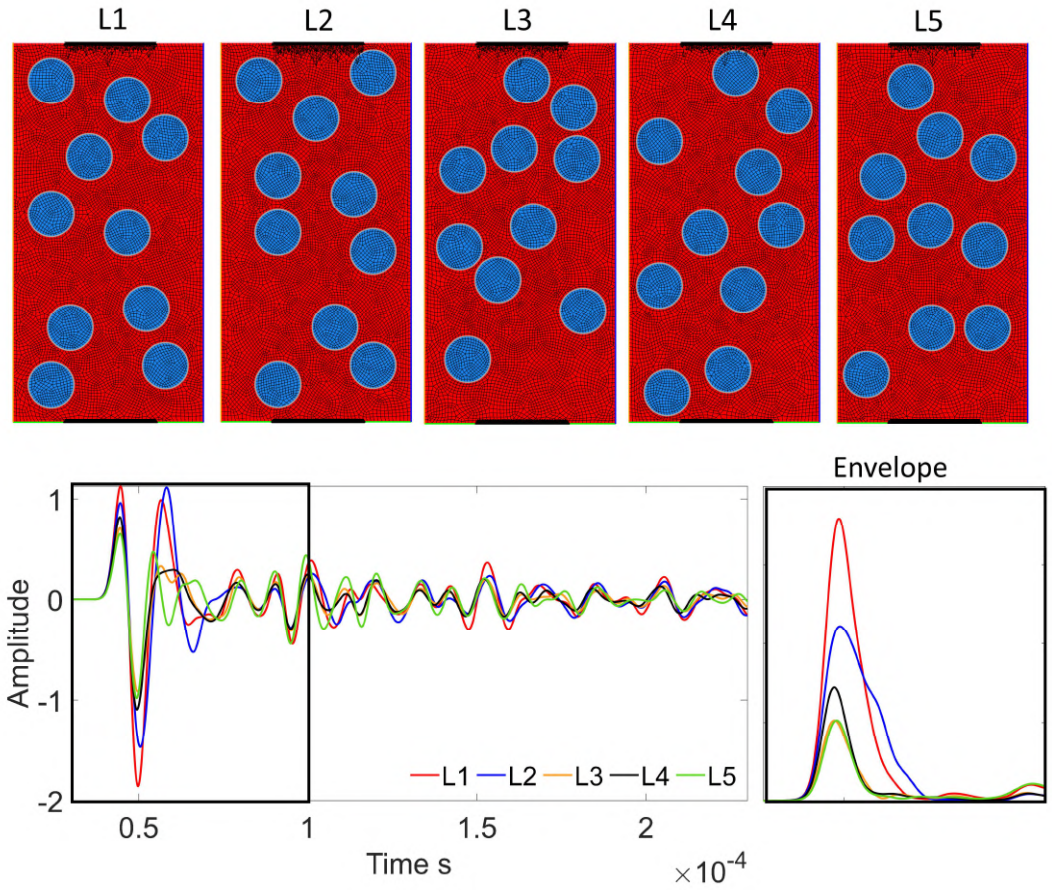

Figure 3. 2. Simulations for Case-1. Top: synthetic samples, the rock mineral matrix occupies the red area while the void pores are the blue circles. Bottom: S-wave waveform acquired for each sample (left) and their energy envelope (right) for the first second of propagation.

To assess if the amplitude changes were driven by the closeness of the pores to the sensors, we run a similar simulation (see Appendix B2) in which the pores were kept at least half-wavelength away from source and receiver to remove their near-field influence on the sensor, we found that the observation regarding waveform similarity is the same for both scenarios. However, the maximum peak amplitude of the envelope is

closer (from 2.40 to 2.76) when the pores are separate from the sensors. From Case-1, we conclude that the location of the pores influences ultrasonic S-wave propagation after the first arrival. The fact that the distribution of the pores into the samples can create a variation in the acquired waveforms (even a small one) strengthens the idea that pore space topology must be considered and likely modelled when analyzing the full waveform. This observation is especially relevant for applying and interpreting coda wave interferometry results in heterogeneous Earth environments, where the travel-time perturbation and changes in velocities vary with the scattering paths (Snieder, 2006; Azzola et al., 2020).

Table 3. 1. Correlation coefficients for Case-1

	L1	L2	L3	L4	L5
L1	1.00	0.93	0.92	0.92	0.71
L2	0.93	1.00	0.84	0.85	0.49
L3	0.92	0.84	1.00	0.96	0.82
L4	0.92	0.85	0.96	1.00	0.79
L5	0.71	0.49	0.82	0.79	1.00

Negligible (0-0.1)
Weak (0.1-0.39)
Moderate (0.4-0.69)
Strong (0.7-0.89)
Very Strong (0.9-1)

3.3.2 Case-2: Pore sizes.

For Case-2, we evaluated the effect of the pore size distribution by keeping constant the number and location of pores (the total porosity remains 22%). We modelled five samples (p12s1, p6s2, p4s3, p3s4, p2s6– Figure. 3.3), having pores with sizes ranging from d=2.42 to 7.82 mm, with the centre of the circles located at the same position in the mesh of the five samples. The lowest correlation between waveforms (Table 3.2) was between samples p12s1 and p6s2 (cc= 0.68 - interpreted as a moderate correlation): while p12s1 shows a quasi-homogeneous distribution of pores in space, p6s2 has two characteristics pore sizes (16% and 50% the size of the wavelength) and the larger λ/d ratio between the samples in Case-2. The correlation between samples is strong in all other cases and highest between samples p4s3 and p2s6 (cc = 0.91). Similarly, the maximum amplitude observed in the envelope (Figure. 3.3) is close (1.77-1.98) for four out of five samples, while sample p4s3 has the highest maximum amplitude (2.94).

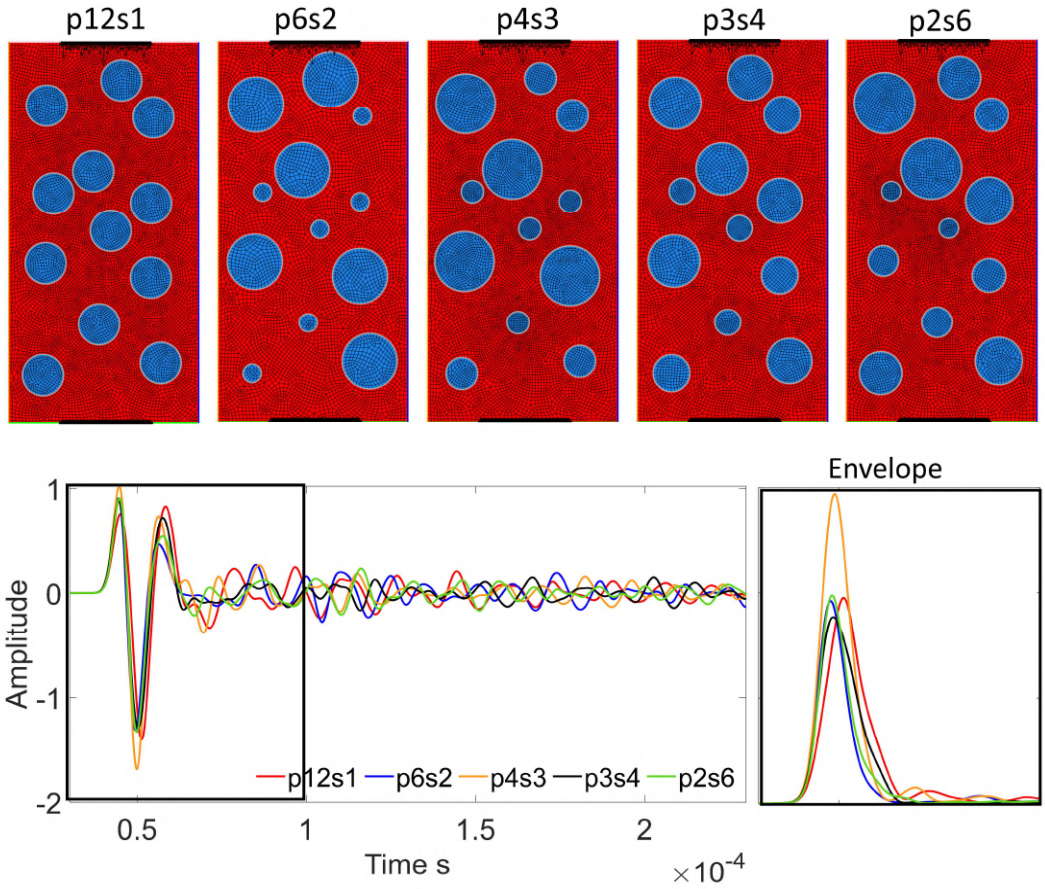

Figure 3. 3. Same as Figure 3.2 for Case-2.

The wave propagation in the five samples of Case-2 is affected by Mie scattering, the differences observed between the waveforms are related to the effect of the ratio λ/d on the dissipation of energy during the wave propagation. The inhomogeneity in pore sizes can redistribute energy later in the coda or dramatically increase the recorded energy (envelope of p4s3). The S-wave velocity ranges from 1345.1 to 1353.3 m/s, which is a close match, but after the first wavelength, there is no simple relationship between the size of the pores and the temporal redistribution of energy, with its description requiring a complete understanding of the multiple-scattering process. From Case-2, we conclude that the size of the pores has a smaller effect on the wave arrival than the amount of the pores but a larger effect on direct and coda wave energies.

Table 3. 2. Correlation coefficients for Case-2.

	p12s1	p6s2	p4s3	p3s4	p2s6
p12s1	1.00	0.68	0.71	0.79	0.73
p6s2	0.68	1.00	0.84	0.82	0.80
p4s3	0.71	0.84	1.00	0.87	0.91
p3s4	0.79	0.82	0.87	1.00	0.88
p2s6	0.73	0.80	0.91	0.88	1.00

Negligible (0-0.1)
Weak (0.1-0.39)
Moderate (0.4-0.69)
Strong (0.7-0.89)
Very Strong (0.9-1)

3.3.3 Case-3: Pore Number

With case-3, we confirm the hypotheses that: (1) porosity cannot predict the full-wave propagation of an elastic wave; and (2) pore space topology has a significant influence on waveforms (e.g., Di Martino et al., 2021). Case-3 consists of 5 wave-propagation models in synthetic samples with the same porosity, but a different number of pores randomly placed in the samples. The samples named N4, N8, N16, N32 and N64 have 4, 8, 16, 32 and 64 pores, respectively (Figure 3.4). To keep the porosity constant, the pore sizes are different between the samples but constant in each sample, with diameters ranging from 2.34 to 9.4 mm. Therefore, the elastic response of Case-3 samples can be described by different scattering theories.

The recorded waveforms vary considerably with the number of pores (Figure 3.4), indicating that the wave propagation in samples with the same porosity varies considerably with pore distribution. The lack of a progressive, smooth increase of the maximum amplitudes (which varies from 0.80 to 9.65, the largest range between the three study cases – see the envelope in figure 3.4) or phases with the number of pores (waveform in Figure 3.4) shows that the location and dimension of pores matters even when wavelengths are of the order of the sample dimension.

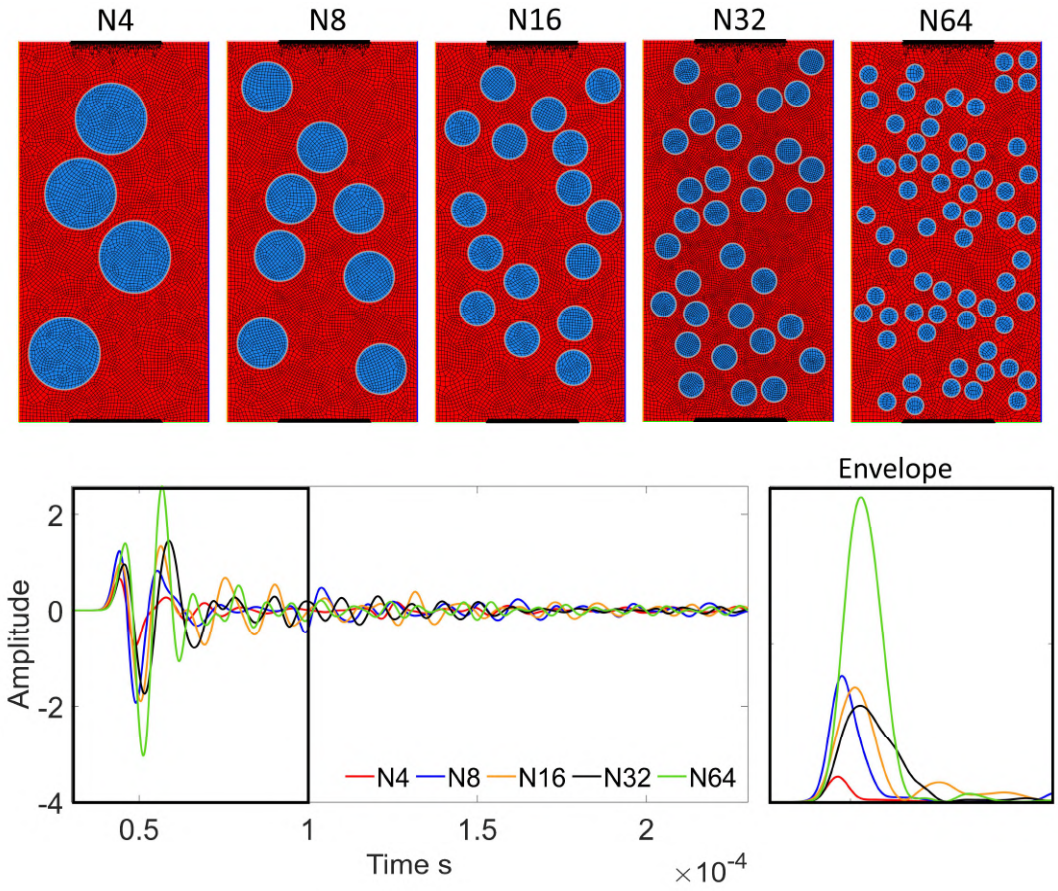

Figure 3. 4. Same as Figure 3.2 for Case-3

The amplitude changes dramatically for sample N64: the density and small size of the pores (d=2.34 mm) make this sample behave as an effective homogenous medium with a short correlation length. Then the measured amplitude is a strong function of the reflection coefficient, the product of the proximity of the pores to the source and the receiver. This observation trades off with the high number of pores that work as scattering points, changing amplitudes and phases of the propagating wave dramatically close to the limit of the Rayleigh scattering domain ($\lambda/d \approx 2\pi$). There is no gradual increase in amplitudes between the other samples (N4, N8, N16, N32), whose elastic responses are better described by Mie scattering. For sample N4, in which the pores have the largest size d= 9.40 mm, we observe the lowest amplitude, suggesting that the presence of large

pores (vesicles) has the strongest effect on phase and amplitude variations. The results for sample N64 can be associated with those obtained for a periodic structure in triangular lattices with metamaterials or arrangements of cavities with sub-wavelength (smaller than half the wavelength) spacing (Colombi et al., 2016). In these, arrangements the inclusions are not considered scatterers but resonators (Achaoui et al., 2013). They are often studied under effective media approximations, with some composites presenting both a Bragg scattering (originated from the structure) and local resonances (Kaina et al., 2013). Further analysis of porous samples with periodic structures could offer more insights into these processes.

The correlation coefficient (*cc*) between samples shows that there is a weak-to-moderate correlation between the waveforms (Table 3.3). The S-wave velocity ranges from 1302 to 1362 m/s, a variation change much larger than the maximum one (10 m/s) observed in Cases 1 and 2. From Case-3, we conclude that, for rock samples of equal porosity, the acquired waveforms are different when the samples have a different number of pores; however, we demonstrated that there is no simple relation between the number of pores, phases and amplitudes. Thus, porosity and number of pores cannot describe the full wave propagation.

Table 3. 3. Correlation coefficients for Case-3.

	N4	N8	N16	N32	N64
N4	1.00	0.78	0.56	0.48	0.52
N8	0.78	1.00	0.72	0.45	0.54
N16	0.56	0.72	1.00	0.68	0.77
N32	0.48	0.45	0.68	1.00	0.68
N64	0.52	0.54	0.77	0.68	1.00

Negligible (0-0.1)
Weak (0.1-0.39)
Moderate (0.4-0.69)
Strong (0.7-0.89)
Very Strong (0.9-1)

3.3.4 Correlations between Cases A, B and C: Energy Ratio Distribution

To better quantify the differences between the three cases we used an attenuation parameter: the energy ratio or the relation between the root-mean-square (RMS) of the wave package and the RMS of the coda window. The distribution of energy ratio for Case-3 (Case_number: different pore density/number) is the largest; this means that there are significant differences in the waveform between the wave package and the coda when using samples with different amounts of pores, sizes and locations. The range is smallest for Case-1 (Case_loc: different pore locations), in which the geometry and number of pores are constant, and the only variable is the location of the pores in the grid. The range of Case-1 (Case_loc) confirms that despite the good correlation estimated between the waveforms of samples L1, L2, L3, L4 and L5, the location of the pores creates indeed a shift in time, amplitudes and phases. Even at these scales and frequencies, waveforms and phases are different depending on the propagation path between source and receiver.

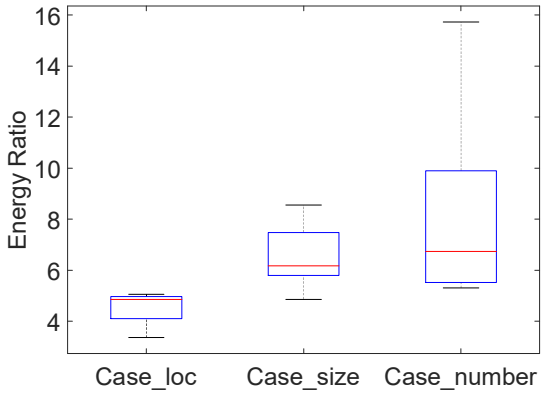

Figure 3. 5. Range of energy ratio between the wave package and the coda window between the samples of each case.

3.3.5 Case-4: Pore space topology resembling the rock sample.

In Case-4, we simulate the wave propagation in a rock sample mimicking the pore-space topology of the basaltic rock sample 1H (Di Martino et al., 2021). To create the mesh, we used a 2D optical image under plane-polarized light and selected the 45 largest pores (pores with an equivalent diameter smaller than 1.5 mm are not comparable with the wavelength) to relate the waveform acquired on the real sample with that obtained in a synthetic sample with spherical pores (Figure 3.6a, Appendix B3). In this case, the mesh comprises 136,854 elements, with a maximum and minimum grid size of 0.21 mm and 0.013 mm, respectively. We computed a waveform of 3 ms using 800,000-time steps with a duration of 0.38 ns each. The area occupied by each of the pores was estimated using ImageJ (Rasband, 2018). Spherical pores of the same area were placed in the grid, mimicking their position on sample R1H. The primary differences are caused by the shape (sphericity level) of the pores as: (1) the locations of the pores have the lowest impact on the waveform shape (Case-1); and (2) the number of pores and area occupied for each pore is the same for both samples. These differences are apparent in the coda, while real and synthetic S waves have similar direct wave packets.

Figure 3.6b, which summarizes our results, shows that the estimated velocities are lower than those predicted with theoretical models (Kuster and Toksöz 1974, called K&T in figure 3.6 and DEM, see Appendix B4). The observations (R1H) cannot be reproduced by the same models as: (1) they describe effective media, which is not the case here given the large size of the pores; (2) they are developed for inclusions with specific aspect ratios (like spheres, disk, and penny cracks), which are not representatives of the shapes of the pores found in natural volcanic rocks; and (3) they assume that the pores act as isolated heterogeneities, while our methodology can handle the stress field between heterogeneities close to each other.

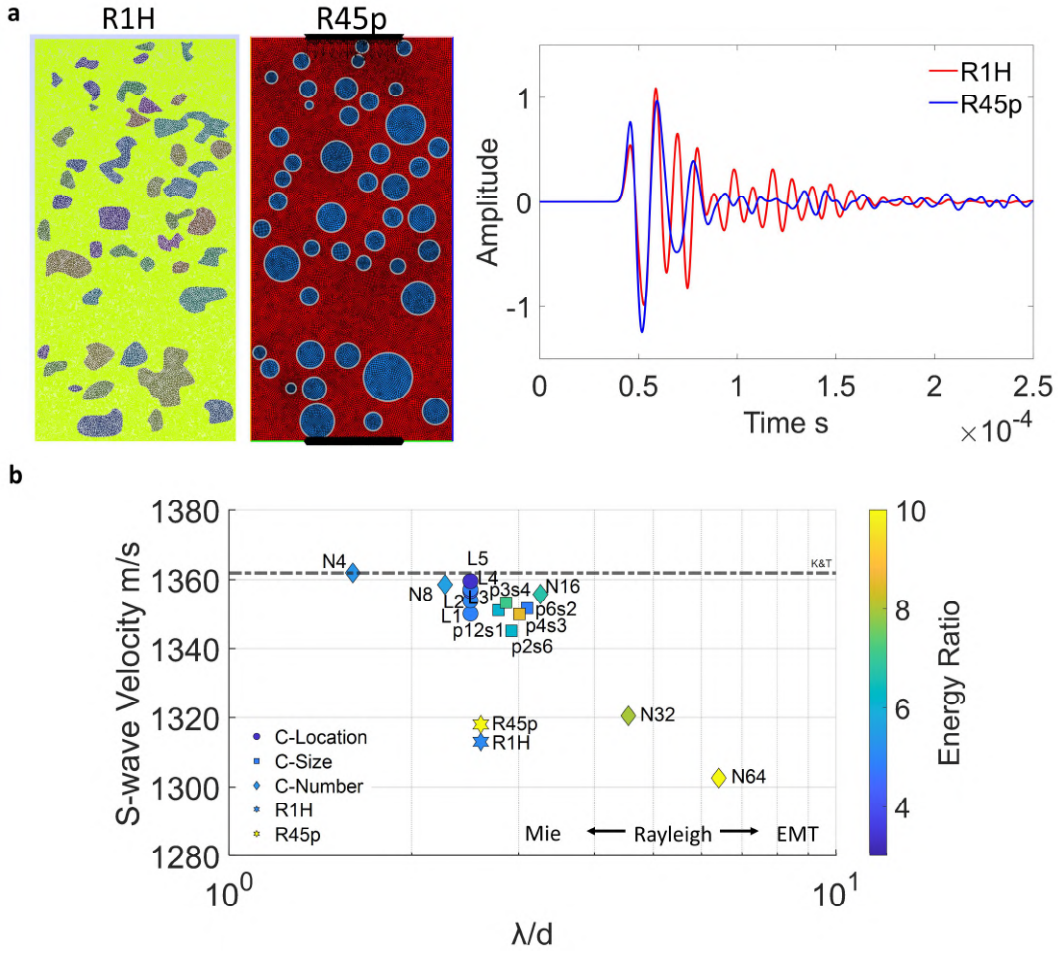

Figure 3. 6. (a) S-wave propagation in a synthetic sample representing the rock sample 1H. In R1H the pore space is reconstructed from digital images while in R45p is simulated; (b) Velocity vs λ/d (λ: wavelength, d: average diameter of the pores in the sample). The color scale represents the ratio between the energy in the main wave package and the coda waves. The dashed line indicates the K&T bound, while the maximum expected velocity is ~1588 m/s. The range of the λ/d axis going towards Mie scattering and Effective Medium Theories (EMT) is shown for reference.

It is necessary to use numerical simulations to constrain or predict the elastic behaviour of porous samples. However, a simple replica of the amount, location, and size of the pores can fit the S-wave packet in this simple scenario (Figure 3.6). Forward modelling travel time and direct-wave amplitude information, thus inverting for pore space, is possible with a relatively simple physical description and ready-to-use

computational tools, like SPECFEM2D (Komatitsch and Vilotte, 1998). On the other hand, the analysis of coda waves is more complicated. The non-sphericity of the pores increases reverberations in the early coda, slightly increasing peak delays, but it also drastically reduces peak amplitudes at later times (e.g., before and after 150μs in Figure 3.6a). Energy ratios for R1H and R45p (5.08 and 10.89 respectively) differ despite having similar S-wave velocities (1312 and 1318 m/s respectively, Figure 3.6b). These results have major consequences on the potential, applicability and interpretation of techniques using scattering as a primary physical trigger at rock and field scales, such as seismic interferometry (Snieder, 2006; Azzola et al., 2020) or absorption imaging (Sketsiou et al., 2020).

From Case-4 we conclude that it is necessary to include a pore-space representative of a realistic propagation medium when analyzing the full waveform because coda waves depend on the pore space geometry. Wavefront distortions are also observed at a regional scale by deviations in the wave propagation path between the source and receiver caused by the Earth's structure's heterogeneities (Magrini et al., 2020). In the same way that petrophysical parameters estimated from rock samples or outcrops represent the properties at the field scale, our results can be upscaled to the reservoir scale, helping constrain petro-elastic and seismic models.

3.4 Conclusions

In this study, we analyzed the pore space as the main driver of the S-wave velocity and amplitude perturbations. We defined the individual contribution of the number of pores, pore sizes and location of the pores on the acquired waveforms by using 2D synthetic samples that resemble volcaniclastic rock samples. The conclusions are that:

- It is not solely porosity that controls elastic wave propagation in heterogeneous samples, as rock samples of equal porosity but different pore space topology

produces different waveforms (i.e., the arrival of the first break, maximum amplitude, phases and coda waves).

- The size of the pores is the primary contributor to changes in S-wave propagation and therefore a trigger of the changes in direction and phase of the propagating wavefield, as suggested by scattering theories.

- The location of the pores has the lowest impact on amplitudes and phases of the direct wave (the range of peak delay values between the 5 samples for Case-1 is 0.0013 ms while this range increases to 0.0033 ms for Case-2 and 0.0045 ms for Case-3); hence its effect could be overlooked when estimating the velocity of elastic waves from ultrasonic wave propagation. However, the increased effect at later times could be of greater significance at the field scale.

- Energy ratios change with pore space topology as coda waves are influenced by the topology of the pores more than the S-wave package. The range of change is small when the only variable is pore location (standard deviation of 0.63 for Case-1 in this study) and larger when the three variables -location, size and number- are involved in the pore space distribution (standard deviation of 3.85 for Case-3, six times larger than for Case-1)

- The S-wave arrival is the only waveform parameter that can be satisfactorily reproduced using an average size and number of pores in a dry volcanic sample without the need for a replica of the pore network (99.5% closeness in this study between samples R1H and R45p).

This work establishes explicit constraints of wave propagation modelling on dry volcanic rocks having a complex pore network. We conclude that models incorporating porosity and pore topology as separate factors must be developed to characterize volcanic materials.

Chapter 4

Reconstructing hydrothermal fluid pathways and storage at the Solfatara crater (Campi Flegrei, Italy) using seismic scattering and absorption.

This chapter is a direct application of attenuation imaging to field data. The dataset corresponds to a metre-scale volume in a volcanic area. Here I show the potential of scattering and absorption imaging to provide quantitative predictions of spatial changes in the field, and their contribution to other geophysical methods for a joining interpretation of hydrothermal systems, looking to reduce uncertainties in the modelling of volcanic environments.

The chapter was written in paper format and was submitted to Volcanology, a section of the journal Frontiers in Earth Science. It was published in March 2022 and the full citation is as follows: Di Martino MDP, De Siena L, Serlanga V and De Landro G (2022). Reconstructing Hydrothermal Fluid Pathways and Storage at the Solfatara Crater (Campi Flegrei, Italy) Using Seismic Scattering and Absorption. *Front. Earth Sci. 10:852510*, DOI: 10.3389/feart.2022.852510. Luca De Siena conceived the idea, and Vincenzo Serlanga and Grazia De Landro provided the dataset of the study area (velocity model and rays). I did all the analysis and wrote the manuscript and the co-authors proofread the manuscript. The analysis was performed using the MuRAT code available at https://github.com/PilarDiMartino/MuRAT_Solfatara. The labels of figures, tables and

supporting information have been renamed to be in line with this thesis. The mention of the “supplemental material” in the paper corresponds to Appendix C in this thesis. In the same order, the references are included in the bibliography section. An extra section (appendix C4) has been added to this thesis to show key previous geophysical results that were used to aid the interpretation of the scattering and absorption maps.

Abstract

Imaging fluid pathways is crucial to characterize processes taking place in hydrothermal systems, a primary cause of volcanic unrest and associated hazards. The joint imaging of seismic absorption and scattering is an efficient instrument to map fluid flow at crustal scale, and specifically in volcanoes; however, this technique has so far been applied to image volcanoes and hydrothermal systems at the kilometre scale. Here, we use data from a meter-scale, active seismic survey inside the shallow structure of the Solfatara crater to obtain the first frequency-dependent near-surface scattering and absorption model of a hydrothermal system. The Solfatara crater is the place used to monitor historic unrest at Campi Flegrei caldera (Italy), a high-risk volcano under continuous surveillance due to its closeness to a densely populated area. Improving the imaging of the shallow part of this system is crucial to broaden the understanding of unrest processes that are progressively characterizing other portions of the eastern caldera. The scattering contrasts highlight the primary structural feature, a fault separating the hydrothermal plume from zones of CO_2 saturation nearing fumaroles. While high-absorption anomalies mark zones of high soil temperatures and CO_2 fluxes, low-absorption anomalies indicate zones of very shallow upflow and are caused by contrasts between liquid-rich and vapour-rich fluids coming from mud pools and fumaroles, respectively. All maps show a SW-NE trend in anomalies consistent with fluid-migration pathways towards the eastern fumaroles. The results provide structural constraints that clarify mechanisms of fluid migration inside the crater. The techniques offer complementary geophysical images to the interpretation of hydrothermal processes and prove that seismic attenuation measurements are suitable to map fluid pathways in heterogeneous media at a detailed scale.

4.1 Introduction

Imaging hydrothermal systems in volcanic areas is crucial to forecasting phreatic eruptions (Mayer et al., 2016), assessing risks of edifice collapse (Rosas-Carbajal et al., 2016) and monitoring the possible evolution toward an unrest stage (Amoroso et al., 2018). Seismic attenuation measurements, like scattering and absorption that are suitable to map structures and feeding systems in volcanic settings (e.g., De Siena et al., 2016), could be applied to image hydrothermal systems. Scattering and absorption are the manifestations of the anelastic attenuation of coherent waves, i.e., the energy lost by seismic waves while propagating through a heterogeneous medium. The presence of fluids mainly controls absorption, triggered by fluid/squirt flow, internal friction, viscosity, and thermal relaxation mechanisms (Barton, 2006), while scattering is caused by the presence of heterogeneities and generally highlights tectonic interactions (De Siena et al., 2016) and lithological contrasts (Napolitano et al., 2020). At the sample scale, ultrasonic attenuation measurements are related to the physical rock properties (Vanorio et al., 2002; Di Martino et al., 2021). At the crustal scale, seismic attenuation is a pivotal instrument to identify and track the location of fluid and melt reservoirs and, thus, to understand magmatic and hydrothermal processes in volcanic environments (e.g., De Siena et al., 2017a; De Landro et al., 2019). Frequency-dependent parameters such as peak-delay time and the attenuation of coda waves are proven proxies of scattering attenuation and absorption (e.g., at Mount St Helens volcano - De Siena et al., 2016). These parameters have shown notable sensitivity to fluid-filled pathways and reservoirs, especially when using active-survey data (Prudencio et al., 2013; Ibáñez et al., 2020).

Peak-delay time (*Pd*) is a measurement of the strength of scattering (Takahashi et al., 2007) that has been recognised as a marker of scattering losses (Calvet and Margerin, 2013; Saito et al., 2002) and it is sensitive to structural and geological features (e.g., Napolitano et al., 2020). Seismic wave propagation in volcanic areas is primarily affected by scattering that dissipates the energy of the coherent waves into coda waves (Sato et al., 2012). The attenuation of coda waves (Qc^{-1}) measured from the decay of seismic envelope energy with time (Aki and Chouet, 1975), is a combination of intrinsic absorption and scattering losses. When coda waves enter the diffusive regime, coda

attenuation directly measures absorption (Shapiro et al., 2000). The multiple scattering/diffusion approximation best describes seismograms in volcanic media, primarily if active sources produce the scattering in the media (Wegler et al., 2003; Prudencio et al., 2013).

The hydrothermal system of Campi Flegrei caldera (Southern Italy, Figure 4.1) is one of the best-studied and most hazardous in the world. Hydrothermal vents have progressively opened in the eastern caldera (Giudicepietro et al., 2021), entering the metropolitan city of Naples (~1 million inhabitants). Hydrothermal activity is one of the causes of ground deformation and seismicity at the caldera (Vanorio et al., 2005; Troise et al., 2006; Cusano et al., 2008; Petrillo et al., 2019; Ricco et al., 2019) and the primary reason for the onset of recent earthquake swarms across the eastern caldera (Petrosino et al., 2018; Tamburello et al., 2019; Akande et al., 2021). There is debate around the source of fluids likely producing the recent unrest, with inputs produced by either a deep contribution from a shallow magma sill (D'Auria et al., 2015; Chiodini et al., 2017), drying of the deep hydrothermal system (Moretti et al., 2018; Troise et al., 2019) or decarbonisation reaction from the caldera basement (Vanorio and Kanitpanyacharoen, 2015). However, there is a general agreement that in the upper 3 km hydrothermal processes are more likely taking place than magmatic ones, with the changes of permeability due to rainfalls, receiving attention as a short-term trigger for seismicity and deformation (Akande et al., 2021; Petrosino and De Siena, 2021). Presently, degassing and seismicity are increasing due to the pressurisation and heating of the hydrothermal system, which triggers energy transfer from the fluids to the host rocks (Chiodini et al., 2021).

Campi Flegrei goes through repeated unrest episodes (Kilburn et al., 2017), releasing carbon dioxide gases and high heat flow from the hydrothermal-magmatic system (Chiodini et al., 2007). The caprock has controlled fluid migrations since the 1980s (Vanorio and Kanitpanyacharoen, 2015; De Siena et al., 2017b; Calò and Tramelli, 2018). These fluid migrations to the surface towards the east caldera, produce seismic and geochemical responses, especially at the Solfatara crater (Di Luccio et al., 2015; De Siena et al., 2017b; Petrosino and De Siena, 2021). This crater opened about 4000 years ago

and, historically, is the first place where the volcano shows signs of unrest (Kilburn and McGuire, 2001). The Solfatara crater (Figure 4.1) is a tuff cone (graben-like structure) 600 m in diameter and 100 m above sea level. Described as a maar-diameter structure (Isaia et al., 2015), it was created by the interaction of supercritical fluids rising from depth and groundwater, leading to eruptions and tephra expulsion. High-angle normal faults and fractured rocks surround the Solfatara crater (Figure 4.1), guiding fluids from depth to fumaroles and mud pools (Bianco et al., 2004). The most active fumaroles across the caldera are located at Solfatara and across the Pisciarelli field, 400 m to the northeast. The two fields are likely connected, as inferred by field data, electromagnetic surveys, and gravity gradiometry (Troiano et al., 2014; Young et al., 2020). The increasing geochemical release and seismic activity between the Solfatara and Pisciarelli hydrothermal areas raise concerns over phreatic and hydrothermal eruptions (Chiodini et al., 2021; Giudicepietro et al., 2021).

Solfatara is a key region where the repeated unrest of the last 50 years has been monitored, becoming one of the best-known, best-monitored, and best-surveyed volcanic craters worldwide. Reserachers have analysed the hydrothermal system at Solfatara by applying ambient noise tomography (e.g., Petrosino et al., 2012; Petrosino and De Siena, 2021), electrical resistivity tomography and self-potential (e.g., Byrdina et al., 2014; Gresse et al., 2017; Troiano et al., 2019), joint geochemical and thermal measurements (e.g., Tamburello et al., 2019; Chiodini et al., 2021); geodetic (e.g., D'Auria et al., 2015), gravity (Young et al., 2020), hydrogeological (e.g., Bruno et al., 2007) magnetotellurics (e.g., Siniscalchi et al., 2019; Troiano et al., 2014); volcano-tectonic (Isaia et al., 2015), seismic and tremor surveys (Saccorotti et al., 2007; Letort et al., 2012; Serra et al., 2016; Bruno et al., 2017; De Landro et al., 2017; Amoroso et al., 2018; Gammaldi et al., 2018; Giudicepietro et al., 2021), and seismic attenuation (De Landro et al., 2019). The first kilometre under Solfatara is imaged at very high resolution; however, there is still uncertainty about the structures that guide fluids from the deforming centre of the Solfatara caldera to its eastern side, specifically to the degassing Pisciarelli field (Young et al., 2020). At Solfatara, the absorption of seismic energy could be attributed mainly to wave-induced fluid flow, a mechanism known for producing significant attenuation in saturated porous rocks (Pride et al., 2004; Tisato and Quintal, 2013). Therefore, the spatial

variation of scattering and absorption can be a marker of both structure and composition of the volcanic medium.

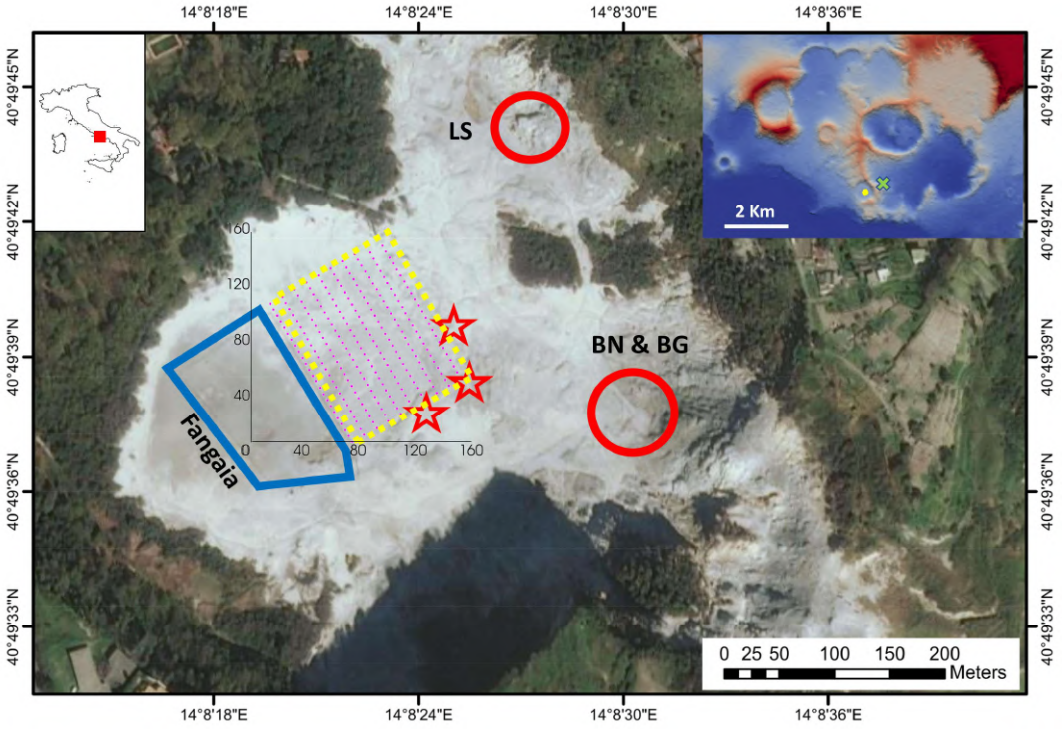

Figure 4. 1. Solfatara Crater. The topography of Campi Flegrei is shown in the upper right corner, with the survey location in yellow and the Pisciarelli fumarole indicated by the green cross. The survey area of the active RICEN experiment is in the yellow box, with station locations in magenta. Main Hydrothermal features: Fangaia (mud pool, blue contour) and fumaroles (LS: Le Stufe, BN: Bocca Nuova, and BG: Bocca Grande). The stars indicate other fumaroles closest to the survey area (after Serra et al., 2016). The inversion grid (black axes) extends between 0 and 160 m in the SN and WE directions. See figure C1.1 for a close-up on the location of stations and seismic shots.

Most field imaging with absorption and scattering is in 2D, with no available results at the meter scale. This study offers the first example of 3D separation of seismic scattering from seismic absorption performed using the open-access code Multi-Resolution Attenuation Tomography (MuRAT3D). The active data from the Repeat Induced Earthquake and Noise (RICEN, Serra et al., 2016) experiment, performed inside

the Solfatara crater in September 2013, offer the ideal dataset to image the shallowest hydrothermal system at Solfatara at the meter-scale. The results provide novel images that complement the available information, improving our insight into the shallow hydrothermal structures and revealing fluid pathway geometries around the main fumaroles.

4.2 Dataset

In this study, we used input seismograms collected during the RICEN experiment (Serra et al., 2016). The network covers 90 x 115 m^2 and comprises 240 sensors distributed over 10 lines (Yellow box in Figure 4.1). The distance between sensors is 5 m, with lines of 24 sensors distanced 10 m apart. The experiment was performed using a vibroseis seismic source from the 100 shot-points triggered; here, we used 20 shots evenly distributed, the best compromise between adequate coverage and avoiding redundancy (see Figure C1.1 in Appendix C, hereinafter C).

The input velocity model is the one obtained by De Landro et al. (2017) using the full dataset of the RICEN array acquisition in a 160 x 160 x 30 m^3 volume. The signals are sampled at a 1000 Hz frequency rate. The seismograms were already pre-processed (cross-correlation with the vibroseis sweep to obtain a source-corrected signal and minimum phase filter to preserve causality; see Serra et al., 2016 and De Landro et al., 2017 for details). The P-wave arrival times of each seismogram are the ones estimated by De Landro et al. (2017) and included in the header of the waveform files in SAC format. We selected 2144 waveforms with source-station distances longer than 50 m. The analysis was carried out on the waveforms that complied with a coda to noise ratio higher than 3 (see Table C2.1). The P-wave energy is contained in the first 0.126 seconds from the P-wave picking and has frequencies above 45 Hz (De Landro et al., 2019). The start of the coda window was selected at 2 seconds from the origin time, with a length of 2 seconds (Figure 4.2).

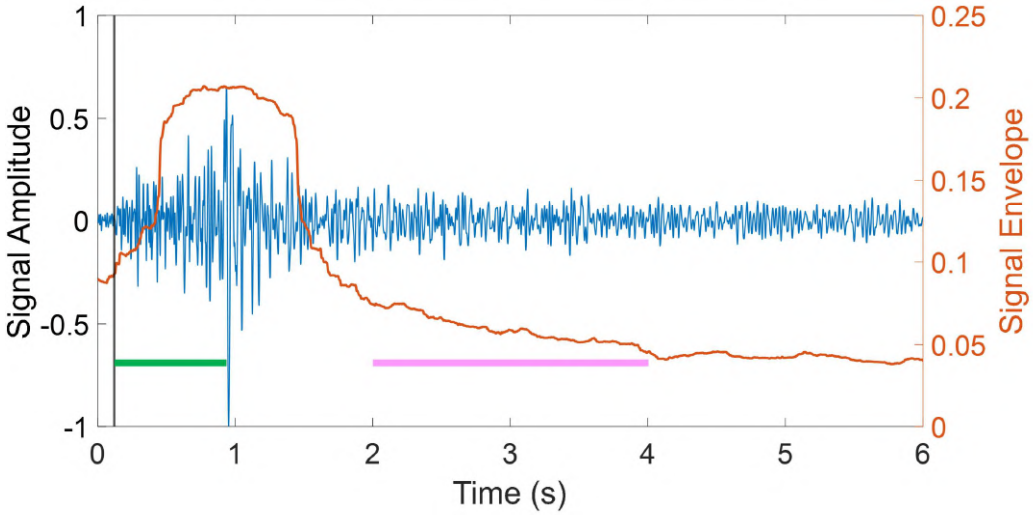

Figure 4. 2. Signal Example. Seismogram (blue) and its envelope (orange). The vertical black thin line marks the P-wave arrival. The coda window section is represented by the pink line, while the green line shows the peak delay measured on this seismogram.

We performed a preliminary study of the seismic signal and its spectrum over different windows to choose the suitable coda window (see Figures C2.1, C2.2). The choice of the coda windows complies with the assumption of stochastic waves contained in the coda section. We bandpass-filtered the seismograms by applying a Butterworth filter of order 4 in four frequency bands centred at 12, 18, 24, and 27 Hz. The coda waves contain stochastic information at this range of frequencies and are dominated by highly scattered surface waves. The envelopes were computed through a smoothed Hilbert transform of the signal using a sliding window of the size of the sampling frequency (Figure 4.2).

4.3 Methods

4.3.1 Peak-delay measurements

We measured peak delay (*Pd*) as the time lag from the onset of the P-wave arrival to the maximum amplitude of the envelope (green line in Figure 4.2). In heterogeneous media, the peak delay should increase linearly with the travel time (Saito et al., 2002) and be related to the P-wave travel time (*tt*) in each frequency band f by:

$$Pd(f) = A(f) + B(f) * tt \quad \text{(Eq. 4.1)}$$

where *A(f)* and *B(f)* are the coefficients of the linear fit (*Pd_L*) (Figure 4.3). Peak delay is mapped by measuring the variations of the logarithm of the *Pd* values *Log(Pd)* relative to a linear trend:

$$\Delta Log\big(Pd(f)\big) = Log\big(Pd(f)\big) - Log(Pd\_L(f)) \quad \text{(Eq. 4.2)}$$

The data values above and below the linear trend represent the variations of the peak delay time, interpreted as high and low scattering (Takahashi et al., 2007). Areas with positive variations indicate that the ray path crosses strong heterogeneous zones (i.e., high scattering attenuation), while negative variations indicate either low scattering or strong absorption (Calvet et al., 2013). Peak delays are then mapped into space assuming sensitivity to the seismic ray, computed in the available velocity model (De Landro et al., 2017).

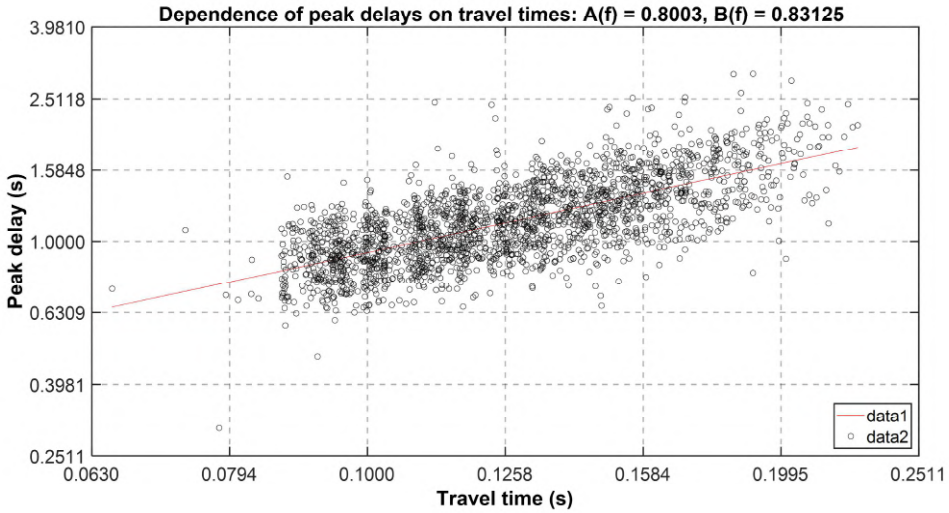

Figure 4. 3. Peak-delay dependence on travel time at 18 Hz. Coefficients A and B define the linear fitting of the data with 95% confidence (A=0.7668 +/- 0.8338, B=0.7941 +/- 0.8684). Minimum and Maximum peak delay (0.3 and 5 seconds respectively) were set to avoid biases on the picking. Given this threshold, the data used for the analysis was reduced to 2081 seismograms at 18 Hz (see Table C2.1).

4.3.2 Coda Attenuation

The energy decay of the coda as a function of frequency and time (Aki and Chuoet, 1975) is given by:

$$(f,t) = S(f)t^{-\propto}exp^{\frac{-2\pi ft}{Qc}} \qquad \text{(Eq. 4.3)}$$

where t is the lapse-time, $S(f)$ is the frequency-dependent source factor, $\propto$ is a constant factor related to the geometrical spreading and Qc is the coda quality factor (inverse of coda attenuation). The coda decay method estimates Qc^{-1} values by linearizing this equation and obtaining a least-square fitting of the logarithm of the envelope energy at a

given frequency versus lapse time (see Sketsiou et al., 2020 for the uncertainties associated with this linearization). A minimum correlation coefficient threshold of 0.8 was imposed for this fitting to select high-quality data. This threshold led to a further reduction of the data used for the analysis (1895 seismograms at 18 Hz); the cut was higher at lower frequencies (see Table C2.1).

The analysis is performed using the inversion approach described by De Siena et al. (2017a). However, this work uses 2D space-weighting functions (Prudencio et al., 2013; Del Pezzo et al., 2016) with the hypothesis that the entire energy of the coda window is contained (thus lost) inside the defined grid. MuRAT3D implements 3D multiple-scattering sensitivity kernels (Del Pezzo et al., 2018) based on Paasschen's equations (Paasschens, 1997) (See C3). To determine the input albedo and extinction length parameters, we followed the approach of Wegler (2003), assuming that the medium is fully diffusive (Scala et al., 2019). An iterative inversion (Gazzola et al., 2019) is used to obtain the Qc^{-1} values at each node. We tested the stability and resolution of the inversion at different grid node spacing through iterative regularizations and checkerboard tests (see Figs C3.1, C3.2 and C3.3). The best parametrization model corresponds to 11 x 11 x 7 nodes (grid spacing 16 m x 16 m x 5 m). The anomalies are well reconstructed laterally; however, at depth, it is only possible to resolve a shallow section (upper ~10 m) for the coda.

Here, we interpret Qc^{-1} as a marker of seismic absorption, which is a common approach at a regional scale when a diffusive regime describes scattering (Calvet and Margerin, 2013; Prudencio et al., 2013; Sketsiou et al., 2020). Nonetheless, also at our very local scale, we checked that Qc^{-1}: (1) does not vary consistently with ray length (Calvet and Margerin, 2013); and (2) that Qc^{-1} has a linear correlation with frequency (Sketsiou et al., 2020) to validate this condition (Figure 4.4). The characteristic length after which the multiple scattering regime occurs is the scattering mean free path (Scala et al., 2019). The scattering mean free path must be larger than the wavelengths, and the source-receiver distance larger than the transport mean free path (Wegler et al., 2003). We measured an average scatter mean free path of ~7.5 m in the area in a wide frequency range (10-40 Hz), which complies with these assumptions (see C3). Scala et al. (2019)

obtained a similar result, estimating a scattering mean free path of ~10 m at 25 Hz in the Solfatara crater using surface waves. Their estimation of attenuation values using mean free path values assumes a homogeneous development of the coda in which the averaged elastic properties are independent of the location of source and receivers. In this study, we included sensitivity kernels in the inversion of coda attenuation values, which shows that only the first 10 meters are resolved because of the close location of the events and stations at the surface (Del Pezzo et al., 2018).

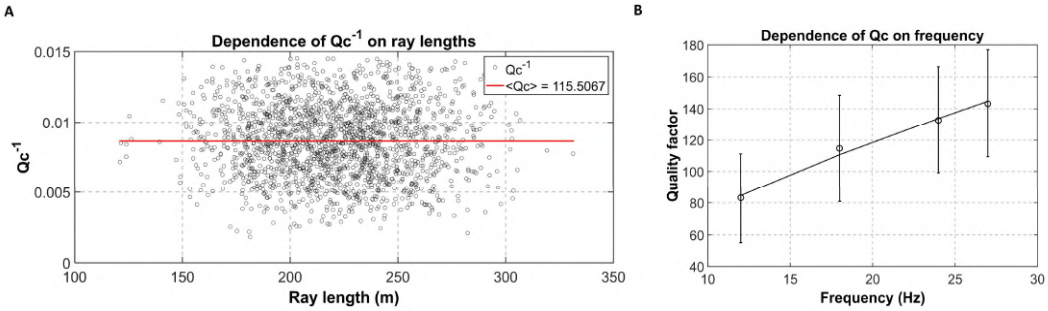

Figure 4. 4. (A) Coda Attenuation Qc^{-1} dependency on ray length at 18 Hz; (B) Qc values estimated at different frequencies.

4.3.3 Tomographic procedures

Scattering attenuation is mapped by the regionalization of the peak delay measurements (see the workflow in Figure 4.5). The underlying principle is that the envelope of direct wave packets broadens due to multiple forward scattering by inhomogeneities (Markov approximation, Saito et al., 2002). We adopted the tomographic method developed by Takahashi et al. (2007) for mapping scattering as follows: (1) measure *Pd* for all the waveforms filtered at the study frequency bands; (2) cross-plot the *Pd* values against travel time (Figure 4.3); (3) perform a linear regression of the dependence of peak delay increasing with travel time; (4) allocate positive and negative variations of *Pd* with respect to the linear trend to identify strong and weak scattering, respectively; (5) map *Pd* in space using regionalization. The regionalization consisted of dividing the mapped volume into

blocks, where each block is crossed by several rays, each ray has an allocated *Pd* value measured from its seismogram, and the average *Pd* of all these rays is given to the block. Then the variations between blocks are smoothed by taking the average of the mean *Pd* values between neighbour blocks; (6) finally, we plot in 3D the spatial variations of peak delay (Figure 4.6).

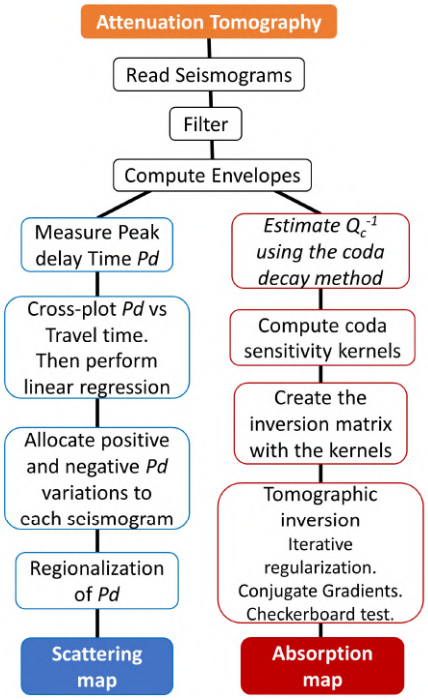

Figure 4. 5. Workflow of the attenuation tomography methods applied to map peak delay (left side) and coda attenuation (right side) for imaging scattering and absorption, respectively.

Absorption is mapped by an inversion procedure of the coda attenuation measurements (see the workflow in Figure 4.5). The method is as follows: (1) compute the seismic envelopes at each study frequency; (2) compute Q_c^{-1} from the least square fitting of the logarithm of the envelope versus time; (3) compute the sensitivity kernels for the event-station couples (Figure C3.3); (4) create the inversion matrix *G* using the computed kernels; (5) perform the tomographic inversion. The linear inversion problem solves the general expression *d=G(m)*; where the data vector *d* contains the *Qc* values

measured for each seismogram, while the operator matrix G, which represents the mathematical relation between the observed and the modelled Qc^{-1}, corresponds to the normalized sensitivity kernels. The model vector m contains the attenuation values Qc^{-1} for each block of the volume. The modelled Qc^{-1} are adjusted to satisfy the observed data by using an iterative regularization that leads to choosing adequate damping parameters using conjugate gradients (Gazzola et al. 2019; Aster et al., 2019). The final choice is performed by minimizing a cost function that includes data residuals and L2-norm misfit (Figure C3.2); (6) We produce a checkboard test to assess the accuracy of the inversion (Figure C3.1). These tests consist of alternating patterns of positive and negative anomalies that must be reconstructed so that the areas with good recovery are assumed to be well constrained; (7) Finally, we plot the coda attenuation variations over the study volume (Figure 4.7).

4.4 Results

Figures 4.6 and 4.7 show the peak-delay and coda-attenuation variation maps. The maps occupy the extension of the input velocity model (Figure 4.1); however, for the peak delay maps, we only interpret the patterns in the area covered by the ray crossing, while for the coda attenuation maps the model resolution is delineated by the results of the checkerboard test. We present the results obtained at different frequency bands, as the size of the heterogeneities could change based on the wavelengths. For the peak-delay maps, we present depth slices every 5 m covering the entire study volume, while for the coda attenuation, we show only the first 10 m. Below this depth, the resolution of the results was inadequate (see Figure C3.1) because:

(1) the sources are located at the same elevation level that the stations (~96-98m), and coda waves mainly reverberate near-source and receiver;

(2) the first abrupt change in the velocity model, to which coda wave attenuation is extremely sensitive (Gabrielli et al., 2020), is around 85 m.a.s.l. (De Landro et al., 2017);

(3) having a regular grid spacing smaller than 10 m on the vertical direction, coda waves do not propagate much at depth, as the wavelengths used are 4 to 8 times larger than the grid cell.

In the coda attenuation maps (Figure 4.7), the Qc^{-1} scale represents relative changes of coda attenuation resolved in the area, not an exact quantification of coda attenuation (for an average Qc value in the crater, see Figure 4.4B). In the inversion, we do not impose the condition of positive Qc^{-1} values, so we also obtain negative values. A description of the physics creating anomalous negative attenuation in volcanoes at Campi Flegrei caldera is given by De Siena et al. (2013). These negative anomalies are proven markers of deformation at regional and volcanic scales, marking interfaces inside the Tyrrhenian Sea (e.g., Nardoni et al., 2021) and Pollino fault network (Napolitano et al., 2020) and dike intrusions/fluid injections at Campi Flegrei (De Siena et al., 2017a). Such interfaces produce reverberations that contrast the diffusion approximation at specific frequencies, thus lowering coda attenuation. These reverberations can be related to the relative positions of sources and interfaces. This has been proven via joint radiative transfer and eikonal equation modelling by Nardoni et al. (2021), who demonstrated that the presence of interfaces, like the Moho, in the medium creates reverberations that lower the inverted Q_c^{-1} depending on the source location. At our scale, they could indicate lateral structural variations that could coincide with fluid-migration pathways.

The absorption models reveal geometries different from those observed in the peak delay map, an indication that coda attenuation and peak delay define different attenuation mechanisms and have different sensitivities. We merged and classified the absorption information from Qc^{-1} and the scattering information from peak delay in a parameter separation map (Figure 4.7) to discriminate fluid paths from fracture networks (De Siena et al., 2016; Napolitano et al., 2020). This map is divided into four quadrants: (1) Low Scattering / Low Absorption LS/LA; (2) High Scattering HS; (3) High

Absorption HA; and (4) High Scattering / High Absorption HS/HA, equivalent to the possible solutions of the attenuation model.

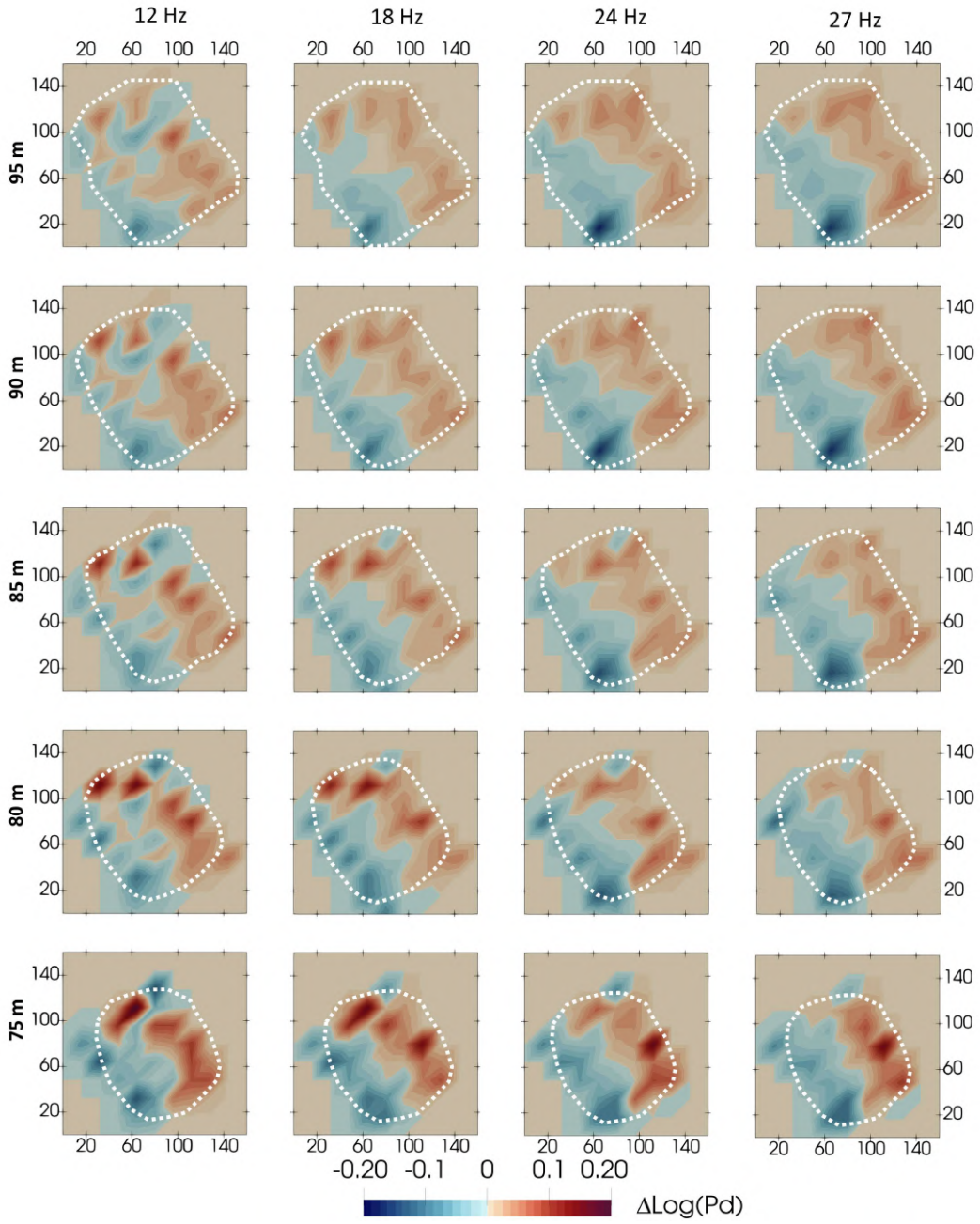

Figure 4. 6. Peak delay variations at different frequencies. The white dashed polygon represents the resolution limits of the retrieved models based on the ray crossing.

4.5 Discussion

Layers of tuff deposits with similar rock properties but different fluid contents characterize the shallow Solfatara crater (see table 1 in Petrosino et al., 2012). Thus, we assume that the changes observed in the absorption and scattering maps (Figures 4.6, 4.7 and 4.8) are not affected by the lithology but are due to the fluid composition, temperature, and the alteration of the host rock caused by hydrothermal fluid and meteoric water infiltration. This rock alteration causes the lack of vegetation in the centre of the crater, where the survey took place (Figure 4.1). To the West of our study volume, there is the Fangaia mud pool. At depth, this zone is characterized by a conductive hydrothermal plume with meteoric water upwelling to the surface (Bruno et al., 2007), while towards the East there is a higher-resistivity zone attributed to the high CO_2 saturation close to the fumaroles (<5 Ωm and 50-100 Ωm respectively, Byrdina et al., 2014).

The peak-delay maps (Figure 4.6) indicate the primary structural change in the zone. The change marks sharply the NW-SE-striking fault proposed by Bruno et al. (2007) in the middle of the crater, which appears as a resistive body in both electrical and magnetotelluric profiles. This buried fault (Isaia et al., 2015) is sealed by a mineralized clay-rich caprock with gaps at the surface due to the presence of the fault/fracture systems (Siniscalchi et al., 2019). Gammaldi et al. (2018) interpreted a fault of similar direction using 2D P-wave velocity images crossing the middle of the crater. They considered it the preferential gas migration path between the deeper hydrothermal source and the main fumaroles. The rocks are highly fractured in the eastern portion of the map (Isaia et al., 2015); here, the high scattering anomaly coincides with the area of most intensive geothermal activity at Solfatara, which is also the one with the highest fumarole concentration. Young et al. (2020) delineated a low-gravity anomaly to the East of the crater (caused by the accumulation of two-phase fluid within highly-fractured and porous host rocks), and a moderate low gravity anomaly to the West that delimitates the Fangaia and is characterized by high CO_2 fluxes. The survey area in this study is located between these two gravity anomalies. A preferential, active path for fluids is located along the SE and NE of the crater structure (described by Bruno et al., 2007 after Del Castillo et al.,

1968). Apart from the prevalent NW-SE fault, the features in the maps follow a cross-cutting SW-NE trend, as inferred also by the very similar V_P anomalies distribution retrieved in the depth range 15 m – 27 m by De Landro et al. (2017). These anomalies are thus directed toward the Pisciarelli field (Isaia et al., 2015) in a way that is consistent with the existence of a migration pathway connecting the two fields (Young et al., 2020; Petrosino and De Siena, 2021).

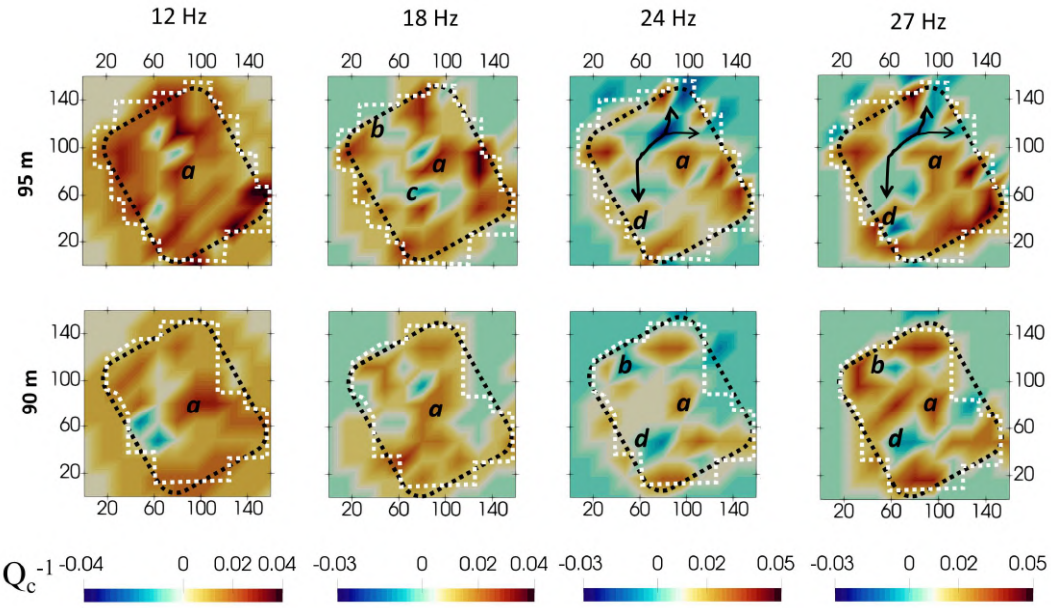

Figure 4. 7. Coda attenuation variations at different frequencies. The white and black dashed polygon represents the resolved and survey area (Figure 4.1), respectively. We scaled the colour legend to the maximum and minimum for each frequency. The labels are described in the main text.

Our Qc^{-1} model is satisfactorily resolved up to ~87 m a.s.l.: this is around ~10 m below the surface (Figure 4.7). Laterally, the structure looks heterogenous, a product of the intense fluid saturation of the pore space in the area, especially at low frequencies (12 Hz). Letort et al. (2012) suggested that seismic noise sources at Solfatara are related to the presence of CO_2 (and steam) bubbles and the propagation of these bubbles into the liquid layer. Saturated rocks strongly attenuate seismic energy when gas bubbles occupy

part of the pore space (Tisato et al., 2015). In the highly-fractured and highly-porous rocks (up to 60% - Mayer et al., 2016) in Solfatara, the measured seismic absorption is likely related to these steam-to-liquid phase changes, taking place close to the surface (Chiodini et al., 2005). At 95 m, the coda attenuation maps show random features (Figure 4.7), likely due to the coexistence of downward flow of liquid water and upward flow of gas near the surface (Siniscalchi et al., 2019).

In Figure 4.7, the primary high Qc^{-1} anomalies (labelled "*a*") correlate with the high soil temperature and high CO_2 flux in the diffuse degassing area, as identified in the central part of the crater by Gresse et al. (2017). Interpretation of the low Qc^{-1} anomalies is more intriguing. They appear in the NW ("*b*") and coincide with the low-frequency high-velocity body that Serra et al. (2016) derived from phase-velocity maps. Similar anomalies appear in correlation with the location of dike intrusions/fluid injections in the centre of the caldera, using data recorded during its major unrest (1983-1984 – De Siena et al. 2017b). At 18 Hz, the narrow low Qc^{-1} anomaly ("*c*") is thus inferred as the most likely location where the fluid flow from the NW-SE fault/fracture system, observed in the peak delay map, reaches the near-surface. Increasing frequencies at the shallowest depth (95 m.a.s.l), the low-Qc^{-1} anomalies ("*arrows*") go from S towards NE, pointing to the LS fumarole (Figure 4.1): this anomaly could indicate a connection between the mud pool and the fumaroles. These mud pools, found at both F and LS (Figure 4.8) are a combination of CO_2 and steam bubbling through hot water (Gresse et al., 2017). We interpret the low Qc^{-1} anomaly "*d*" that appears at 24 and 27 Hz frequencies as the subsurface transition between the hot water/liquid-rich fluid coming from the Fangaia pool and the CO_2/vapour-rich fluid from the plume below BG/BN fumaroles. This encounter point intensifies at depth, and it is most evident 90 m.a.s.l. It appears to be the SW portion of the area where hydrothermal circulation takes place (Bruno et al., 2007).

The area of the survey is characterized by: (1) a high-absorption area; and (2) a well-localized high-scattering and high-absorption area; while (3) there is no clear high-scattering zone, primarily a marker of sealing formations, like clays (Napolitano et al., 2020). The clay cap expected in this zone (Siniscalchi et al., 2018) is likely below our depth penetration, as the fault/fracture system breaks it near the surface. These results

suggest that the principal attenuation mechanism across the shallow hydrothermal is the fluid flow interaction on the highly porous and fractured rocks. In Figure 4.8, high absorption (in orange) increases towards the mud pools area, where the degassing is less intense. Here, (i.e., the southern region of this model), we imaged strong variations of *ΔLog(Pd)* and Qc^{-1}, especially at high frequencies. This observation is fully consistent with attenuation images by De Landro et al. (2019): they retrieved the lowest Q_P values in the investigated volume (i.e., the strongest attenuation) in this area, adjacent to the eastern part of the Fangaia mud-pool, where mineralized liquids saturate the shallow subsoil. The high-scattering/high-absorption zone (in red) appears below the main vents, where the degassing occurs.

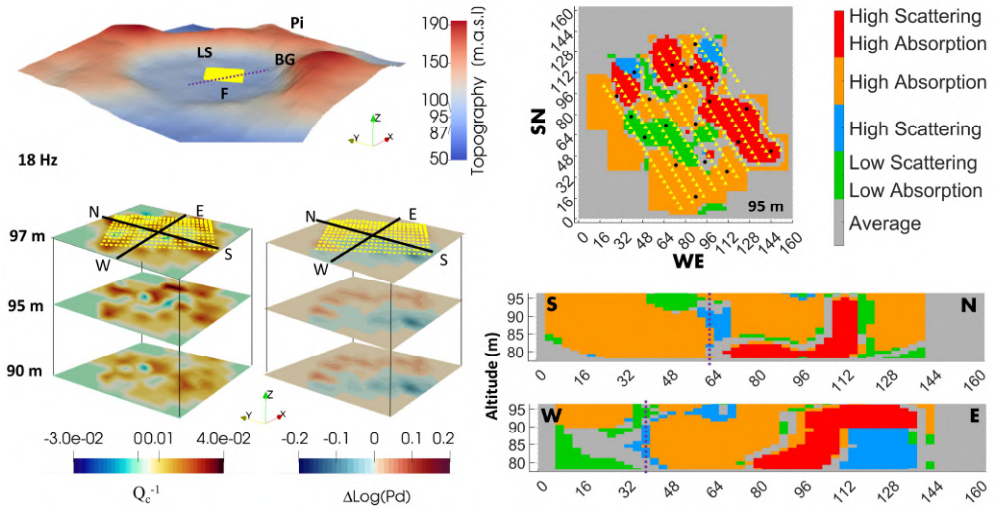

Figure 4. 8. Left: The topography image indicates the location of the survey area (yellow rectangle), the main fumaroles, and the interpreted NW-SE fault from our results (dashed purple line). Absorption and scattering sections across the first ten meters are stacked below the topography, showing the trace of two vertical sections (SN and WE). Right: Parameter maps obtained at 18 Hz by separating the mapped values in their parameter space for the four sections (the location of the stations and sources is indicated by the yellow triangles and the black circles, respectively).

In dry volcanic samples, the level of heterogeneity observed in coda waves produced by changes in pore space topology is already quite complex (Di Martino et al.,

2021). At Solfatara, the host rocks are highly altered by intense hydrothermal alteration that increases porosity and permeability and reduces elastic wave velocity (Mayer et al., 2016), intensifying the attenuation responses. Once combined with evidence from rock physics, our maps could offer complementary information to retrieve fluid composition and saturation levels (e.g., Amoroso et al., 2017) at scales that bridge field seismology and rock observations.

The Solfatara crater has a unique significance, as it is where unrest episodes at Campi Flegrei have historically been monitored (Kilburn and McGuire, 2001). While vents continuously degas at its centre, the Pisciarelli fumarolic-hydrothermal area increased in 2009 on the outer eastern flank of the crater (Figure 4.1). Today, this is the most hazardous sector of the caldera, characterized by an active hydrothermal system often producing phreatic and small hydrothermal explosions (Isaia et al., 2021), and where fluids are progressively migrating east producing earthquakes (Petrosino and De Siena, 2021).

While the severity of a larger eruption is usually linked to a magmatic ejection, in this paper the mapped features are only produced by fluid flow interactions. From our study, it is impossible to determine if they are related to a magmatic source degassing at depth. Regardless, the scattering mapping of the hydrothermal system shows how a highly dipping fault is the primary contributor to fluid migration from depth (Figure 4.6). As previously highlighted by gravity gradiometry (Young et al., 2020), the fluid migrations feeding Pisciarelly are shallow (Figure 4.8) and start from the primary Solfatara feeder (Siniscalchi et al., 2019). Absorption marks the shallow pathways followed by these fluids, which migrate east towards Pisciarelli within the first few meters of the volcano (Figure 4.7). These traces likely extend further east, representing the most impending hazard for people leaving near the Solfatara crater.

4.6 Conclusions

We present scattering and absorption 3D models and an interpreted separation map of these attenuation parameters for the shallow hydrothermal system at Solfatara crater, inside Campi Flegrei caldera. The model delineates the NW-SE fault that separates fluids flowing through the mud pool (W) and vapour-filled structures near fumaroles (NE and SW). The lateral variations of absorption and scattering provide the first seismic evidence of fluid-migration pathways, previously inferred by field and gravity surveys. These fluids are generated under Fangaia and eventually reach the Pisciarelli fumaroles, outside the crater.

This work is the first application of 3D scattering and absorption imaging to a shallow hydrothermal system, providing models at meter-scale resolutions. The results depend on the complexity of the crater structure and support previous inferences about how these features constrain fluid migrations. On the other hand, within a relatively-homogeneous geological matrix, separating the attenuation mechanisms (i.e., scattering from absorption) demonstrated the high potential to detect fluid upflow and identify different fluid compositions. Our results offer a highly-resolved picture of the pathways taken by hazardous fluids to rise to the surface and migrate east, from Solfatara towards the metropolitan city of Naples. This approach can improve the modelling of very-shallow hydrothermal systems, especially if combined with different geophysical responses and interpreted using rock-physics observations.

Chapter 5

Conclusions

Volcanoes are highly heterogeneous environments. Seismic imaging through heterogeneous structures is strongly affected by incoherent scattering and attenuation, thus modelling seismic wavefields in volcanoes is challenging. This thesis provided valuable insight into model seismic attenuation parameters that can be up-scaled to model geophysical observations in the field. It is well known that seismic responses from the propagation of elastic waves, produced by either passive or active triggers, will be strongly affected by the petrophysical properties of the heterogeneous medium, which generates perturbation that attenuates the propagating seismic energy.

As it is complex to define the perturbations taking place in the medium, we tend to think that in nature only fluids will control the attenuation of seismic waves. The first necessary step required toward forward-modelling seismic responses is to characterize the medium petrologically, and mineralogically and define any parameters that could affect the wavefield within the rock matrix. This has been done in chapter 2 at the laboratory scale. In this chapter, I outlined how the intrinsic properties of the host rocks drive seismic attenuation by correlating the petro-mineralogical characteristics obtained from image data processing and analysis, with the coda attenuation measured at ultrasonic frequencies. The individual contribution of factors like mineral content, size and alteration level; and pore space size, shape and porosity was analysed. The results indicate that even when all these parameters influence the attenuation of ultrasonic waves, the pore space topology appears to be the main driver in volcanic samples characterized by

large vesicles. Frequency-dependent absorption and scattering imaging can be modelled starting from these advanced petrophysical measurements at a laboratory scale and linked to petrophysical and microstructural characteristics of the host rocks.

The second step towards understanding wave propagation in the rock is modelling, as I needed to understand how much we can model for the medium of interest, how similar are the observation, and how much this could relate to what is actually observed at the surface. This has been done in chapter 3, where the focus was on disentangling the processes taking place in dry volcanic rock matrices by modelling simple but realistic scenarios of the pore space in real heterogeneous rocks. With the computational modelling, I tackle the direct and scattering seismic wavefield using the observations quantified in chapter 2. After the individual assessment of parameters like the size, shape, density and location of the pores, it was proved that for rocks of similar porosity, the pore space topology is indeed a primary regulator of ultrasonic wave propagation.

The final scope has always been upscaling. Now upscaling is challenging, as translating results from nanometres (nanoindentation), micrometres (digital rock physics), millimetres (laboratory), meters (near-surface) and kilometres (field) has its trade-off. To understand if the outcomes observed in this thesis from ultrasonic data at the laboratory scale can be used to interpret seismic data at the field scale, the best possible approach is to test it by stepping up one scale, i.e., analysing data at the meter scale. This was done in Chapter 4, where active seismic data from a meter-scale volume of the Solfatara crater were used. I consider this was an ideal scenario because by working with a volcano the results are for sure a representation of a highly heterogeneous medium, and on the other hand, the environment is relatively stable because of the short array of the studied volume. This is important to be able to use the attenuation markers that have been studied in the previous chapters. By the imaging application at Solfatara, I observed that attenuation by scattering and absorption mechanisms in a highly porous medium can provide structural constraints and also map fluid flow pathways. While this medium is clearly fluid- and gas-filled, the experience acquired in rock physics allows an

interpretation of coda attenuation and scattering parameters that takes into account the effect of porosity of the rock matrix.

The individual results obtained in each chapter of this thesis come all together in providing a better understanding of the interactions between petro-mineralogical properties and attenuation attributes at both the rock sample and the near-surface scale. While the observations at these scales are different, scattering attenuation parameters succeeded in delivering complementary information about the propagation medium. I have gained a deep insight into how mechanisms and observations used at the field scale work at the laboratory scale. Through its laboratory, modelling and field data applications, this thesis represents a primary effort toward the calibration of stochastic imaging attributes in heterogeneous media.

Future work

Despite the efforts done in this study to overcome the experimental challenges of acquiring coda waves in rock samples, better laboratory calibrations are still needed to record suitable waveforms for performing analysis on coda waves, and to establish the guidelines for the appropriate experimental setting.

Now that we recognized the influence of the pore space on the wave propagation in dry heterogeneous rocks, the next step is to include fluid in the experiments, to constrain the attenuation markers for fluid-saturated volcanic rocks, which will be closer to the natural case when upscaling.

Conducting further modelling work using 3D meshes will improve the constraints of the results presented in this study, this leads to testing the best approach to include unstructured meshes that can be shaped based on the petrological and mineralogical characterization of the sample.

The future research aim is to implement a code for modelling the full anisotropic waveforms in the rock samples. Build reliable forward models of the seismic wavefield in the sample, based on their most important petrophysical and mineralogical controllers, and make a sensitivity analysis of the contributions of each rock property. In this way, the robustness and accuracy of the model results can be evaluated by understanding the relationship between the input parameters and their impact on the outputs model.

Appendix A

Supporting Information for "Petro-mineralogical controls on coda attenuation in volcanic rock samples"

A1 - Porosity and velocity measurements

The sample preparation and initial description was performed by VBPR (Table A1.1). The samples were cored in the Rock Physics Laboratory at the University of Aberdeen. The specimens are cylindrical cores of around 2.54 cm in diameter and 5.08 to 6.35 cm in length. The samples ends were polished using a polishing wheel to decrease roughness and washed with water to remove any rest of particles. The length-to-diameter ratio lies between 2 to 2.5 which is consistent with the minimum aspect ratio recommended to avoid end constraint effects when measuring amplitudes in the laboratory (ASTM 2000).

Table A1. 1 Sample's description

ID	DEPTH M	D	FACIES	DESCRIPTION	SECONDARY FEATURES	LENGTH CM	DIAMETER CM	Λ_{sw} (MM)
1H	641.4	X	A	Small isolated vesicles, densely plagioclase phyric	Fresh	4.99	2.57	15.0
2H	889	X	P	Olivine phyric, dispersed irregular micro-vesicles	Fresh	4.91	2.56	6.4
3H	889	X	P	Olivine phyric, dispersed irregular micro-vesicles	Fresh	5.06	2.57	5.2

4H	954.6	X	T	Medium to large irregular vesicles, partly connected	Possible minor dissolution?	5.12	2.56	25.4
5H	1020.7	Z	A	Small aligned vesicles, elongate to irregular	Fresh	5.11	2.57	13.0
6H	1038.1	X	P	Densely olivine phyric, medium size vesicular	Mostly fresh	5.06	2.56	25.3
7H	1179.1	X	P	Moderately vesicular to amygdaloidal, medium size	Partly to completely filled vesicles	5.14	2.56	19.3
8H	1230.9	Z	P	Clay rich, minor vesicle evidence	Highly altered	5.06	2.56	8.7
9H	1686.2	Z	P	Moderately vesicular, some larger coalesced	Mostly fresh, pale grey vesicle coatings	5.10	2.56	15.0
10H	1686.2	Z	P	Moderately vesicular, some larger coalesced	Mostly fresh, pale grey vesicle coatings	5.05	2.55	12.5
11H	1689.7	X	P	Densely vesicular, small, minor coalescence	Mostly fresh, rare zeolite fills(detached)	4.98	2.55	12.1
12H	1716.4	X	P	Large mostly isolated vesicles	Weakly altered to fresh, rare zeolite filled vesicles	5.07	2.56	9.1
13H	1716.4	X	P	Large mostly isolated vesicles	Weakly altered to fresh, rare zeolite filled vesicles	4.99	2.56	12.8
14H	1727.9	Z	P	Medium isolated vesicles	Weakly altered, zeolite coating/partial fill	4.99	2.56	10.6
15H	1729.6	Z	P	Medium to large irregular vesicles	Weakly altered around vesicle rims	4.88	2.57	13.4
16H	1729.6	Z	P	Medium to large irregular vesicles	Weakly altered around vesicle rims	4.97	2.56	14.1
17H	1738	Z	P	Massive medium crystalline	Weakly altered	5.07	2.56	11.2
18H	1747.8	Z	P	Medium-sized moderately vesicular	Partial to complete zeolite fills, highly altered	4.44	2.57	15.2

19H	337.5	Z	A	Small to medium vesicles, olivine phyric	Fresh	6.30	2.56	18.9
20H	692.8	X	P	Highly vesicular, medium-sized	Weakly altered, possible minor dissolution?	5.12	2.56	12.5
21H	818.1	Z	P	Highly vesicular, small vesicles	Weakly altered, minor linings in places	6.47	2.55	8.6
22H	969	Z	P	Small to medium dispersed vesicles	Weakly altered	5.04	2.56	13.5
23H	1122.8	Z	P	Moderately vesicular, medium size	Moderately altered, oxidized throughout	6.39	2.56	11.0
24H	1283	Z	I	Angular fragments of basalt in altered matrix	Altered	5.09	2.55	11.2
25H	1456.7	Z	P	Moderate to densely vesicular, mostly detached	Weakly altered, trace oxidation throughout	6.54	2.56	9.8

Note. Column 'D' refers to the direction of the core plugs: 'Z' perpendicular and 'X' parallel to the main core axis, respectively. The facies are A: Aa lava and P: Pahoehoe lava. Column λ_{Sw} refers to the S-wave wavelength computed at the individual central frequency recorded at the ultrasonic waveform for each sample.

Petrophysical properties were measured on the cored samples at ambient room temperature (~18-20℃) and atmospheric pressure (1 bar). To measure the porosity of the core plugs a Helium porosimeter was used: the core plug is put into a tight chamber, a known volume of Helium gas is injected (from a different chamber) at a defined pressure, then the equilibrium pressure of the two chambers is recorded, allowing to determine the grain volume. The calliper measurements are used to generate the volumes of the core plug, making it possible to calculate the bulk and grain density and porosity, such that:

$$Bulk\ Density = \frac{Weight\ (g)}{Bulk\ volume\ (cc)}$$

$$Grain\ Density = \frac{weight\ (g)}{Bulk\ volume\ (cc) * (1 - \frac{Pore\ volume\ (\%)}{100})}$$

$$Porosity\ \% = \frac{Bulk\ volume - Grain\ volume}{Bulk\ volume} * 100$$

As part of this study, we also estimated porosity from the polished thin sections (2D). Two different methods were used: (1) binary segmentation of the light microscopy images using ImageJ software; and (2) manual segmentation of BSE images using Aviso software. The computed porosity values were close and comparable with the 3D porosity measured in the rock samples (RP-plug) (Figure A1.1); the higher differences observed in sample 4H between the measured and computed values are likely due to the large vesicles of the sample that make it quite heterogeneous at the core scale (Figure A5.1). These results give us confidence to extrapolate analysis done on the thin sections (2D) as a reliable representation of the sample (3D).

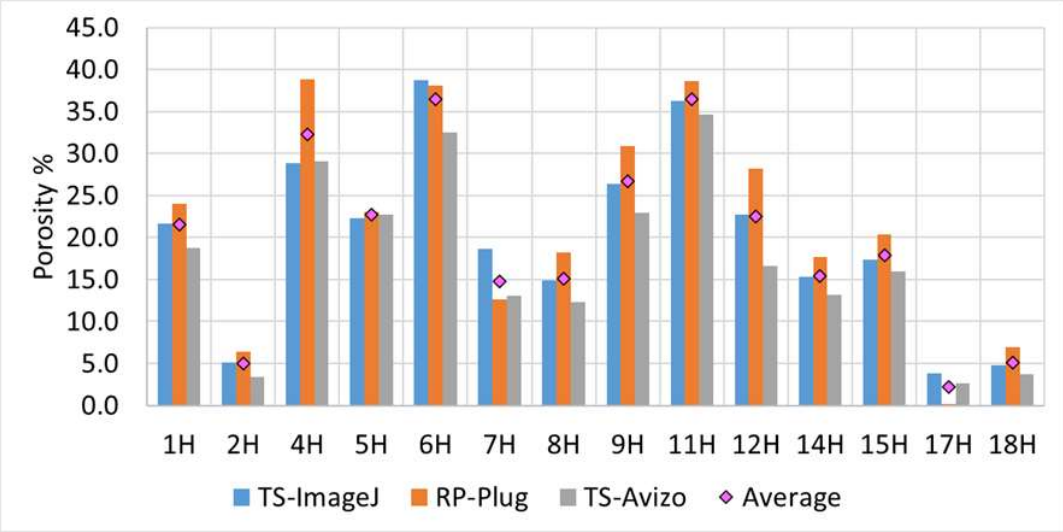

Figure A1. 1. Porosity in the sample obtained by three different methods and its average; computed from 2D images (TS-ImageJ and TS-Avizo) and measured in the laboratory on the 3D core plugs (RP-plug).

Velocity estimation.

The samples were oven-dried at 40 ℃ for about 24 hours before acquiring ultrasonic waveforms. We measured ultrasonic velocities (see section 2.3.1 in Chapter 2 for details on the acquisition system). The induced *P* wave was straightforwardly identified as the first break on the waveforms (Pa in Fig. A1.2). To pick the *S* wave arrivals (Sa), we changed the polarization of the transducer in three different settings: (1) with the transducers aligned, (2) with the source transducer rotated by 90 degrees (around its own axis), and (3) after inverting the sample to change the source/receiver position. The picked arrival times are corrected to account for the natural delay of the electronics. The velocity of the phases was calculated then by dividing the length of the samples by the wave-arrival time.

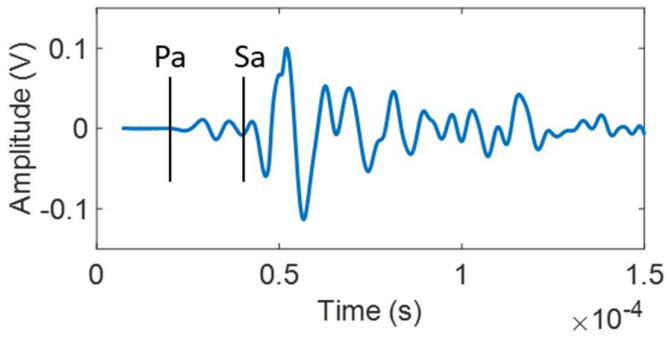

Figure A1. 2. Picking of P- (Pa) and S- wave (Sa) arrival times on the ultrasonic waveform recorded in sample 1H.

A2 – Rock Physics cross-plots

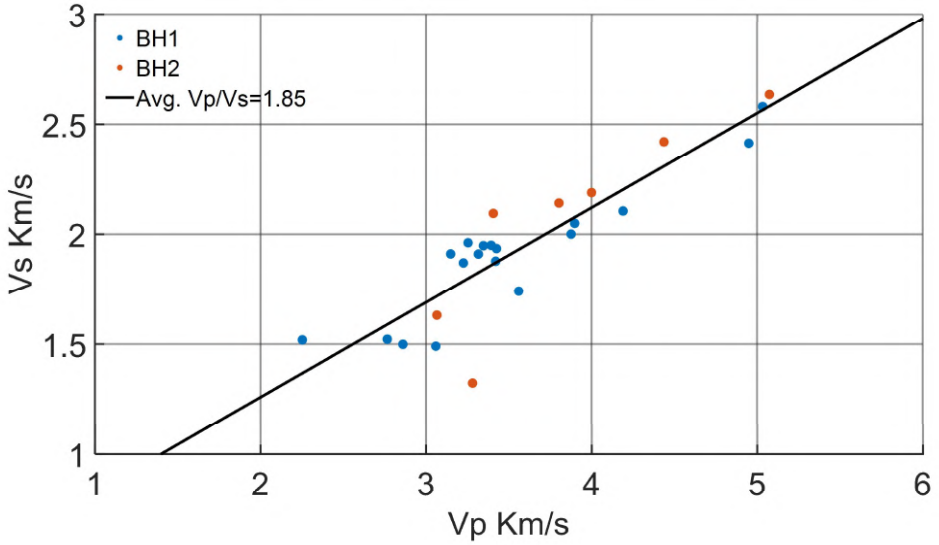

Figure A2. 1. P-wave velocity versus S-wave velocity of the volcanic rock samples.

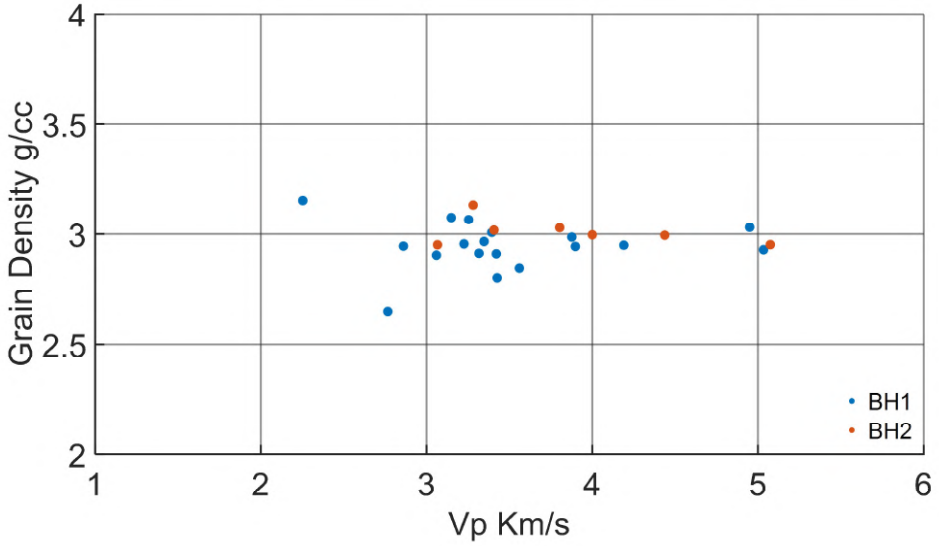

Figure A2. 2. P-wave velocity versus grain density of the volcanic rock samples.

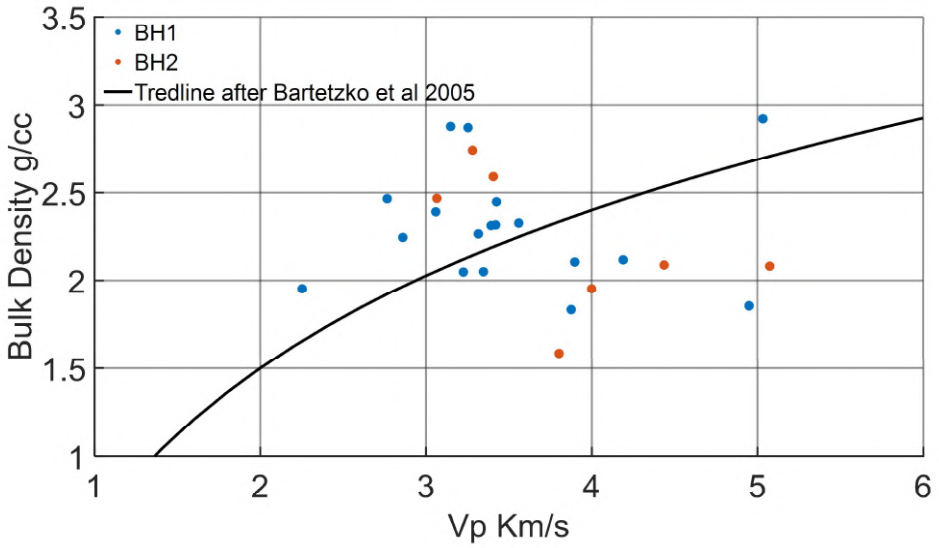

Figure A2. 3. P-wave velocity versus bulk density of the volcanic rock samples.

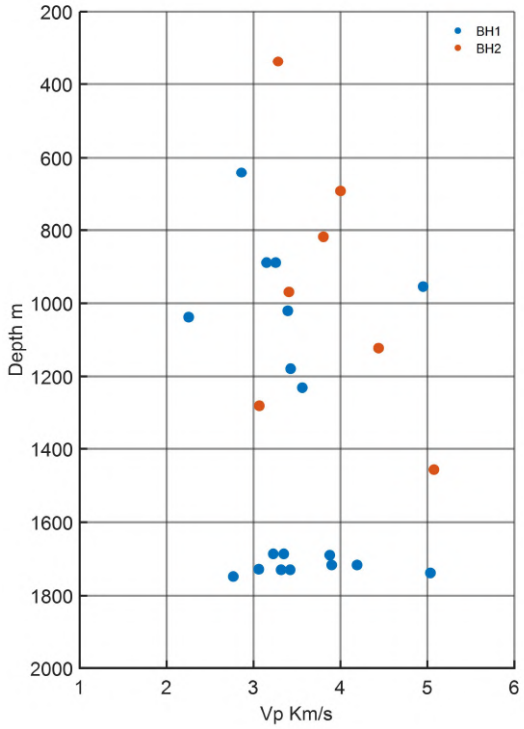

Figure A2. 4. P-wave velocity versus Depth.

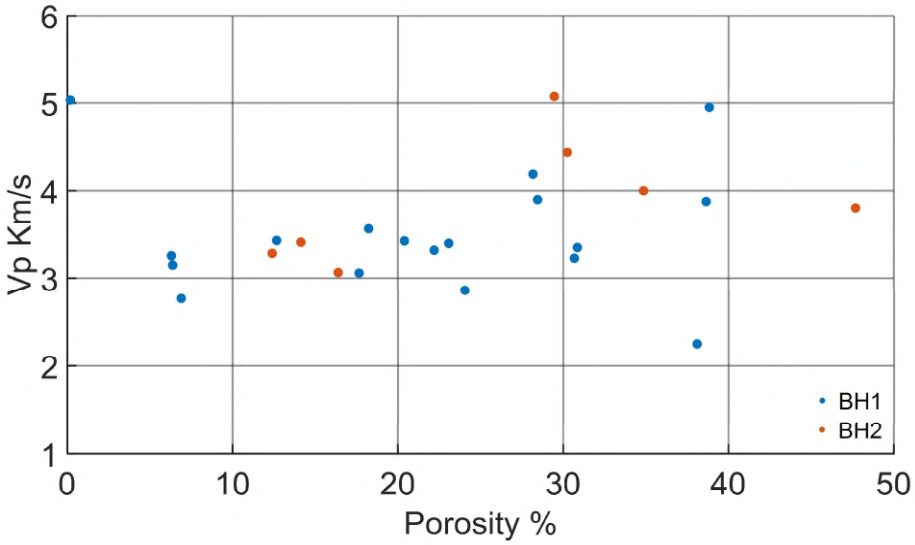

Figure A2. 5. Porosity versus P-wave velocity of the volcanic rock samples.

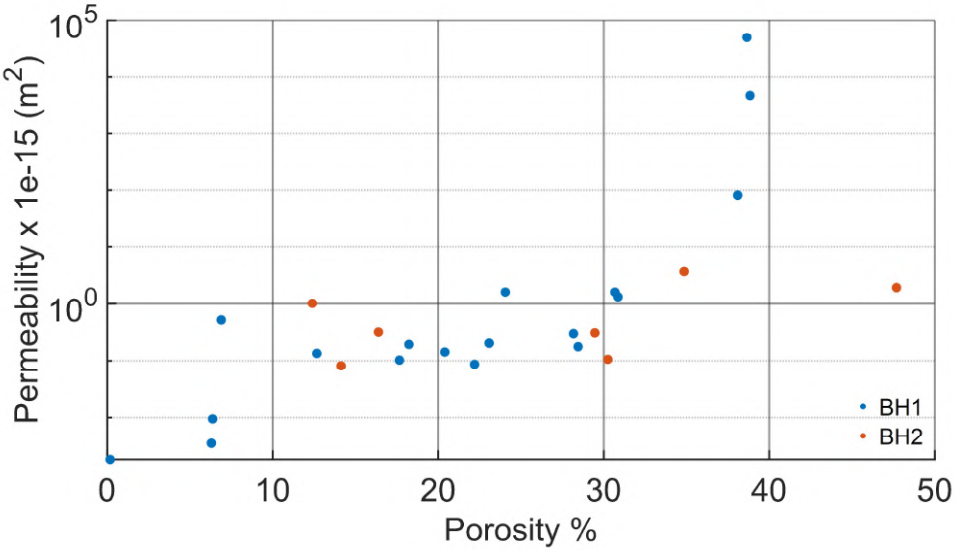

Figure A2. 6. Porosity versus permeability of the volcanic rock samples.

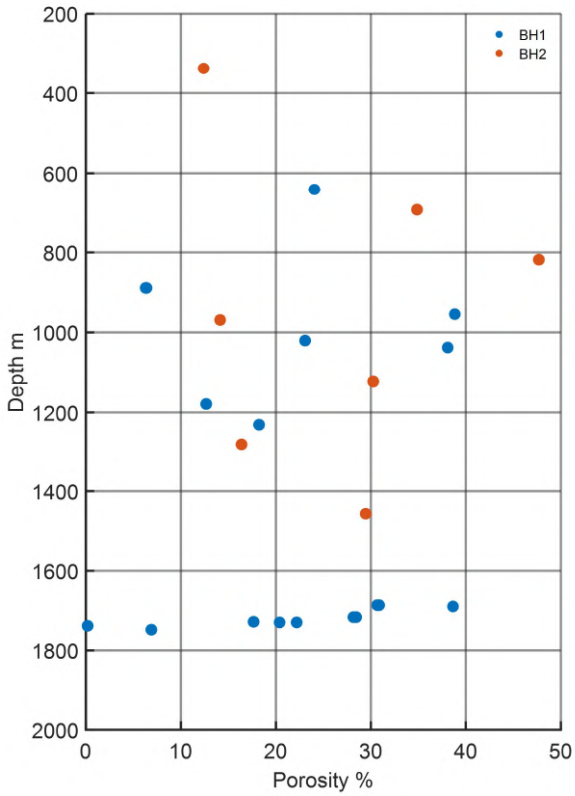

Figure A2. 7. Porosity versus Depth

A3 – Laboratory Experiments to record coda waves

The seismic survey was performed at the Rock Physics laboratory of the University of Aberdeen and the Rock Physics laboratory of Curtin University.

A3.1 Influence of electronics

A test was done to evaluate the influence of the acquisition parameters in the coda-attenuation values; it was found that inputs such as the pulser voltage (amount of voltage that provides power to the pulser and allows to maintain a constant source amplitude) and the receiver gain (that controls the amplification/attenuation of signals processed by the receivers) must be constant for all the measurements because small changes in these values dramatically affect the propagation of the signal in the coda part of the waveform. The waveforms for *P*- and *S*- waves were re-acquired for the core samples after selecting common input parameters for the acquisition, to guarantee consistency when comparing results between datasets.

A3.2 The assembly of the experiment

The samples were placed in vertical position (its long axis) into a chamber that secured the source and receiver transducers, located at the top and bottom side-ends of the sample, respectively. Two experimental set-ups were tested (Figure A3.1):

1. Near ambient confining pressure was applied by tightening the core chamber; through finger-tight of butterfly screws. This approach causes variations in the waveform due to inconsistencies in the pressure applied to hold the core in the chamber (Figure A3.1a). For this reason, it was decided to use a torque wrench to apply a constant force on the top bolt to ensure good transducer-sample coupling; however, the error associated with the repeatability of the experiment is still considerable.

2. The transducers were placed in a box-holder coupled to an internal spring to guarantee equal pressure conditions, as it allows the coupling force to be independent of the assembly system (Figure A3.1b). To ensure repeatability, these holders were attached to a bracket system to give stability and to hold the sample in the middle of both transducers while keeping them aligned.

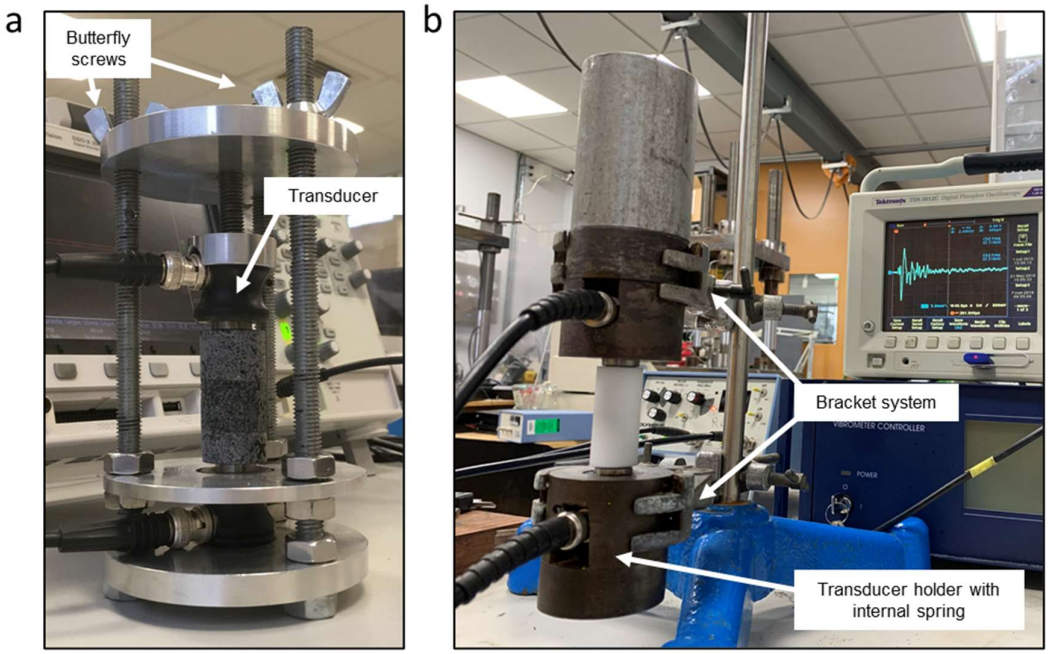

Figure A3. 1. Experimental set-up for the acquisition of ultrasonic waveforms at the rock physics laboratories of the University of Aberdeen (a) and Curtin University (b), note the aluminium block in (b) is not applying any force to the transducer, was only used to check the equilibrium of the holder-transducer-sample system.

A3.3 The coupling sample transducer

To achieve a good signal propagation without the need of applying pressure to pair the assembly, it was decided to glue the *P* wave transducers to both sides of the samples. In this case, we worked with the *P* wave transducers because their diameter coincided with the diameter of the samples of 1 inch. The glue applied was common 'super-glue', the sample-transducer was left to dry for a couple of hours and then the measurements were acquired. It resulted in a good strategy for measuring *P* wave arrival times. However, we

stopped using this approach because: (1) the characteristics of the transducers (Accuscan type, characterized by a narrow bandwidth and limited axial resolution) were inappropriate to record long signals accurately, forbidding coda analysis; and (2) it was necessary to immerse samples and transducers in acetone overnight to separate them, which could damage both the sample and equipment. The *S* wave transducers used are of the type Videoscan, which are advised for attenuating or scattering materials. We tried to improve the contact between these transducers and the sample by adding Treacle syrup to the side-ends of the core samples. We did not notice any improvement on the waveforms.

A3.4 The LDI method

Laser Doppler Interferometer (LDI) is a relatively new non-invasive method for measuring *P* and *S* wave velocities in rock sample (Lebedev et al., 2011). A piezoelectric transducer is used as the source while the LDI measures the velocity (or displacement) at the surface of the sample in a small area (micrometer scale) along the direction of the laser beam. The apparatus used allows measuring velocity at a frequency range of 2.5 MHz. To generate a source an *S* wave transducer was coupled to the bottom side of the cylindrical sample (located in vertical axis direction). A reflective tape was glued at the top side of the sample to reflects light backwards, then the vibration was detected by the LDI. The measurements were made at the centre of the sample. (Figure A3.2). Unfortunately, most of the core samples in our dataset are extremely attenuative making it impossible to achieve a good signal-to-noise ratio to acquire a good waveform.

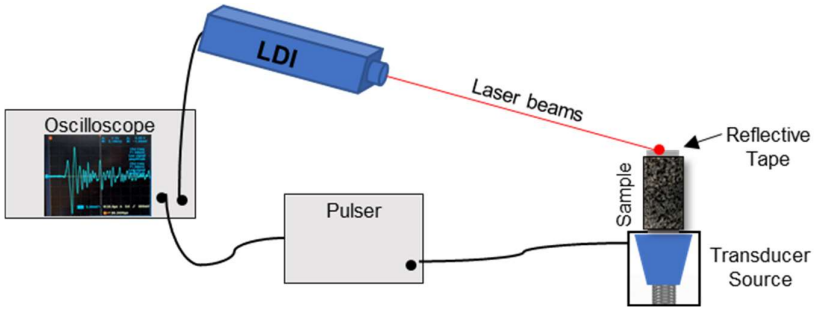

Figure A3. 2. Schematic illustration of the experimental set-up for the LDI measurements.

A3.5 The stress associated method

To test the change in velocity and coda signals when applying pressure to the samples we devise and experiment using a hook cell that allows applying axial and confining pressure simultaneously to the samples (Figure A3.3). As the idea was to preserve the conditions of the samples (i.e. we do not want to generate new cracks), the confining pressure and maximum axial pressure (to keep the equilibrium state) was computed by considering the initial hydrostatic pressure from the depth where the cores were extracted. The available equipment was designed to work with samples twice the diameter size of the core plugs (2 inches), then it was necessary to create a 'rubber' jacket to: (1) hold the sample; (2) fit the space in the pressure chamber; and (3) improve boundary conditions by absorbing coherent waves at the boundaries of the sample.

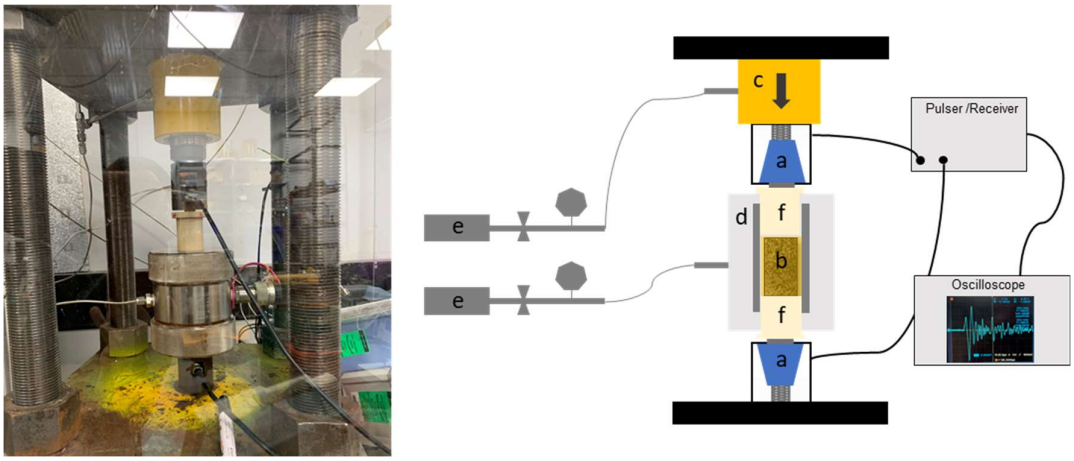

Figure A3. 3. Schematic of the experiment. a: transducer in box holder with spring attached; b: jacketed rock sample; c: hydraulic uniaxial; d: sample chamber with confining stress; e: pressure control; f: Piston.

- *Creation of the Jacket*

The material used to create the jacket is a mixture of polyether elastomer (Erapol CCM75A). The components were mixed and poured into a Teflon mould (previously

created) with the dimensions of the required jacket. After allowing 1- week time for cure the casting was demoulded. Despite several attempts to avoid trapped air in the jacket, the chemical components and small pouring space created small inhomogeneity which could have effects on amplitude recordings. Rubbers jackets are known to weaken boundary reflection (Wei and Fu, 2014); however, in our case, some high-frequency resonances were generated when applying confining pressure to the jacket. This is probably due to the chemical features of our jacket. Then only uniaxial pressure was applied with low increments from 0 to 1 MPa.

A4 – Coda Window

The acquired waveforms have a length of 4e-04 seconds. We decided to use a common coda window for all the samples starting at 1.75e-04 seconds and with a length of 1.75e-04 (Figure A4.1a). In the envelope of the signal (Figure A4.1b), we noticed small increases across the decreasing coda decay. These increases are related to reverberations from the ends of the samples (seismic multiples). To understand the effect of these secondary reflections in our sample we analysed the wave propagation on an aluminium plug (Figure A4.1d) with dimensions similar to the rock samples. In the corresponding waveform, the reflections are evident after three times the first wave arrival, both in the envelope (Figure A4.1e) and in the spectrogram (Figure A4.1f). These multiples have high magnitudes, as expected in aluminium, which has very low attenuation. In the spectrogram of our rock sample (Figure A4.1c), the magnitudes of these multiples are not comparable with the magnitude of the direct wave package. Indeed, if we change the colour scale to appreciate better the magnitudes at later times, the multiples arrivals (after the first two multiples) for the rock sample are irrelevant (Figure A4.2). We thus decided to neglect the effect of these secondary increases and to choose a long coda window starting at 1.75e-04 seconds from the origin time, which is at least four times the arrival time of the S-wave. This choice allows removing the first multiple, which is by far the most intense in the coda. The second multiple is removed in 92% of the cases.

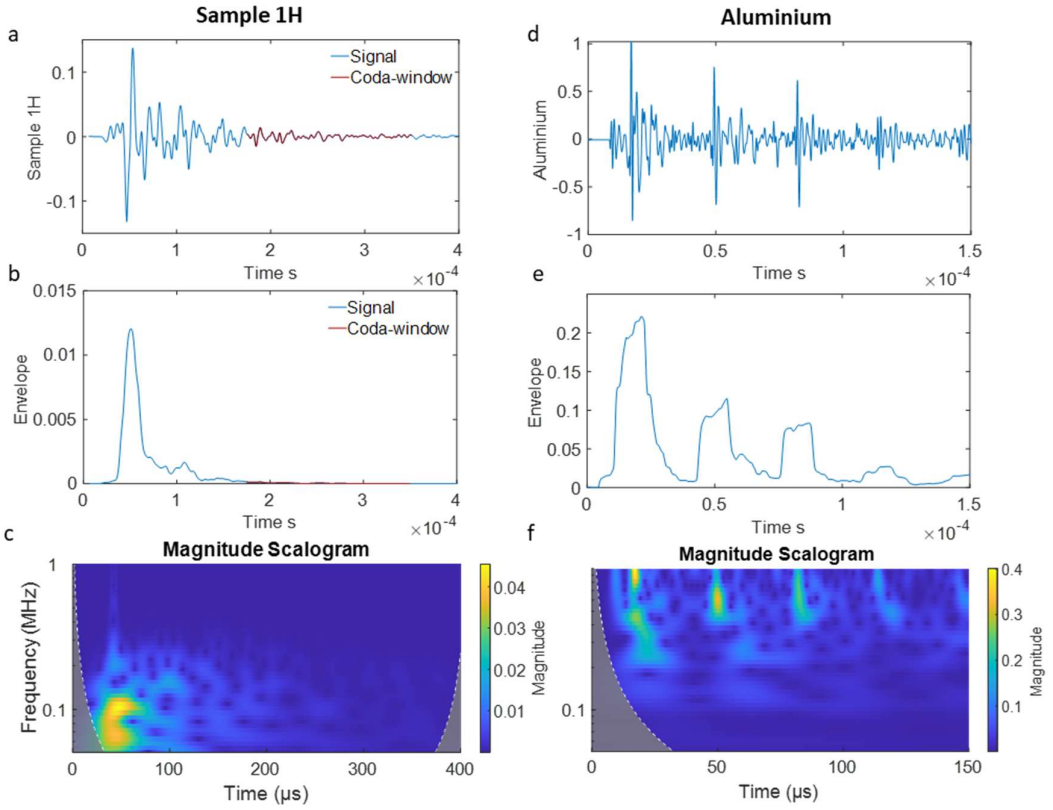

Figure A4. 1. Selection of the coda window. Ultrasonic waveform for sample 1H (a), its envelope (b) and the scalogram of the signal (c). Ultrasonic waveform for aluminium sample (d), its envelope (e) and the scalogram of the signal (f).

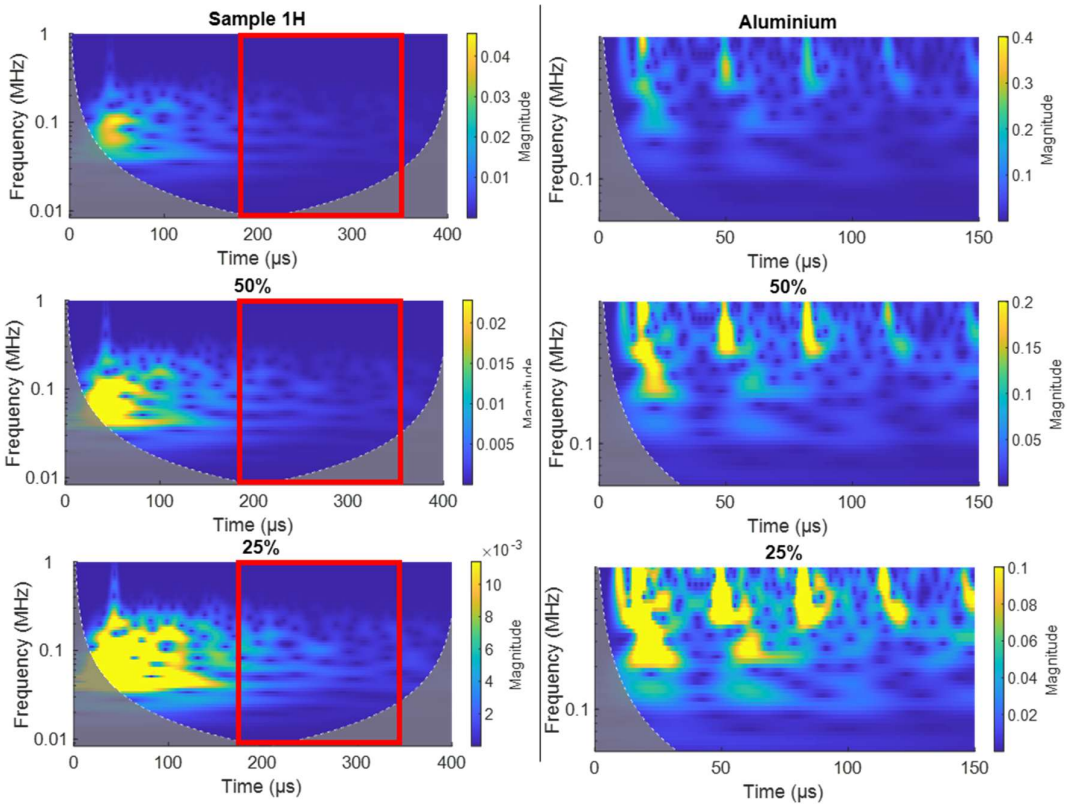

Figure A4. 2. Magnitude scalogram. Rock sample (left) and aluminium sample (right). By changing the colour scale to 50% and 25% of the maximum amplitude, the multiple arrivals are more easily visible. The coda window corresponds to the area in the red box, which does not have a noticeable influence from the multiples.

Qc values for different coda windows selection.

Four methods were tested (e.g., sample 4H in the figure below):

1. **Fixed coda**: coda start at 175 μs and end at 350 μs for the entire dataset.
2. **Early coda**: coda window starts after the S wave package (from 50% decay of its maximum amplitude) and ends before the first multiple.

3. **S wave related coda**: coda starts after 5 times after the S wave arrival time with a fixed length of 200 µs.

4. **Maximum amplitude related coda**: coda start 4 times after the time at which the maximum amplitude of the signal occurs, with a constant length of 100µs.

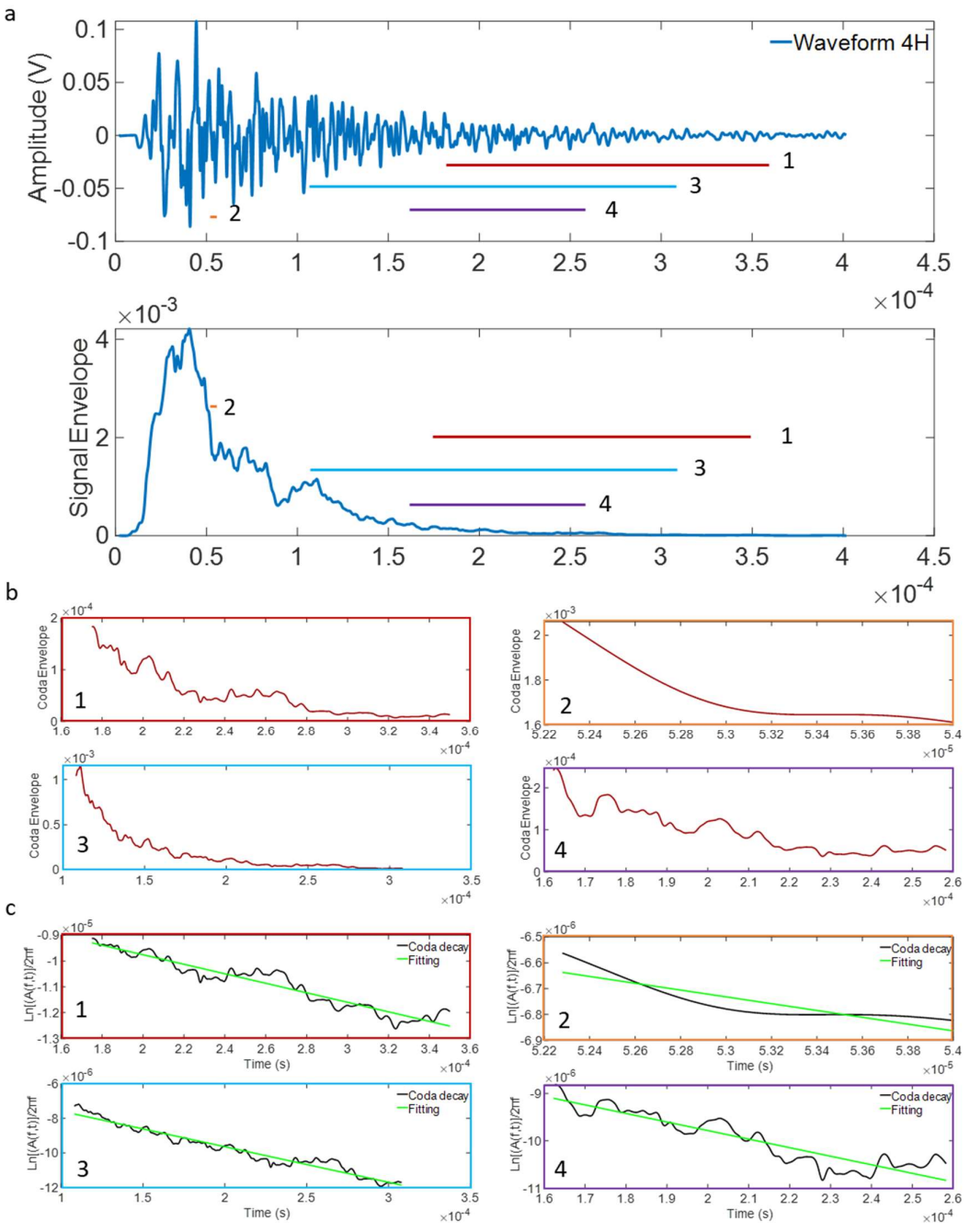

Figure A4. 3. Coda window selection and Qc computation foe sample 4H.

The early coda window approach was unsuccessful within our dataset because the coda lengths had to vary from 1.7 to 30 μs, given the different elastic properties of the samples. This is a difference of 40 to 750 data points. We consider that having less than 250 data points (10 μs window) makes the calculation of Qc unreliable. We decided not to use the S-wave coda related window because we were not confident in the picking of the S wave arrival, which was challenging in some samples. For the maximum amplitude related coda, the location of the coda window in the seismogram varies between samples, it goes from as early as 120-200 μs in sample 2H to as late as 300-400 μs for sample 19H. We believe this compromises the comparison between different samples. We opted for a fixed coda window between 175 and 350 μs for the entire dataset. This window selection (1) is the best approach to be able to compare results between samples, (2) takes out the uncertainty associated with the arrival picking, (3) removes the effect of the first multiple for all the samples and it starts after the second multiple in 92% of the samples, (4) avoid the low s/n ratio at the end of the seismograms, (5) the correlation coefficient of the fitting line to compute Qc is above R=0.60 for all the samples and above R=0.80 for 60% of the samples, and (6) it is similar to the window selection approach used when analysing field data.

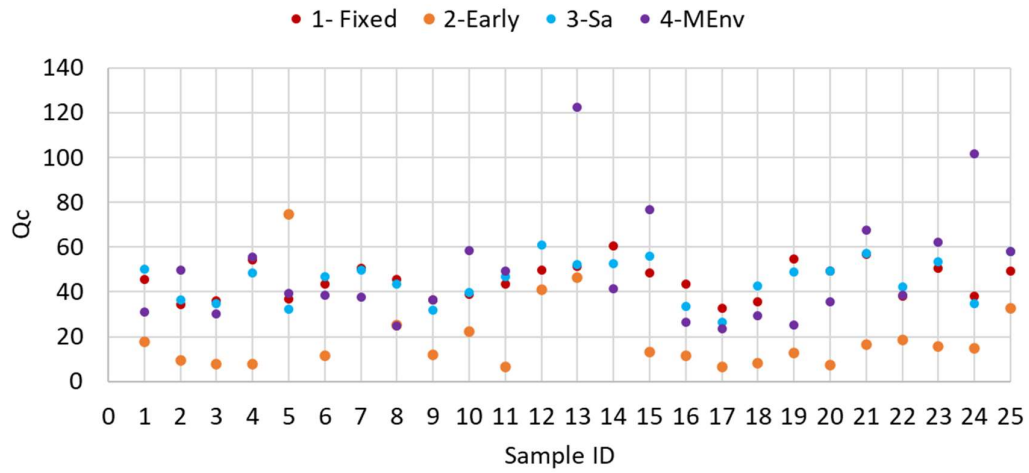

Figure A4. 4. Qc values computed for 4 coda window types (1: fixed late coda, 2: variable early coda; 3: related to S wave arrival time; 4: related to maximum amplitude in the envelope). Methods 1 and 3 gave relatively similar *Qc* values, both with R values above 0.60; Method 2 has outliers values for samples 7 and 14 and has 6 samples with R values lower than 0.60; Method 4 has outliers for samples 12, 13 and 24, and 10 samples with R values lower than 0.60.

A5 – Thin sections

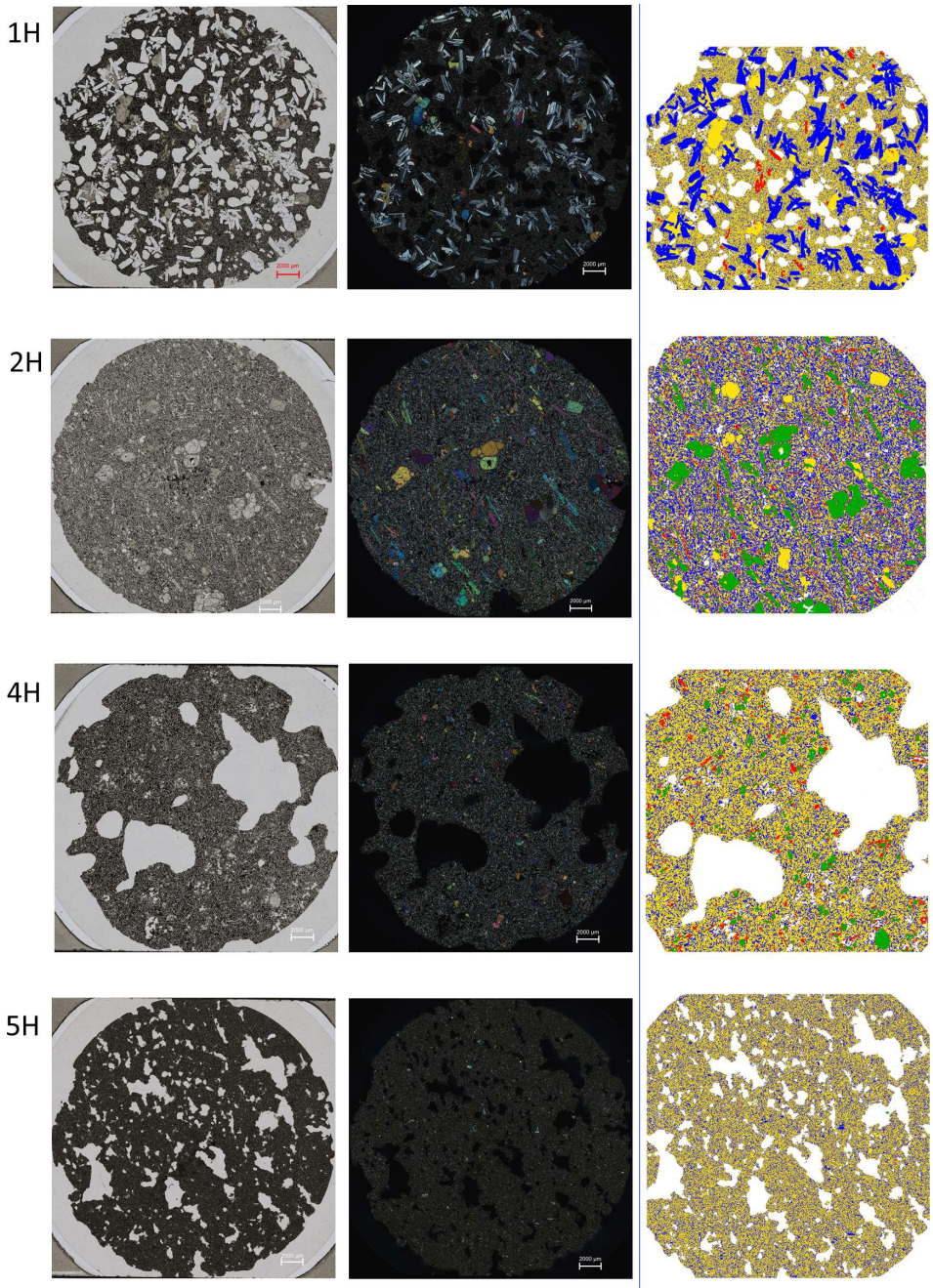

Optical images under plane polarised light (first column) and crossed-polarised (second column)

Phase identification map taken in a scanning electron microscope (TIMA system)

- Amphibole
- Feldspars
- Pyroxene
- Olivine
- Zeolites
- Others

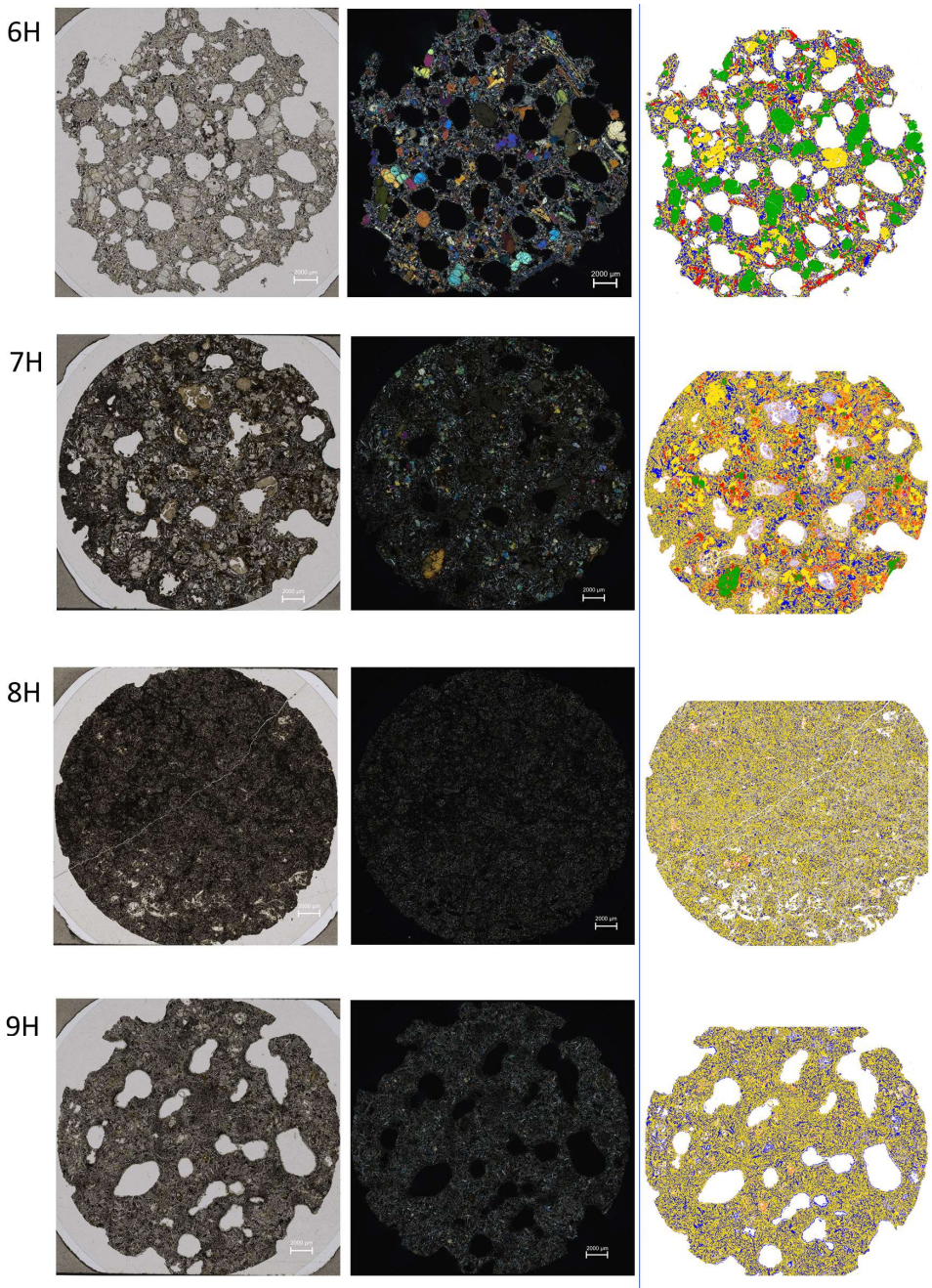

Optical images under plane polarised light (first column) and crossed-polarised (second column)

Phase identification map taken in a scanning electron microscope (TIMA system)

- Amphibole
- Feldspars
- Pyroxene
- Olivine
- Zeolites
- Others

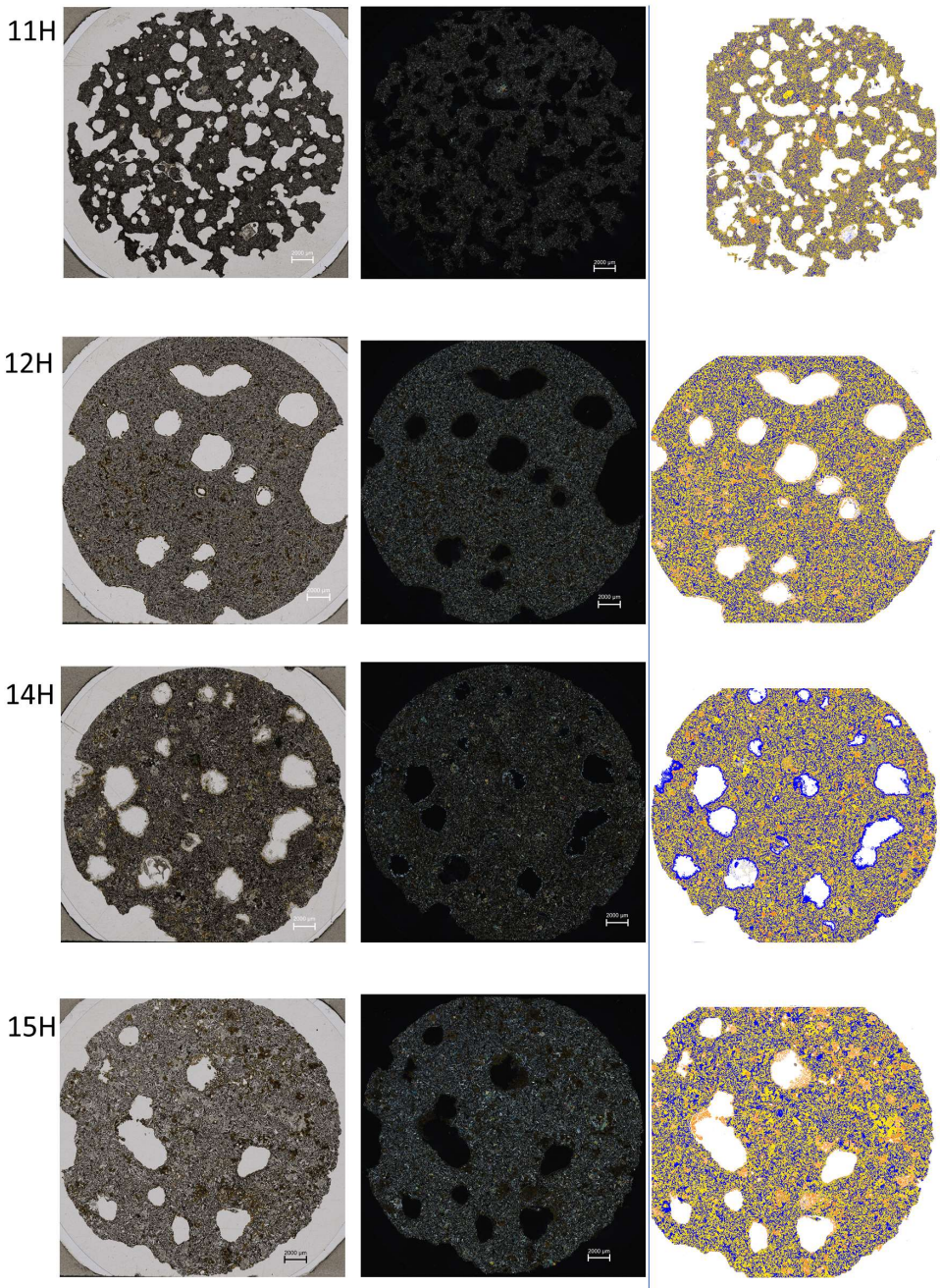

Optical images under plane polarised light (first column) and crossed-polarised (second column)

Phase identification map taken in a scanning electron microscope (TIMA system)

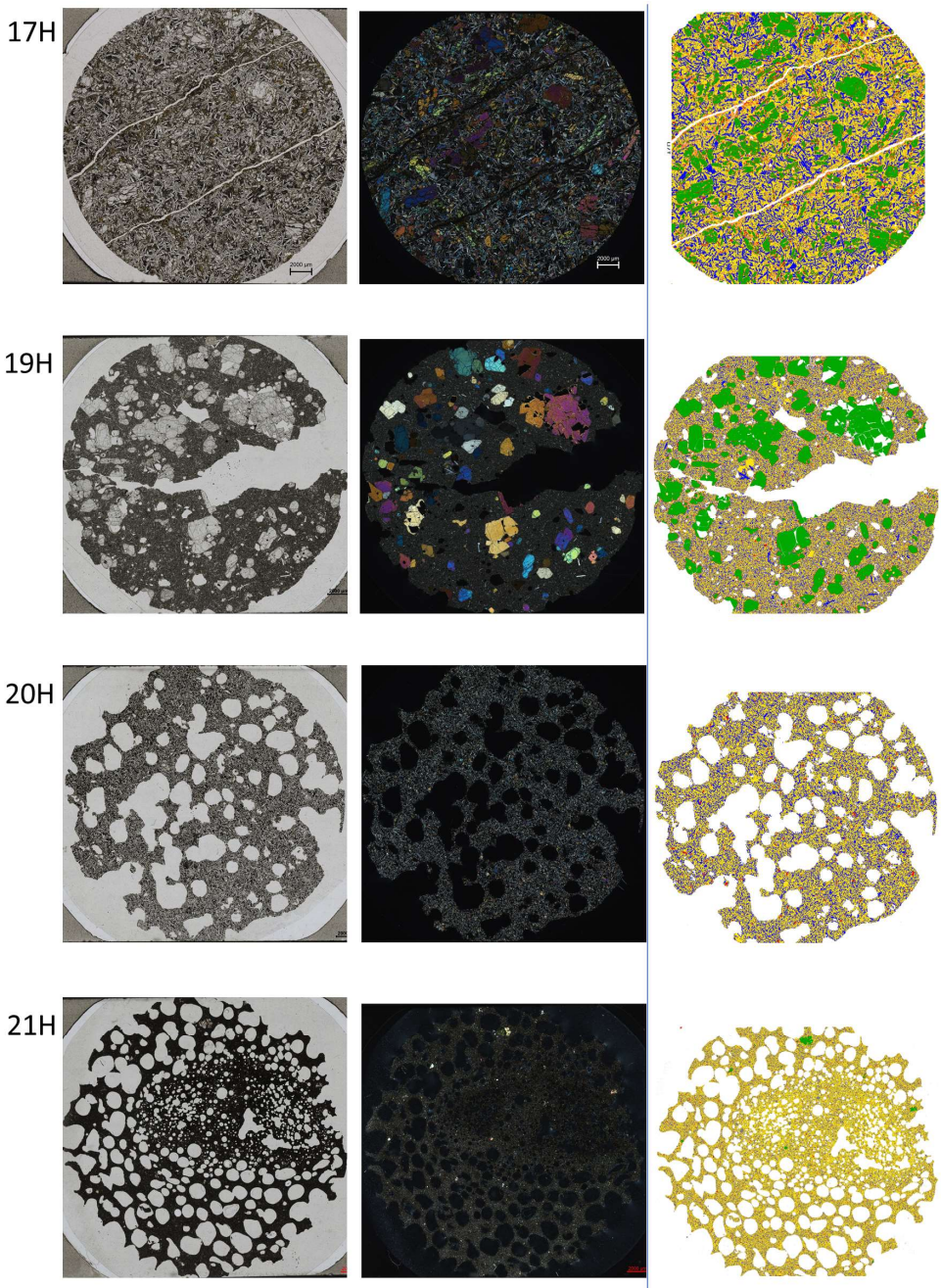

Optical images under plane polarised light (first column) and crossed-polarised (second column)

Phase identification map taken in a scanning electron microscope (TIMA system)

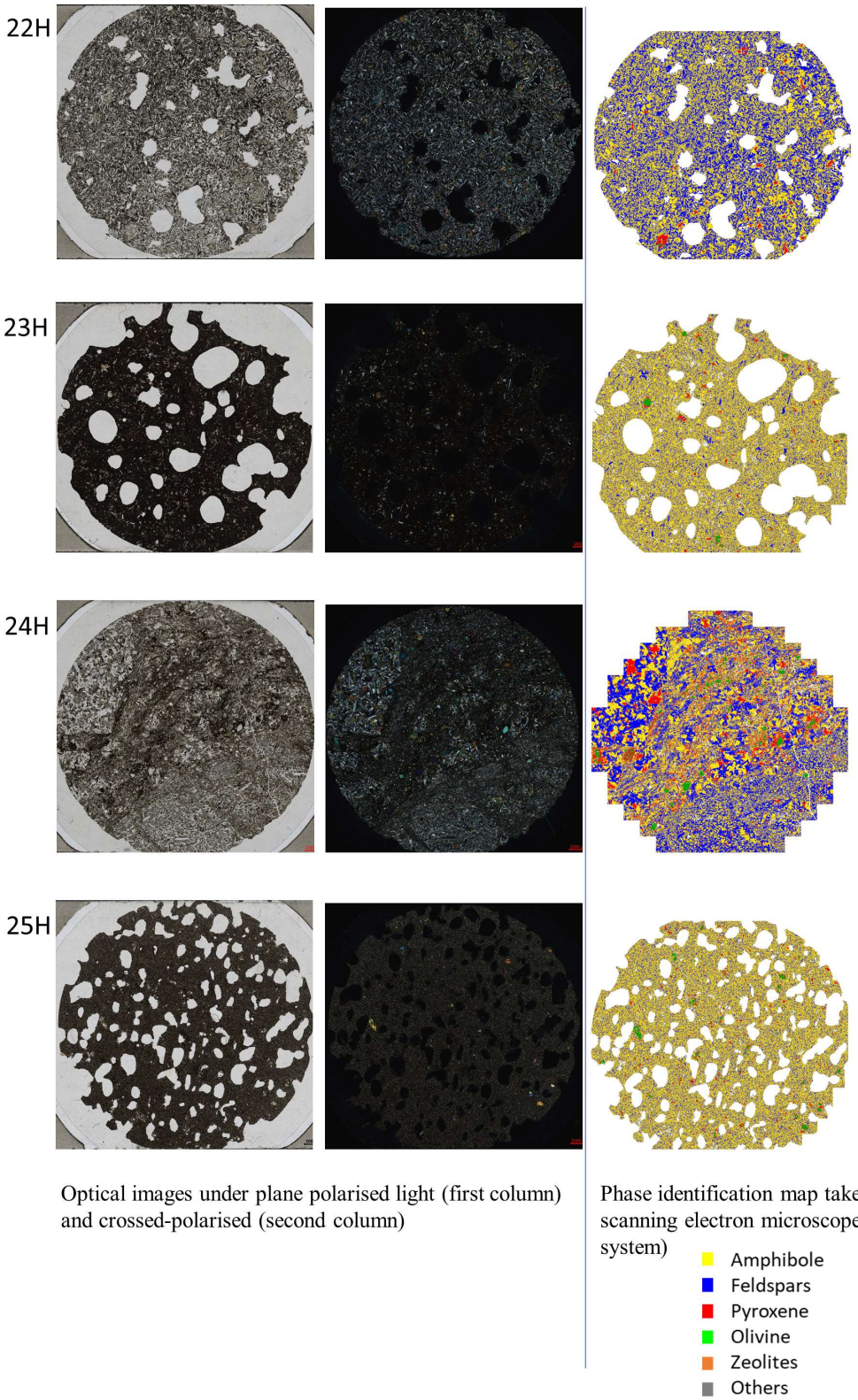

Figure A5. 1. Thin sections: microscopy scan and mineral mapping.

A6. Mineral distribution per sample

Table A6. 1. Mass % per phase.

Sample	*Amphibole*	*Feldspars*	*Pyroxene*	*Olivine*	*Zeolites*	*Others*
1H	53.24	42.26	1.36	0.24	0.07	2.83
2H	42.43	38.90	4.17	11.06	0.38	3.06
4H	60.53	28.68	3.61	4.62	0.27	2.29
5H	63.48	32.30	0.48	0.29	0.08	3.37
6H	40.63	28.68	7.16	21.29	0.35	1.89
7H	54.97	25.90	6.29	2.94	8.22	1.69
8H	66.53	29.01	0.53	0.65	0.90	2.37
9H	61.58	32.74	0.17	0.32	2.75	2.45
11H	57.17	36.11	0.38	0.50	3.16	2.67
12H	53.65	36.13	0.42	0.24	6.17	3.38
14H	48.87	40.84	0.66	0.28	5.87	3.48
15H	51.65	36.25	0.72	0.32	7.87	3.20
17H	44.72	24.81	5.38	17.63	5.63	1.82
18H	41.83	30.64	5.63	0.13	19.46	2.31
19H	45.25	22.61	3.26	26.28	0.39	2.21
20H	62.19	33.19	1.42	0.41	0.24	2.55
21H	77.05	19.01	1.58	1.43	0.56	0.37
22H	49.17	42.71	1.46	0.46	0.03	6.16
23H	69.12	26.80	1.32	0.84	0.16	1.76
24H	45.31	39.81	9.58	1.40	0.55	3.35
25H	68.79	25.62	1.78	1.33	0.19	2.28

Table A6. 2. List of shear-wave velocity for mineral groups.

Mineral	Vs mm/µs
Amphiboles	3.77 [a]
Feldspars	2.39 [b]
Olivine	4.91 [b]
Pyroxene	2.72 [b]
Zeolites	3.50-4.77 [b]

Note. [a]Ji et al. (2013). [b]Mavko et al. (2009)

Table A6. 3. Grain size % per sample

Midpoint [µm]	*1H*	*2H*	*4H*	*5H*	*6H*	*7H*	*8H*	*9H*	*11H*	*12H*	*14H*	*15H*	*17H*	*18H*	*19H*	*20H*	*21H*	*22H*	*23H*	*24H*	*25H*
3.66	0.10	0.07	0.10	0.11	0.07	0.20	0.57	0.21	0.32	0.13	0.14	0.16	0.08	0.18	0.08	0.04	0.23	0.07	0.14	0.11	0.11
4.44	0.24	0.15	0.22	0.26	0.11	0.31	0.66	0.33	0.62	0.19	0.21	0.22	0.17	0.21	0.22	0.13	0.42	0.17	0.34	0.32	0.28
5.39	0.39	0.24	0.34	0.42	0.16	0.43	0.84	0.47	0.87	0.28	0.32	0.31	0.27	0.27	0.35	0.24	0.55	0.28	0.54	0.50	0.45
6.55	0.45	0.27	0.39	0.52	0.18	0.47	0.89	0.51	0.96	0.31	0.35	0.34	0.29	0.27	0.43	0.28	0.61	0.32	0.61	0.57	0.53
7.95	0.89	0.53	0.74	1.04	0.33	0.90	1.67	1.00	1.90	0.59	0.71	0.64	0.57	0.48	0.85	0.57	1.13	0.63	1.18	1.18	1.03
9.65	1.25	0.71	0.98	1.49	0.44	1.17	2.25	1.36	2.56	0.82	0.99	0.87	0.79	0.60	1.20	0.81	1.47	0.86	1.57	1.74	1.39
11.72	1.67	0.90	1.25	2.06	0.56	1.46	2.99	1.73	3.17	1.08	1.33	1.12	1.04	0.75	1.65	1.08	1.86	1.09	2.00	2.40	1.77
14.23	1.82	0.93	1.23	2.35	0.58	1.43	3.04	1.72	3.04	1.14	1.39	1.23	1.16	0.81	1.80	1.12	2.00	1.15	2.10	2.51	1.79
17.28	2.06	1.13	1.26	2.83	0.70	1.49	3.23	1.79	3.19	1.32	1.58	1.44	1.36	0.99	2.09	1.24	2.41	1.34	2.36	2.62	1.98
20.98	2.59	1.67	1.46	3.70	1.00	1.82	3.77	2.13	3.99	1.77	2.00	1.96	1.74	1.41	2.68	1.57	3.15	1.91	2.98	3.02	2.44
25.48	3.40	3.04	2.37	5.29	1.85	2.66	4.70	2.95	4.96	2.80	2.81	2.95	2.64	2.37	3.82	2.51	4.51	3.17	4.28	3.62	3.64
30.94	4.43	5.34	4.47	6.94	3.50	4.09	6.41	4.63	6.89	4.59	3.79	4.48	4.35	3.73	5.30	5.01	6.62	4.92	6.27	4.31	6.49
37.57	4.48	3.57	3.00	6.90	2.07	3.56	6.41	3.89	7.34	3.18	3.10	3.31	2.92	2.57	4.98	2.86	6.64	4.10	6.45	4.15	5.39
45.62	5.28	4.37	4.24	8.00	2.77	4.64	7.62	5.12	8.21	3.96	3.68	4.06	3.55	3.07	5.94	4.40	7.61	5.00	7.72	4.52	7.14
55.39	6.05	4.54	5.08	8.98	3.08	5.49	8.50	6.05	8.91	4.42	4.32	4.61	3.80	3.25	6.54	5.31	8.36	5.42	8.77	4.62	8.44
67.26	6.55	4.48	5.93	9.53	3.18	6.10	8.99	6.89	8.93	5.18	4.82	5.17	3.95	3.34	6.94	6.36	8.56	5.75	9.39	4.73	9.57
81.68	6.82	5.03	7.82	10.03	3.91	6.78	9.54	7.69	8.48	6.50	5.70	6.11	4.30	3.67	6.96	7.85	8.84	5.95	9.63	4.98	10.42
99.18	6.19	5.47	8.88	9.85	4.50	7.40	8.81	8.43	7.69	7.29	6.65	6.54	4.79	4.00	6.42	9.23	8.97	6.30	8.80	4.85	10.19
120.44	5.08	6.20	10.12	8.16	5.51	7.62	7.38	8.51	6.96	8.75	7.08	7.23	5.10	4.35	5.25	10.45	8.48	6.65	7.59	5.06	9.05
146.25	3.91	7.02	10.48	5.93	6.62	7.29	5.55	8.49	4.82	9.29	7.71	7.30	5.52	4.61	3.97	10.53	7.27	6.95	6.34	5.00	7.44
177.59	3.22	7.27	10.20	3.37	7.52	6.77	3.28	7.44	3.06	9.33	8.10	7.55	6.12	5.48	2.40	10.16	5.04	7.11	4.41	4.79	5.44
215.65	2.52	6.56	8.46	1.54	7.45	5.65	1.87	6.51	1.98	9.17	7.37	7.18	6.87	6.23	1.16	8.45	3.05	6.96	3.22	4.22	2.85
261.87	1.54	6.51	5.27	0.51	6.75	4.82	0.65	5.22	0.65	7.43	7.49	6.97	7.56	6.27	0.82	5.33	1.36	6.74	1.77	4.56	1.49
318.00	1.43	5.86	2.59	0.12	6.52	3.79	0.22	3.67	0.28	5.64	5.94	5.54	6.90	6.69	0.81	2.28	0.59	5.50	0.90	4.55	0.38
386.15	1.47	4.96	1.45	0.07	4.84	3.20	0.17	1.98	0.10	2.62	4.51	4.99	6.93	6.59	1.28	1.12	0.05	4.79	0.32	4.92	0.00
468.91	2.43	3.40	0.82	0.00	4.77	2.48	0.00	0.77	0.14	1.57	2.28	2.90	5.96	6.23	1.64	0.76	0.00	3.13	0.11	4.38	0.17
569.41	4.06	2.75	0.40	0.00	3.46	3.12	0.00	0.49	0.00	0.58	3.00	2.72	3.31	5.84	3.15	0.17	0.00	2.31	0.08	3.51	0.00
691.45	3.68	2.03	0.14	0.00	4.62	1.85	0.00	0.00	0.00	0.08	1.79	1.70	1.87	6.16	3.00	0.13	0.00	1.08	0.13	4.89	0.13
839.64	6.01	0.69	0.00	0.00	4.03	0.96	0.00	0.00	0.00	0.00	0.50	0.16	2.61	5.62	4.22	0.00	0.24	0.36	0.00	1.79	0.00
1019.60	4.50	2.38	0.30	0.00	3.84	1.29	0.00	0.00	0.00	0.00	0.34	0.23	2.32	2.77	3.60	0.00	0.00	0.00	0.00	1.01	0.00
1238.12	4.59	1.01	0.00	0.00	4.55	0.34	0.00	0.00	0.00	0.00	0.00	0.00	1.18	0.90	5.27	0.00	0.00	0.00	0.00	0.55	0.00
1503.48	0.93	0.89	0.00	0.00	0.52	0.41	0.00	0.00	0.00	0.00	0.00	0.00	0.00	0.31	5.21	0.00	0.00	0.00	0.00	0.00	0.00

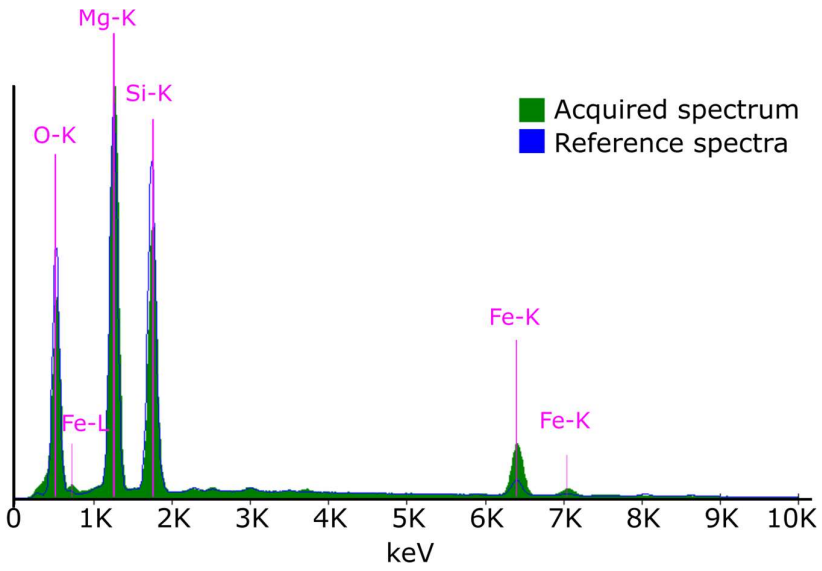

Figure A6. 1. Phases identification using TIMA. Example for the spectrum of Olivine.

A7. Statistical parameters

Table A7. 1. Statistical parameters from the velocity fluctuations in volcanic rock samples.

Sample	*ε %*	*a (mm)*
	Standard deviation of velocity fluctuations	*Scale length of heterogeneity*
1H	11.0	0.29
2H	12.5	0.08
4H	8.2	1.19
5H	10.2	0.39
6H	10.5	0.55
7H	11.8	0.22
9H	9.0	0.71
11H	11.1	0.41
12H	8.6	0.61
14H	8.1	0.55
15H	8.4	0.65
18H	11.2	0.14
20H	12.6	0.09
21H	10.3	0.53
22H	12.8	0.25
23H	9.4	0.39
25H	8.7	0.85

A8 – *Qc* vs frequency content

The ultrasonic experiments were performed using a source transducer with a characteristic frequency of 1 MHz. However, the frequency content on the output signals (seismograms) varies between samples (λ reported in Table A1.1). The median frequency content in the dataset is 150 kHz. The lowest central frequency recorded was around 70 kHz (sample 19H), while the highest frequency observed was ~350 kHz (sample 3H). The results in the paper correspond to coda attenuation values (Qc^{-1}) computed at a central frequency of 150 kHz for all the samples. Here we re-plot figures 2.6 and 2.12 (Figures A8.1 and A8.2, respectively) presenting the attenuation values as a function of the wavelength of each sample. Observing the plots scaled by the wavelength does not change the analysis of the results. We also tested how the frequency affects the coda attenuation by computing *Qc* values at a range of frequencies from 50 to 400 kHz (Figure A8.3). As expected, we observe that *Qc* increases linearly with frequency, the slope of the linear relationship varies at an acceptable level between samples (the minimum slope is 0.23 for sample 14H and the maximum slope is 0.40 for sample 17H).

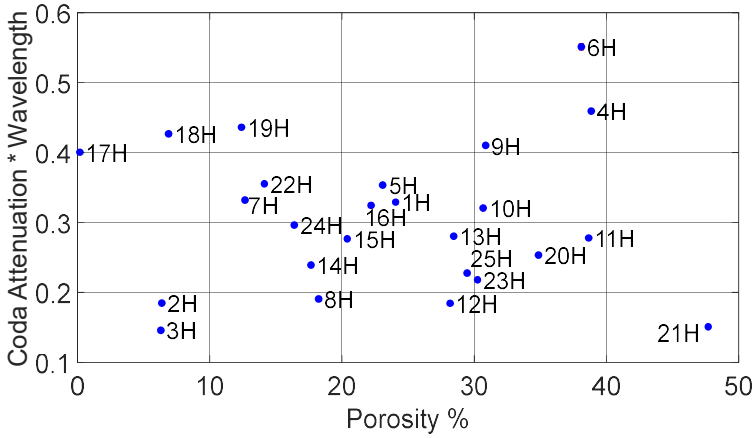

Figure A8. 1. Coda attenuation values computed at a central frequency of 150 kHz and scaled by the wavelength recorded at each sample versus porosity.

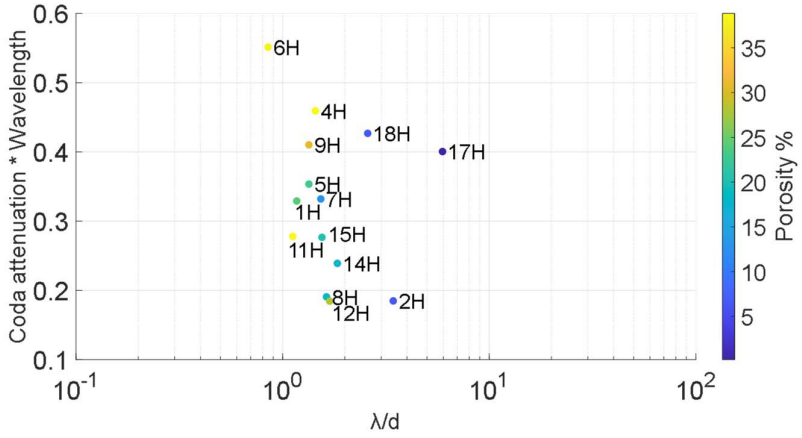

Figure A8. 2. Coda attenuation values computed at a central frequency of 150 kHz and scaled by the wavelength recorded at each sample versus the ratio λ/d (λ: seismic wavelength at 150 kHz, d: the size of heterogeneities related to the equivalent diameter of the pores in the sample).

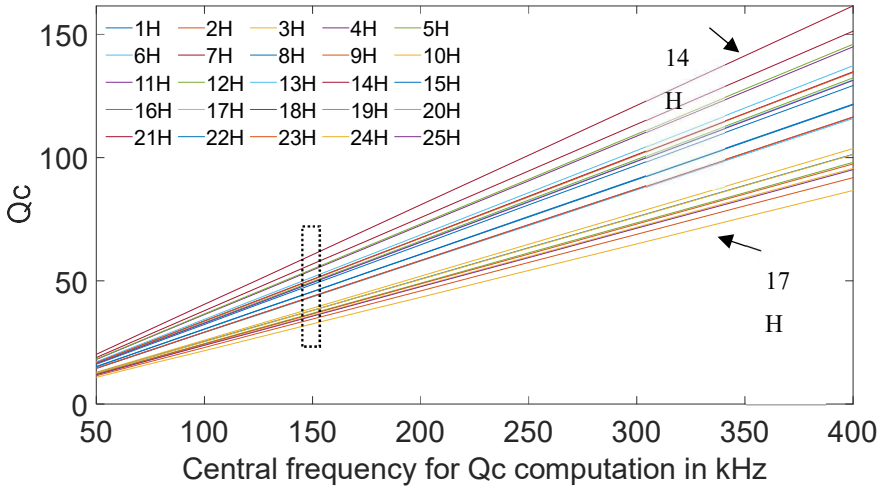

Figure A8. 3. Qc vs central frequency per sample. The dashed box represents the *Qc* values computed at a central frequency of 150kHz, these are the values used to present the results in the main manuscript.

Appendix B

Supplementary Material for "Pore space topology controls ultrasonic waveforms in dry volcanic rocks"

B1. Parameters for modelling in SPECFEM2D

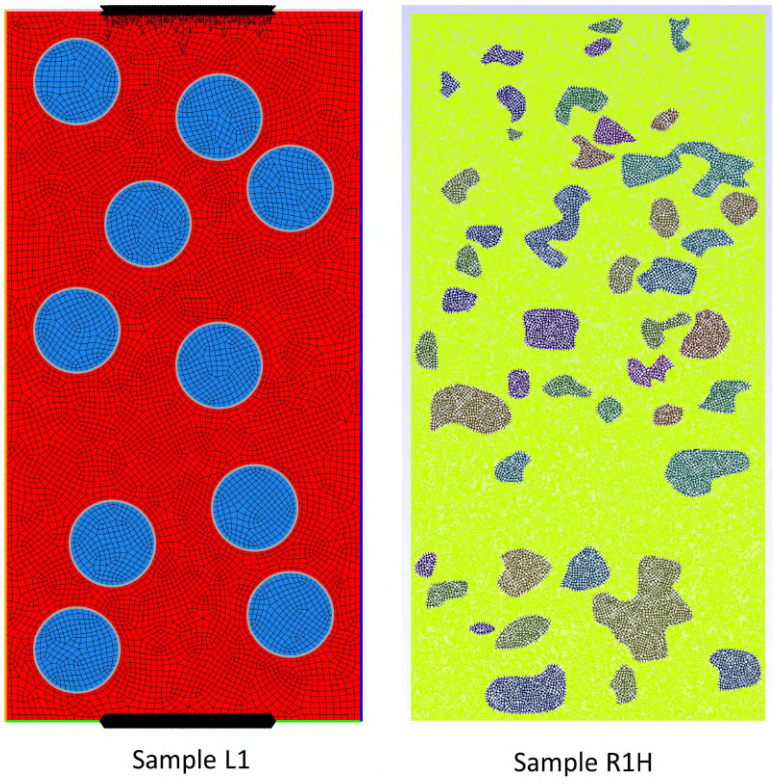

Figure B1. 1. Mesh for synthetic rock samples L1 and R1H

Table B1. 1. Input Parameters for the simulations.

Input Parameter	**Synthetic rocks**	**R1H**
Simulation	Forward	Forward
Partitioning method	Scotch	Scotch
Control nodes per element	4	9
Number of steps NSTEP	100,000	800,000
Time step DT	4.0 e-09 s	0.38 e-09 s
Time Stepping	Newmark (2^{nd})	Newmark (2^{nd})
Wave Type	SH	SH
Boundary Conditions*	Stacey, absorbing boundary	Stacey, absorbing boundary
Models	2	2
Model 1 (rock matrix)	ρ= 2940 kg/cc Vp= 2860 m/s Vs= 1490 m/s	ρ= 2940 kg/cc Vp= 2860 m/s Vs= 1490 m/s
Model 2 (pores)	ρ= 1020 kg/cc Vp= 330 m/s Vs= 0 m/s	ρ= 1020 kg/cc Vp= 330 m/s Vs= 0 m/s
Source	Ricker	Ricker
Dominant Source Frequency	100 kHz	100 kHz
Source Amplification Factor	1.0d10	1.0d10
Receiver seismo-type	Displacement	Displacement

*Note that PML boundary conditions are not implemented in SPECFEM2D for SH propagation.

Table B1. 2. Parameters for the mesh creation using GMSH (http://gmsh.info/)

Setting up mesh	**Synthetic**	**R1H**
Total Number of Elements	8,945	136,854
Total number of nodes	8,794	164,534
Number of grid points in the mesh	141,617	2,026,108
Absorbing boundaries	Top, left, bottom, right	Top, left, bottom, right
Free Boundaries	none	none
Elements in contact with absorbing surface	304	1504
Xmin / Xmax	0.0 / 2.5e-2	0.0 / 2.5e-2
Zmin / Zmax	0.0 / 5.0e-5	0.0 / 5.0e-5
Max grid size	9.618 e-4	2.129 e-4
Min grid size	1.129 e-4	1.299 e-5
Max/min ratio	8.519	16.379
Minimum GLL point distance	1.949 e-5	2.245 e-6
Average GLL point distance	2.822 e-5	3.249 e-6

B2. Case-C: Testing near-field influence on the sensors .

Here we present simulations representative of Case-1 (assessing the role of the location of the pores). However, we decided to design samples in which the pores were located at least λ/2 away from the sensors, to discard the effect of the vicinity of the pores to the receiver and source. The correlation coefficients for Case-C show a very strong agreement between the waveforms (Table B2.1). The observations are the same for both scenarios: In samples of the same porosity, with the same number of pores, of the same size and geometry, but in different locations, the correlation between the waveforms is strong (>0.90). Therefore, when the other parameters are constant, the location of the pores has the lowest impact on the S-wave propagation.

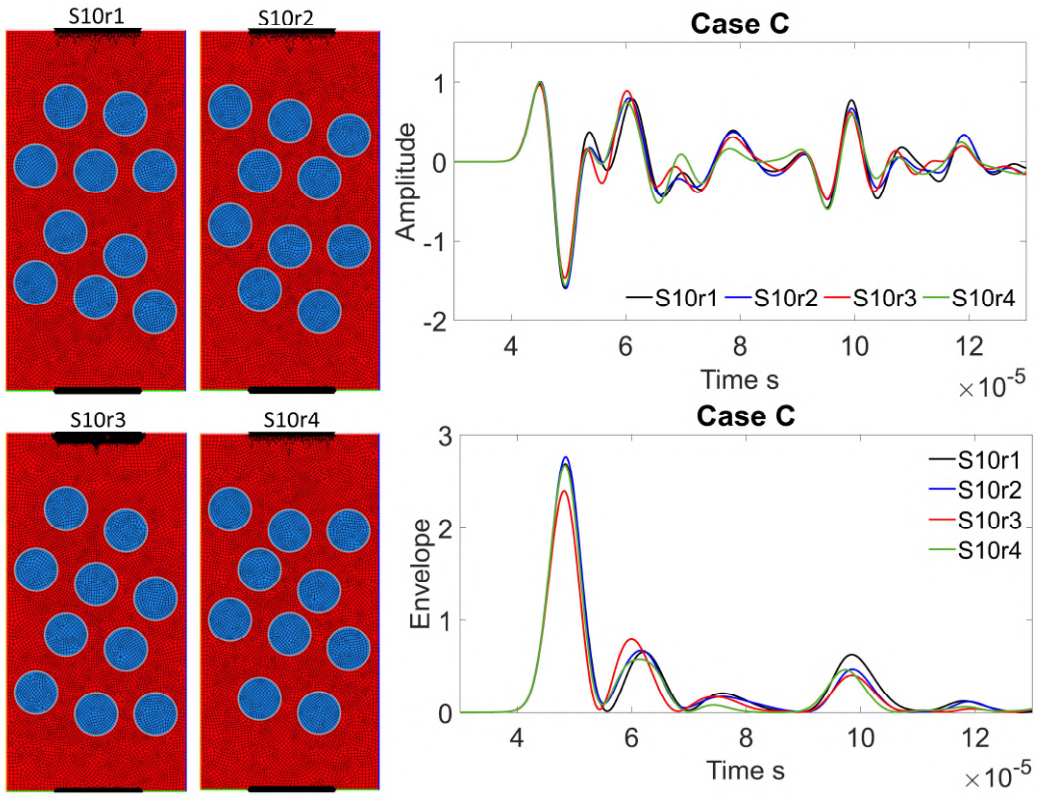

Figure B2. 1. Case-C Similar to Figure 1 for Case-1. Here the location of the pores between samples was changed systematically and kept at least 1/2λ from source and receiver to remove their near-field influence on the sensors.

Table B2.1. Correlation coefficients for Case-C

	S10	S10r1	S10r2	S10r3
S10	1	0.9731	0.9497	0.9423
S10r1	0.9731	1	0.9649	0.9552
S10r2	0.9497	0.9649	1	0.9523
S10r3	0.9423	0.9552	0.9523	1

B3. Creation of synthetic sample R45p

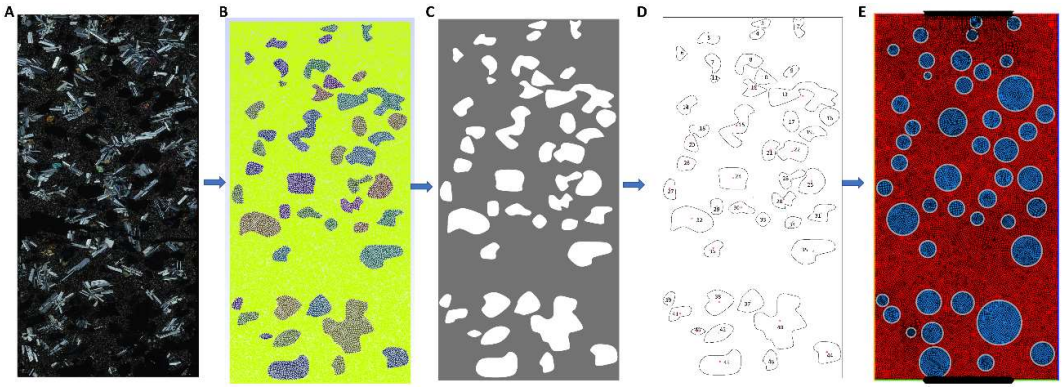

We used a light microscope image of sample 1H (A) to manually create a mesh (in Gmesh) with a representation of the largest 45 pores (B: sample R1H). A segmented image (C) was generated (in ImageJ) and measurements of each pore were computed (D, values in table below). The area fraction was converted to mm^2; then we estimated the ratio of a sphere that occupies that area ($a=\pi R^2$) to be used in the mesh of sample R45p (E). The waveform for R45p was computed using 300,000-time steps with a duration of 1 ns each.

#	area px	perimeter	circ	AR	Round	Solidity	Area %	Area mm^2	Ratio mm
2	3352	281.91	0.53	1.88	0.53	0.81	0.23	2.75	0.94
3	2548	223.24	0.64	2.26	0.44	0.96	0.18	2.09	0.82
4	2344	191.72	0.80	1.80	0.56	0.97	0.16	1.92	0.78
5	3880	283.28	0.61	2.19	0.46	0.86	0.27	3.18	1.01
6	2238	192.45	0.76	1.38	0.72	0.93	0.15	1.84	0.76
7	4253	270.88	0.73	1.58	0.64	0.90	0.29	3.49	1.05
8	7413	411.79	0.55	1.82	0.55	0.83	0.51	6.08	1.39
9	2697	210.84	0.76	1.86	0.54	0.96	0.19	2.21	0.84

10	4958	302.64	0.68	1.54	0.65	0.96	0.34	4.07	1.14
11	1040	130.13	0.77	1.32	0.76	0.95	0.07	0.85	0.52
12	5209	358.13	0.51	1.32	0.76	0.80	0.36	4.27	1.17
13	22730	1046.43	0.26	3.00	0.33	0.66	1.57	18.65	2.44
14	5266	296.58	0.75	1.71	0.58	0.93	0.36	4.32	1.17
15	14374	710.71	0.36	2.34	0.43	0.73	0.99	11.79	1.94
16	5936	291.71	0.88	1.13	0.88	0.98	0.41	4.87	1.25
17	5863	293.32	0.86	1.37	0.73	0.98	0.41	4.81	1.24
18	4149	259.48	0.77	1.66	0.60	0.95	0.29	3.40	1.04
19	5745	335.26	0.64	2.09	0.48	0.89	0.40	4.71	1.22
20	3960	249.62	0.80	1.36	0.73	0.98	0.27	3.25	1.02
21	5435	298.74	0.77	1.58	0.64	0.93	0.38	4.46	1.19
22	10448	426.38	0.72	1.56	0.64	0.92	0.72	8.57	1.65
23	4683	266.21	0.83	1.32	0.76	0.97	0.32	3.84	1.11
24	12577	438.45	0.82	1.30	0.77	0.98	0.87	10.32	1.81
25	10855	409.30	0.81	1.30	0.77	0.96	0.75	8.91	1.68
26	5597	385.06	0.47	2.12	0.47	0.77	0.39	4.59	1.21
27	4470	271.14	0.76	1.69	0.59	0.98	0.31	3.67	1.08
28	5787	375.40	0.52	1.66	0.60	0.80	0.40	4.75	1.23
29	3652	230.13	0.87	1.31	0.76	0.98	0.25	3.00	0.98
30	4835	310.64	0.63	2.26	0.44	0.92	0.33	3.97	1.12
31	6667	373.81	0.60	1.64	0.61	0.86	0.46	5.47	1.32
32	18240	581.63	0.68	1.83	0.55	0.91	1.26	14.96	2.18
33	3169	211.91	0.89	1.00	1.00	0.97	0.22	2.60	0.91
34	3432	227.10	0.84	1.46	0.69	0.98	0.24	2.82	0.95
35	16720	559.10	0.67	1.94	0.52	0.93	1.16	13.72	2.09

36	5020	284.84	0.78	1.45	0.69	0.94	0.35	4.12	1.14
37	9212	378.96	0.81	1.24	0.81	0.97	0.64	7.56	1.55
38	11195	426.70	0.77	1.21	0.82	0.95	0.77	9.18	1.71
39	2669	199.48	0.84	1.38	0.73	0.97	0.18	2.19	0.83
40	35467	941.09	0.50	1.26	0.79	0.79	2.45	29.10	3.04
41	5007	304.31	0.68	2.12	0.47	0.94	0.35	4.11	1.14
42	8198	372.33	0.74	2.00	0.50	0.98	0.57	6.73	1.46
43	1593	167.34	0.72	1.98	0.50	0.96	0.11	1.31	0.64
44	10002	403.36	0.77	1.22	0.82	0.94	0.69	8.21	1.62
45	17533	552.82	0.72	1.98	0.51	0.93	1.21	14.38	2.14
46	4769	275.18	0.79	1.49	0.67	0.95	0.33	3.91	1.12

B4. Comparison with theoretical models.

In this section, we compare the dynamic shear modulus (computed from the acquired waveforms) with the effective shear modulus estimated from the Kuster and Toksöz

Kuster and Toksöz (1974) expressions for the effective shear (μ*) moduli:

$$(\mu_{KT}^{*} - \mu_m)\frac{(\mu_m + \vartheta_m)}{(\mu_{KT}^{*} + \vartheta_m)} = \sum_{i=1}^{N} x_i(\mu_i - \mu_m)Q^{mi}$$

Coefficients Q describe the effect of inclusions 'i' of spherical shapes in a background medium 'm'. (Berryman, 1995).

$$Q^{mi} = \frac{\mu_m + \vartheta_m}{\mu_i + \vartheta_m} \qquad \vartheta = \frac{\mu}{6}\frac{(9K+8\mu)}{(K+2\mu)}$$

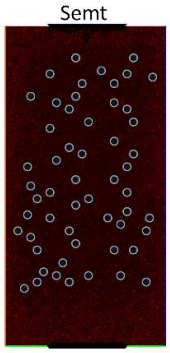

We designed an extra sample (Semt), representative of an effective medium to test the accuracy of the comparisons with the theoretical approximation. This sample has 55 pores of 1.2 mm diameter, which represent 4.97% porosity. The properties for both the matrix and the pores are the same used for the rest of the synthetic samples. Given the small size of the pores, the characteristic length of the elements in the mesh was reduced by 80% and the time step of the simulation was adjusted to 1.0 nanoseconds. Computational limitations restricted us from simulating wave propagation for a sample with 22% porosity that complied with the effective medium theory, this might be assessed in further work.

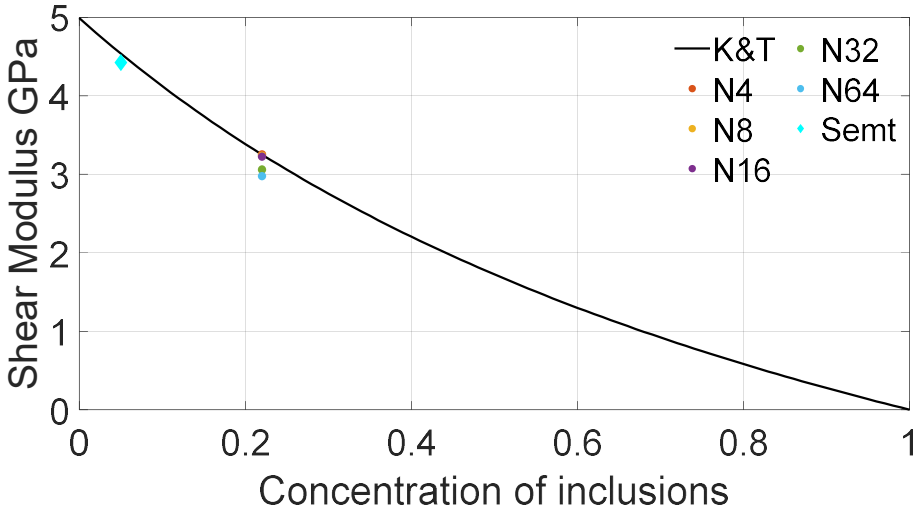

The difference between the theoretical modulus and the one estimated from the simulations for sample Semt is 0.01 GPa for shear modulus (i.e., 0.14% error). While for the synthetic samples the shear modulus diverges between 1.3 and 0.08 GPa with the K&T trend (i.e., 18.8 to 1.15% difference among the samples). These differences are explained by the fact that the samples designed for the simulations done in this study do not comply with the assumptions and limitations of these theories.

B5. Ultrasonic propagation of elastic waves in synthetics samples.

In figures B5.1, B5.2, and B5.3, I present propagation images (in displacement) of the ultrasonic wavefield at different times to observe its interaction with the pore space distribution. The sample geometry is shown at T_0 for all the synthetic samples. Similarly, in the cases presented in figures 3.2 3.3 and 3.4, the porosity value is 22% in all the samples. The closest image to the S-wave arrival time is shown at time step T_10000 (time: $4x10^{-5}$ seconds), while the image at time step T_40000 (time: $8x10^{-5}$ second) is presented to interpret the scattered arrivals in coda waves.

Figure B5.1 is an additional version of Case-3 (i.e., analysis of the effect of the density or number of pores in the waveforms, see section 3.3.3). From time steps T_2000 to T_8000 the displacement field is altered as soon as the wavefield encounters each pore. Then at time step T_10000 the contact with the receiver (i.e., the first break for the S-wave arrival) is different for each sample: in sample nS4 the wavefield has already completely interacted with the receiver, in sample nS10 the first contact is in the centre of the area covered by the receiver, in sample nS20 the first contact is at the middle-right area of the receiver, while in sample nS45 the wave has not arrived yet. These observations explain the different S-wave velocities between the four samples (nS4: 1384.6 m/s, nS10: 1350 m/s, nS20: 1347.9 m/s, and nS45: 1296.8 m/s) despite having the same geometry, composition, porosity and acquisition parameters. The amplitudes of the envelope for the S-wave package between T_10000 and T_20000 are related to the level of dispersion of the wavefield, for example, sample ns45 has amplitudes of two to five times the rest of the samples (nS4: 1.8, nS10: 3.6, nS20: 2.3, and nS45: 10.2). Despite having the maximum number of pores, the regular pattern of the pore arrangement in sample nS45 produce a stable propagation in which the polarity is steady from source to the receiver as observed in the propagation images. On the other hand, this is the reason for the continuous decay of amplitudes in this sample observed in its waveform, while in sample nS10 the scattered arrivals are more heterogeneous, and relatively higher peaks appear on the waveform (see the peak around time step T_40000) at times in which the wavefield homogeneously covers the entire receiver area as observed in the propagation

images. This also justifies the fact that amplitudes of the envelope for sample nS10 are higher than for samples nS20 and nS4 in which the wavefield is more dispersed.

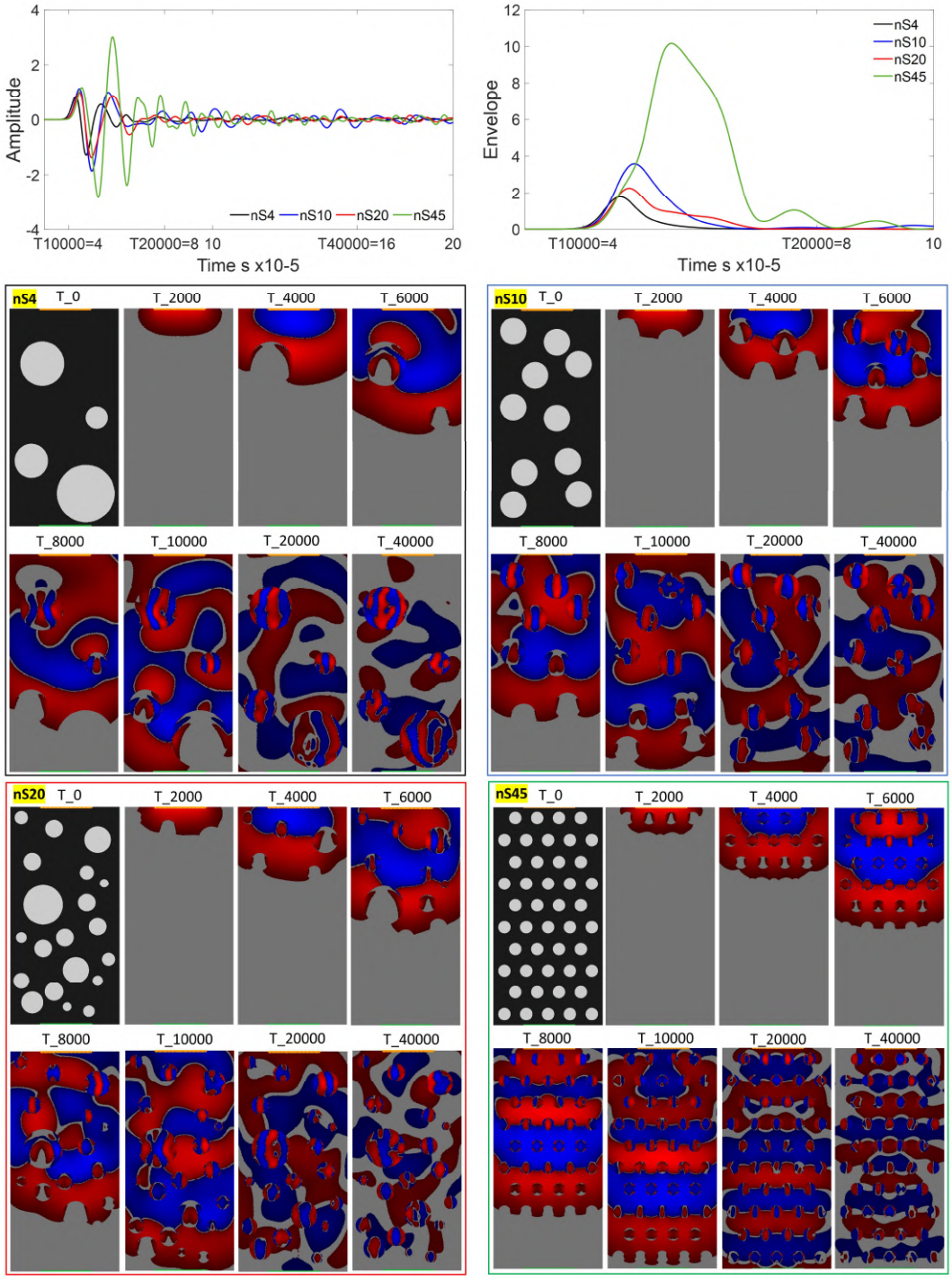

Figure B5. 1. Waveforms, envelopes, and propagation images for 4 synthetic samples in which the number of pores varies between samples. Similar to Case-3: Figure 3.4

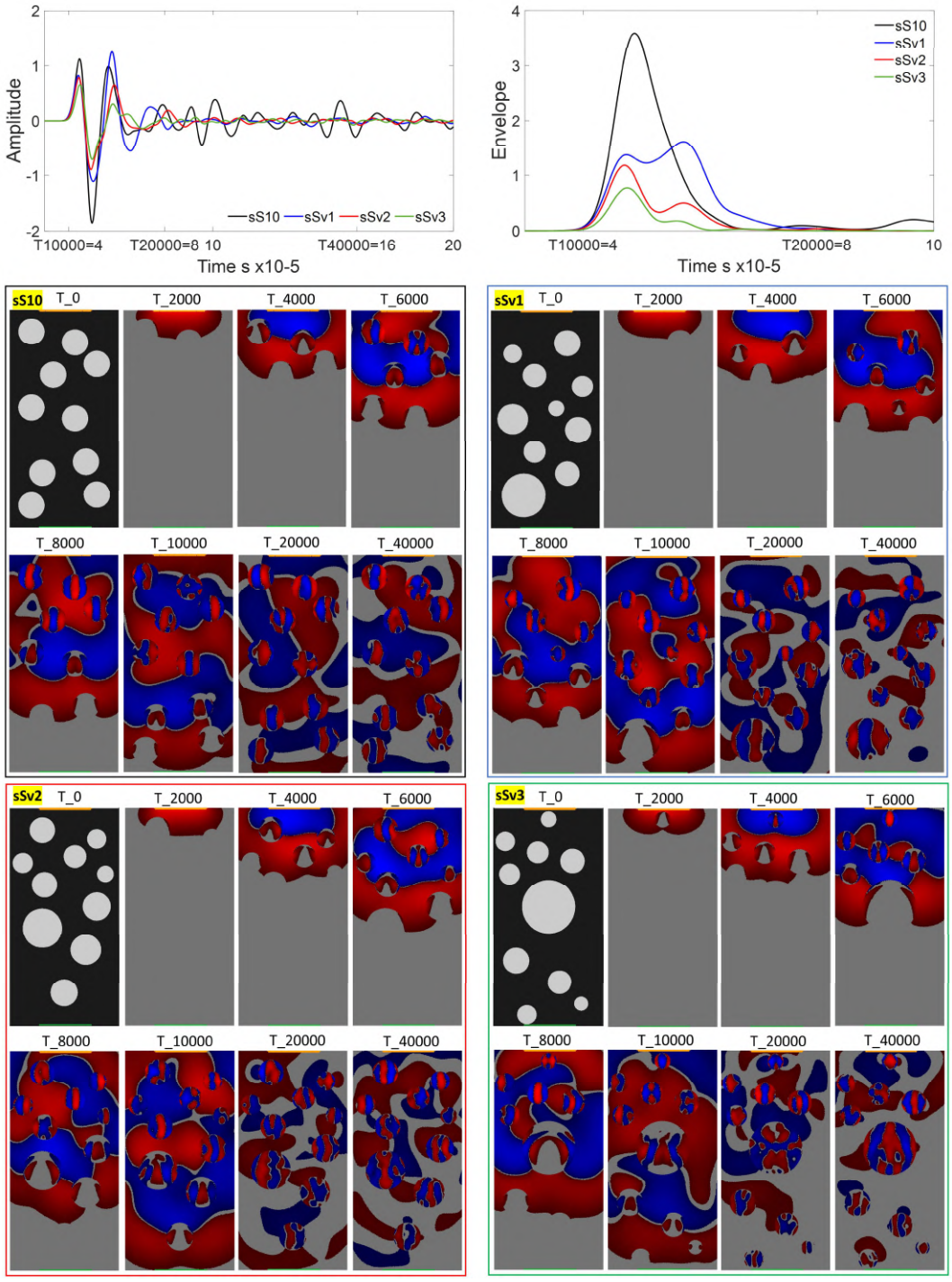

Figure B5. 2. Waveforms, envelopes, and propagation images for 4 synthetic samples in which the size of pores varies between samples. Similar to Case-2: Figure 3.3

Figure B5.2 is an additional version of Case-2 (i.e., analysis of the effect of the size of the pores in the waveforms see section 3.3.2). In figure B5.2, given that the samples have the same number of pores, the propagation of the wavefield from time step T_0 to T_10000 is more similar than in figure B5.1, but the different sizes of the pores between samples still affect both the arrival time and the extent of the first contact with the receiver: in sample sS10 (equal to sample nS10 -figure B5.1) at time step T_10000 there is a small contact of the wavefield with the centre of the receiver zone, while in samples sSv1 and sSv2 the contact covers more area of the receiver zone, whereas sample sSv3 has not arrived yet to the receiver at time step T_10000. As mentioned before, this explains the differences in S-waves velocities between the samples (sS10: 1350 m/s, sSv1: 1359.4 m/s, sSv2: 1359 m/s, and sSv3: 1347.4 m/s). The highest envelope amplitude is obtained when the pores have the same size (sample sS10). If we compare the propagation images between T_10000 and T_20000 for the four samples, the wavefield looks more homogenous in sample sS10 and it gets more dispersed trough samples sSv1 and sSv2 and has the maximum dispersion (visually) in sample sSv3, thence the decreases in the amplitudes of the envelopes from sample sS10 to sample sSv3 (maximum peak amplitude sS10: 3.59, sSv1: 1.6, sSv2: 1.2, sSv3: 0.8). The three samples with different pore sizes (sSv1, sSv2 and sSv3) have a second high peak on the envelope, produce by the redistribution of energy caused by the inhomogeneities in pore sizes. In sample sSv1 the second peak has higher amplitudes than the primary peak (1.6 versus 1.3), probably related to the disposition of the pores in the zone close to the receiver. At later times (time step T_40000) the multiple scattering processes have dispersed the energy in the samples.

Figure B5.3 is an additional version of Case-1 (i.e., analysis of the effect of the location of the pores in the waveforms see section 3.3.1). Here the four samples have the same number of pores of equal size. The differences in the S-wave propagation are a result of the location of the pores in the sample. In the waveforms, we observed a high similarity between the shape of the traces (in comparison with the waveforms of Figures B5.1 and B5.2). By looking at the propagation images between time steps T_2000 and T_10000, it is evident how the location of the pores displaces the ultrasonic wavefield and produces a different arrival time of the first break. At time step T_10000 the propagation images

show that samples sS10 and sSr1 have a similar arrival, hence these samples have the closest S-wave velocity (sS10: 1350 m/s and sSr1: 1353.8 m/s). In sample sSr3 the arrival touches the receiver zone in a larger area, then this sample has the largest velocity (sSr3: 1357.2 m/s), while sample sSr2 has not had contact with the receiver at time step T_10000, therefore this sample has the lower velocity (sSr2: 1345.5 m/s). The S-wave velocities between samples are close but different, therefore the distribution of the pore in the sample is creating a variation in the acquired waveforms despite having the same porosity, number and size of pores. In this case, the amplitude variation in the envelope of the samples (maximum peak amplitude, sS10: 3.59, sSr1: 2.21, sSr2: 1.25, sSr3: 1.44) between time steps T_10000 and T_20000 is a result of the closeness of the pores to the source and receiver. In appendix B2, I presented Case-C, in which the location of the pores has been evaluated by keeping them at ½ λ distance from source and receiver to remove the near-field influence of the sensor. In Case-C the amplitude envelope between the samples is similar (maximum peak amplitude values for the samples are s10r1: 2.69, s10r2: 2.76, s10r3: 2.40, s10r4: 2.67). The coda waves at later times (time step T_40000) follows an alike trend (amplitude and shape) in the waveforms because the redistribution of energy by the scattered arrivals is less disturbed when the heterogeneities have the same dimensions, as explained by the scattering theories. Therefore, given that the number and size of the pores are equal between the samples the scattered wavefield is similar in figure B5.3.

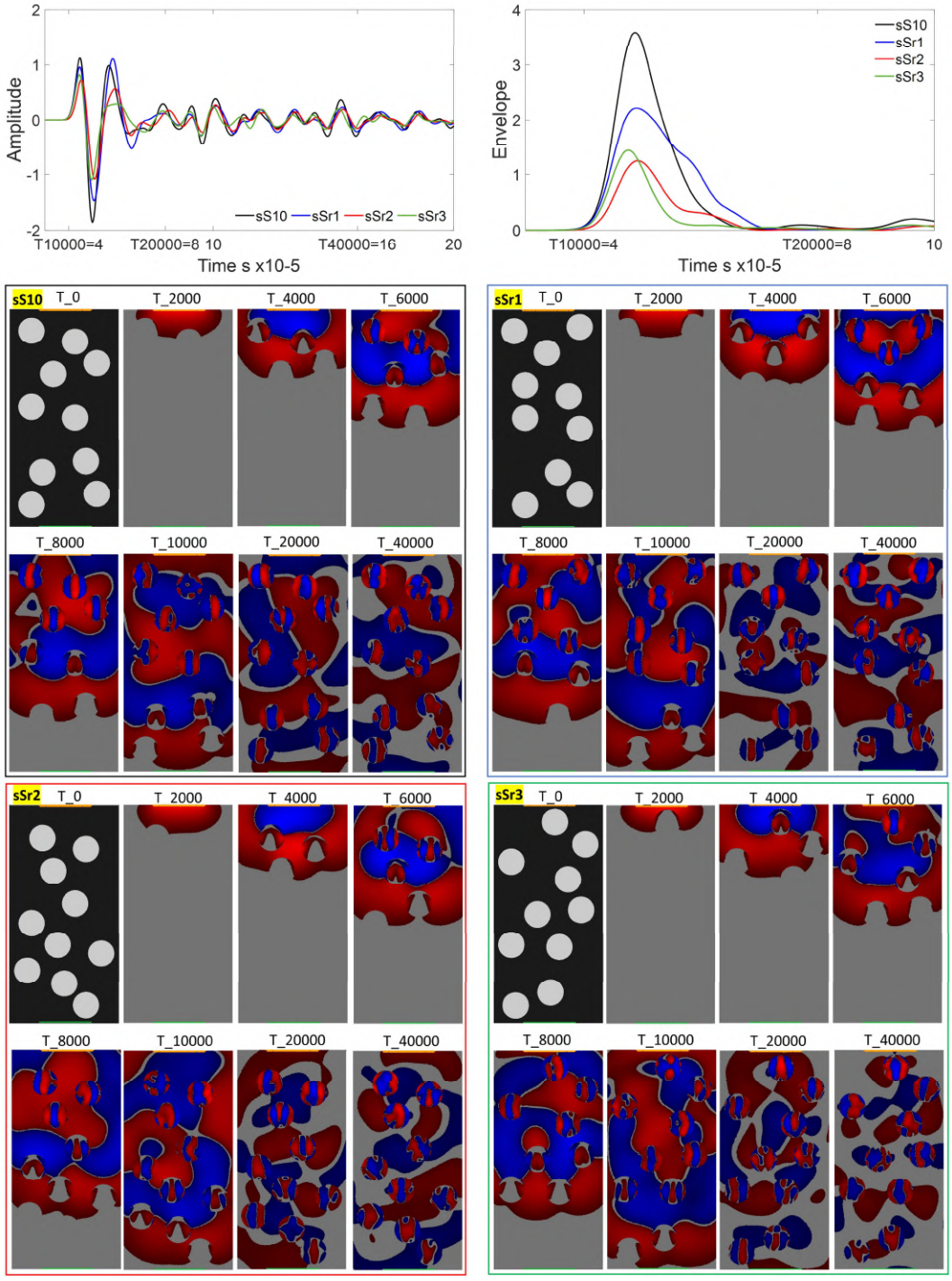

Figure B5. 3. Waveforms, envelopes, and propagation images for 4 synthetic samples in which the location of pores varies between samples. Similar to Case-1: Figure 3.2

Appendix C

Supplemental material for "Reconstructing hydrothermal fluid pathways and storage at the Solfatara crater (Campi Flegrei, Italy) using seismic scattering and absorption"

C1. Survey: source and stations

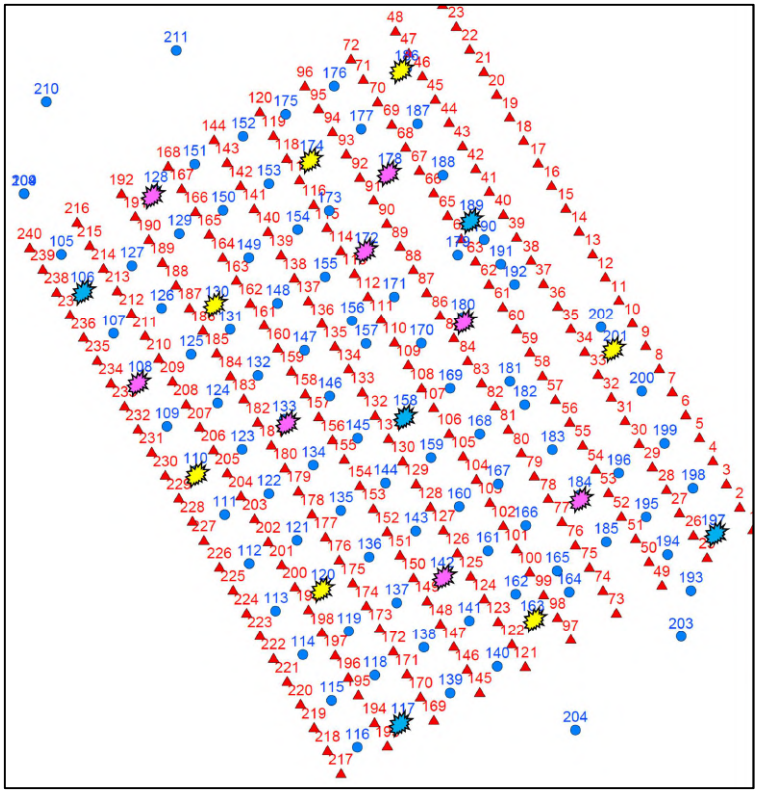

Figure C1. 1. Location of stations (triangles) and events (circles). The 20 sources used in this study are highlighted with the explosion shapes.

C2. Signal Analysis

Table C2. 1. Inversion controls for each frequency band.

Parameter	**12 Hz**	**18 Hz**	**24 Hz**	**27 Hz**
Frequency Band	8-16 Hz	12-24 Hz	16-32 Hz	18-36 Hz
C/N <3 **Coda to Noise Ratio**	0.3%	0.3% (=2137 seismograms)	0.09%	0.05%
Outside Peak delay limits (0.3 to 5 s)	3.4%	2.6% (=2081 seismograms available for analysis)	2.5%	2.8%
cc< 0.8 **Correlation coefficient for the coda decay method**	37.6%	11.3% (=1895 seismograms available for analysis)	2.9%	1.4%
Damping	0.1	0.07	0.05	0.04

Note: Percentages refers to the data discarded

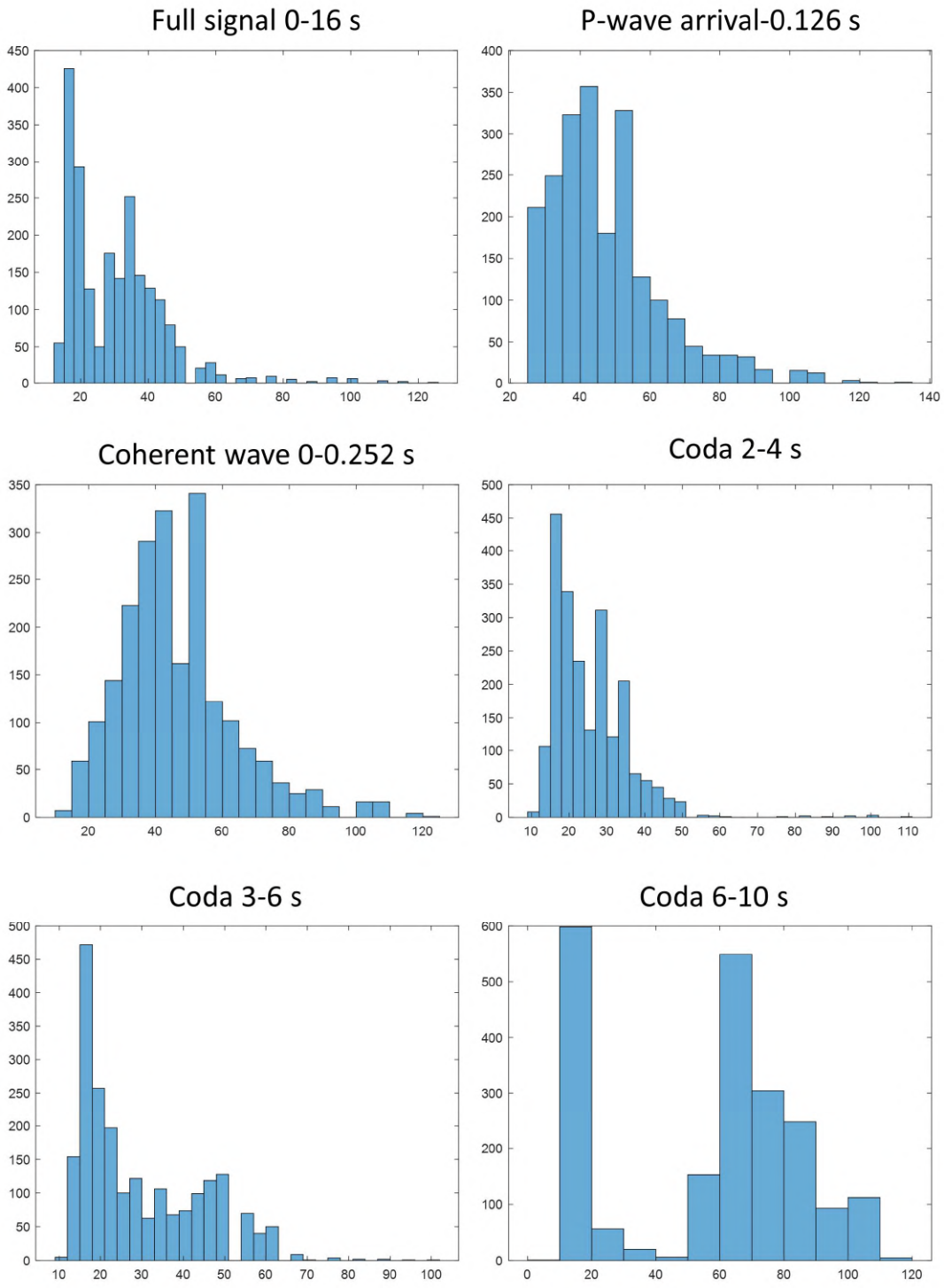

Figure C2. 1. Histogram of maximum frequency in the spectrum of the unfiltered signal at different windows in time.

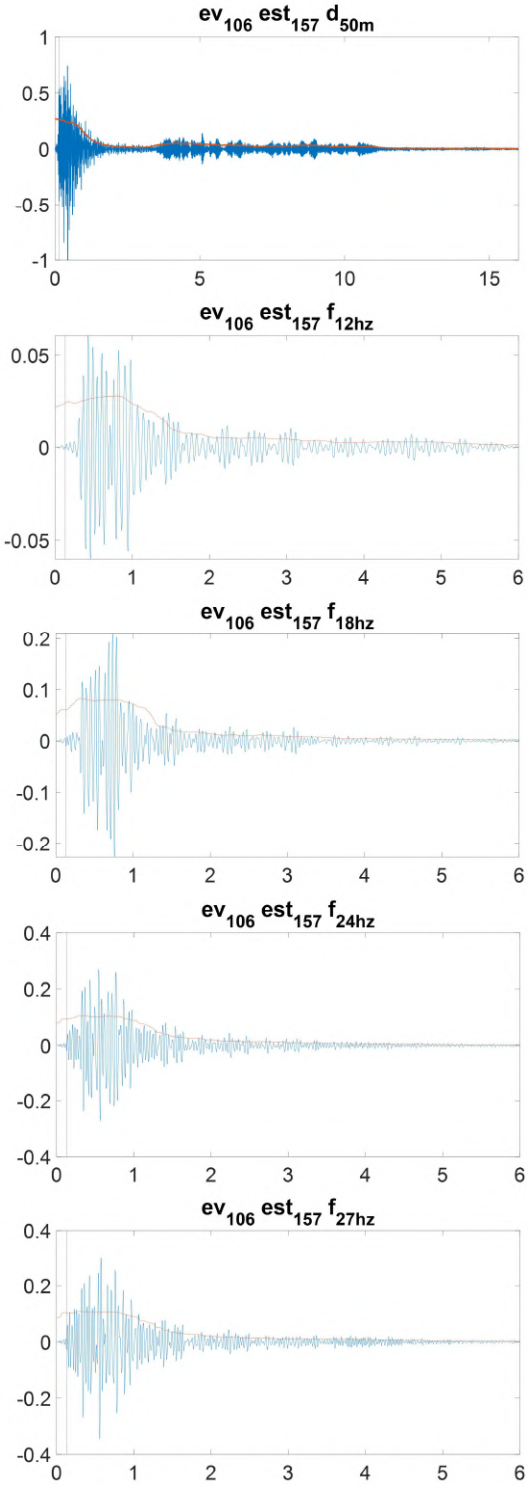

Figure C2. 2. Example of seismic signal for source 106 (figure C1.1) recorded at station 157 located at 50 m. The upper panel is the full signal unfiltered, while the rest are filtered at 12, 18, 24 and 27 Hz from top to bottom.

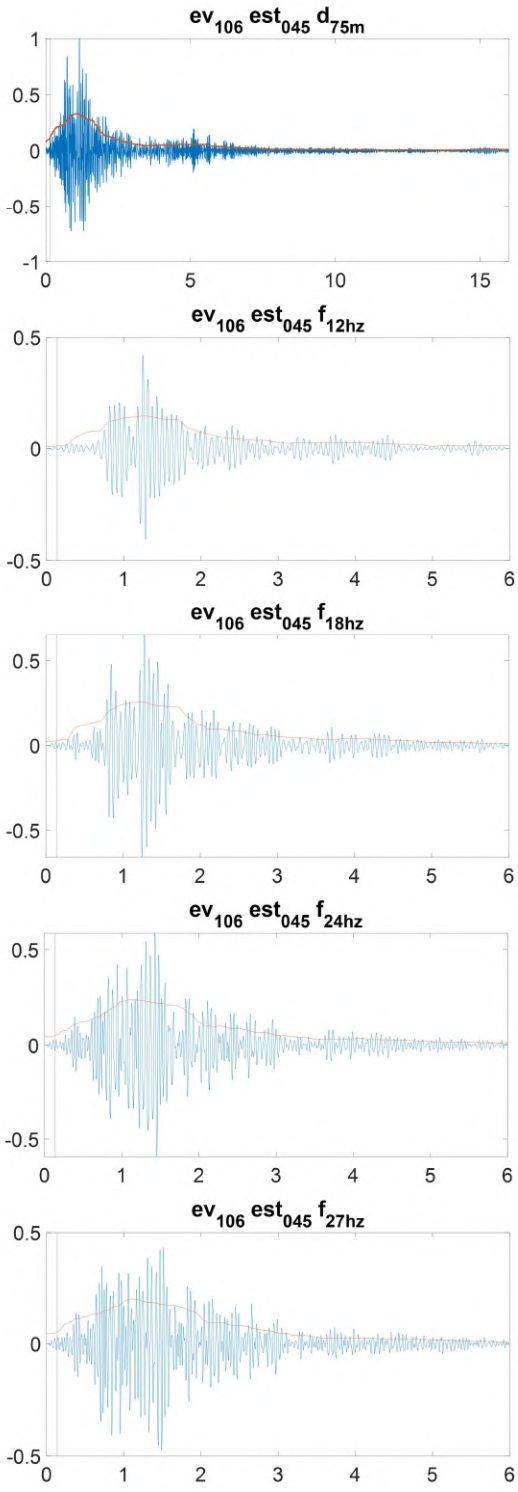

Figure C2. 3. Example of seismic signal for source 106 (figure C1.1) recorded at station 45 located at 75 m. The upper panel is the full signal unfiltered, while the rest are filtered at 12, 18, 24 and 27 Hz from top to bottom.

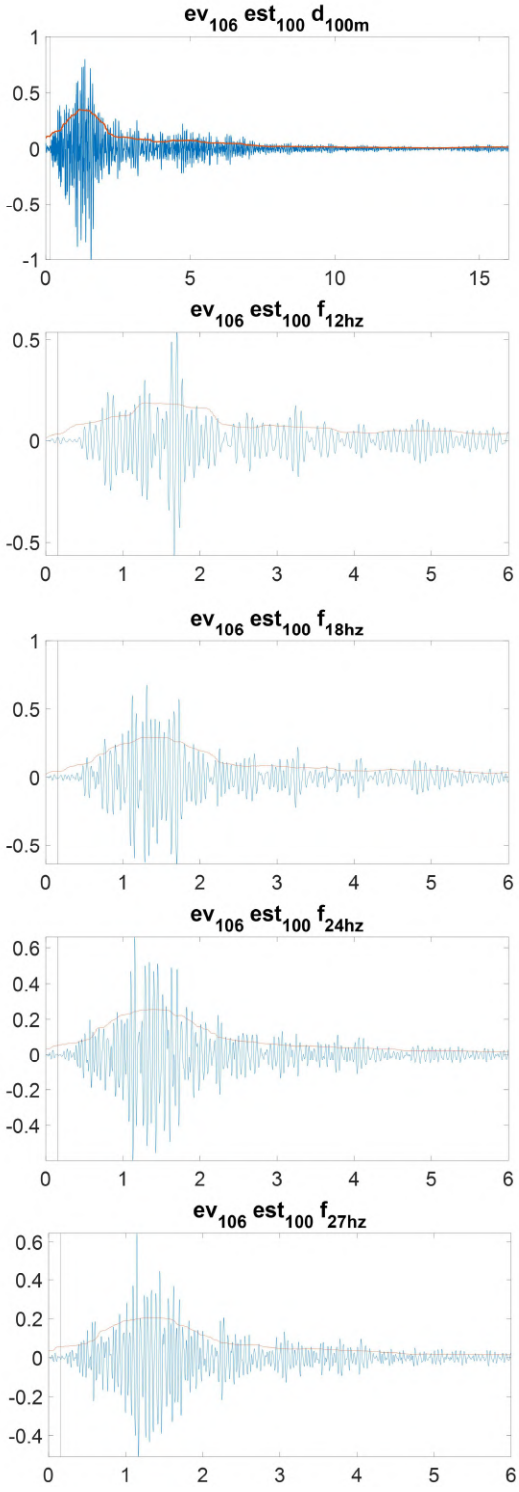

Figure C2. 4. Example of seismic signal for source 106 (figure C1.1) recorded at station 100 located at 100 m. The upper panel is the full signal unfiltered, while the rest are filtered at 12, 18, 24 and 27 Hz from top to bottom.

C3. Stability and resolution of the inversion of Coda Attenuation

Here, we report a mathematical description of the lapse-time-dependent sensitivity kernels for coda attenuation imaging as described by Sketsiou et al., (2020). The energy envelope of the seismogram is defined by Paasschens (1997) using an approximation of the Energy transport equation.

$$E_{i,j}^{3D}[r_{i,j},t] \approx \frac{We^{[-Le^{-1}vt]}}{4\pi r_{i,j}^2 v}\delta\left[t-\frac{r_{i,j}}{v}\right] + WH\left[t-\frac{r_{i,j}}{v}\right]\frac{\left(1-\frac{r_{i,j}^2}{v^2t^2}\right)^{\frac{1}{8}}}{\left(\frac{4\pi vt}{3BoLe^{-1}}\right)^{\frac{3}{2}}}e^{[-Le^{-1}vt]}G[vtBoLe^{-1}\left(1-\frac{r_{i,j}^2}{v^2t^2}\right)^{\frac{3}{4}}]$$

Where $G[s]=e^{s}\sqrt{1+2.026/s}$; δ and H are the Dirac dental and Heaviside step functions; *W* the source energy; *v* the seismic velocity; and *Bo* and Le^{-1} the albedo and extinction length parameters.

Then the 3D kernels are solved by:

$$K_{i,j}^{3D}[\emptyset,t,Bo,Le^{-1},v]=\int_0^T E^{3D}[r_{s\emptyset},\tau,Bo,Le^{-1},v]E^{3D}[r_{\emptyset r},T-\tau,Bo,Le^{-1},v]d\tau$$

Where ∅ is the space point with coordinates {i,j,z}, $r_{s\emptyset}$ and $r_{\emptyset r}$ are the point to source and -receiver distance, respectively. The steps taken to obtain Bo and Le^{-1} follows Wegler (2003):

1. We filter the seismograms in the frequency range 12-36 Hz using a Butterworth bandpass filter;
2. we compute the envelope of the energy signal for each seismogram *W(r,t)*;

3. we choose the analysis window at time *t* with starting point one sample after the S-wave arrival time and a 9 seconds length;

4. we find the least square solution that fits the following equation

$$log\left[t^{\frac{3}{2}}W(r,t)\right] = a_1 + a_2 t + a_3 \frac{1}{t}$$

where a_2=-*b* is the coefficient of intrinsic attenuation; d=-r^2/4*a_3 is the diffusivity, *and* here *r* is the source-receiver distance;

5. we compute the scattering mean free path as *mfp=3*d/Vs ;*

6. we filter the data to satisfy the assumption *mfp* < *r/10*, then we compute the attenuation coefficients n_s=*1/mfp* and n_i=*b/Vs ;*

7. finally, albedo and extinction length are $Bo = \frac{n_s}{(n_i+n_s)}$ and $Le = \frac{1}{(n_i+n_s)}$, respectively.

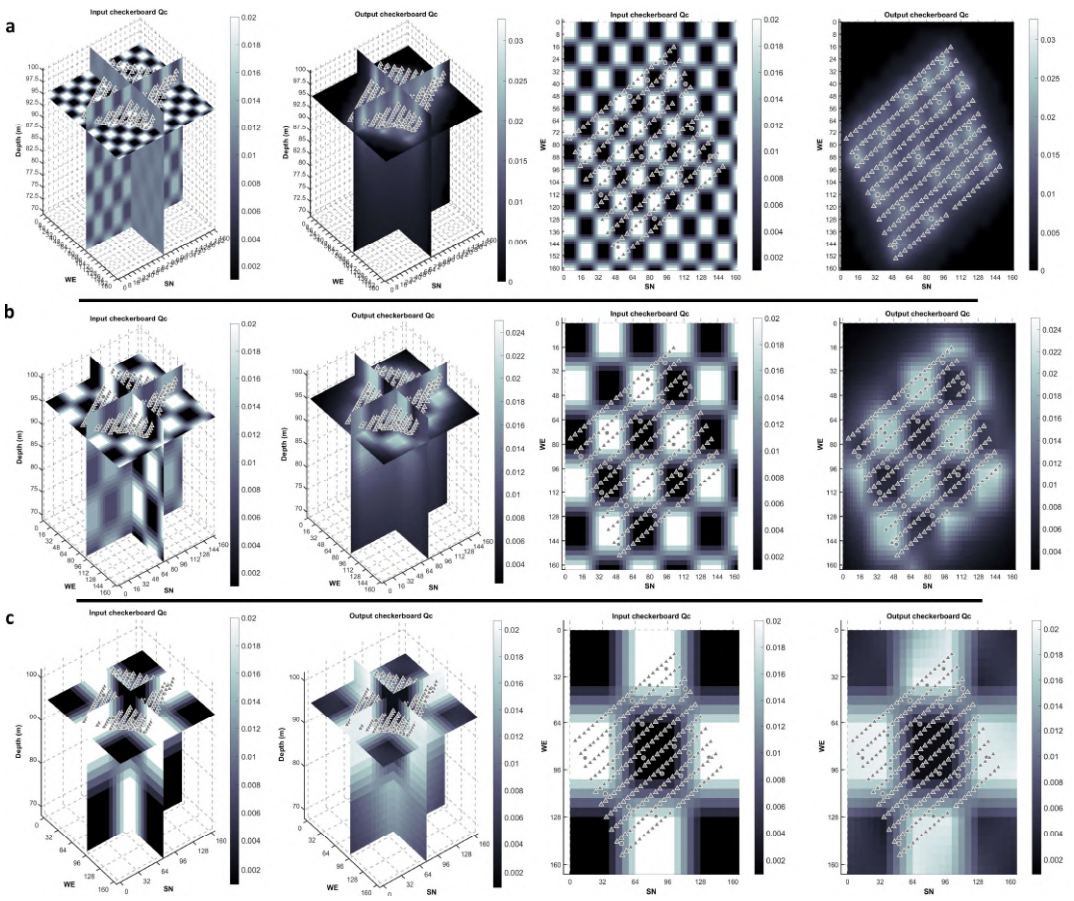

Figure C3. 1. Checkerboard test for the inversion performed at 18 Hz and three different node parameterizations: (a) 21x21x13;(b) 11x11x7; (c) 6x6x4. The results in the manuscript correspond to panel (b). Note that for the parameterization of panel (a) the anomalies are not well reconstructed, while for panel (b) the sign and location of the anomalies are retrieved in the area occupied by the stations; the output of panel (c) is well resolved laterally but does not represent an improvement in the inversion (see Picard plot in Figure C3.2). The depth slices (right panels) are at 95 m. The resolution at depth is only reliable in the first 10 m, below this depth it is not possible to resolve the anomalies because the sensitivity kernels (Figure C3.3) used in this analysis depend on the source-station locations. Given that sources are located at the surface it is not possible to go deeper into the resolution of the coda results.

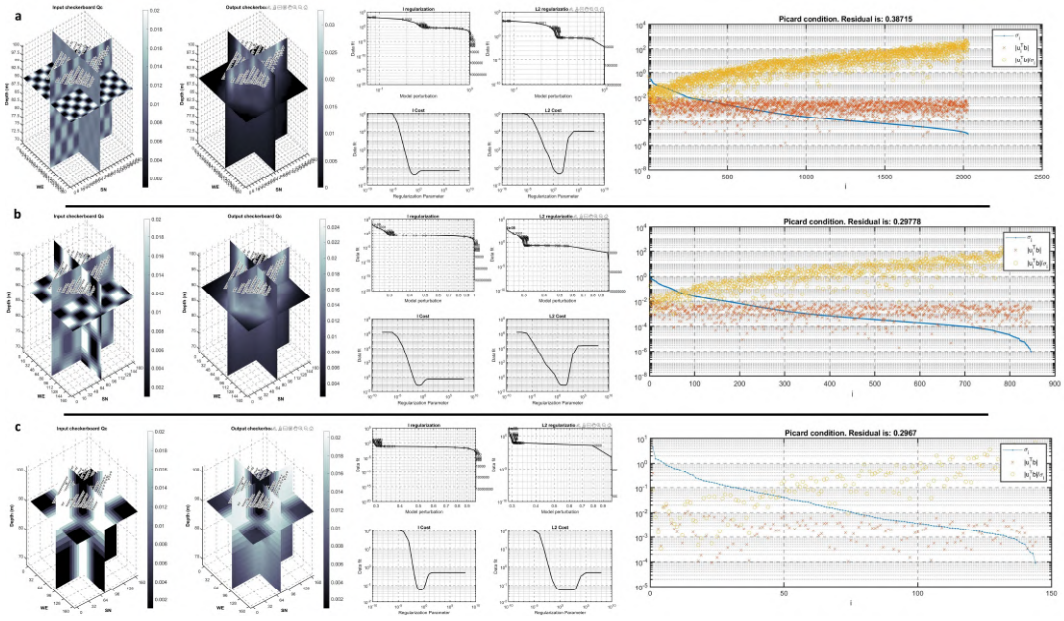

Figure C3. 2. L-curve (left) and Picard plot (right) for inversion performed at 18 Hz for three different nodes parameterizations:(a)21x21x13; (b) 11x11x7;(c) and 6x6x4. The results in the manuscript correspond with panel (b). The chosen damping parameters at each frequency are in Table C2.1.

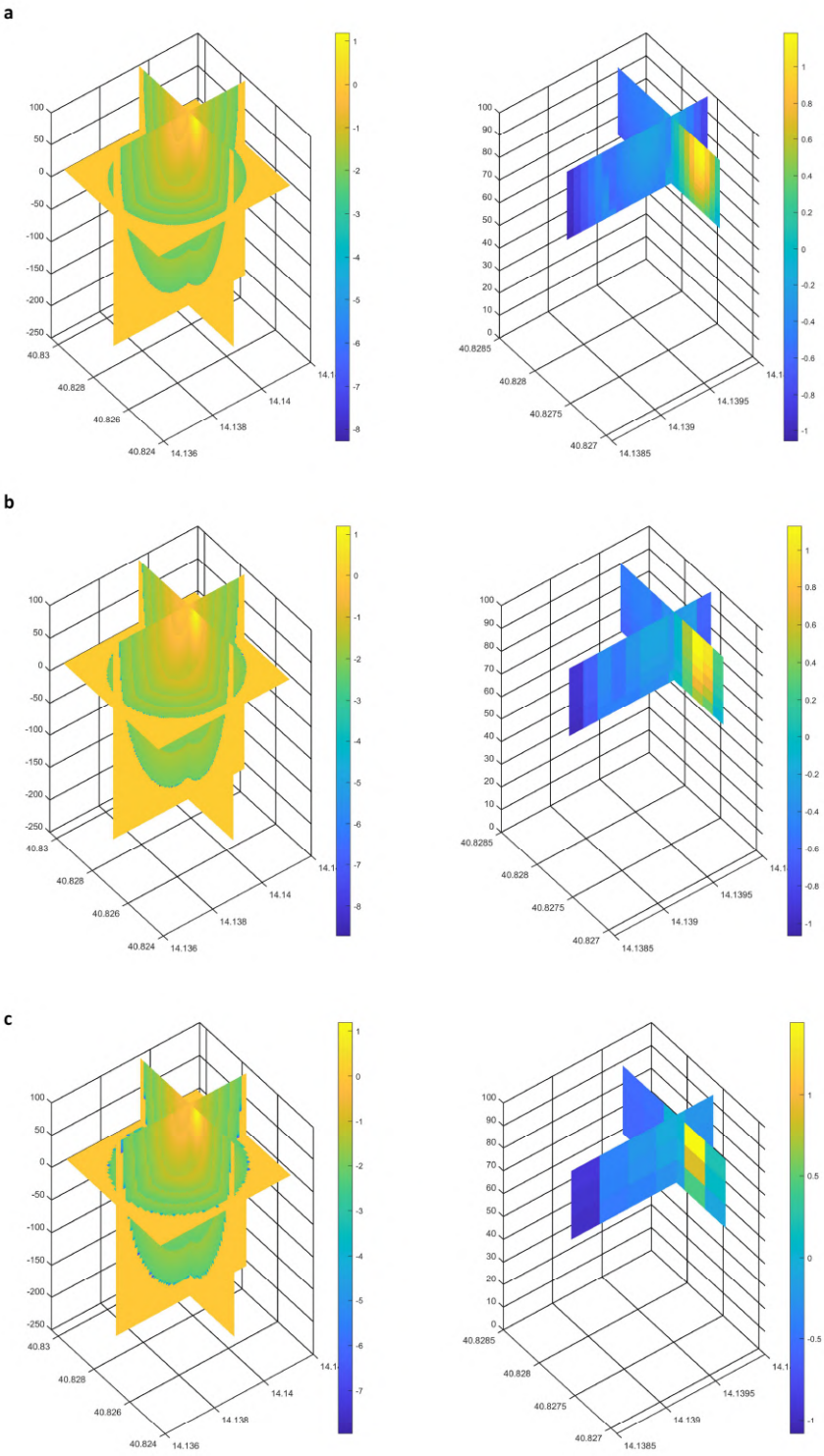

Figure C3. 3. Sensitivity Kernels for the inversion performed at 18 Hz and three different node parameterizations: (a) 21x21x13;(b) 11x11x7; (c) 6x6x4. The results in the manuscript correspond to panel (b).

C4. Previous geophysical studies at Solfatara.

The following figures comprise key previous geophysical surveys that were used to aid the interpretation of the peak delay (Figure 4.6) and Qc maps (Figure 4.7). The survey area is highlighted on each image.

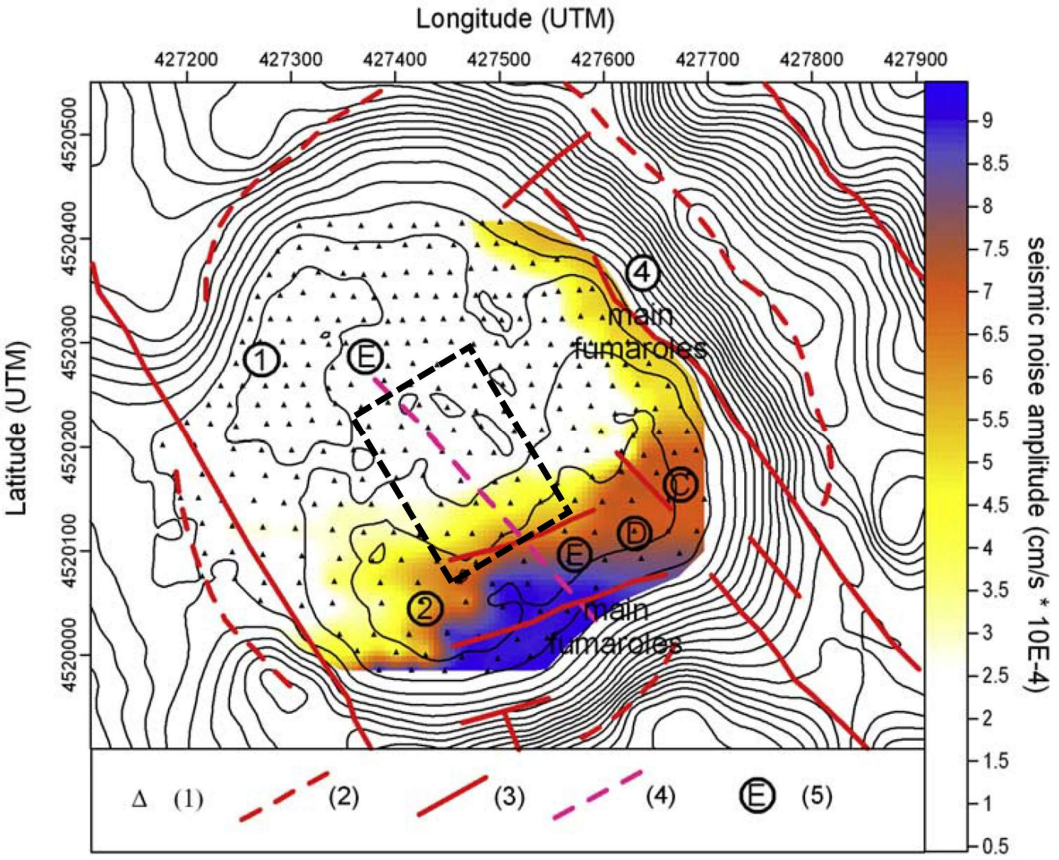

Figure C4. 1. NW-SE striking fault (dashed magenta line) proposed by Bruno et al. (2007), the survey area used for the peak delay maps is superposed (black dashed rectangle). Modified from Figure 8 in Bruno et al. (2007) which full caption reads: *Spatial distribution of the amplitude of seismic noise at Solfatara crater. Symbols: (1), mesh of measuring positions; (2) caldera borders; (3) regional faults; (4), proposed ''E-E'' fault; (5), location of the anomalies discovered by the geophysical surveys.*

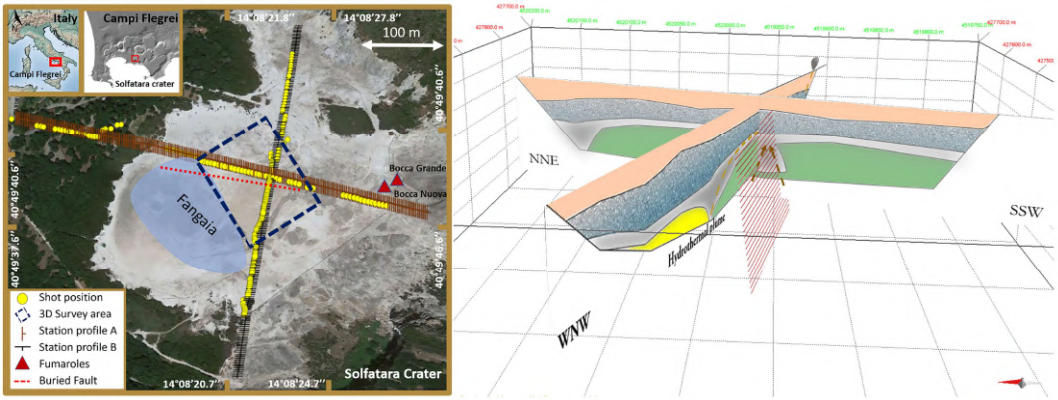

Figure C4. 2. NW-SE striking fault (dashed red line) proposed by Gammaldi et al. (2018); the survey area used for the peak delay maps is superposed (blue dashed rectangle). Modified from figures 1 (left) and 6 (right) in Gammaldi et al 2018, whose full captions read: Fig. 1. *Solfatara crater location and RICEN experiment acquisition layout. In the embedded upper box, we represent the position of the Campi Flegrei caldera respect to Italy on the left side; the shaded relief of the two calderas and crater rims of CFc are on the right side. In the main box the Solfatara crater is shown with the arrays positions, the Fangaia area and the main fumaroles position. The symbol legend is in the lower box*. And Fig. 6. *Multi 2D sketch: Join interpretation of the two models with the fault mapped in Fig. 1 correlated with the fluids contents associated to the deep hydrothermal plume and the shallow gas releasing evidence.*

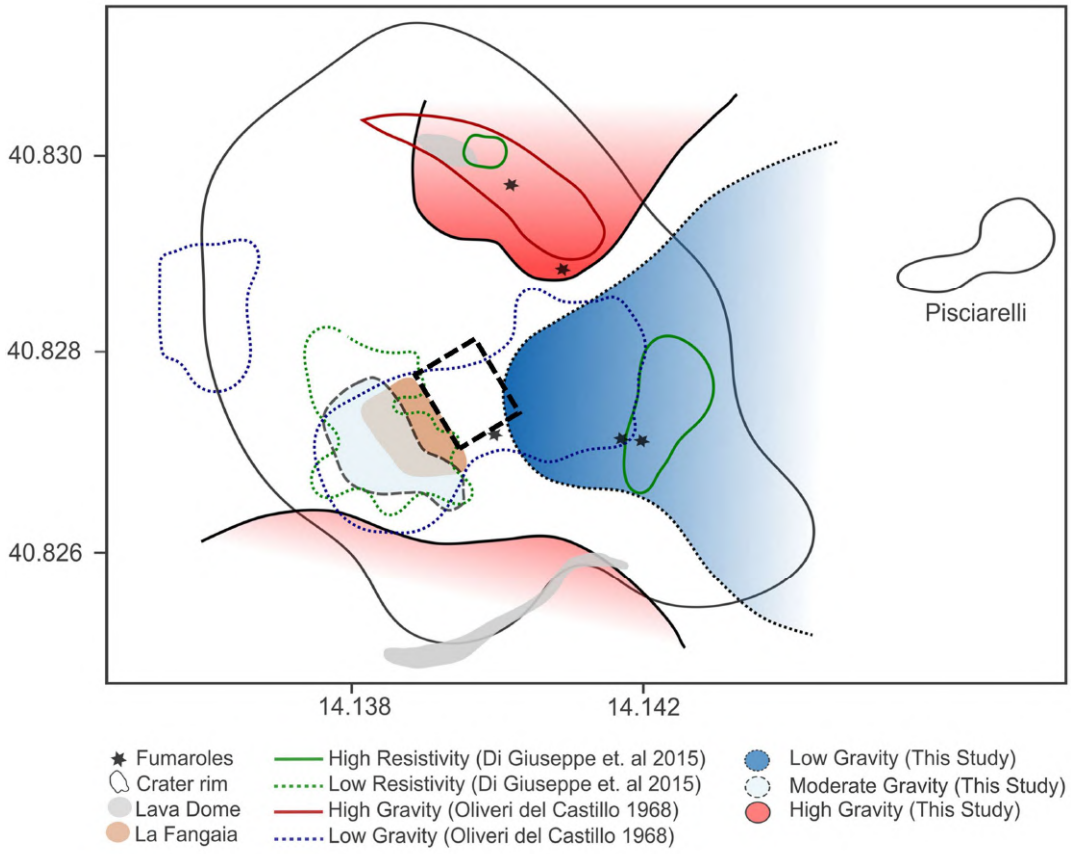

Figure C4. 3. Gravimetric constrains on the Hydrothermal System of the Campi Flegrei Caldera. The survey area used for the peak delay maps is superposed (black dashed rectangle). Modified from figure 9 in Young et al. (2020) which caption reads: *Comparison sketch of previous electrical resistivity (2015) and gravity (1968) anomalies of the Solfatara crater with the LRA data from this study. Dotted lines denote low-amplitude anomalies, dashed lines denote moderately low amplitude anomalies, and solid lines denote high-amplitude anomalies. The crater outline, Pisciarelli, La Fangaia, fumaroles, and lava domes are shown. The color scheme to identiy the LRA gravity anomalies is given in the legend.*

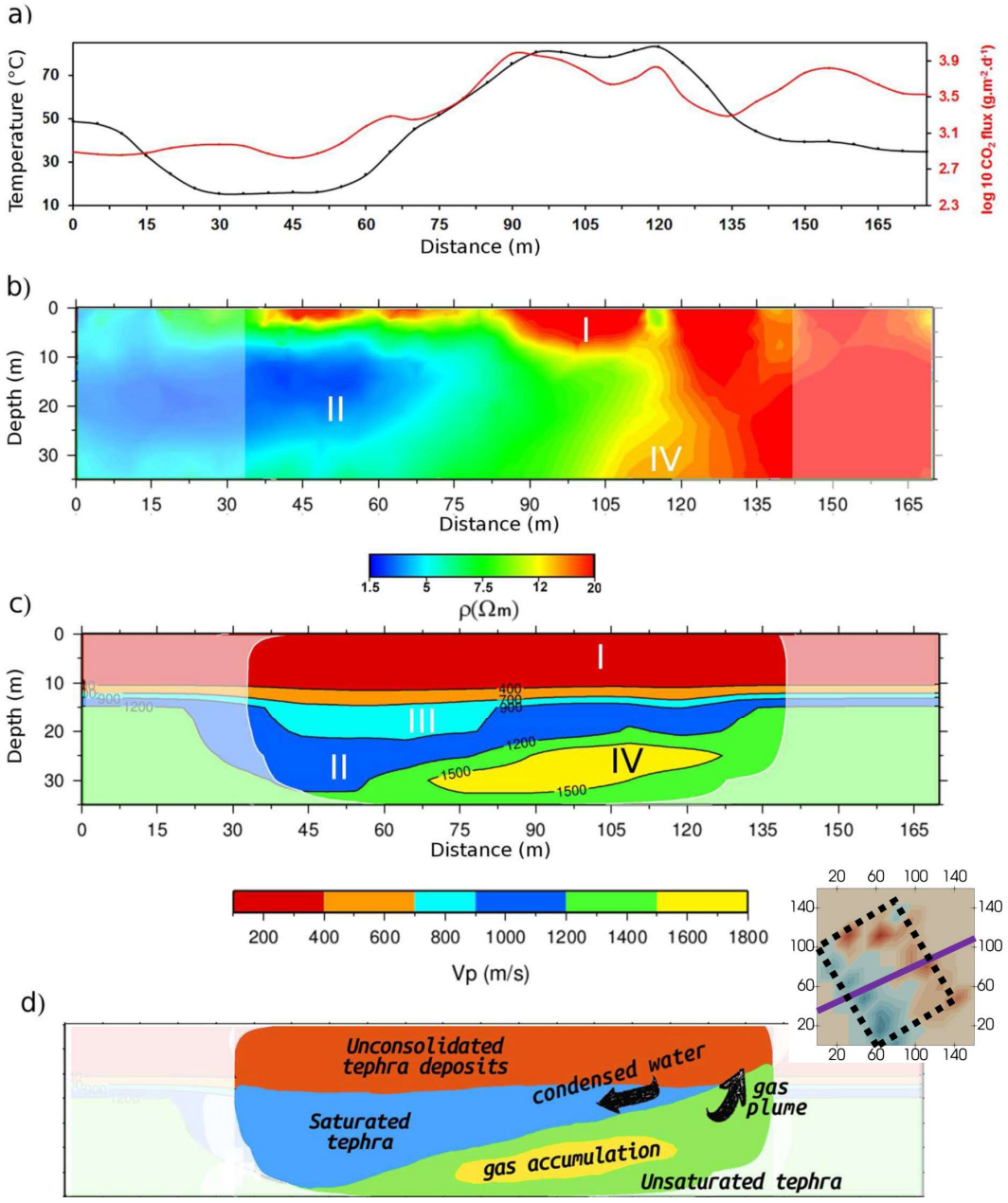

Figure C4. 4. SW-NE migration trend (purple line on peak delay map) from the Fangaia mud pool to the fumaroles, as inferred by De Landro et al. (2017). Modified from figure 4 in De Landro et al. (2017) which full caption reads: *Comparison between temperature (black line) and CO2 flux (red line) in (**a**), resistivity cross section in (**b**) and P-wave velocity model projected onto the cross-section D in Fig. 3a in (**c**). (**d**) Schematic representation of geological features and fluid flux direction, discussed in the interpretation.*

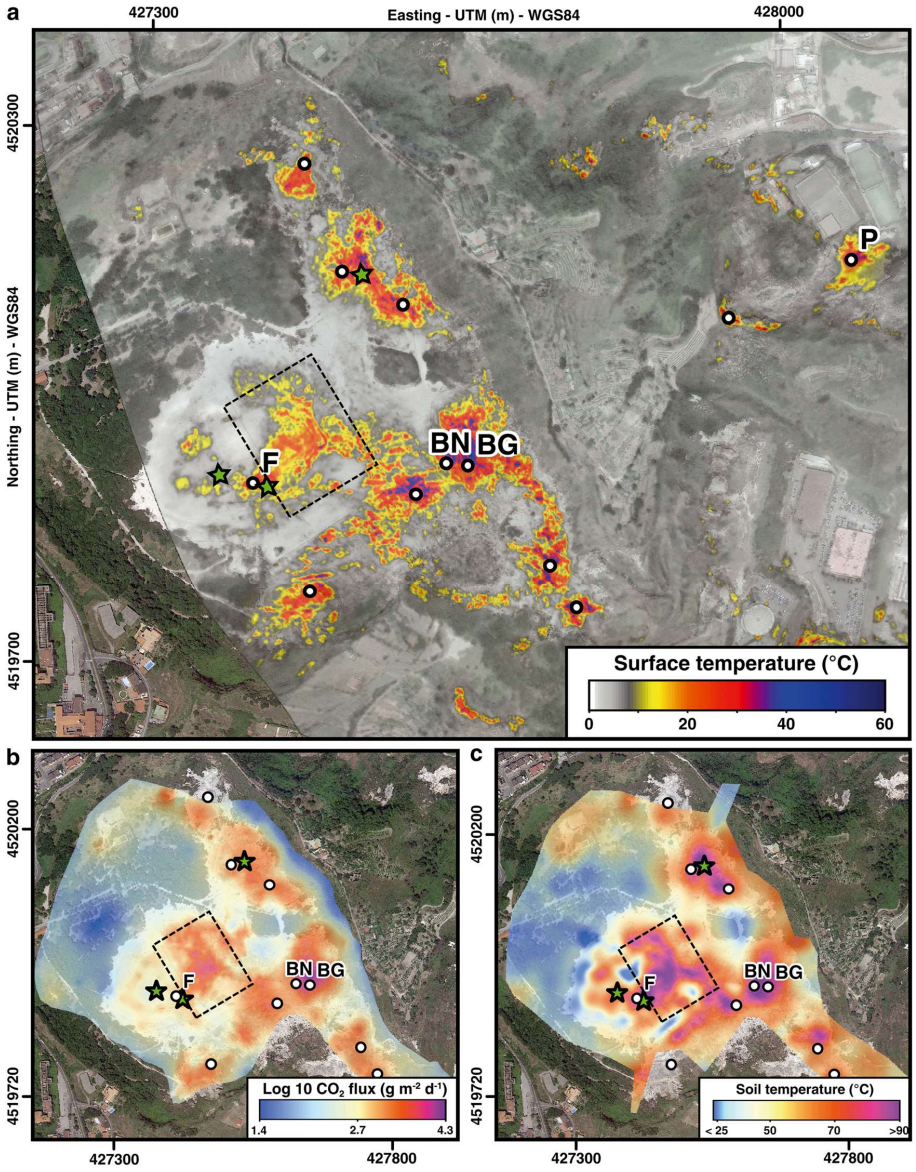

Figure C4. 5. Correlation of high Qc^{-1} anomalies (labelled "*a*" In figure 4.7) with high soil temperature and high CO_2 flux in the diffuse degassing area, as identified in the central part of the crater by Gresse et al. (2017). The survey area used for the coda attenuation maps is superposed (dashed black rectangle) to indicate the survey location. Modified from figure 5 in Gresse et al (2017) which full caption reads: *Solfatara satellite image (2014) draped with (a) surface infrared thermal image (°C), (b) soil CO2 flux (g m−2 d−1), and (c) soil temperature (°C) at 30 cm depth. These values were interpolated using a geostatistical ordinary kriging method (isotropic Gaussian semivariogram model). Main vents are indicated with black circles: Bocca Grande (BG) and Bocca Nuova (BN) fumaroles, and the Fangaia mud pool (F). Location of surface liquid water is represented with green stars.*

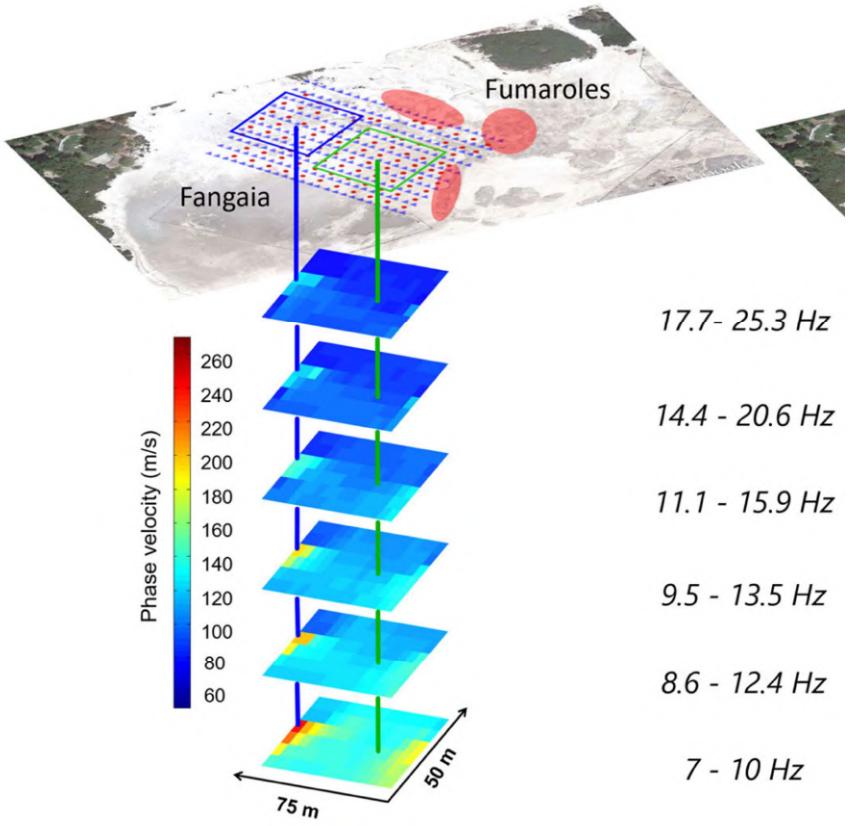

Figure C4. 6. Correlation of the low Qc^{-1} anomaly (labelled "b" in figure 4.7) with the low-frequency and high-velocity body that Serra et al. (2016) derived from the phase-velocity map. Modified from Figure 7 in Serra et al (20116). *Spatial versus frequency representation of phase velocity maps. Different frequency bands classically investigate different depths for surface waves. Colour bars, variation of the phase for the two different subgrids; blue and green squares at the surface, spatial extension of the subgrids; vertical lines (blue and green), centre of the two subgrids and associated to one pixel of the velocity maps. The overall map of the Solfatara is superimposed on the set of sources (red) and receivers (blue), where the location of the Fangaia and fumaroles (red points) is also indicated.*

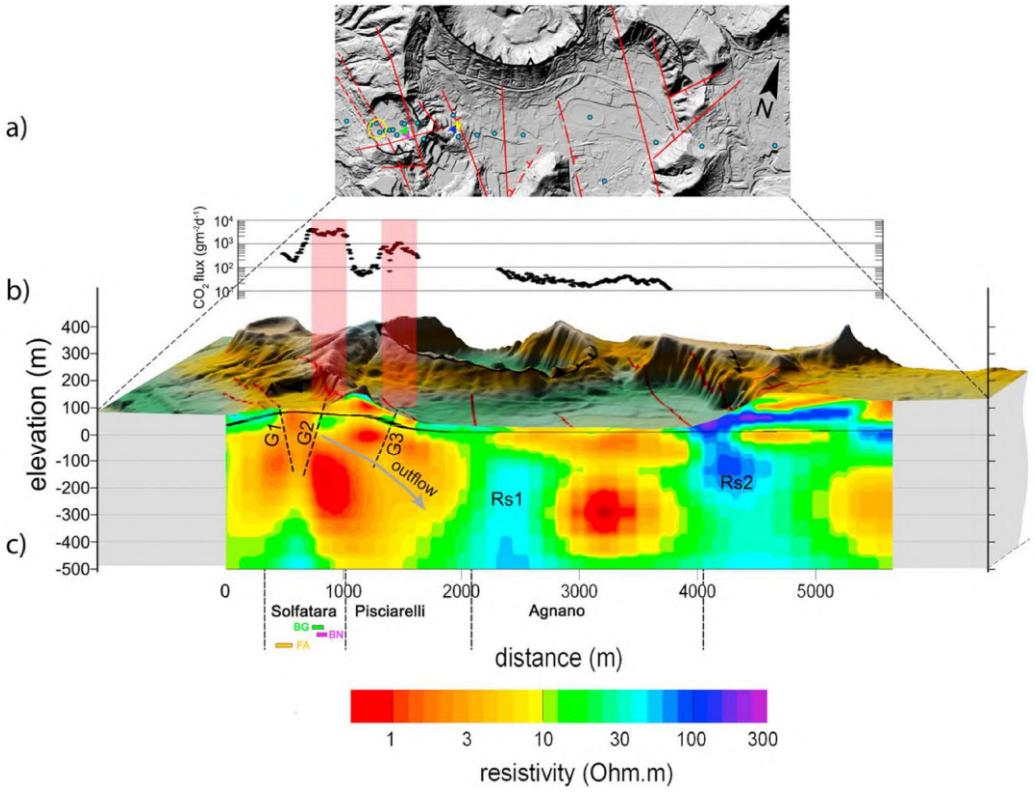

Figure C4. 7. Fluid migrations starting from Solfatara and feeding Pisciarelly. The fault/fracture system breaks near the surface hiding the clay-rich caprock (that seals the interpreted NW-SE fault –Figure 4.6-) on the attenuation parameter map (Figure 4.8) as suggested by Siniscalchi et al. 2019. Here the figure is modified from Figure 9 in Siniscalchi et al. (2019) whose full caption reads: *Comparison between the shallow portion of the resistivity model and independent data. (a) Map of the main caldera structures and faults (redrawn after Isaia et al., 2015; Piochi et al., 2015; Vilardo et al., 2010); red lines represent the faults already reported in Figure 1; green, violet, and blue triangles, respectively, represent the BG, BN, and Pisciarelli fumaroles; yellow circle represents the Fangaia mud pool; the yellow star represents the CF23 borehole. (b) CO_2 flux measured along the AMT profile (red shaded boxes highlight the spatial correspondence between geochemical and resistivity data, marking zones of high CO_2 flux and degassing vents). (c) Shallow resistivity distribution (vertical exaggeration 2:1) and the water table level; the structures reported in Figure 9c are the same shown in Figure 9a. Labels G1–G3 in Figure 9c are gaps in the clay cap due to fracture zones as discussed in the text. Note that Figures 9b and 9c are not in scale with Figure 9a.*

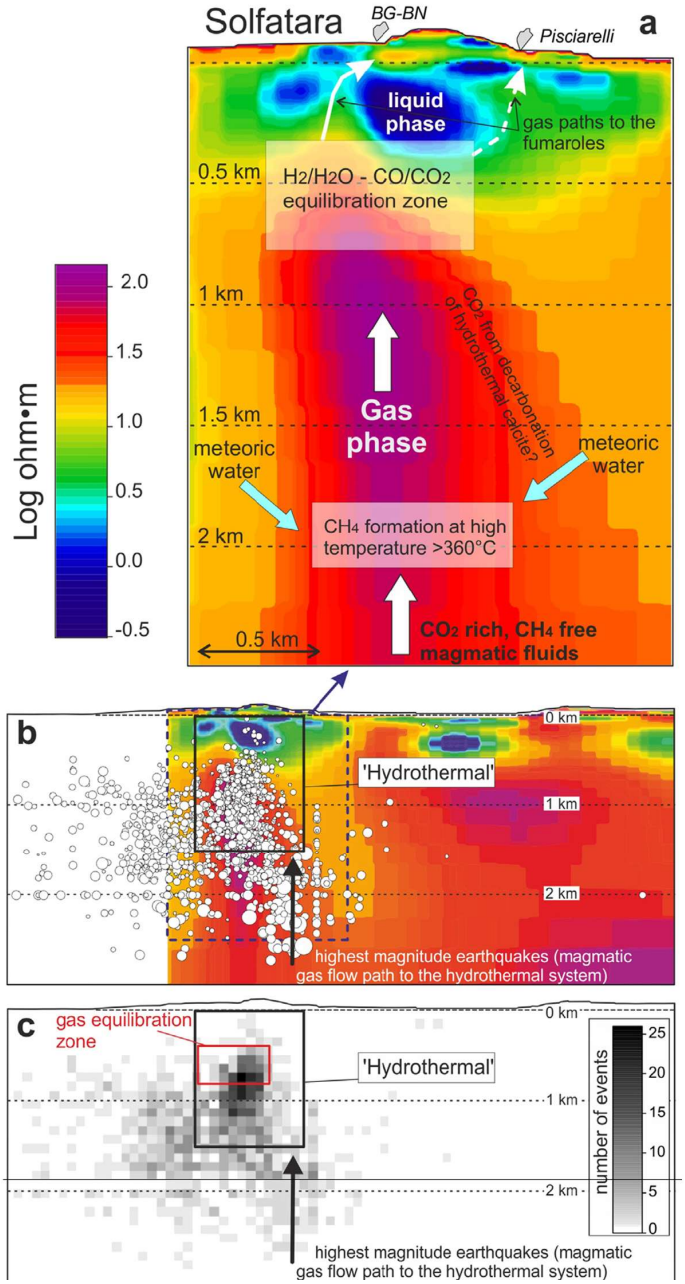

Figure C4. 8. Geochemical release and seismic activity between the Solfatara and Pisciarelli hydrothermal areas. Modified from figure 7 in Chiodini et al (2021) which full caption reads: *Conceptual model and seismicity. a) Geochemical conceptual model of the hydrothermal system feeding the Solfatara-Pisciarelli manifestations sketched over a resistivity section (redrawn from Siniscalchi et al., 2019). b) section (A'-A" in Fig. 1A) showing the relations between earthquake location (distance <0.6 km from the section) and resistivity. The dimension of the white circles is proportional to the magnitude of the events. c) 2 D density map of earthquakes in the A'-A" section (computed as the number of events projected on cells of 100 × 100 m^2). The 'hydrothermal' box is a section of a parallelepiped of 1.2 × 1.2 × 1.5 km assumed to contain the hydrothermal system (see the text and Fig. 9).*

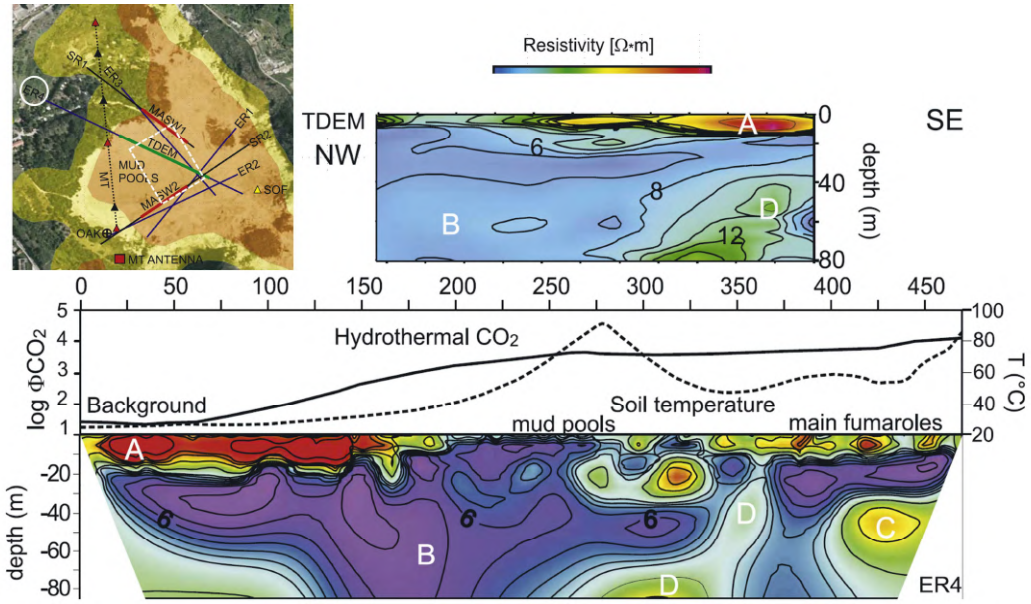

Figure C4. 9. Resistivity profiles (TDEM: transient-domain electromagnetic and ER4: dipole-dipole) crossed the survey area (white dashed rectangle). Modified from figures 1 and 3 in Bruno et al. (2007). The full caption of figure 3 read: *NW-SE striking electrical 'ER4' and TDEM profiles with CO_2 flux [Chiodini et al., 2001] and temperature [Chiodini et al., 2005] patterns plotted along the profile strike. Electrical anomaly "D" dipping to the NW, with ρ of 12–20 Ω m is consistently found along profiles ER4 and TDEM.*

Table 1. Description of the Main Lithological and Stratigraphical Characteristics of the Solfatara Tephra, From Base Upward[a]

	Lithostratigraphic Unit	Lithology	Section 1	Section 3	Section 4	Section 6
Top	Tephra of vent 2	Fine-ash surge beds with minor pumice fallout layers and lenses, and lithic blocks. The beds are undulated to plane-parallel. This deposit is coarser and thicker in the eastern and northern parts of the crater. It thins radially from vent 2 and drapes unconformably parts of the inner walls of crater 1.	Thickness = 0–13 m. The thickness variation is due to pinch-out of the surge sequence against the inner walls of crater 1.	Thickness = 2–14 m. The thickness variation is due to pinch-out of the surge sequence against the inner walls of crater 1 and to partial draping of crater 1 rim.	Thickness = 3 m.	Thickness = 1.7 m.
			Angular Unconformity 2			
	Tephra of vent 1	Coarse- to fine-ash surge beds and minor scattered or aligned coarse pumice fragments and lithic blocks. The beds are massive to plane parallel, and yellowish to green in color. They contain abundant accretionary lapilli. This deposit is exposed along all the inner crater slopes.	Thickness ≥15 m, base not exposed.	Thickness = 7 m.	Thickness = 6 m.	Thickness = 3.9 m.
			Angular Unconformity 1			
Bottom	Basal Breccia	Very coarse breccia deposit with a fine grained ash matrix. It is composed by variably altered lithic fragments (tuff and lava) and scoria bombs. It is exposed along the eastern inner crater walls.	Not exposed	Thickness = 8 m.	Thickness = ca. 2 m.	Thickness ≥4 m, base not exposed.

[a]See the text for discussion. Sections numbers are the same of the structural analysis, reported in Figure 1.

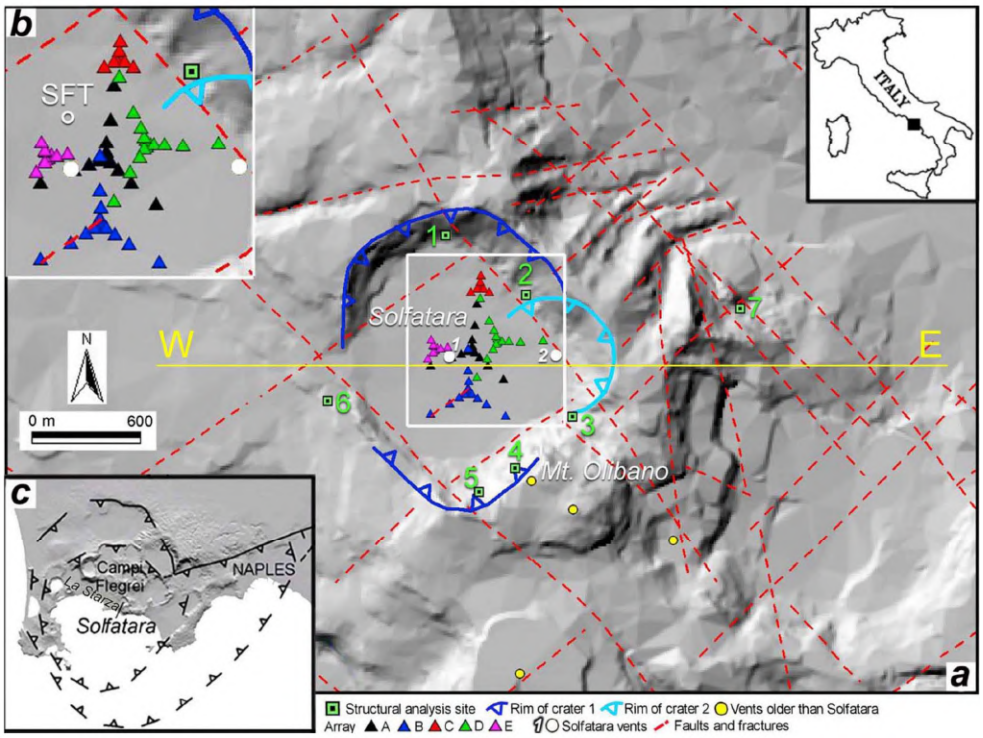

Figure C4. 10. Top: Description of the Main Lithological and Stratigraphical Characteristics of the Solfatara Tephra from table 1 in Petrosino et al 2012. Bottom: Figure 1 in Petrosino et al. (2012) which full caption reads: *(a) Structural sketch map of the Solfatara volcano and surroundings, with seismic array geometry, vents and structural analysis site locations, and W-E cross-section profile; (b) detail of the array geometry, and location of SFT seismic station; (c) location of the study area in the Campi Flegrei caldera (after Orsi et al. [1996]).*

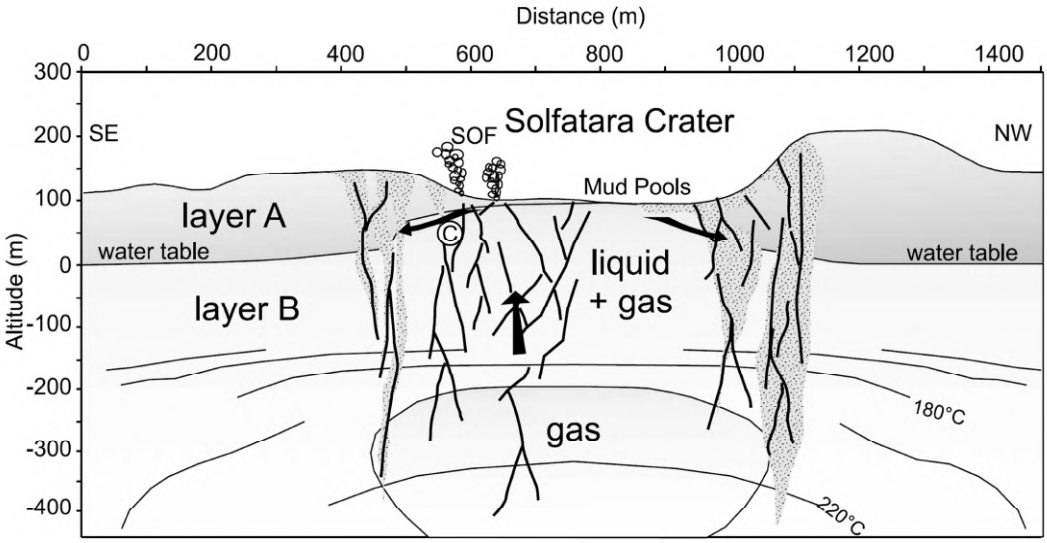

Figure C4. 11. Hydrothermal circulation: Transition between the hot water/liquid-rich fluid coming from the Fangaia pool and the CO2/vapour-rich fluid from the plume below BG/BN fumaroles. Modified from figure 14 in Bruno et al (2007) which full caption reads: *Hydrothermal model of Solfatara caldera along a NW-striking cross section. The top of saturated zone, including its shape, the extent of the gas-saturated zone, and the position of isotherms are hypothetical and have been located according to the findings of our surveys. Isotherms and liquid surfaces are about 200 m deeper than those reported by Chiodini et al. [2003]. The faults shown are also hypothetical and are drawn only for discussion purposes.*

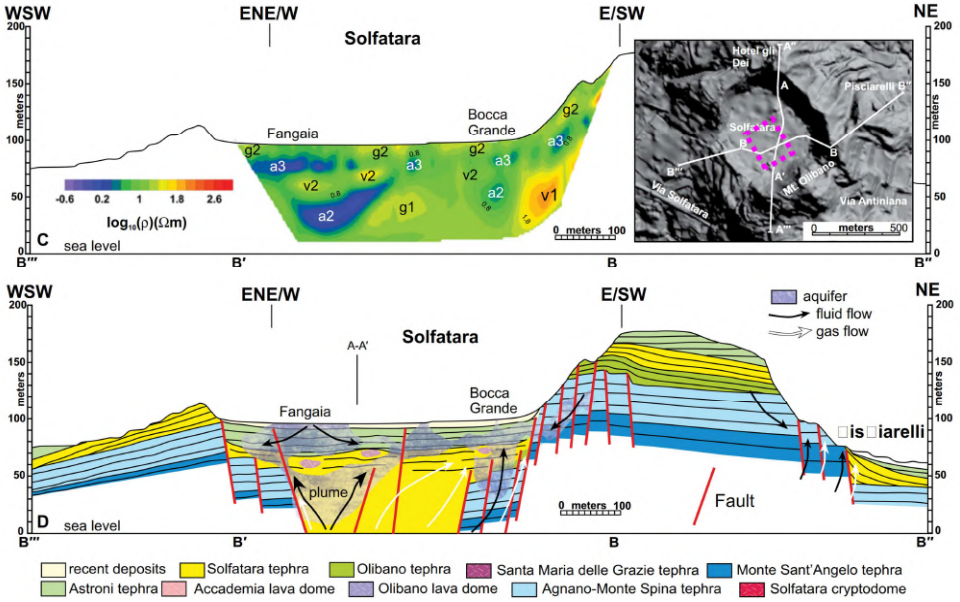

Figure C4. 12. Resistivity profile (B'''-B'-B-B'') crossing the survey area (pink dashed line); Migration pathway connecting Solfatara with Pisciarelli; NW-SE fault mapped in the middle of the Solfatara crater; lateral lithological changes from Fangaia mud pool to Boca Grande fumarole. Modified from figure 12 in Isaia et al (2015) which caption reads: *(C) Electrical resistivity tomography profile across the Solfatara crater (ρ—resistivity). Labelled bodies are discussed in text. (D) Geological cross section (2× vertical exaggeration)*

Appendix D

Seismic envelopes at the laboratory scale from rock physics measurements

The first computational approach applied in this thesis to model seismic wavefield at sample scale was radiative transfer theory. This analysis was presented at the EGU 2019 general assembly. Here I have downscaled the full modelling of stochastic seismic envelopes from heterogeneities to rock sample scales and ultrasonic frequencies, using existing codes applied to the field scale and adapting them to 3D propagation.

D1 Rationale

Fracture- and fluid-induced heterogeneities in rocks generate scattering sources that attenuate direct wave seismic energy. This scattered energy is recorded later in seismograms and is measurable as coda envelopes, which hold information about fracture networks and fluid content in the rock. Seismic coda analysis has the potential to provide useful information about fracture systems and fluid-flow processes, while coda imaging is currently a state-of-art technique in highly heterogeneous media.

These techniques have already been applied at field scale (10^1-10^3 m) to characterize lithospheric and volcanic settings (e.g. Calvet and Margerin, 2013; De Siena et al., 2013) however, the connection between smaller-scale rock physics (10^{-3}-10^{-1} m) and seismic scattering parameters is still unclear. In this study, we developed computational tools that use rock physics observations to model seismic envelopes at core plug scale (mm-cm) in the laboratory. We use field-dependent measurements of seismic heterogeneity, like fracturing, porosity and saturation, as inputs for constructing synthetic

coda envelopes. The computational framework applied is radiative transfer theory (RTT), which allows us to compute envelopes that are comparable with experimental data.

The synthetic envelopes are computed using stochastic parameters and follow a Born approximation. We use as input the information obtained from the statistical distribution of fractures previously estimated in a sandstone core plug. The results can be up-scaled to model seismic attenuation observations at field scale; the outcomes provide a novel and useful approach for quantifying fractures network directly from seismic coda analysis. The algorithm is already able to model the response of the envelopes of the coda attenuation, from field-dependent measurements of heterogeneities at a laboratory scale.

D2 Background

Fractures have always played a main role in characterizing reservoirs as these usually are the main path for fluid movement, therefore getting to know the features of the fracture network is a significant task for the exploitation of hydrocarbon reservoirs, storage of CO_2 or development of geothermal energy process. It is known that seismic waves propagating through a fractured rock are attenuated (Pyrak-Nolte et al., 1990; Barbosa et al., 2019), then using wave attenuation parameters to extract information on fracture characteristics (density, orientation, length, filling material) is a relevant approach for describing fractured reservoirs. The concept is that if we consider a fracture network as small heterogeneities embedded in the media, each time that the propagating seismic wave encounters the boundaries of a crack, it gives rise to a scattering event, and then numerous incoherent waves produced by these cracks will arrive at the receiver, and will be displayed in the seismogram as coda waves (Aki and Chouet,1975), whose envelopes will contain the information of these fractures. Several studies have begun to examine seismic attenuation data from fractured media (e.g., Hunziker et al., 2018; Willies et al., 2006). Goodfellow et al. (2015) used active and passive ultrasonic measurements to observe changes in attenuation properties in a sandstone sample during tri-axial deformation, they concluded that the formation of large fractures generates scattering that attenuated the high-frequency signals. In like manner, Shih and Frehner (2016) stated that seismic coda analysis provides useful information about the fracture system based on the

observations that seismic coda will display a signature frequency in the presence of a fracture, which is triggered by the resonance effect (Krauklis-wave) in the fracture. Most recently, Wang et al. (2017) modelled fracture dimension and orientation information using reflection data from ultrasonic measurements at laboratory scale.

A common approach to describe the energy transport through a scattering medium is Radiative Transfer Theory –RTT-, which provides theoretical energy coda envelopes that are comparable with experimental data (De Siena et al., 2013). Radiative transfer theory can be analytically solved using Monte Carlo simulations (Hoshiba, 1991; Sato et al., 2012; Margerin et al., 2000; Yoshimoto, 2000; Bal et al., 2000), this approach is frequently used to synthesize the decay of the seismic energy density through envelopes of seismograms (Wei and Fu, 2014), the method considers that energy particles walk randomly through the heterogeneous medium, moving along ballistics ray paths between scattering events (Przybilla and Korn, 2008). The parameters deduced from the envelopes of the waveform energy have been used instead of the complete waveform when characterizing heterogeneous media because they can be interpreted in a simpler way. Przybilla et al. (2006) demonstrate the accuracy of computing synthetic envelopes through RTT by comparing them to envelopes created using finite-difference simulations in 3D elastic media.

D3 Input Data

The input values come from the analysis of the statistical distribution of fractures estimated in a Hopeman sandstone core plug which was deformed with a confining pressure of 35 MPa and pore fluid pressure of 10 MPa. The core plug has dimensions of 20 mm diameter and 40 mm length, porosity around 25%, and P- and S- wave velocity at the intact stage were measured at the Rock Physics Lab of the UoA with an estimated Vp/Vs ratio of 1.57

Post-failure SEM-BSE digital images (Fig. D1) were used to identify the porosity and micro-cracks. Then a fracture network image was generated using FracPaQ (Healy

et al., 2017), from which stochastics parameters such as the variance of the fracture trace length, density and intensity of the fractures were computed. (Fig D1).

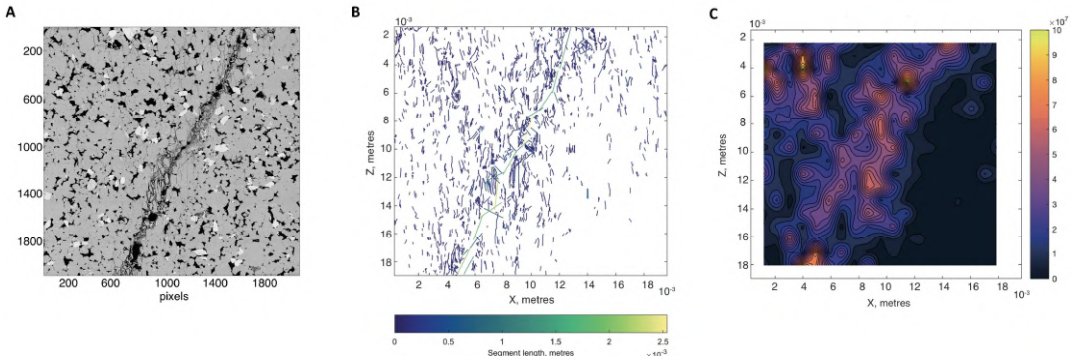

Figure D. 1. (A) Post-failure SEM-BSE digital image, the black areas are porosity and microcracks; (B) Segment length map of the fracture network from the image in panel A; (C) Estimated density of trace segments. After Rizzo et al., 2018.

The scattering coefficients equations to be used requires initial data such as correlation lengths, fluctuations of the media, frequency and velocity. These data values come from field-dependent measurements of heterogeneities (fracture trace length, intensity and density previously quantified) which were used for constructing the synthetic coda envelopes. After some analysis of the statistical data, the correlation was chosen as follow: the correlation length a was estimated from the variance of the trace length, while the mean squared fluctuations (ε^2) was estimated from the average intensity and density of the fractures for the 2D and 3D analysis respectively.

D4 Computational framework

The computational framework applied is radiative transfer theory (RTT). This is a common approach to describe energy transport through a scattering medium, which provides theoretical energy coda envelopes that are comparable with experimental data (De Siena et al., 2013). The main assumptions of RTT are (Przybilla and Korn, 2008):

(1) fluctuations of the inhomogeneities are weak; (2) wavelength and correlation length of the heterogeneities are of comparable size and (3) the energy of scattered wave packets can be stacked.

The synthetic envelopes are computed using stochastic parameters and follow a Born approximation. We consider wave mode conversion and S-waves polarization. The single-scattering coefficients by random elastic in-homogeneities in isotropic media are developed by Sato et al. (2012) and we have followed the same approach for the four-wave modes (P-to-P, P-to-S, S-to-S, and S-to-P scattering):

$$g^{PP}(\theta,\alpha,\omega) = \frac{K_0^4}{4\pi}|X_r^{PP}(\theta,\alpha)|^2 P\left(\frac{2K_0}{\gamma_0}\sin\frac{\theta}{2}\right)$$

$$g^{PS}(\theta,\alpha,\omega) = \frac{1}{\gamma_0}\frac{K_0^4}{4\pi}\left|X_\theta^{PS}(\theta,\alpha)\right|^2 P\left(\frac{K_0}{\gamma_0}\sqrt{1+\gamma_0^2-2\gamma_0\cos\theta}\right)$$

$$g^{SP}(\theta,\alpha,\omega) = \gamma_0\frac{K_0^4}{4\pi}|X_r^{SP}(\theta,\alpha)|^2 P\left(\frac{K_0}{\gamma_0}\sqrt{1+\gamma_0^2-2\gamma_0\cos\theta}\right)$$

$$g^{SS}(\theta,\alpha,\omega) = \frac{K_0^4}{4\pi}\left(\left|X_\theta^{SS}(\theta,\alpha)\right|^2 + |X_\alpha^{SS}(\theta,\alpha)|^2\right) P\left(2K_0\sin\frac{\theta}{2}\right)$$

Where the angular-dependent scattering pattern is given by the Born approximation:

$$X_r^{PP}(\theta,\alpha) = \frac{1}{\gamma_0^2}\left[\nu\left(-1+\cos\theta+\frac{2}{\gamma_0^2}\sin^2\theta\right)-2+\frac{4}{\gamma_0^2}\sin^2\theta\right]$$

$$X_\theta^{PS}(\theta,\alpha) = -\sin\theta\left[\nu\left(1-\frac{2}{\gamma_0}\cos\theta\right)-\frac{4}{\gamma_0}\cos\theta\right]$$

$$X_r^{SP}(\theta,\alpha) = \frac{1}{\gamma_0^2}\sin\theta\cos\alpha\left[\nu\left(1-\frac{2}{\gamma_0}\cos\theta\right)-\frac{4}{\gamma_0}\cos\theta\right]$$

$$X_{\theta}^{SS}(\theta,\alpha) = \cos\alpha\,[\nu\,(\cos\theta - \cos 2\theta) - 2\cos 2\theta]$$

$$X_{\alpha}^{SS}(\theta,\alpha) = \sin\alpha\,[\nu\,(\cos\theta - 1) + 2\cos\theta]$$

An exponential ACF is used to describe the media, the angular dependence of the PSDF terms is $P(m) = \frac{8\pi\varepsilon^2 a^3}{(1+a^2m^2)^2}$; De Siena et al. (2013) defined the PSDF as the key function to describe the scattering properties of the medium and stated that its form must be chosen in order to represent real coda envelopes.

The terms in these equations represent:

K_0= wavenumber, pre-computed as $K_o=2\pi f/V_s$

Υ_0= velocity ratio, pre-computed as $\Upsilon_0= V_p/ V_s$

ν = Birch's law factor. This factor denotes a linear relationship between the velocity of the wave and the density of the rock medium. Typical values for sandstones in the lithosphere could be around ~0.25. For this study, the factor was determined using the velocity and density data of the sample obtaining an average value of ν = 0.65.

ε^2= at regional scale 'epsilon' is related to the fractional fluctuation of the wave velocity. In this study we assume no changes in velocity along with the sample, then is considered that the perturbations are produced by the presence of cracks, from these assumptions we can use the estimated average density of fractures as ε^2 for the 3D scenario and the average intensity of fracture for the 2D case.

a= correlation length. At laboratory scale is usually related to the average grain and pores size of the sample (Wei and Fu, 2014), order of magnitude 10^{-7} km. For this analysis, it

was used the variance of the trace length of the fractures, which has a higher order of magnitude than the grain size (~10^{-6} km). When estimating the correlation length is important to consider (1) the ratio between wavelength and fracture length, as scattering attenuation is dominant when the correlation length is close to the wavelength of the incident wave (Wang et al., 2017); (2) Decreasing the correlation length, the probability of conversion increases, while anisotropy decreases (Przybilla et al., 2006); and (3) Increasing the correlation length and/or ε^2 produces smaller mean free paths hence, a larger number of interactions (De Siena et al., 2013).

The coda envelope is produced by multiple single scattering events in which the scattering patterns are provided by the single scattering coefficients. On the other hand, the total scattering coefficient, for each wave mode, is defined over all the directions, using: $g_0^{XY} = \frac{1}{2\pi} \oint g^{XY}\, d\theta\, d \propto$, where X and Y could be either P wave or S wave mode, to represent the four possible propagations.

When a wavefront scatters its ray-path tend to take a new direction that is usually limited to a range of possibilities. Each wave mode will have a different preference propagation direction, and all of these are pre-computed using a look-up table method, in order to make the computation more efficient (Fig. D2). From a total of 1000 possible angles, the system restricts the location to up to 201 options (for each azimuth and elevation angle) and these are stored and randomly selected at each scatter point. The scattering patterns have different preferential directions. For the PP case, the scattering is dominant in the forward direction, while in the P to S conversion there is a wider range of probabilities, thus sampling the medium more times. The direction for S to P scattering is not expected, however, it was not being neglected and the probability of occurrence is included as well in the simulation.

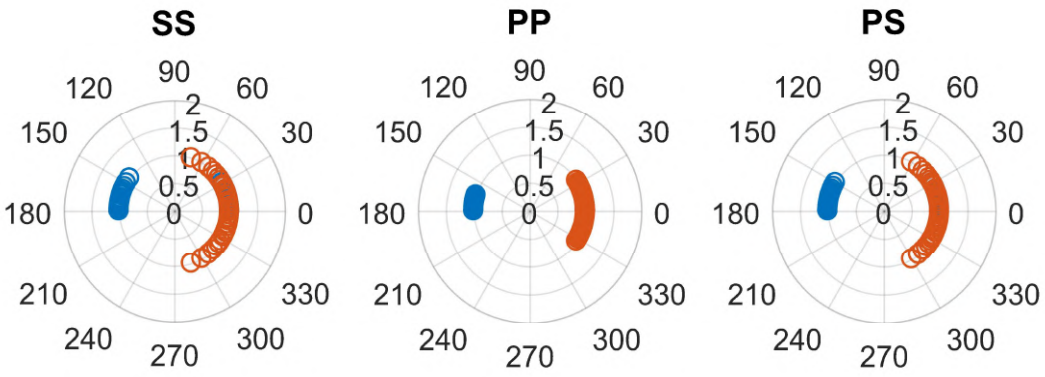

Figure D. 2. Representation of the look-up table for the scattering pattern. Probabilities of scattering direction previously computed. Azimuth (orange) and elevation (blue) angles are chosen at each scattering point (Figure D.3) for SS, PP and PS conversion, The angles in this figure were estimated for a central frequency of 0.2 MHz, using correlation length: 2.204 e-6 and ε2:0.019

The outgoing wave propagation direction is described by Yoshimoto (2000), assuming an isotropic source radiation and isotropic scattering (uniform probability distribution). The first direction of propagation is given by the azimuthal angle $\alpha = 2\pi Z_1$ and take-off angle (for the 3D analysis) $\theta = \mathrm{acos}(1 - 2Z_2)$, being Z_1 and Z_2 in both cases random numbers, independents of each other, between 0-1. The initial direction of the particles in Cartesians coordinates is determined by $di0 = [\cos\alpha \sin\theta \quad \sin\alpha \sin\theta \quad \cos\theta]$ (Przybilla et al., 2006), while the new propagation direction after a scattering event is $dir = [\cos\alpha r \sin\theta r \quad \sin\alpha r \sin\theta r \quad \cos\theta r]$

The conversion probability is given by:

- The probability of a P mode that continues propagating as P wave after scattering is $g_1^{PP} = \frac{g_0^{PP}}{(g_0^{PP}+g_0^{PS})}$ and the probability of conversion to S wave is $g_1^{PS} = 1 - g_1^{PP}$

- The probability of an S mode that continues propagating as S wave after scattering is $g_1^{SS} = \frac{(g_{1\theta}^{SS}+g_{1\alpha}^{SS})}{(g_0^{SS}+g_0^{SP})}$ and the probability of conversion to S wave is $g_1^{SP} = 1 - g_1^{SS}$, where $g_{1\theta}^{SS} = \frac{g_{0\theta}^{SS}}{(g_0^{SS}+g_0^{SP})}$ and $g_{1\alpha}^{SS} = \frac{g_{0\alpha}^{SS}}{(g_0^{SS}+g_0^{SP})}$

The total number of particles that represent the energy was fixed as 10,000 for a sampling length of 1.85e-03 seconds.

The average distance travelled, known as the mean free path, is dependent on the total scattering coefficients as $mfp = [g_0^{PP} + g_0^{PS} \quad g_{0\theta}^{SS} + g_{0\alpha}^{SS} + g_0^{SP}]^{-1}$, and the distance travelled between two scattering events is $fpl = -mfp * \log(Z)$, where Z is a random number between 0 and 1.

Computational simulation

The particle is shot from a point source and moves following seismic ray theory in a distance defined by the mean free path (Fig. D3). Once the propagating wave finds an obstacle in its path (fracture, porosity, fluid) it experiences a scattering event, a new propagation direction is randomly estimated and may also change wave mode, based on the probability of the wave continuing as itself or changing mode (a new mean free path is computed as well). The energy contribution of the particle at each scattering event is calculated at the receiver and a control is also activated to check if the propagation time of the particle is too large. Therefore, to assure if the signal will indeed arrive at the receptor transducer, we need to limit the travel time of the entire scattering process as well as to compute the energy probability that (1) the particle will scatter into a direction that arrives at the station and (2) will not scatter with anything else in the path. Finally, an estimation of the average energy density at each source-receiver arrival provides the data (decay of the total energy) for the generation of the synthetic envelope.

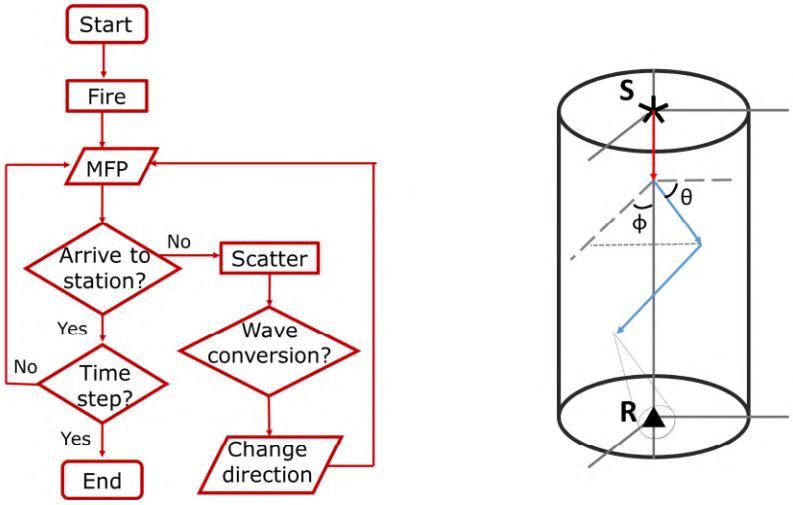

Figure D. 3. Flow chart of the computational simulation (left) and a sketch of the scattering propagation (right).

Boundary conditions

At the laboratory scale, the propagation gets complicated due to the sample size limitations, and the biases produced by reflections and conversions of coherent waves taking place at the boundaries of the sample (Zhang et al. 2014; Wei and Fu 2014). Therefore, to be able to compare the synthetic envelopes with those generated in laboratory ultrasonic measurements, it is necessary to include in the analysis the effects of particle energy reaching the side ends of the rock sample, two scenarios were modelled (Fig. D4): (1) the energy being absorbed (i.e.. never returning), and (2) being reflected (i.e.. continuing the scattering processes into the sample). For the first case the process end, while for the second a specular reflection is assumed at the boundary. However, we are missing to account for when both circumstances take place, this is a small percentage of the energy is absorbed and the rest reflected, probably the closest scenario to the real case.

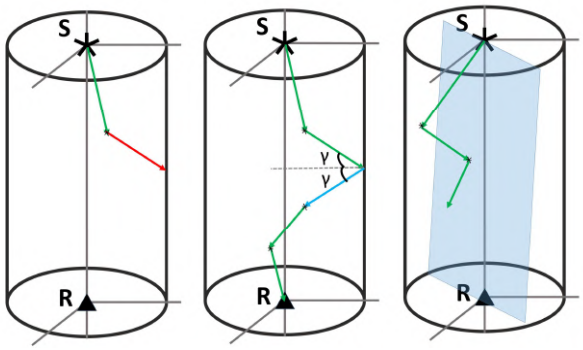

Figure D. 4. Schematic illustration of the boundary conditions when the particle impact the physical boundary of the rock sample: for the case of being absorbed (left panel: never returning) or reflected (middle panel: continuing scattering), and a sketch of scattering produced at the surface of shear failure (right).

The digital image of the sandstone rock sample (Fig. D1) shows an evident shear failure plane, produced by a cluster of cracks aligned. The effects of fractures on the propagation of seismic waves can be modelled as boundary conditions (Pyrak-Nolte et al., 1990), therefore the observed fault plane was included in the modelling as a boundary condition (Fig D4r). In this case, when the propagating wave reaches this plane the simulation results in a new scattering event. The basic premises of the model is that at dry conditions wave energy continue propagating in an isotropic media with no change in acoustic impedance produced by the presence of the cracks (i.e. there is no velocity and/or density discontinuity), and then a new propagation direction and possible mode conversion take place to continue with the process.

D5 Results and Discussion

The synthetic envelopes were generated for the stochastic fracture data using RTT. Figure D5.A shows a greater magnitude of the energy density for the reflective case, this can be associated with a larger propagating time, which allows more energy contribution events to be counted at the receiver during the simulation, compared with the absorption case. Wei and Fu (2014) compared absorption and reflection boundary conditions on synthetic

envelopes and found an unexpected similarity that we do not observe in our study (Fig. D5), they attributed this matching of the envelopes to the heterogeneity of the sample, the length-to-diameter ratio, and the specular direction in the reflective case. We have found, however, similarities in the scenario that include the failure plane (Fig 5B). This could be explained by the presence of the failure plane that confines the majority of the particle energy, therefore few events reach the boundaries. Thus, the shear plane acts as a new scattering source that keeps the forward scattering close to the source-receiver path (plane-axis) and away from the boundaries of the sample.

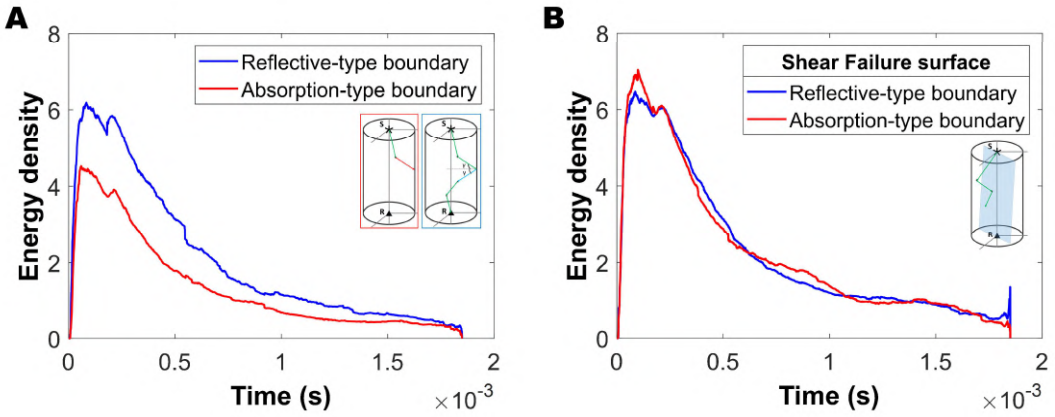

Figure D. 5. Synthetic envelopes generated using the statistical distribution of fractures in a core sample as input data. Results take into account scattering by heterogeneities induced by the presence of fractures and the absorption/reflection at the sample boundary (A), and an additional scattering place at the shear failure surface in which the travelling particle will always scatter (B).

In figure D5 information from the statistical distribution of fracture was used, but any other stochastic measurement can be applied as soon as reliable values of correlation lengths and fluctuations of the media are derived to be introduced as input data in the code. For instance, in figure D6 we show synthetic envelopes for different configurations of fracture networks. Note that larger correlation lengths and larger epsilon values produce smaller mean free paths, however, it reduced the ranges of angles for conversion probabilities.

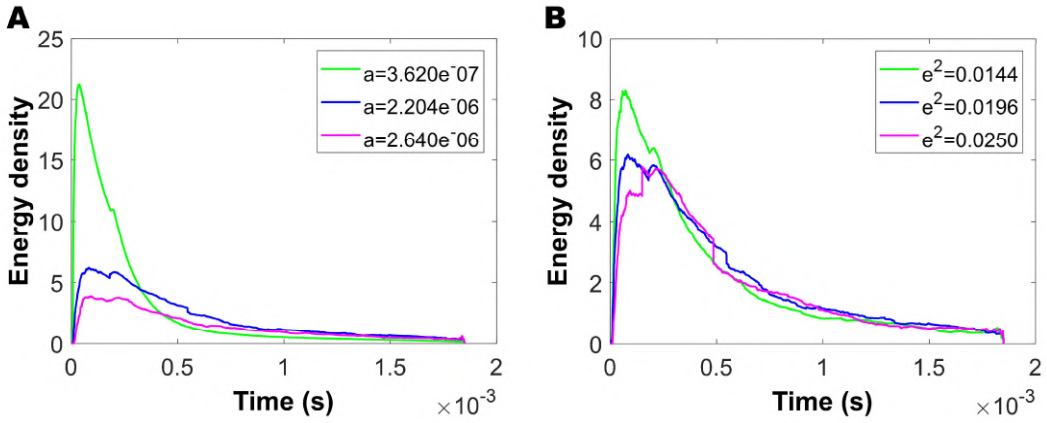

Figure D. 6. Synthetic envelopes response (reflective-type boundary case) for different fracture network configurations. (A) variations of the correlation length 'a', and (B) variations of the mean squared fluctuations 'ε^2'. The blue curves represent the same scenarios for both panels and Fig. D5.

Bibliography

Achaoui, Y., Laude, V., Benchabane, S., and Khelif, A. (2013). Local resonances in phononic crystals and in random arrangements of pillars on a surface. *Journal of Applied Physics*, 114(10), 104503. https://doi.org/10.1063/1.4820928

Adam, L. and Otheim, T. (2013). Elastic laboratory measurements and modeling of saturated basalts. *Journal of Geophysical Research: Solid Earth*, 118(3), 840–851. https://doi.org/10.1002/jgrb.50090

Adelinet, M., Fortin, J., Guéguen, Y., Schubnel, A., and Geoffroy, L. (2010). Frequency and fluid effects on elastic properties of basalt: Experimental investigations. *Geophysical Research Letters*, 37(2), https://doi.org/10.1029/2009GL041660

Adelinet, M. and Le Ravalec, M. (2015). Effective medium modeling: How to efficiently infer porosity from seismic data?. *Interpretation*, 3(4), SAC1–SAC7. https://doi.org/10.1190/INT-2015-0065.1

Akande, W. G., Gan, Q., Cornwell, D. G., and De Siena, L. (2021). Thermo‐Hydro‐Mechanical Model and Caprock Deformation Explain the Onset of an Ongoing Seismo‐Volcanic Unrest. *Journal of Geophysical Research: Solid Earth*, 126(3). https://doi.org/10.1029/2020JB020449

Aki, K. (1969). Analysis of the seismic coda of local earthquakes as scattered waves. *Journal of Geophysical Research*, 74(2), 615–631. https://doi.org/10.1029/JB074i002p00615

Aki, K. and Chouet, B. (1975). Origin of coda waves: Source, attenuation, and scattering effects. *Journal of Geophysical Research*, 80(23), 3322–3342. https://doi.org/10.1029/JB080i023p03322

Aki, K. and Richards, P.G. (1980), *Quantitative seismology: theory and methods*, W. H. Freeman, San Francisco.

Amoroso, O., Russo, G., De Landro, G., Zollo, A., Garambois, S., Mazzoli, S., et al. (2017). From velocity and attenuation tomography to rock physical modeling: Inferences on fluid-driven earthquake processes at the Irpinia fault system in southern Italy: From Seismic Tomography to Rock Modeling. *Geophysical Research Letters*, 44(13), 6752–6760. https://doi.org/10.1002/2016GL072346

Amoroso, O., Festa, G., Bruno, P. P., D'Auria, L., De Landro, G., Di Fiore, et al. (2018). Integrated tomographic methods for seismic imaging and monitoring of volcanic caldera structures and geothermal areas. *Journal of Applied Geophysics*, 156, 16-30. https://doi.org/10.1016/j.jappgeo.2017.11.012

Andrä, H., Combaret, N., Dvorkin, J., Glatt, E., Han, J., Kabel, et al. (2013). Digital rock physics benchmarks—Part I: Imaging and segmentation. *Computers and Geosciences*, 50, 25–32. https://doi.org/10.1016/j.cageo.2012.09.005

Aster, R. C., Borchers, B., and Thurber, C. H. (2019). Iterative Methods. In *Parameter Estimation and Inverse Problems* (pp. 151–179). Elsevier. https://doi.org/10.1016/B978-0-12-804651-7.00011-0Barton, N. (2006). *Rock Quality, Seismic Velocity, Attenuation and Anisotropy* (1st ed). CRC Press. https://doi-org.dbgw.lis.curtin.edu.au/10.1201/9780203964453

AVIZO (2019.3). Avizo User's Guide. Thermo Fisher Scientific., https://www.thermofisher.com

Azzola, J., Schmittbuhl, J., Zigone, D., Lengliné, O., Masson, F., and Magnenet, V. (2020). Elastic Strain Effects on Wave Scattering: Implications for Coda Wave Interferometry (CWI). *Journal of Geophysical Research: Solid Earth*, 125(3). https://doi.org/10.1029/2019JB018974

Baechle, G. T., Colpaert, A., Eberli, G. P., and Weger, R. J. (2008). Effects of microporosity on sonic velocity in carbonate rocks. *The Leading Edge*, 27(8), 1012–1018. https://doi.org/10.1190/1.2967554

Bal, G. and Moscoso, M. (2000). Polarization effects of seismic waves on the basis of radiative transport theory, *Geophysical Journal International*, vol. 142, no. 2, pp. 571-585.

Barbosa, N. D., Caspari, E.,Rubino, J. G., Greenwood, A.,Baron, L., and Holliger, K. (2019). Estimation of fracture compliance from attenuation and velocity analysis of full-waveform sonic log data. *Journal of Geophysical Research: Solid Earth*, 124, 2738–2761.https://doi.org/10.1029/2018JB016507

Barton, N. (2006). *Rock Quality, Seismic Velocity, Attenuation and Anisotropy* (1st ed). CRC Press. https://doi-org.dbgw.lis.curtin.edu.au/10.1201/9780203964453

Benson, P. M., Vinciguerra, S., Meredith, P. G., and Young, R. P. (2008). Laboratory Simulation of Volcano Seismicity. *Science*, 322(5899), 249–252. https://doi.org/10.1126/science.1161927

Berland, J., Bogey, C., and Bailly, C. (2006). Low-dissipation and low-dispersion fourth-order Runge–Kutta algorithm. *Computers and Fluids*, 35(10), 1459–1463. https://doi.org/10.1016/j.compfluid.2005.04.003

Berryman, J.G., (1995). Mixture theories for rock properties. In *Rock Physics and Phase Relations: a Handbook of Physical Constants*, ed. T.J. Ahrens. Washington, DC: American. Geophysical Union, pp. 205–228. https://doi.org/10.1029/RF003p0205

Best, A.I., McCann, C., and Sothcott, J. (1994). The relationships between the velocities, attenuations and petrophysical properties of reservoir sedimentary rocks1. *Geophysical Prospecting*, 42(2), 151–178. https://doi.org/10.1111/j.1365-2478.1994.tb00204.x

Best, A.I., Sothcott, J., and McCann, C. (2007). A laboratory study of seismic velocity and attenuation anisotropy in near‐surface sedimentary rocks. *Geophysical Prospecting*, 55(5), pp. 609‐625. https://doi.org/10.1111/j.1365-2478.2007.00642.x

Beucher, S., and Meyer, F., (1993). The morphological approach to segmentation: the watershed transformation. In: Dougherty, E.R. (Ed.), *Mathematical Morphology in Image Processing*, Marcel Dekker, NY, pp. 433–481.

Bianco, F., Del Pezzo, E., Saccorotti, G., and Ventura, G. (2004). The role of hydrothermal fluids in triggering the July–August 2000 seismic swarm at Campi Flegrei, Italy: Evidence from seismological and mesostructural data. *Journal of Volcanology and Geothermal Research,* 133(1–4), 229–246. https://doi.org/10.1016/S0377-0273(03)00400-1

Biryukov, A., Tisato, N., and Grasselli, G. (2016). Attenuation of elastic waves in bentonite and monitoring of radioactive waste repositories. *Geophysical Journal International*, 205(1), 105–121. https://doi.org/10.1093/gji/ggv548

Blair, D.P. (1990). A direct comparison between vibrational resonance and pulse transmission data for assessment of seismic attenuation in rock. *Geophysics*, 55(1), 51–60. https://doi.org/10.1190/1.1442771

Bruno, P. P. G., Ricciardi, G. P., Petrillo, Z., Di Fiore, V., Troiano, A., and Chiodini, G. (2007). Geophysical and hydrogeological experiments from a shallow hydrothermal

system at Solfatara Volcano, Campi Flegrei, Italy: Response to caldera unrest. *Journal of Geophysical Research*, 112(B6), B06201. https://doi.org/10.1029/2006JB004383

Bruno, P. P. G., Maraio, S., and Festa, G. (2017). The shallow structure of Solfatara Volcano, Italy, revealed by dense, wide-aperture seismic profiling. *Scientific Reports*, 7(1), 17386. https://doi.org/10.1038/s41598-017-17589-3

Butler, R. (2020). Bulk, shear and scattering attenuation beneath Hawaiian Volcanos and in the oceanic crust extending to the Aloha Cabled Observatory. *Geophysical Journal International*, 223(1), 543–560. https://doi.org/10.1093/gji/ggaa309

Byrdina, S., Vandemeulebrouck, J., Cardellini, C., Legaz, A., Camerlynck, C., Chiodini, G., et al., (2014). Relations between electrical resistivity, carbon dioxide flux, and self-potential in the shallow hydrothermal system of Solfatara (Phlegrean Fields, Italy). *Journal of Volcanology and Geothermal Research*, 283, 172–182. https://doi.org/10.1016/j.jvolgeores.2014.07.010

Calò, M., and Tramelli, A. (2018). Anatomy of the Campi Flegrei caldera using enhanced seismic tomography models. *Scientific Reports*, 8(1), 1-12

Calvet, M. and Margerin, L. (2013). Lapse-Time Dependence of Coda Q: Anisotropic Multiple-Scattering Models and Application to the Pyrenees. *Bulletin of the Seismological Society of America*, 103(3), 1993–2010. https://doi.org/10.1785/0120120239

Calvet, M., Sylvander, M., Margerin, L., and Villaseñor, A. (2013). Spatial variations of seismic attenuation and heterogeneity in the Pyrenees: Coda Q and peak delay time analysis. *Tectonophysics*, 608, 428–439. https://doi.org/10.1016/j.tecto.2013.08.045

Calvet, M. and Margerin, L. (2016). Impact of grain shape on seismic attenuation and phase velocity in cubic polycrystalline materials. *Wave Motion*, 65, 29–43. https://doi.org/10.1016/j.wavemoti.2016.04.001

Carcione, J. M. (Ed.). (2015). *Wave Fields in Real Media* (Third Edition). Elsevier. https://doi.org/10.1016/B978-0-08-099999-9.00001-7

Cheng, W., Carcione, J. M., Qadrouh, A. N., Alajmi, M., and Ba, J. (2020). Rock Anelasticity, Pore Geometry and the Biot–Gardner Effect. *Rock Mechanics and Rock Engineering*, 53(9), 3969–3981. https://doi.org/10.1007/s00603-020-02155-7

Chiodini, G. (2005). Carbon dioxide diffuse degassing and estimation of heat release from volcanic and hydrothermal systems. *Journal of Geophysical Research*, 110(B8), B08204. https://doi.org/10.1029/2004JB003542

Chiodini, G., Selva, J., Del Pezzo, E., Marsan, D., De Siena, L., D'Auria, L., et al. (2017). Clues on the origin of post-2000 earthquakes at Campi Flegrei caldera (Italy). *Scientific Reports*, 7(1), 4472. https://doi.org/10.1038/s41598-017-04845-9

Chiodini, G., Caliro, S., Avino, R., Bini, G., Giudicepietro, F., De Cesare, et al. (2021). Hydrothermal pressure-temperature control on CO2 emissions and seismicity at Campi Flegrei (Italy). *Journal of Volcanology and Geothermal Research,* 414, 107245. https://doi.org/10.1016/j.jvolgeores.2021.107245

Clarke, J., Adam, L., van Wijk, K., and Sarout, J. (2020). The influence of fluid type on elastic wave velocity and attenuation in volcanic rocks. *Journal of Volcanology and Geothermal Research*, 403, 107004. https://doi.org/10.1016/j.jvolgeores.2020.107004

Cnudde, V. and Boone, M.N. (2013). High-resolution X-ray computed tomography in geosciences: A review of the current technology and applications. *Earth-Science Reviews*, 123, 1–17. https://doi.org/10.1016/j.earscirev.2013.04.003

Colombi, A., Roux, P., Guenneau, S., Gueguen, P., and Craster, R. V. (2016). Forests as a natural seismic metamaterial: Rayleigh wave bandgaps induced by local resonances. *Scientific Reports*, 6(1), 19238. https://doi.org/10.1038/srep19238

Cusano, P., Petrosino, S., and Saccorotti, G. (2008). Hydrothermal origin for sustained Long-Period (LP) activity at Campi Flegrei Volcanic Complex, Italy. *Journal of Volcanology and Geothermal Research*, 177(4), 1035–1044. https://doi.org/10.1016/j.jvolgeores.2008.07.019

D'Auria, L., Massa, B., Cristiano, E., Del Gaudio, C., Giudicepietro, F., Ricciardi, G., et al. (2015). Retrieving the Stress Field Within the Campi Flegrei Caldera (Southern Italy) Through an Integrated Geodetical and Seismological Approach. *Pure and Applied Geophysics*, 172(11), 3247–3263. https://doi.org/10.1007/s00024-014-1004-7

David, E. C. and Zimmerman, R. W. (2012). Pore structure model for elastic wave velocities in fluid-saturated sandstones. *Journal of Geophysical Research: Solid Earth*, 117, B7210. https://doi.org/10.1029/2012JB009195

De Landro, G., Serlenga, V., Russo, G., Amoroso, O., Festa, G., Bruno, P. P., et al. (2017). 3D ultra-high resolution seismic imaging of shallow Solfatara crater in Campi Flegrei

(Italy): New insights on deep hydrothermal fluid circulation processes. *Scientific Reports*, 7(1), 3412. https://doi.org/10.1038/s41598-017-03604-0

De Landro, G., Serlenga, V., Amoroso, O., Russo, G., Festa, G., and Zollo, A. (2019). High Resolution Attenuation Images From Active Seismic Data: The Case Study of Solfatara Volcano (Southern Italy). *Frontier in Earth Sciences*, 7, 295. https://doi.org/10.3389/feart.2019.00295

De Siena, L., Del Pezzo, E., Thomas, C., Curtis, A., and Margerin, L. (2013). Seismic energy envelopes in volcanic media: In need of boundary conditions. *Geophysical Journal International*, 195(2), 1102–1119. https://doi.org/10.1093/gji/ggt273

De Siena, L., Calvet, M., Watson, K. J., Jonkers, A. R. T., and Thomas, C. (2016). Seismic scattering and absorption mapping of debris flows, feeding paths, and tectonic units at Mount St. Helens volcano. *Earth and Planetary Science Letters*, 442, 21–31. https://doi.org/10.1016/j.epsl.2016.02.026

De Siena, L., Amoruso, A., Del Pezzo, E., Wakeford, Z., Castellano, M., and Crescentini, L. (2017a). Space-weighted seismic attenuation mapping of the aseismic source of Campi Flegrei 1983-84 unrest. *Geophysical Research Letters*, 44, 1740-1748. https://doi.org/10.1002/2017GL072507

De Siena, L., Chiodini, G., Vilardo, G., Del Pezzo, E., Castellano, M., Colombelli, S., et al., (2017b). Source and dynamics of a volcanic caldera unrest: Campi Flegrei, 1983–84. *Scientific Reports*, 7(1), 8099. https://doi.org/10.1038/s41598-017-08192-7

Del Pezzo, E., Martini, M., and Milana, G. (1991). Site response using coda-wave techniques: Applications to short period data from central and southern Italy. *Pure and Applied Geophysics*, 136(1), 127–141. https://doi.org/10.1007/BF00878891

Del Pezzo, E., Ibañez, J., Prudencio, J., Bianco, F., and De Siena, L. (2016). Absorption and scattering 2-D volcano images from numerically calculated space-weighting functions. *Geophysical Journal International*, 206(2), 742–756. https://doi.org/10.1093/gji/ggw171

Del Pezzo, E., De La Torre, A., Bianco, F., Ibanez, J., Gabrielli, S., and De Siena, L. (2018). Numerically Calculated 3D Space-Weighting Functions to Image Crustal Volcanic Structures Using Diffuse Coda Waves. *Geosciences*, 8(5), 175. https://doi.org/10.3390/geosciences8050175

Delcamp, A., Roberti, G., and de Vries, B. V. W. (2016). Water in volcanoes: evolution, storage and rapid release during landslides. *Bulletin of Volcanology*, 78(12), 1-12. DOI: 10.1007/s00445-016-1082-8

Di Luccio, F., Pino, N. A., Piscini, A., and Ventura, G. (2015). Significance of the 1982–2014 Campi Flegrei seismicity: Preexisting structures, hydrothermal processes, and hazard assessment. *Geophysical Research Letters*, 42(18), 7498-7506

Di Martino, M. D. P., De Siena, L., Healy, D., and Vialle, S. (2021). Petro-mineralogical controls on coda attenuation in volcanic rock samples. *Geophysical Journal International*, 226(3), 1858–1872. https://doi.org/10.1093/gji/ggab198

Dou, Q., Sun, Y., and Sullivan, C. (2011). Rock-physics-based carbonate pore type characterization and reservoir permeability heterogeneity evaluation, Upper San Andres reservoir, Permian Basin, west Texas. *Journal of Applied Geophysics*, 74(1), 8–18. https://doi.org/10.1016/j.jappgeo.2011.02.010

Durán, E. L., Adam, L., Wallis, I. C., and Barnhoorn, A. (2019). Mineral Alteration and Fracture Influence on the Elastic Properties of Volcaniclastic Rocks. *Journal of Geophysical Research: Solid Earth*, 124(5), 4576–4600. https://doi.org/10.1029/2018JB016617

Eide, C. H., Schofield, N., Lecomte, I., Buckley, S. J., and Howell, J. A. (2018). Seismic interpretation of sill complexes in sedimentary basins: Implications for the sub-sill imaging problem. *Journal of the Geological Society*, 175(2), 193–209. https://doi.org/10.1144/jgs2017-096

Faccenda, M., Ferreira, A. M. G., Tisato, N., Lithgow‐Bertelloni, C., Stixrude, L., and Pennacchioni, G. (2019). Extrinsic Elastic Anisotropy in a Compositionally Heterogeneous Earth's Mantle. *Journal of Geophysical Research: Solid Earth*, 124(2), 1671‐1687. https://doi.org/10.1029/2018JB016482

Fazio, M., Benson, P. M., and Vinciguerra, S. (2017). On the generation mechanisms of fluid‐driven seismic signals related to volcano‐tectonics. *Geophysical Research Letters*, 44(2), 734‐742. https://doi.org/10.1002/2016GL070919

Fliedner, M. and White, R., (2001). Sub-basalt imaging in the Faeroe-Shetland Basin with large-offset data. *First break*, 19.5, 247-252.

Fortin, J., Stanchits, S., Vinciguerra, S., and Guéguen, Y. (2011). Influence of thermal and mechanical cracks on permeability and elastic wave velocities in a basalt from Mt. Etna

volcano subjected to elevated pressure. *Tectonophysics*, 503(1–2), 60–74. https://doi.org/10.1016/j.tecto.2010.09.028

Fortin, J., and Guéguen, Y. (2021). Porous and cracked rocks elasticity: Macroscopic poroelasticity and effective media theory. *Mathematics and Mechanics of Solids*, 26(8), 1158–1172. https://doi.org/10.1177/10812865211022034

Fu, B.-Y., Fu, L.-Y., Wei, W., and Zhang, Y. (2016). Boundary-reflected waves and ultrasonic coda waves in rock physics experiments. *Applied Geophysics*, 13(4), 667–682. https://doi.org/10.1007/s11770-016-0583-8

Fu, L.-Y., Fu, B.-Y., Sun, W., Han, T., and Liu, J. (2020). Elastic wave propagation and scattering in prestressed porous rocks. *Science China Earth Sciences*, 63, 1309-1329. https://doi.org/10.1007/s11430-019-9615-3

Fujisawa, K. and Takei, Y. (2009). A new experimental method to estimate viscoelastic properties from ultrasonic wave transmission measurements. *Journal of Sound and Vibration*, 323(3–5), 609–625. https://doi.org/10.1016/j.jsv.2009.01.016

Fukushima, Y., Nishizawa, O., Sato, H. and Ohtake, M. (2003). Laboratory study on scattering characteristics of shear waves in rock samples. *Bulletin of the Seismological Society of America*, 93(1), 253–263. https://doi.org/10.1785/0120020074

Gabrielli, S., De Siena, L., Napolitano, F., and Del Pezzo, E. (2020). Understanding seismic path biases and magmatic activity at Mount St Helens volcano before its 2004 eruption. *Geophysical Journal International*, 222(1), 169–188. https://doi.org/10.1093/gji/ggaa154

Gallagher, J. W., and Dromgoole, P. W. (2007). Exploring below the basalt, offshore Faroes: A case history of sub-basalt imaging. *Petroleum Geoscience*, 13(3), 213–225. https://doi.org/10.1144/1354-079306-711

Gammaldi, S., Amoroso, O., D'Auria, L., and Zollo, A. (2018). High resolution, multi-2D seismic imaging of Solfatara crater (Campi Flegrei Caldera, southern Italy) from active seismic data. *Journal of Volcanology and Geothermal Research,* 357, 177–185. https://doi.org/10.1016/j.jvolgeores.2018.03.025

Garia, S., Pal, A. K., Ravi, K., and Nair, A. M. (2019). A comprehensive analysis on the relationships between elastic wave velocities and petrophysical properties of sedimentary rocks based on laboratory measurements. *Journal of Petroleum Exploration and Production Technology*, 9(3), 1869–1881. https://doi.org/10.1007/s13202-019-0675-0

Gazzola, S., Hansen, P.C. and Nagy, J.G. (2019). IR Tools: a MATLAB package of iterative regularization methods and large-scale test problems. *Numer Algor*, 81, 773–811. https://doi.org/10.1007/s11075-018-0570-7

Geuzaine, C., and Remacle, J.-F. (2009). Gmsh: A 3-D finite element mesh generator with built-in pre- and post-processing facilities. *International Journal for Numerical Methods in Engineering*. 79, 1309-1331. https://doi.org/10.1002/nme.2579

Giudicepietro, F., Chiodini, G., Avino, R., Brandi, G., Caliro, S., De Cesare, W., et al. (2021). Tracking Episodes of Seismicity and Gas Transport in Campi Flegrei Caldera Through Seismic, Geophysical, and Geochemical Measurements. *Seismological Research Letters,* 92(2A), 965–975. https://doi.org/10.1785/0220200223

Goodfellow, S.D., Tisato, N., Ghofranitabari, M., Nasseri, M.H.B. and Young, R.P. (2015). Attenuation Properties of Fontainebleau Sandstone During True-Triaxial Deformation using Active and Passive Ultrasonics. *Rock Mechanics and Rock Engineering,* vol. 48, no. 6, pp. 2551-2566.

Gresse, M., Vandemeulebrouck, J., Byrdina, S., Chiodini, G., Revil, A., Johnson, T. C., et al. (2017). Three-Dimensional Electrical Resistivity Tomography of the Solfatara Crater (Italy): Implication for the Multiphase Flow Structure of the Shallow Hydrothermal System: Resistivity Model of Solfatara Crater. *Journal of Geophysical Research: Solid Earth*, 122(11), 8749–8768. https://doi.org/10.1002/2017JB014389

Grêt, A., Snieder, R., and Scales, J. (2006). Time-lapse monitoring of rock properties with coda wave interferometry: Time-lapse monitoring of rock properties. *Journal of Geophysical Research: Solid Earth*, 111(B3). https://doi.org/10.1029/2004JB003354

Guo, M.-Q., and Fu, L.-Y. (2007). Stress associated coda attenuation from ultrasonic waveform measurements: Stress associated coda attenuation. *Geophysical Research Letters*, 34(9). https://doi.org/10.1029/2007GL029582

Guo, M.-Q., Fu, L.-Y., and Ba, J. (2009). Comparison of stress-associated coda attenuation and intrinsic attenuation from ultrasonic measurements. *Geophysical Journal International*, 178(1), 447–456. https://doi.org/10.1111/j.1365-246X.2009.04159.x

Healy, D., Rizzo, R.E., Cornwell, D.G., Farrell, N.J.C., Watkins, H., Timms, N.E., Gomez-Rivas, E. and Smith, M. (2017). FracPaQ: A MATLAB™ toolbox for the quantification of fracture patterns. *Journal of Structural Geology*, vol. 95, pp. 1-16.

Heap, M. J. (2019). P- and S-wave velocity of dry, water-saturated, and frozen basalt: Implications for the interpretation of Martian seismic data. Icarus, 330, 11–15. https://doi.org/10.1016/j.icarus.2019.04.020

Heap, M. J., Villeneuve, M., Albino, F., Farquharson, J. I., Brothelande, E., Amelung, F., et al., (2020). Towards more realistic values of elastic moduli for volcano modelling. *Journal of Volcanology and Geothermal Research*, 390, 106684. https://doi.org/10.1016/j.jvolgeores.2019.106684

Heap, M. J., and Violay, M. E. (2021). The mechanical behaviour and failure modes of volcanic rocks: a review. *Bulletin of Volcanology*, 83(5), 1-47. https://doi.org/10.1007/s00445-021-01447-2

Holliger, K. and Levander, A. R. (1992). A stochastic view of lower crustal fabric based on evidence from the Ivrea Zone. *Geophysical Research Letters*, 19(11), 1153–1156. https://doi.org/10.1029/92GL00919

Holliger, K. and Levander, A. (1994). Seismic structure of gneissic/granitic upper crust: Geological and petrophysical evidence from the Strona-Ceneri Zone (northern Italy) and implications for crustal seismic exploration. *Geophysical Journal International*, 119(2), 497–510. https://doi.org/10.1111/j.1365-246X.1994.tb00137.x

Holtzman, B. K., Kohlstedt, D.L., Zimmerman, M.E., Heidelbach, F., Hiraga, T. and Hustoft, J. (2003). Melt Segregation and Strain Partitioning: Implications for Seismic Anisotropy and Mantle Flow. *Science*, 301(5637), 1227–1230. https://doi.org/10.1126/science.1087132

Hoshiba, M. (1991). Simulation of multiple-scattered coda wave excitation based on the energy conservation law. *Physics of the Earth and Planetary Interiors*, vol. 67, no. 1, pp. 123-136.

Hu, J., Fu, L.-Y., Wei, W., and Zhang, Y. (2018). Stress-Associated Intrinsic and Scattering Attenuation from Laboratory Ultrasonic Measurements on Shales. *Pure and Applied Geophysics*, 175(3), 929–962. https://doi.org/10.1007/s00024-017-1705-9

Hurwitz, S., Kipp, K. L., Ingebritsen, S. E., and Reid, M. E. (2003). Groundwater flow, heat transport, and water table position within volcanic edifices: Implications for volcanic processes in the Cascade Range. *Journal of Geophysical Research: Solid Earth*, 108(B12). doi:10.1029/2003JB00256

Hunziker, J., Favino, M., Caspari, E., Quintal, B., Rubino, J.G., Krause, R. and Holliger, K. (2018). Seismic Attenuation and Stiffness Modulus Dispersion in Porous Rocks Containing Stochastic Fracture Network. *Journal of Geophysical Research: Solid Earth*, vol. 123, no. 1, pp. 125-143.

Ibáñez, J. M., Castro-Melgar, I., Cocina, O., Zuccarello, L., Branca, S., Del Pezzo, E., et al. (2020). First 2-D intrinsic and scattering attenuation images of Mt Etna volcano and surrounding region from active seismic data. *Geophysical Journal International*, 220(1), 267–277. https://doi.org/10.1093/gji/ggz450

Igel, H. (2016). Seismic Waves and Sources. In *Computational Seismology: A Practical Introduction*. Oxford University Press. https://doi.org/10.1093/acprof:oso/9780198717409.001.0001

Ikeda, K., Goldfarb, E. J., and Tisato, N. (2020). Calculating Effective Elastic Properties of Berea Sandstone Using the Segmentation‐Less Method Without Targets. *Journal of Geophysical Research: Solid Earth*, 125(6). https://doi.org/10.1029/2019JB018680

Isaia, R., Vitale, S., Di Giuseppe, M. G., Iannuzzi, E., D'Assisi Tramparulo, F., et al. (2015). Stratigraphy, structure, and volcano-tectonic evolution of Solfatara maar-diatreme (Campi Flegrei, Italy). *Geological Society of America Bulletin*, 127(9–10), 1485–1504. https://doi.org/10.1130/B31183.1

Jerram, D. A., Millett, J. M., Kück, J., Thomas, D., Planke, S., Haskins, E., Lautze, N., and Pierdominici, S. (2019). Understanding volcanic facies in the subsurface: A combined core, wireline logging and image log data set from the PTA2 and KMA1 boreholes, Big Island, Hawai`i. *Scientific Drilling*, 25, 15–33. https://doi.org/10.5194/sd-25-15-2019

Ju, Y., Yang, Y., Peng, R., and Mao, L. (2013). Effects of Pore Structures on Static Mechanical Properties of Sandstone. *Journal of Geotechnical and Geoenvironmental Engineering*, 139(10), 1745–1755. https://doi.org/10.1061/(ASCE)GT.1943-5606.0000893

Kaina, N., Fink, M., and Lerosey, G. (2013). Composite media mixing Bragg and local resonances for highly attenuating and broad bandgaps. *Scientific Reports*, 3(1), 3240. https://doi.org/10.1038/srep03240

Karato, S., and Weidner, D. J. (2008). Laboratory Studies of the Rheological Properties of Minerals under Deep-Mantle Conditions. *Elements*, 4(3), 191–196. https://doi.org/10.2113/GSELEMENTS.4.3.191

Kilburn, C. R. and McGuire, B. (2001). *Italian volcanoes* (No. 1). Terra Publishing.

Kilburn, C., De Natale, G. and Carlino, S. (2017). Progressive approach to eruption at Campi Flegrei caldera in southern Italy. Nat Commun 8, 15312. https://doi.org/10.1038/ncomms15312

Klimentos, T., and McCann, C. (1990). Relationships among compressional wave attenuation, porosity, clay content, and permeability in sandstones. *Geophysics*, 55(8), 998–1014. https://doi.org/10.1190/1.1442928

Komatitsch, D., and Vilotte, J.-P. (1998). The Spectral Element Method: An Efficient Tool to Simulate the Seismic Response of 2D and 3D Geological Structures. *Bulletin of the Seismological Society of America*, 88(2), 368-392

Komatitsch, D., and Tromp, J. (1999). Introduction to the spectral element method for three-dimensional seismic wave propagation, *Geophysical Journal International*, 139 (3), 806–822. https://doi.org/10.1046/j.1365-246x.1999.00967.x

Komatitsch, D., and Tromp, J. (2003). A perfectly matched layer absorbing boundary condition for the second-order seismic wave equation. *Geophysical Journal International*, 154(1), 146–153. https://doi.org/10.1046/j.1365-246X.2003.01950.x

Kuster, G. T., and Toksöz, M. N. (1974). Velocity and attenuation of seismic waves in two‐phase media: Part I. Theoretical formulations. *Geophysics*, 39(5), 587‐606. https://doi.org/10.1190/1.1440450

Lebedev, M., Bóna, A., Pevzner, R., and Gurevich, B. (2011). Elastic anisotropy estimation from laboratory measurements of velocity and polarization of quasi-P-waves using laser interferometry. *Geophysics*, 76(3), WA83–WA89. https://doi.org/10.1190/1.3569110

Letort, J., Roux, P., Vandemeulebrouck, J., Coutant, O., Cros, E., Wathelet, M., et al. (2012). High-resolution shallow seismic tomography of a hydrothermal area: Application to the Solfatara, Pozzuoli: High-resolution shallow seismic tomography. *Geophysical Journal International*, 189(3), 1725–1733. https://doi.org/10.1111/j.1365-246X.2012.05451.x

Lisitsa, V., Bazaikin, Y., and Khachkova, T. (2020). Computational topology-based characterization of pore space changes due to chemical dissolution of rocks. *Applied Mathematical Modelling*, 88, 21–37. https://doi.org/10.1016/j.apm.2020.06.037

Liu, C., Wei, J., Di, B., Gong, F., Shuai, D., and Li, H. (2017). Experimental study of wave propagation in random media with different heterogeneity scales. *Journal of Geophysics and Engineering*, 14(4), 878–887. https://doi.org/10.1088/1742-2140/aa6b2e

Lucet, N., and Zinszner, B. E. (1992). Effects of heterogeneities and anisotropy on sonic and ultrasonic attenuation in rocks. *Geophysics*, 57(8), 1018–1026. https://doi.org/10.1190/1.1443313

Magrini, F., Diaferia, G., Boschi, L., and Cammarano, F. (2020). Arrival-angle effects on two-receiver measurements of phase velocity. *Geophysical Journal International*, 220(3), 1838–1844. https://doi.org/10.1093/gji/ggz560

Margerin, L., Campillo, M. and Van Tiggelen, B. (2000). Monte Carlo simulation of multiple scattering of elastic waves, *Journal of Geophysical Research*, vol. 105, no. B4, pp. 7873-7892.

Markussen, Ø., Dypvik, H., Hammer, E., Long, H., and Hammer, Ø. (2019). 3D characterization of porosity and authigenic cementation in Triassic conglomerates/arenites in the Edvard Grieg field using 3D micro-CT imaging. *Marine and Petroleum Geology*, 99, 265–281. https://doi.org/10.1016/j.marpetgeo.2018.10.015

Martini, F. and Bean, C., (2002). Sub-basalt seismic imaging using optical-to-acoustic model building and wave equation datuming processing. *Marine and Petroleum Geology*, 27, 555-562.

Matsunami, K. (1991). Laboratory tests of excitation and attenuation of coda waves using 2-D models of scattering media. *Physics of the Earth and Planetary Interiors*, 67(1–2), 36–47. https://doi.org/10.1016/0031-9201(91)90058-P

Mavko, G., Mukerji, T., and Dvorkin, J. (2009). *The Rock Physics Handbook: Tools for Seismic Analysis of Porous Media* (2nd ed.). Cambridge University Press; Cambridge Core. https://doi.org/10.1017/CBO9780511626753

Mayer, K., Scheu, B., Montanaro, C., Yilmaz, T. I., Isaia, R., Aßbichler, D., et al. (2016). Hydrothermal alteration of surficial rocks at Solfatara (Campi Flegrei): Petrophysical properties and implications for phreatic eruption processes. *Journal of Volcanology and Geothermal Research,* 320, 128–143. https://doi.org/10.1016/j.jvolgeores.2016.04.020

Mayor, J., Calvet, M., Margerin, L., Vanderhaeghe, O., and Traversa, P. (2016). Crustal structure of the Alps as seen by attenuation tomography. *Earth and Planetary Science Letters*, 439, 71–80. https://doi.org/10.1016/j.epsl.2016.01.025

McKenzie, C. K., Stacey, G. P., and Gladwin, M. T. (1982). Ultrasonic characteristics of a rock mass. *International Journal of Rock Mechanics and Mining Sciences and Geomechanics Abstracts*, 19(1), 25–30. https://doi.org/10.1016/0148-9062(82)90707-0

Moretti, R., Troise, C., Sarno, F., and De Natale, G. (2018). Caldera unrest driven by CO2-induced drying of the deep hydrothermal system. *Scientific Reports*, 8(1), 8309. https://doi.org/10.1038/s41598-018-26610-2

Mukerji, T. and Prasad, M. (2007). Image Processing of Acoustic Microscopy Data to Estimate Textural Scales and Anisotropy in Shales. In M. P. André, et al., (Eds.), *Acoustical Imaging* (Vol 28, pp. 21–29). Springer Netherlands.

Napolitano, F., De Siena, L., Gervasi, A., Guerra, I., Scarpa, R., and La Rocca, M. (2020). Scattering and absorption imaging of a highly fractured fluid-filled seismogenetic volume in a region of slow deformation. *Geoscience Frontiers*, 11(3), 989–998. https://doi.org/10.1016/j.gsf.2019.09.014

Nardoni, C., De Siena, L., Cammarano, F., Magrini, F., and Mattei, E. (2021). Modelling regional-scale attenuation across Italy and the Tyrrhenian Sea. *Physics of the Earth and Planetary Interiors*, 318, 106764. https://doi.org/10.1016/j.pepi.2021.106764

Nishizawa, O. and Fukushima, Y. (2008). Laboratory Experiments of Seismic Wave Propagation in Random Heterogeneous Media. In: Sato H, Fehler M (eds) *Earth Heterogeneity and Scattering Effects on Seismic Waves, Advances in Geophysics*, 50, Academic Press, New York, Chap. 8, pp 219–246

Norris, A. N. (1985). A differential scheme for the effective moduli of composites. *Mechanics of Materials*, 4(1), 1–16. https://doi.org/10.1016/0167-6636(85)90002-X

Nur, A., Mavko, G., Dvorkin, J., and Galmudi, D. (1998). Critical porosity: A key to relating physical properties to porosity in rocks. *The Leading Edge*, 17(3), 357–362. https://doi.org/10.1190/1.1437977

Obermann, A., Planès, T., Larose, E., Sens-Schönfelder, C., and Campillo, M. (2013). Depth sensitivity of seismic coda waves to velocity perturbations in an elastic heterogeneous medium. *Geophysical Journal International*, 194(1), 372–382. https://doi.org/10.1093/gji/ggt043

Paasschens, J., 1997. *Solution of the time-dependent Boltzmann equation*. Phys. Rev. E. 56, 1135.

Parolai, S. (2014). Shear wave quality factor Qs profiling using seismic noise data from microarrays. *Journal of Seismology*, 18(3), 695–704. https://doi.org/10.1007/s10950-014-9440-5

Petrillo, Z., D'Auria, L., Mangiacapra, A., Chiodini, G., Caliro, S., and Scippacercola, S. (2019). A perturbative approach for modeling short‐term fluid‐driven ground deformation episodes on volcanoes: A case study in the Campi Flegrei caldera (Italy). *Journal of Geophysical Research: Solid Earth*, 124, 1036–1056. https://doi.org/10.1029/2018JB015844

Petrosino, S., Damiano, N., Cusano, P., Di Vito, M. A., de Vita, S., and Del Pezzo, E. (2012). Subsurface structure of the Solfatara volcano (Campi Flegrei caldera, Italy) as deduced from joint seismic-noise array, volcanological and morphostructural analysis: subsurface structure of solfatara. *Geochemistry, Geophysics, Geosystems*, 13(7), https://doi.org/10.1029/2011GC004030

Petrosino, S., Cusano, P., and Madonia, P. (2018). Tidal and hydrological periodicities of seismicity reveal new risk scenarios at Campi Flegrei caldera. *Scientific Reports*, 8(1), 1-12

Petrosino, S. and De Siena, L. (2021). Fluid migrations and volcanic earthquakes from depolarized ambient noise. *Nature Communications*, 12(1), 6656. https://doi.org/10.1038/s41467-021-26954-w

Pistone, M., Fife, J. L., Tisato, N., Caricchi, L., Reusser, E., Ulmer, P., Mader, K., and Marone, F. (2021). Seismic Attenuation During Magma Vesiculation: A Combination of Laboratory Constraints and Modeling. *Geophysical Research Letters*, 48(8). https://doi.org/10.1029/2020GL092315

Planès, T., and Larose, E. (2013). A review of ultrasonic Coda Wave Interferometry in concrete. *Cement and Concrete Research*, 53, 248–255. https://doi.org/10.1016/j.cemconres.2013.07.009

Pride, S. R., J. G. Berryman, and J. M. Harris (2004), Seismic attenuation due to wave-induced flow, *Journal of Geophysical Research*, 109, B01201, doi:10.1029/2003JB002639

Prokhorov, D., Lisitsa, V., and Bazaikin, Y. (2021). Digital image reduction for the analysis of topological changes in the pore space of rock matrix. *Computers and Geotechnics*, 136, 104171. https://doi.org/10.1016/j.compgeo.2021.104171

Prudencio, J., Del Pezzo, E., Garcia-Yeguas, A., and Ibanez, J. M. (2013). Spatial distribution of intrinsic and scattering seismic attenuation in active volcanic islands - I: Model and the case of Tenerife Island. *Geophysical Journal International*, 195(3), 1942–1956. https://doi.org/10.1093/gji/ggt361

Prudencio, J., Aoki, Y., Takeo, M., Ibáñez, J. M., Del Pezzo, E., and Song, W. (2017). Separation of scattering and intrinsic attenuation at Asama volcano (Japan): Evidence of high volcanic structural contrasts. *Journal of Volcanology and Geothermal Research*, 333–334, 96–103. https://doi.org/10.1016/j.jvolgeores.2017.01.014

Przybilla, J., Korn, M. and Wegler, U. (2006). Radiative transfer of elastic waves versus finite difference simulations in two-dimensional random media. *Journal of Geophysical Research: Solid Earth*, vol. 111, no. 4.

Przybilla, J. and Korn, M. (2008). Monte Carlo simulation of radiative energy transfer in continuous elastic random media-three-component envelopes and numerical validation. *Geophysical Journal International*, 173(2), 566–576. https://doi.org/10.1111/j.1365-246X.2008.03747.x

Pyrak-Nolte, L.J., Myer, L.R. and Cook, N.G.W. (1990).Transmission of seismic waves across single natural fractures. *Journal of Geophysical Research*, vol. 95, no. B6, pp. 8617-8638.

Rahimi, H., Hamzehloo, H., and Kamalian, N. (2010). Estimation of coda and shear wave attenuation in the volcanic area in SE Sabalan Mountain, NW Iran. *Acta Geophysica*, 58(2), 244–268. https://doi.org/10.2478/s11600-009-0023-8

Rasband, W.S. (2018). *ImageJ*, U. S. National Institutes of Health, Bethesda, Maryland, USA, https://imagej.nih.gov/ij/, 1997-2018.

Rasht‐Behesht, M., Huber, C., and Mancinelli, N. J. (2020). Detectability of Melt‐Rich Lenses in Magmatic Reservoirs From Teleseismic Waveform Modeling. *Journal of Geophysical Research: Solid Earth*, 125(9), e2020JB020264.

Ricco, C., Petrosino, S., Aquino, I., Del Gaudio, C., and Falanga, M. (2019). Some Investigations on a Possible Relationship between Ground Deformation and Seismic Activity at Campi Flegrei and Ischia Volcanic Areas (Southern Italy). *Geosciences*, 9(5), 222. https://doi.org/10.3390/geosciences9050222

Rizzo, R. E., Healy, D., Heap, M. J., and Farrell, N. J. (2018). Detecting the onset of strain localization using two-dimensional wavelet analysis on sandstone deformed at different

effective pressures. *Journal of Geophysical Research: Solid Earth*, Vol 123, pp 10,460–10,478.

Rosas-Carbajal, M., Komorowski, J.-C., Nicollin, F., and Gibert, D. (2016). Volcano electrical tomography unveils edifice collapse hazard linked to hydrothermal system structure and dynamics. *Scientific Reports*, 6(1), 29899. https://doi.org/10.1038/srep29899

Rosenkrantz, E., Bottero, A., Komatitsch, D., and Monteiller, V. (2019). A flexible numerical approach for non-destructive ultrasonic testing based on a time-domain spectral-element method: Ultrasonic modeling of Lamb waves in immersed defective structures and of bulk waves in damaged anisotropic materials. *NDT and E International*, 101, 72–86. https://doi.org/10.1016/j.ndteint.2018.10.002

Rossetti, L. M., Healy, D., Hole, M. J., Millett, J. M., de Lima, E. F., Jerram, D. A., and Rossetti, M. M. M. (2019). Evaluating petrophysical properties of volcano-sedimentary sequences: A case study in the Paraná-Etendeka Large Igneous Province. *Marine and Petroleum Geology*, 102, 638–656. https://doi.org/10.1016/j.marpetgeo.2019.01.028

Rowley, P., Benson, P. M., and Bean, C. J. (2021). Deformation-controlled long-period seismicity in low-cohesion volcanic sediments. *Nature Geoscience*, *14*(12), 942–948. https://doi.org/10.1038/s41561-021-00844-8

Saccorotti, G., Petrosino, S., Bianco, F., Castellano, M., Galluzzo, D., La Rocca, M., et al. (2007). Seismicity associated with the 2004–2006 renewed ground uplift at Campi Flegrei Caldera, Italy. *Physics of the Earth and Planetary Interiors*, 165(1–2), 14–24. https://doi.org/10.1016/j.pepi.2007.07.006

Saito, T., Sato, H., Ohtake, M. (2002). Envelope broadening of spherically outgoing waves in three dimensional random media having power law spectra. *Journal of Geophysical Research*, 107. https://doi.org/10.1029/2001JB000264

Sarout, J. (2012). Impact of pore space topology on permeability, cut-off frequencies and validity of wave propagation theories. *Geophysical Journal International*, 189, 481-492. doi: 10.1111/j.1365-246X.2011.05329.x

Sato, H., Fehler, M. C., and Maeda, T. (2012). *Seismic Wave Propagation and Scattering in the Heterogeneous Earth*: Second Edition. Springer Berlin Heidelberg. https://doi.org/10.1007/978-3-642-23029-5

Scala, A., Serra, M., Festa, G., and Roux, P. (2019). Insight Into the Wave Scattering Properties of the Solfatara Volcano, Campi Flegrei, Italy. *Frontier in Earth Sciences*, 7, 307. https://doi.org/10.3389/feart.2019.00307

Serra, M., Festa, G., Roux, P., Gresse, M., Vandemeulebrouck, J., and Zollo, A. (2016). A strongly heterogeneous hydrothermal area imaged by surface waves: The case of Solfatara, Campi Flegrei, Italy. *Geophysical Journal International*, 205(3), 1813–1822. https://doi.org/10.1093/gji/ggw119

Sertçelik, F. (2012). Estimation of coda wave attenuation in the East Anatolia fault zone, Turkey. *Pure and Applied Geophysics*, 169(7), 1189–1204. https://doi.org/10.1007/s00024-011-0368-1

Shapiro, N. M., Campillo, M., Margerin, L., Singh, S.K., Kostoglodov, V. and Pacheco, J. (2000). The Energy Partitioning and the Diffusive Character of the Seismic Coda. *Bulletin of the Seismological Society of America*, 90(3), 655–665. https://doi.org/10.1785/0119990021

Shea, T., Houghton, B. F., Gurioli, L., Cashman, K. V., Hammer, J. E., and Hobden, B. J. (2010). Textural studies of vesicles in volcanic rocks: an integrated methodology. *Journal of Volcanology and Geothermal Research*, 190(3-4), 271-289. doi: 10.1016/j.jvolgeores.2009.12.003

Shih, P.-.R. and Frehner, M. (2016). Laboratory evidence for Krauklis-wave resonance in fractures and implications for seismic coda wave analysis. *Geophysics*, vol. 81, no. 6, pp. T285-T293.

Singh, A., Regenauer‐Lieb, K., Walsh, S. D. C., Armstrong, R. T., Griethuysen, J. J. M., and Mostaghimi, P. (2020). On Representative Elementary Volumes of Grayscale Micro‐CT Images of Porous Media. *Geophysical Research Letters*, 47(15). https://doi.org/10.1029/2020GL088594

Siniscalchi, A., Tripaldi, S., Romano, G., Chiodini, G., Improta, L., Petrillo, Z., et al. (2019). Reservoir Structure and Hydraulic Properties of the Campi Flegrei Geothermal System Inferred by Audiomagnetotelluric, Geochemical, and Seismicity Study. *Journal of Geophysical Research: Solid Earth*, 124(6), 5336–5356. https://doi.org/10.1029/2018JB016514

Sivaji, C., Nishizawa, O., Kitagawa, G., and Fukushima, Y. (2002). A physical-model study of the statistics of seismic waveform fluctuations in random heterogeneous media: Seismic waves in random heterogeneous media. *Geophysical Journal International*, 148(3), 575–595. https://doi.org/10.1046/j.1365-246x.2002.01606.x

Sketsiou, P., Napolitano, F., Zenonos, A., and De Siena, L. (2020). New insights into seismic absorption imaging. *Physics of the Earth and Planetary Interiors*, 298, 106337. https://doi.org/10.1016/j.pepi.2019.106337

Snieder, R. (2006). The theory of coda wave interferometry. *Pure and Applied Geophysics*, 163(2–3), 455–473. https://doi.org/10.1007/s00024-005-0026-6

Spetzler, J., Sivaji, C., Nishizawa, O., and Fukushima, Y. (2002). A test of ray theory and scattering theory based on a laboratory experiment using ultrasonic waves and numerical simulation by finite-difference method: Laboratory test of ray and scattering theory. *Geophysical Journal International*, 148(2), 165–178. https://doi.org/10.1046/j.1365-246X.2002.01001.x

Stacey, R. (1988). Improved transparent boundary formulations for the elastic-wave equation. *Bulletin of the Seismological Society of America*, 78(6), 2089–2097. https://doi.org/10.1785/BSSA0780062089

Subramaniyan, S., Quintal, B., Tisato, N., Saenger, E. H., and Madonna, C. (2014). An overview of laboratory apparatuses to measure seismic attenuation in reservoir rocks: Apparatuses to measure seismic attenuation. *Geophysical Prospecting*, 62(6), 1211–1223. https://doi.org/10.1111/1365-2478.12171

Takahashi, T., Sato, H., Nishimura, T., and Obara, K. (2007). Strong inhomogeneity beneath Quaternary volcanoes revealed from the peak delay analysis of S -wave seismograms of microearthquakes in northeastern Japan. *Geophysical Journal International*, 168(1), 90–99. https://doi.org/10.1111/j.1365-246X.2006.03197.x

Tamburello, G., Caliro, S., Chiodini, G., De Martino, P., Avino, R., Minopoli, C., et al. (2019). Escalating CO2 degassing at the Pisciarelli fumarolic system, and implications for the ongoing Campi Flegrei unrest. *Journal of Volcanology and Geothermal Research,* 384, 151–157. https://doi.org/10.1016/j.jvolgeores.2019.07.005

Tape, C., Liu, Q., and Tromp, J. (2007). Finite-frequency tomography using adjoint methods—Methodology and examples using membrane surface waves, *Geophysical Journal International*, 168 (3), 1105–1129, https://doi.org/10.1111/j.1365-246X.2006.03191.x

TIMA (2019). TESCAN Orsay Holding. Document, version 1.31. file:///D:/TIMA%201.6/TIMA/help/HTML5/TIMA/Introduction.htm

Tisato, N., and Madonna, C. (2012). Attenuation at low seismic frequencies in partially saturated rocks: Measurements and description of a new apparatus. *Journal of Applied Geophysics*, 86, 44–53. https://doi.org/10.1016/j.jappgeo.2012.07.008

Tisato, N. and Quintal, B. (2013). Measurements of seismic attenuation and transient fluid pressure in partially saturated Berea sandstone: Evidence of fluid flow on the mesoscopic scale. *Geophysical Journal International*, 195(1), 342–351. https://doi.org/10.1093/gji/ggt259

Tisato, N., Quintal, B., Chapman, S., Podladchikov, Y., and Burg, J. (2015). Bubbles attenuate elastic waves at seismic frequencies: First experimental evidence. *Geophysical Research Letters*, 42(10), 3880–3887. https://doi.org/10.1002/2015GL063538

Toksöz, M.N., Johnston, D.H., and Timur, A. (1979), Attenuation of seismic waves in dry and saturated rocks: I. Laboratory measurements, *GEOPHYSICS*, 44: 681-690. https://doi.org/10.1190/1.1440969

Troiano, A., Di Giuseppe, M. G., Patella, D., Troise, C., and De Natale, G. (2014). Electromagnetic outline of the Solfatara–Pisciarelli hydrothermal system, Campi Flegrei (Southern Italy). *Journal of Volcanology and Geothermal Research,* 277, 9–21. https://doi.org/10.1016/j.jvolgeores.2014.03.005

Troiano, A., Isaia, R., Di Giuseppe, M.G., Tramparulo, F.D.A, and Vitale, S. (2019). Deep Electrical Resistivity Tomography for a 3D picture of the most active sector of Campi Flegrei caldera. *Scientific Reports,* 9, 15124. https://doi.org/10.1038/s41598-019-51568-0

Troise, C., G. De Natale, and Christopher R. J. Kilburn. (2006). *Mechanisms of Activity and Unrest at Large Calderas*. London: Geological Society.

Troise, C., De Natale, G., Schiavone, R., Somma, R., and Moretti, R. (2019). The Campi Flegrei caldera unrest: Discriminating magma intrusions from hydrothermal effects and implications for possible evolution. *Earth-Science Reviews*, 188, 108–122. https://doi.org/10.1016/j.earscirev.2018.11.007

Tromp, J., Komatitsch, D., and Liu, Q. (2008). Spectral-Element and Adjoint Methods in Seismology. *Communications in Computational Physics*, 32(1), 1-32.

Vanorio, T., Prasad, M., Patella, D., and Nur, A. (2002). Ultrasonic velocity measurements in volcanic rocks: Correlation with microtexture. *Geophysical Journal International*, 149(1), 22–36. https://doi.org/10.1046/j.0956-540x.2001.01580.x

Vanorio, T., Virieux, J., Capuano, P., and Russo, G. (2005). Three-dimensional seismic tomography from P wave and S wave microearthquake travel times and rock physics characterization of the Campi Flegrei Caldera. *Journal of Geophysical Research*, 110(B3), B03201. https://doi.org/10.1029/2004JB003102

Vanorio, T. and Kanitpanyacharoen, W. (2015). Rock physics of fibrous rocks akin to Roman concrete explains uplifts at Campi Flegrei Caldera. *Science*, 349(6248), 617–621. https://doi.org/10.1126/science.aab1292

Vedanti, N., Malkoti, A., Pandey, O. P., and Shrivastava, J. P. (2018). Ultrasonic P- and S-Wave Attenuation and Petrophysical Properties of Deccan Flood Basalts, India, as Revealed by Borehole Studies. *Pure and Applied Geophysics*, 175(8), 2905–2930. https://doi.org/10.1007/s00024-018-1817-x

Wagner, L. S., Anderson, M. L., Jackson, J. M., Beck, S. L., and Zandt, G. (2008). Seismic evidence for orthopyroxene enrichment in the continental lithosphere. *Geology*, 36(12), 935-938. https://doi.org/10.1130/G25108A.1

Wang, D., Qu, S.L., Zhao, Q., Yin, X.Y. and Zhou, F. (2017). Laboratory studies of ultrasonic wave response of fractures with different lengths: Anisotropy characteristics and coda analysis. *Ultrasonics*, vol. 80, pp. 101-112.

Wegler, U. (2003). Analysis of multiple scattering at Vesuvius volcano, Italy, using data of the TomoVes active seismic experiment. *Journal of Volcanology and Geothermal Research,* 128(1–3), 45–63. https://doi.org/10.1016/S0377-0273(03)00246-4

Wei, W. and Fu, L.-Y. (2014). Monte Carlo simulation of stress-associated scattering attenuation from laboratory ultrasonic measurements. *Bulletin of the Seismological Society of America*, 104(2), 931–943. https://doi.org/10.1785/0120130082

Willis, M.E., Burns, D.R., Rao, R., Minsley, B., Toksöz, M.N. and Vetri, L. (2006). Spatial orientation and distribution of reservoir fractures from scattered seismic energy. *Geophysics*, vol. 71, no. 5, pp. O43-O51.

Withers, P.J., Bouman, C., Carmignato, S., Cnudde, V., Grimaldi, D., Hagen, C.K., et al. (2021). X-ray computed tomography. Nature Reviews Methods Primers 1, 18. https://doi.org/10.1038/s43586-021-00015-4

Woodburn, N., Hardwick, A., Masoomzadeh, H. and Travis, T., (2014). Improved signal processing for sub-basalt imaging. Hydrocarbon Exploration to Exploitation West of Shetlands. *Geological Society of London, Special Publications*, 397, 163-171.

Xu, S. and Payne, M. A. (2009). Modeling elastic properties in carbonate rocks. *The Leading Edge*, 28(1), 66–74. https://doi.org/10.1190/1.3064148

Yoshimitsu, N., Furumura, T., and Maeda, T. (2016). Geometric effect on a laboratory-scale wavefield inferred from a three-dimensional numerical simulation. *Journal of Applied Geophysics*, 132, 184–192. https://doi.org/10.1016/j.jappgeo.2016.07.002

Yoshimoto, K., Sato, H., and Ohtake, M. (1993). Frequency-dependent attenuation of P and S waves in the Kanto area, Japan, based on the Coda-Normalization method. *Geophysical Journal International*, 114(1), 165–174. https://doi.org/10.1111/j.1365-246X.1993.tb01476.x

Yoshimoto, K. (2000). Monte Carlo simulation of seismogram envelopes in scattering media. *Journal of Geophysical Research: Solid Earth*, vol. 105, no. B3, pp. 6153-6161.

Young, N., Isaia, R., and Gottsmann, J. (2020). Gravimetric Constraints on the Hydrothermal System of the Campi Flegrei Caldera. *Journal of Geophysical Research: Solid Earth*, 125(7). https://doi.org/10.1029/2019JB019231

Zhang, X. and Sharma, P. (2005). Inclusions and inhomogeneities in strain gradient elasticity with couple stresses and related problems. *International Journal of Solids and Structures*, 42(13), 3833–3851. https://doi.org/10.1016/j.ijsolstr.2004.12.005

Zhang, Y., Fu, L.-Y., Zhang, L., Wei, W., and Guan, X. (2014). Finite difference modeling of ultrasonic propagation (coda waves) in digital porous cores with un-split convolutional PML and rotated staggered grid. *Journal of Applied Geophysics*, 104, 75–89. https://doi.org/10.1016/j.jappgeo.2014.02.012

Zhao, H., Xiao, Q., Huang, D., and Zhang, S. (2014). Influence of Pore Structure on Compressive Strength of Cement Mortar. *The Scientific World Journal*, 2014, 1–12. https://doi.org/10.1155/2014/247058

Zimmerman, R. W. (1991). Elastic moduli of a solid containing spherical inclusions. *Mechanics of Materials*, 12(1), 17–24. https://doi.org/10.1016/0167-6636(91)90049-6